Mark Johan Meijerink

Coating of $MoSi_2$ healing particles for self-healing thermal barrier coatings

TU Delft

Coating of $MoSi_2$ healing particles for self-healing thermal barrier coatings

By

Mark Johan Meijerink

in partial fulfilment of the requirements for the degree of

Master of Science

in Chemical Engineering
and Materials Science and Engineering

at the Delft University of Technology,

to be defended publicly on Friday October 9, 2015 at 16:00.

Supervisor:	Dr. ir. W.G. Sloof	TU Delft
Thesis committee:	Prof. dr. Ir. S van der Zwaag,	TU Delft
	Dr. ir. W.G. Sloof,	TU Delft
	Dr. ir. J.R. van Ommen,	TU Delft
	Dr. E.M. Kelder,	TU Delft

This thesis is confidential and cannot be made public until December 31, 2015.

TU Delft

Abstract

To increase lifetime of the protective thermal barrier coatings (TBC) in jet engines and other gas turbines, a self-healing approach based on $MoSi_2$ healing particle addition is considered. However, due to rapid oxygen transport in yttria-stabilized zirconia (YSZ), a common TBC material, premature oxidation is a major problem. This thesis investigates the feasibility of coating $MoSi_2$ sacrificial particles with a protective Al_2O_3 shell to prevent this oxidation, while still retaining particle availability upon damage. Two different chemical methods, namely a sol-gel procedure and atomic layer deposition with residual chemical vapor deposition were successfully utilized to coat $MoSi_2$ healing particles.

The microcapsule composition and integrity has been investigated by means of scanning electron microscopy coupled with energy dispersive x-ray spectroscopy, x-ray diffraction and x-ray photoelectron spectroscopy. The results demonstrate that after calcining at 1200 °C for 1h in argon α-Al2O3 shell can be formed and the shell remains intact. Subsequently the heat treated encapsulated particles were embedded in YSZ matrix followed by healing tests at 1100 and 1200 °C. The crack-healing tests proved that the shells produced by both methods remain intact at high temperatures, but also the coatings have a protective effect compared to uncoated MoSi2. Moreover, the embedded particles show a crack healing effect, indicating the feasibility of this self-healing concept.

Samenvatting

Om de levensduur van thermal barrier coatings (TBCs) in gasturbines en vliegtuigmotoren te verlengen, wordt een zelfherstellende coating overwogen, gebaseerd op de toevoeging van $MoSi_2$ deeltjes aan deze coating. Een uitdaging in dit systeem is echter de zeer snelle oxidatie van deze deeltjes door de hoge snelheid van zuurstoftransport in yttria stabilized zirconia (YSZ). In dit werk wordt daarom de haalbaarheid van het aanbrengen van een Al_2O_3 beschermlaag op de $MoSi_2$ deeltjes onderzocht, die het zelfherstellende mechanisme niet blokkeren. Hiervoor zijn twee verschillende chemische methoden voor het aanbrengen van deze coating vergeleken, namelijk sol-gel en Atomic Layer Deposition met residual Chemical Vapor Deposition (ALD/rCVD).

De eigenschappen en microstructuur van de met beide methoden succesvol geproduceerde microcapsules zijn geanalyseerd met behulp van scanning electron microscopy (SEM) gecombineerd met energy dispersive x-ray spectroscopy (EDS), x-ray diffraction (XRD) en x-ray photoelectron spectroscopy (XPS). Deze resultaten geven duidelijk aan dat het mogelijk is om na calcineren in argon op 1200 °C gedurende 1 uur, een beschermlaag van α-alumina gevormd kan worden en dat deze laag intact blijft. Deze microcapsules zijn daarna ingebed in YSZ, gevolgd door hersteltesten op 1100 en 1200 °C. Deze testen lieten zien dat de capsules inderdaad in staat zijn de deeltjes te beschermen, vergeleken met niet beschermde deeltjes en intact blijven op hoge temperaturen. Ook het composiet blijk van enig zelfherstellend vermogen, wat aangeeft dat dit inderdaad een interessant concept is.

List of Tables

List of Figures

List of abbreviations

ALD = Atomic Layer Deposition
rCVD = Residual Chemical Vapor deposition
YSZ = Yttria Stabilized Zirconia
TBC = Thermal Barrier Coating
TGO = Thermally Grown Oxide
BC = Bond Coat
PZC = Point of Zero Charge
TMA = Trimethylaluminium
SEM = Scanning Electron Microscopy
EDS = Energy-Dispersive x-ray Spectroscopy
XRD = X-Ray Diffraction
BET = Brunauer-Emmett-Teller physical adsorption model
XPS = X-ray Photo-electron Spectroscopy
ICP-OES = Inductively Coupled Plasma Optical Emission Spectroscopy
XRF = X-Ray Fluorescence
TGA = Thermo-Gravimetric Analysis
DSC = Differential Scanning Calorimetry
EPMA = Electron Probe MicroAnalysis
SPS = Spark Plasma Sintering
SG-10g = wind sifted $MoSi_2$ particles coated with 10g aluminium tri-sec-butoxide per 10g $MoSi_2$
SG-20g = wind sifted $MoSi_2$ particles coated with 20g aluminium tri-sec-butoxide per 10g $MoSi_2$
ALD-25C = wind sifted $MoSi_2$ particles coated with the ALD/rCVD method using 25 cycles
ALD-40C = wind sifted $MoSi_2$ particles coated with the ALD/rCVD method using 40 cycles
$MoSi_2B$ = $MoSi_2$ particles containing 2 wt% alloyed boron
PSD = Particle size distribution
BSE = BackScatter Electron image

Table of contents

1-Introduction

1.1 General

In 1972, the club of Rome brought to public attention one of the major problems humanity faces. In their well-known report [1] the limits to economic growth and increasing human prosperity are described, focusing particularly on the limited supply of oil. As oil is currently the main source of fuel for transportation and suitable alternatives are not able to supply enough fuel in a cost-effective manner, it is vital to use current reserves as efficiently as possible.

This is especially true for gas turbines and other high-temperature turbines. A good example is the aviation industry, where fuel costs for jet engines can account for as much as 30% of the overall costs of a flight [2]. According to Carnot's theorem, the best way to increase efficiency would be to increase the operating temperature [3]. However, current turbines already operate at temperatures significantly above the creep limit of the used nickel superalloys [4]. To prevent breakdown of the structural parts, a (~0.5 mm thick) thermal barrier coating (TBC) in combination with internal gas cooling are applied to prevent overheating. This allows especially the most creep-sensitive parts, the turbine blades, to endure these extreme environments [5].

However, due to thermal expansion coefficient mismatch between the TBC, usually made of yttria-stabilized zirconia (7 wt% Y_2O_3–ZrO_2, YSZ) and the nickel superalloys, application of these coatings is difficult and significant mismatch stresses arise during heating and cooling of the engine. Even though a (~250 µm) bond coat (BC) with a (0.6-3.0 µm) thermally grown oxide (TGO) for oxidation protection of the superalloy is applied, this mismatch together with the growth of the oxide layer results in unavoidable crack growth and spallation damage in the TBC and frequent replacement of the coating is therefore required [6]. However, the work of Carabat et al. [7] used a different approach to repair damage autonomously, based on the inclusion of sacrificial $MoSi_2$ healing particles that oxidize, expand and fill the crack when it is close to the particle.

1.2 Protection of healing particles

There is however a challenge still to be overcome with this proposed system. This is because YSZ is very transparent to oxygen at the turbine operating temperatures (1250-1500K depending on engine and location in the TBC [5]) and therefore significant premature oxidation of $MoSi_2$ is present. To prevent premature oxidation, a shell has to be applied around these particles that both protects against oxidation and allows cracks to grow through it to allow for oxidation when damage is present. Based on a preliminary literature study, which can be found in appendix I, the most suitable materials for such a coating were found to be α-alumina (α-Al_2O_3), zircon ($ZrSiO_4$) and mullite ($Al_6Si_2O_{13}$).

However, application of coatings on $MoSi_2$ has rarely been investigated, mainly due to the excellent oxidation resistance of the bulk material at high temperature, resulting from the formation of a thick homogeneous SiO_2 layer. For small (10-30 µm) particles, this formation of a native oxide layer would not be feasible though, as this would require most of the particle to be oxidized even before incorporation into the TBC [7]. Therefore a protective coating has to be applied beforehand and during the aforementioned preliminary literature study, the most suitable methods were found to be sol-gel and Atomic Layer Deposition (ALD) routes.

The goal of this research is therefore to find an optimal route to produce $MoSi_2$ particles coated with α-Al_2O_3 that prevents significant premature oxidation, while at the same time allowing cracks to grow through the coating. This will be done by optimizing sol-gel and ALD techniques followed by thermal treatment to create different coatings. First, particles will be coated with both methods and they will be compared on thickness and morphology. This is followed by heat treatment experiments and subsequent comparison of resulting microstructure, which includes crystallinity, defect types and defect concentrations obtained, hardness and grain size. Oxidation tests will also be performed on the final particles and compared to a developed diffusion model to investigate oxidation resistance and follow microstructural development during operation. Finally, healing tests will be performed to show the validity of the self-healing concept and the possibility of crack propagation through the coating.

The structure of this report is as follows. Chapter 2 introduces the background needed to understand the TBC system, the self-healing system, the chemical methods to apply coatings and the subsequent heat treatment. In chapter 3, the thermodynamics of the system are described, followed by the development of a diffusion model. Chapter 4 then describes the experiments performed for synthesis and characterization of the coated particles, testing performance and validating the diffusion model. The results of these experiments are then shown and discussed in chapter 5, followed by the main conclusions in chapter 6 and recommendations for continuation of the research in chapter 7. Furthermore, the original research plan is described in appendix II.

2-Theory

This chapter introduces the main concepts regarding self-healing thermal barrier coatings and provide an overview of the most essential literature on coating particles. First, the thermal barrier coating system will be described in more detail, together with an introduction of the self-healing system, the particle shell and the materials involved. This is followed by an introduction of the two main chemical coating methods, sol-gel and Atomic Layer Deposition (ALD/rCVD) and how their individual chemistries can be optimized for obtaining protective shells. Furthermore, theory of the required subsequent heat treatment is also described. Finally, an introduction of crack propagation through the shell is presented.

2.1 Thermal barrier coatings

2.1.1 Regular thermal barrier coatings

A thermal barrier coating (TBC) is any type of coating that is used to limit heat transport across this coating. Such coatings are present in many different applications, but as mentioned in the introduction, the focus in this work is on TBCs for gas turbines. A gas turbine is a type of internal combustion engine, which consists of three stages: the rotating compression area, the combustion zone and the exhaust, as is shown in Figure 2.1a.

Gas turbines use compressed air and chemical energy contained in the fuel to produce high-temperature, high-pressure gas to power the rotating compressor at the start of the engine, which is connected to the exhaust area by a shaft. The remaining available work is either used to power any other devices connected to the shaft (an electricity generator for example) or can exit the exhaust area at high velocity to produce thrust (such as in a jet engine). Although current gas turbines are already an efficient way to convert energy, with modern combined cycle (in which waste heat is used by a regular steam turbine) electricity producing gas turbines reaching a turbine thermal efficiency of 39.5% and a total efficiency of nearly 60% [8], significant improvements are still possible. According to Carnot's theorem, increasing operating temperature could still result in a significant efficiency gain [3].

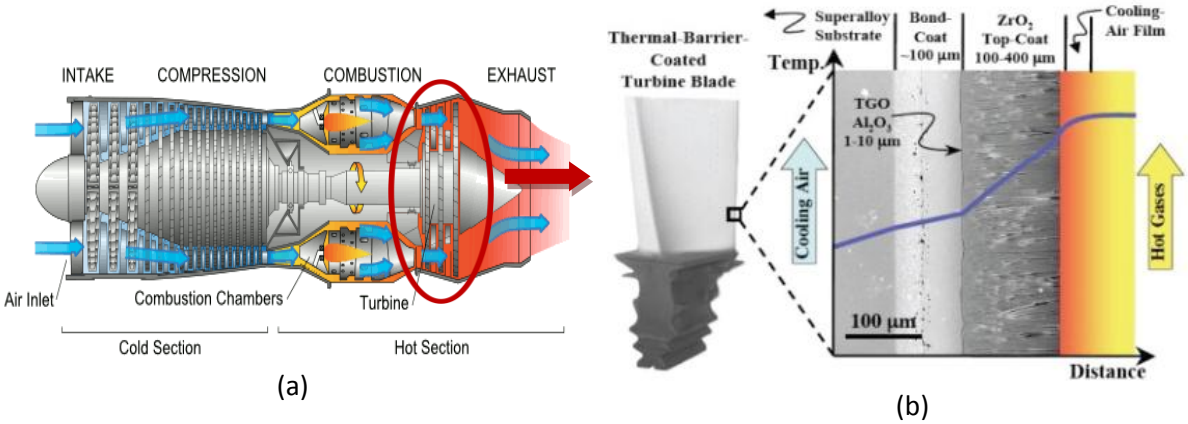

Figure 2.1: *Jet engine layout (a) and interface between turbine blade and hot gas (b). [9], [10]*

To allow for these high operating temperatures, advanced cooling methods and increasingly complex layers of coatings are necessary to surpass the temperature limits of currently used nickel superalloys, especially in the most critical component: the turbine blades. An overview of the current

coating system is shown in Figure 2.1b [10], in which the superalloy turbine blade is shown on the left. Cold air is blown through these turbine blades to cool them [11] and allow a temperature gradient to exist. The blade is coated with a ~100-250 µm bond coat (BC) containing significant amounts of aluminium. This aluminium is oxidized to produce a continuously growing Al_2O_3 thermally grown oxide (TGO) to protect the blade against high temperature oxidation. Compositions of these superalloys and bond coats are very complex and shown in the preliminary study in appendix I.

On top of this TGO, a 0.1-0.5 mm TBC is present to protect the entire blade against the immense heat of the combusted gases, which can reach a gas temperature in excess of 1500 °C [8]. Finally a film of cooling air is also blown along the outside of the blade to limit heat transport from the hot gas to the surface of the TBC, allowing for a maximum TBC surface temperature of roughly 1200 °C . This however still requires a thermal gradient of 200 °C over the coating to reach the limit of the nickel superalloys [4]. For this reason, TBCs are often made from partially yttria stabilized zirconia (YSZ) containing roughly 7 wt% yttria, although other materials are also under investigation [12].

However, almost all thermal barrier coatings are oxides, which suffer from an important drawback: their low thermal expansion coefficient compared to nickel superalloys. This results in a significant thermal expansion mismatch and subsequent compressive stresses in the TBC during cooling of the gas turbine. Because oxides are relatively brittle, these stresses generate small cracks in the TBC, especially close to the interface with the TGO [6]. This process is shown in Figure 2.2a. These small cracks can then coalesce to form larger cracks and cause further delamination. Combined with the compressive stresses, this can cause buckling and finally complete spallation of the TBC in certain areas when the cracks start to grow perpendicular to the coating, as can be seen in Figure 2.2b. Because of the sensitivity of the nickel superalloys to higher temperatures, the final result is extremely rapid degradation of the turbine blade. To prevent degradation and possible catastrophic failure, TBCs have to be inspected and replaced regularly [13].

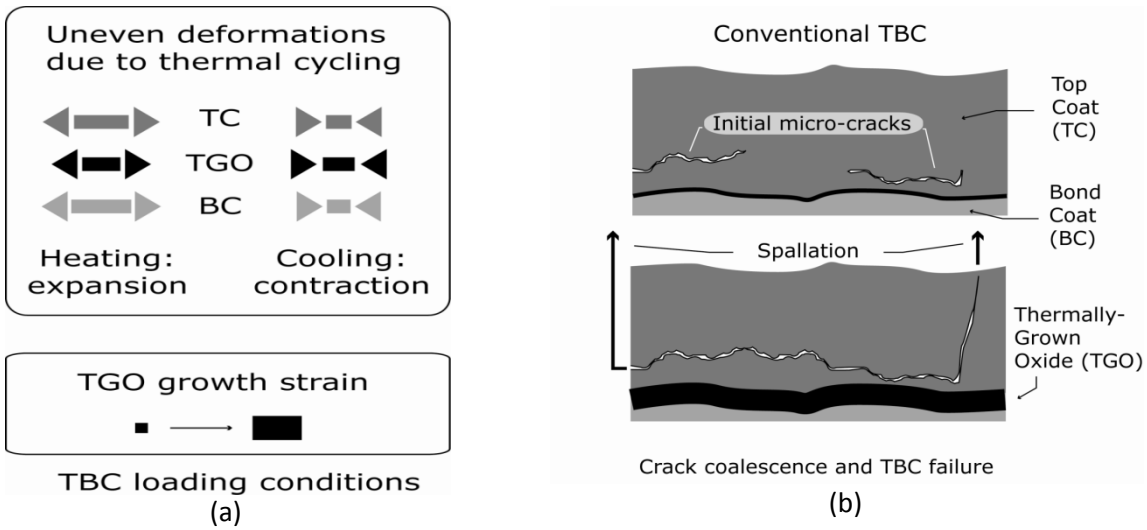

Figure 2.2: *Causes of spallation in TBCs illustrated with (a) showing the source of compressive stresses and (b) the coalescence of microcracks and spallation. [14]*

2.1.2 Self-healing in thermal barrier coatings

Instead of damage management, which consists of complete replacement of the coating once it is too damaged to continue functioning, another option is the use of self-healing materials. These materials are able to repair damage before failure occurs and can thereby prolong the lifespan of

materials [15]. A method for applying the self-healing concept to TBCs was suggested by W.G. Sloof and S. van der Zwaag [16]. This concept introduces $MoSi_2$ particles of 20 to 25 µm as a self-healing agent, coated with a shell of Al_2O_3 to prevent oxidation. These particles are then introduced in the TBC, close to the TGO, where most of the damage forms.

The self-healing mechanism is based on the oxidation of $MoSi_2$ to form SiO_2 and gaseous MoO_3 according to reaction 2.1. When a crack grows through the shell, the particle is exposed to oxygen and the reaction is able to proceed. Because the molar volume of $2SiO_2$ is larger than the molar volume of $MoSi_2$, the material will expand to 238% of the original volume upon complete oxidation and is therefore able to fill the crack with SiO_2, while the MoO_3 sublimates and escapes through the pores of the YSZ. SiO_2 can also react with the matrix of ZrO_2 to form $ZrSiO_4$, better known as zircon. As the toughness of zircon is higher than the toughness of YSZ, complete strength recovery and crack healing is possible under the right conditions [17]. This self-healing mechanism is also illustrated in Figure 2.3.

$$2\,MoSi_{2\,(s)} + 7\,O_{2\,(g)} \rightarrow 2\,MoO_{3\,(g)} + 4\,SiO_{2\,(s)} \qquad (2.1)$$

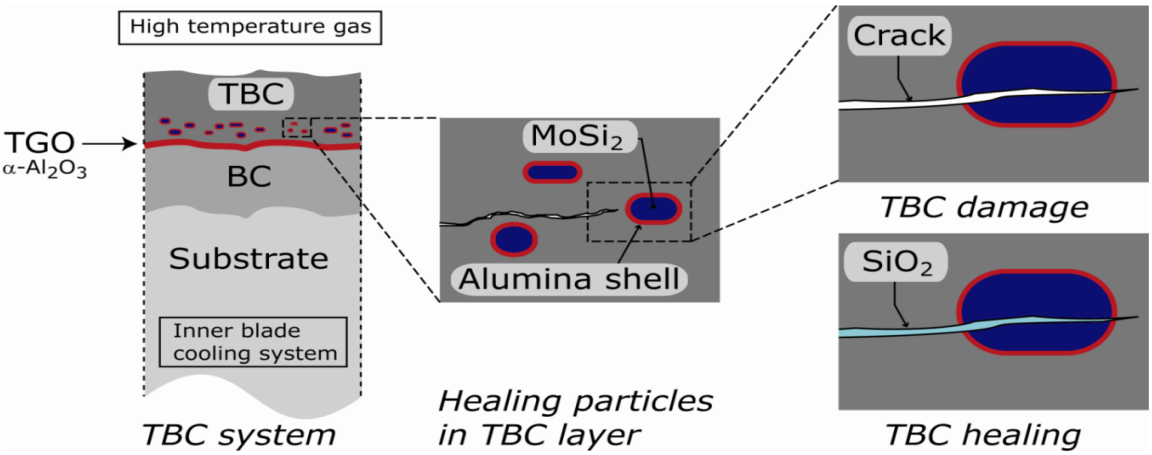

Figure 2.3: ***The self-healing thermal barrier coating system with on the left the whole turbine blade coating system, zooming in on the particles on the right. Upper part is before healing and the lower part after healing. [18]***

2.1.3 Protective shells for self-healing capsules

As mentioned before, $MoSi_2$ poses challenges though. The material is supposed to oxidize rapidly at temperatures between 1000 °C and 1200 °C in an oxygen-containing atmosphere with a partial oxygen pressure P_{O2} between 10 and 10000 Pa[19]. Furthermore, YSZ is very transparent to oxygen, indicated by its common use as solid oxide fuel cell barrier material [20]. The YSZ used in TBCs is also very porous to accommodate the compressive stresses to a certain extend [6].

Although bulk $MoSi_2$ can form a protective SiO_2 coating at temperatures above 800 °C, the thickness of this coating usually several µm [21], which would consume a significant part of the particle material. The formation of SiO_2 would also lead to a reaction with ZrO_2 to form zircon. To prevent this from happening, a coating is necessary. Appendix I shows the different materials investigated for this study, recommending Al_2O_3 as the most optimal shell material, while other interesting choices are mullite ($Al_6Si_2O_{13}$) and zircon ($ZrSiO_4$).

The main purposes of this shell are to protect the particle itself from high-temperature oxidation and to allow a crack to grow through the coating. Therefore the main requirement for this shell is to have a low diffusion of oxygen and counterions. Other requirements for low diffusion is the absence or minimization of defects that can act as a fast diffusion pathway. This includes, among others, pores, cracks, grain boundaries and vacancies. This also requires the final shell to be completely closed and of homogeneous thickness. The diffusion of oxygen through the coating will be discussed in more detail in chapter 3 however.

It is also important that defects do not form during manufacture of these shells, the TBC system or during operation in the coating. According to previous research, especially cracks are likely to occur [22]. These cracks form due to stress build-up caused by either phase transformations and associated volume changes or excessive oxidation of the substrate $MoSi_2$ and resulting volume expansion. Stress build-up from phase transformations can be prevented by ensuring a stable and fully densified phase is created before operation. In the case of Al_2O_3, the only stable phase is the α phase or corundum structure, but many transition aluminas are known and usually form before the α phase [23]. Therefore, proper heat treatment to obtain the α phase and obtain full densification is required to form the final coating.

The interfaces of the shell with the substrate and the TBC itself could also act as another form of stress. This is partially due to growth stress from SiO_2 oxidation on the substrate side, which is another important reason to limit diffusion through the shell. Another possibility on both sides of the shell is the mismatch in thermal expansion. The coefficients of thermal expansion for Al_2O_3 and $MoSi_2$ are very similar however, resulting in low stresses in the coating on this side. There is however a thermal expansion mismatch between YSZ and the particles, which would probably result in stress build-up around the particles. This is studied in more detail by Turteltaub et al. [14]

For crack propagation through the shell and into the particle, Turteltaub [14] found that interface strength is a critical factor. The preferred interface should be strong at the TBC side and should be relatively weak at the particle side. Flaws in the particle could help due to coalescence of the two cracks. This also holds for cracks in the shell that do not reach either of the interfaces, but in this case the crack would not necessarily grow through the protective layer and reach the particle, which is undesired. If the crack would reach sufficiently far into the shell, accelerated local oxidation due to a thinner coating might fracture the shell completely anyway though. However, flaws in the shell should still be avoided because they could initiate cracks when stresses are present. A more elaborate discussion on the interfaces with both sides is presented in chapter 3.

2.1.4 Material properties of main components

To understand the self-healing TBC system better, some information on the materials involved is also necessary. Therefore, some information on Al_2O_3, $MoSi_2$, YSZ and the healing products SiO_2 and $ZrSiO_4$ is presented here, along with the most important thermal properties in Table 2.1.

Alumina (Al_2O_3) is one of the most well-studied ceramics due to its many applications which are the result of its excellent properties and its availability. Alumina in its stable α phase is a very hard and relatively strong ceramic that has an extremely high melting temperature of 2072 °C [24]. This high melting temperature in combination with other favourable thermal properties, such as a low coefficient of thermal expansion, as is shown in Table 2.1 and its low ionic conductivity at high temperatures, making it a very good candidate for corrosion protection scales [25].

The only thermodynamically stable phase is α-Al_2O_3, which crystallizes in the corundum crystal structure shown in Figure 2.4. However, many other metastable phases are known and many of them have important uses, resulting from their often high surface areas. One of the more famous examples is the extensive use of γ-Al_2O_3 as both a catalyst and a catalyst support [26]. These metastable phases are usually divided by packing of the oxygen anion lattice in either an FCC (for γ, δ, θ and η among others) or HCP (for α, κ and χ) packing [23]. The difference between the separate phases is the distribution of the Al^{3+} cations in the anion lattice.

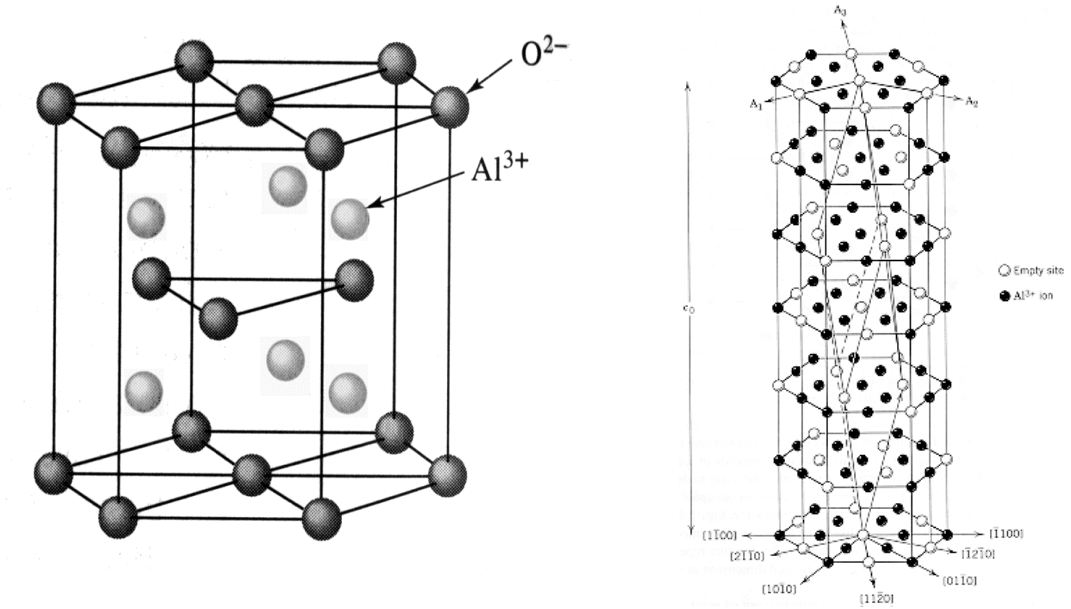

(a) (b)

Figure 2.4: ***The corundum crystal structure with (a) showing the regular structure with both Al^{3+} and O^{2-} [27] and (b) showing the locations of the empty alumina sites in the structure [28].***

Molybdenum disilicide ($MoSi_2$) is one of the thermodynamically stable intermetallic phases of molybdenum and silicon, the phase diagram of which is shown in Figure 2.5. Usually considered to be a ceramic, its high melting point of 2030 °C [29] makes this material an interesting refractory. Due to its intermetallic nature, its electrical conductivity is high [29]. Bulk $MoSi_2$ is also resistant to high temperature oxidation due to the formation of a protective SiO_2 scale at high temperatures. Due to the combination of these properties, $MoSi_2$ is often used as a heating element in applications that require high temperatures.

The crystal structure of $MoSi_2$ is tetragonal (space group I4/mmm), although a metastable hexagonal structure also exists at low temperatures [30]. The stable tetragonal structure is shown in Figure 2.6.

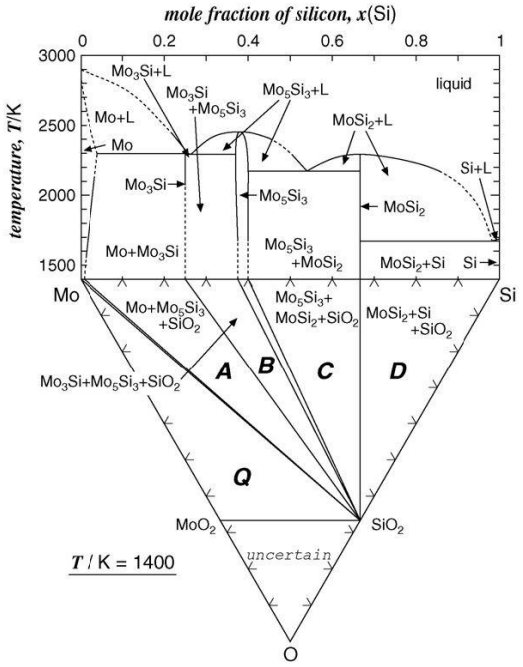

Figure 2.5: *The temperature dependent phase diagram of molybdenum and Silicon, along a three component phase diagram of Mo, Si and O at 1200 °C. [31]*

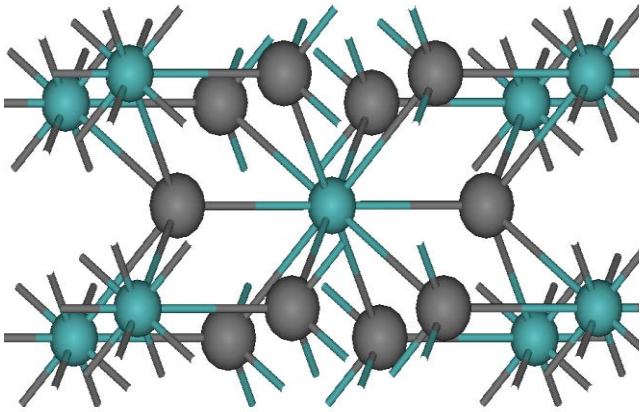

Figure 2.6: *The crystal structure of the thermodynamically stable tetragonal structure of $MoSi_2$. [30]*

Zirconia or ZrO_2 is another refractory ceramic that is well-known for its high temperature stability. It is in fact one of the most refractory oxides currently known, with a melting point of 2715 °C. However, pure zirconia has three known phase transformations, namely the low temperature monoclinic phase (<1170 °C), the intermediate tetragonal phase (1170 °C - 2340 °C) and the high temperature cubic phase (>2340 °C). These phase transformations are associated with significant volume changes; an 8% increase in the case of the tetragonal to monoclinic transformation. High temperature phases are also difficult to retain due to the transformation temperatures being relatively high too.

High temperature phases can however be stabilized by doping with other oxides. The most common oxide for stabilization is yttria (Y_2O_3) and can stabilize both the tetragonal and the cubic phase at room temperature. Adding sufficient yttria (roughly 18 mole%) even results in the cubic phase being the thermodynamically stable phase at room temperature, as is shown in the ZrO_2-rich zirconia-yttria phase diagram in Figure 2.7[32]. Usually, only 7-8 mole% of yttria is used though, stabilizing the cubic phase enough to be metastable at room temperature when quenching from the liquid phase, resulting in cubic yttria stabilized zirconia (YSZ). The crystal structure of this cubic YSZ is shown in Figure 2.8, with Y^{3+} substituting randomly for Zr^{4+}, forming oxygen vacancies in the process, according to reaction 2.2 in the Krüger-Vink notation.

$$Y_2O_3 \rightarrow 2\,Y_{Zr}^{'} + 3\,O_O + V_O^{\circ\circ} \qquad (2.2)$$

These oxygen vacancies and their mobility at high temperature are the reason that YSZ is very conductive to oxygen at higher temperatures. Although this can be useful for some applications, such as fuel cells[33], it is detrimental to any system that is sensitive to high-temperature oxidation [6].

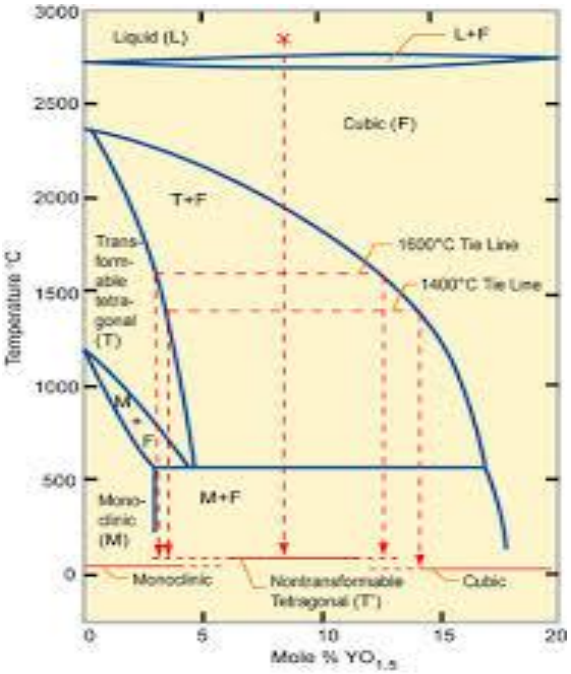

Figure 2.7: *The ZrO_2-Y_2O_3 phase diagram in the ZrO_2 rich region, showing the different phases of zirconia and their stability depending on temperature and yttria content. [32].*

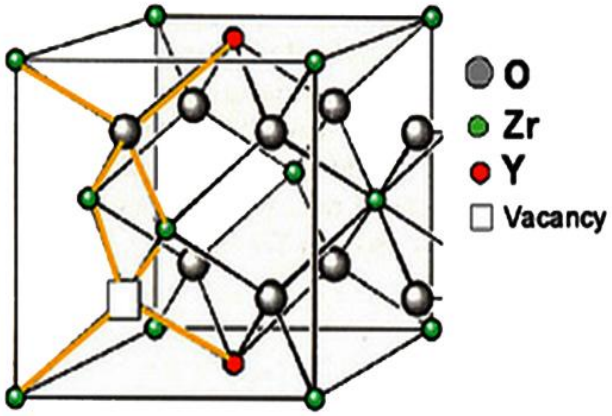

Figure 2.8: *The crystal structure of cubic YSZ with Y substituting randomly for Zr [33].*

The main healing agent in the TBC system is SiO_2, another very important and well-studied ceramic. Although less temperature-resistant than the other ceramics mentioned before, it is still a refractory material with a melting temperature of 1713 °C [34]. Silica is one of the main constituents of earth's crust and besides having very interesting high-temperature properties, is also known for the many different (usually metastable) crystal structures it can form, especially in combination with other oxides such as Al_2O_3, CaO, MgO or iron oxides. These are known as the silicates and many are important minerals.

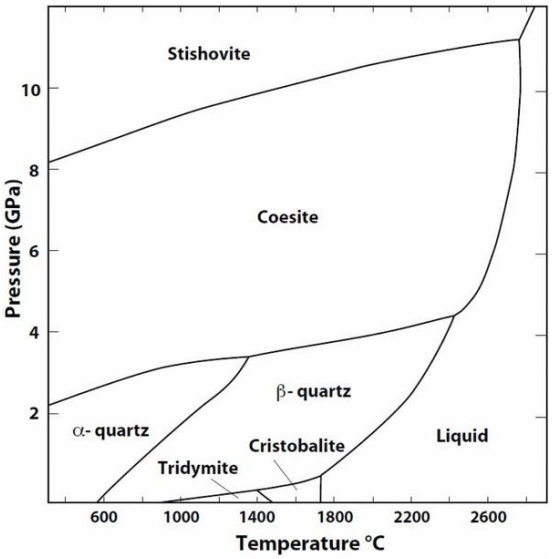

Figure 2.9: *The temperature-pressure phase diagram of silica [35].*

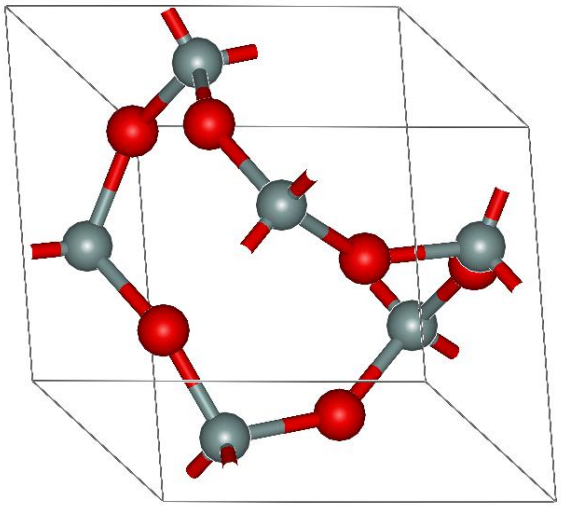

Figure 2.10: *Crystal structure of trigonal α quartz [36].*

Pure SiO_2 can exist in multiple phases, depending on temperature. Trigonal α quartz is the most stable room temperature crystal structure, but at higher temperatures hexagonal β quarts, tridymite and cristobalite become more stable, as is shown in the SiO_2 phase diagram in Figure 2.9 [35]. Whether tridymite is stable or metastable is sometimes disputed however, mainly because small amounts of impurities are required for the transformation from quartz to tridymite. In very pure silica, quartz will directly transform into cristobalite [37]. All crystal structures are however based on SiO_2 tetrahedra, as is illustrated in Figure 2.10, which shows the crystal structure of α-quartz. Along with these crystal structures, another form of these tetrahedra is amorphous silica, which is also often formed and remarkably stable. This is illustrated by glass, the most well-known amorphous form of SiO_2 (along with some other components).

When SiO_2 reacts with the YSZ according to reaction 2.3, zircon or zirconium silicate ($ZrSiO_4$) gets formed. This extremely resilient silicate of zirconia is both very tough and strong for a ceramic material. Because of this and its suitable thermal properties [32], complete strength recovery of the TBC is possible. The zircon structure is similar to the SiO_2 structure in that it also consists of tetrahedra, but in zircon the ZrO_4 and SiO_4 tetrahedra alternate. They crystallize in a body-centered tetragonal crystal structure (space group I 4_1/amd), which is shown in Figure 2.11.

$$\mathbf{ZrO_{2\,(s)} + SiO_{2\,(s)} \rightarrow ZrSiO_{4\,(s)}} \qquad \mathbf{(2.3)}$$

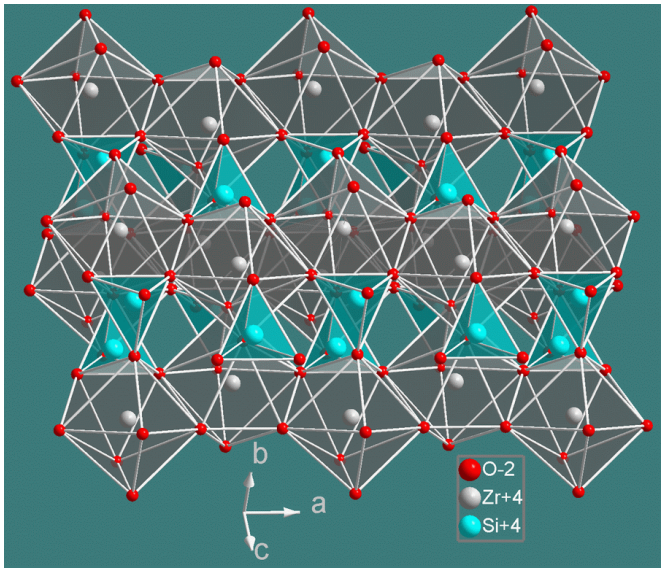

Figure 2.11: *Crystal structure of zirconium silicate [17].*

Table 2.1: *Important thermal properties, namely melting temperature, coefficient of thermal expansion and thermal conductivity of the main materials tabulated based on data from the (Japanese) National Institute of Materials Science (NIMS).*

Material	Melting temperature (°C)	Coefficient of thermal expansion (10^{-6} K^{-1})	Thermal conductivity (W m^{-1} K^{-1})
Al_2O_3	2072	8.0	39
$MoSi_2$	2030	7-10	70
ZrO_2 7mol%Y_2O_3	2715	10.3	2
SiO_2	1713	0.59	1.4
$ZrSiO_4$	1676*	5.0	3.5

*Decomposes

2.2 Sol-gel

Although it is now understood that the materials involved in the self-healing system are suitable, this will only hold if produced in a suitable manner. One of the methods selected in appendix I that would be able to achieve the required final microstructure described in both appendix I and chapter 2.1.3 is the sol-gel method, which will be introduced here.

2.2.1 Sol-gel chemistry

A sol-gel process is difficult to define and currently many different definitions exist. These definitions vary in whether the degree of mixing and homogeneity should be on the atomic level or if colloidal mixing could also be considered sol-gel processing. Another point of discussion is whether sol-gel can also include the processing of a single oxide or that only multicomponent oxides should be included. Furthermore, novel sol-gel techniques allow for the production of certain nitrides, sulfides and carbides, raising the question to whether sol-gel should be restricted to oxides. To avoid any confusion, in this thesis the broad definition of a sol-gel process from the book of A.C. Pierre [38] will be used, which reads: "A sol-gel process is a colloidal route used to synthesize ceramics with an intermediate stage including a sol and/or a gel state."

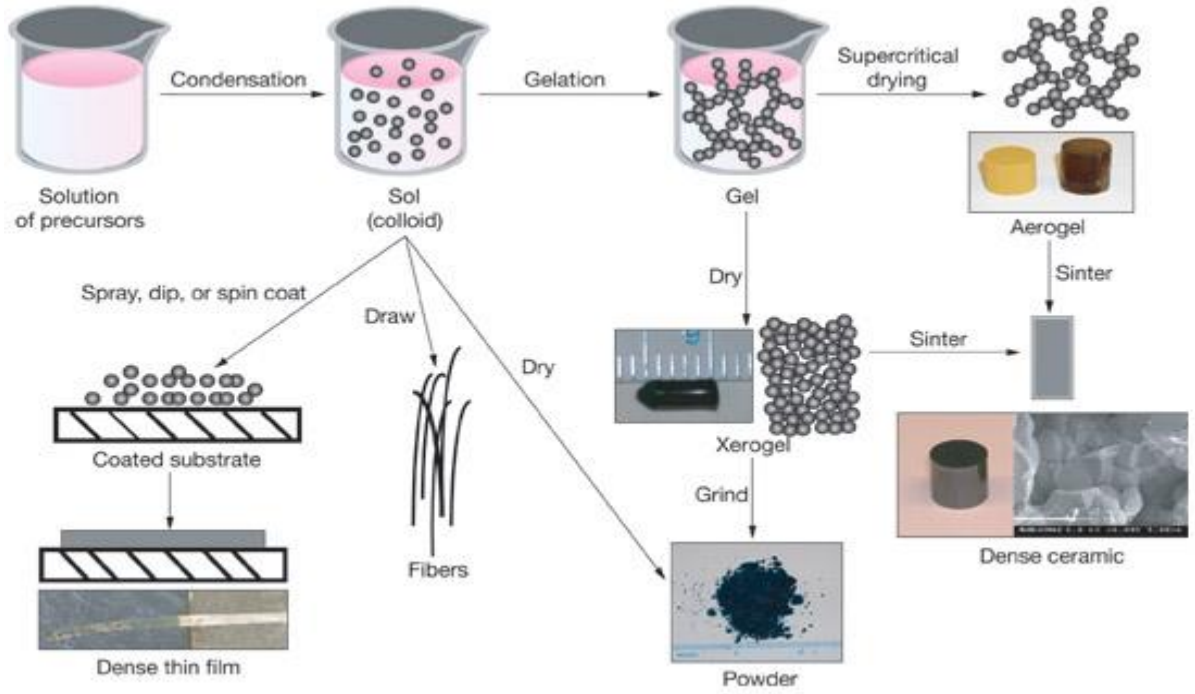

Figure 2.12: ***A schematic representation of the sol-gel process, with multiple possible microstructures depending on processing route [39].***

This process is schematically shown in Figure 2.12 and highlights that any sol-gel process consists of multiple steps and starts with the preparation of a solution or multiple separate solutions of precursors. This solution should then condensate, either by a chemical reaction or by removal of the solvent to form a sol. A sol is a colloidal solution, which means it is a stable suspension of colloidal solid particles. This can consist of either very small particles of bulk material or large macromolecules (usually consisting of 10^3 atoms or more) [40]. It should be noted here that stable is of course relative. A sol usually has a tendency to evolve to a more gel-like state and is only stable for a limited amount of time. This is usually not a problem, as long as the sol is stable long enough for its application.

When this sol evolves to a gel, a network starts to form. Particles connect or macromolecules bond, rigidifying the system. This network still contains a significant amount of liquid, but due to its significant and abrupt increase in viscosity, does not completely behave like a liquid anymore [38]. Due to the small particles and homogeneous distribution of components in the liquid, the resulting gel is very homogeneous. This results in a very homogeneous end material as well.

After the sol or gel is formed, it is first dried to remove the liquid phase completely. In the case of gels, this dried gel is called a xerogel if dense or an aerogel if porous. Many drying and forming processes can be used to obtain a variety of materials and components. Gels with sufficient viscosity can be formed easily but will retain their shape while drying and solidifying. Sols do not necessarily need to gelate before being applied. Especially in the case of coatings, several techniques exist to apply a sol to a substrate and have gelation initiate afterwards, as is also shown in Figure 2.12. This is especially useful if phase separation is an issue for the sol-gel system [38]. When sol-gel is used to form ceramic components, a subsequent heat treatment is often required to obtain the desired final phase(s). This heat treatment for alumina gels will be described in chapter 2.4.

One of the challenges of sol-gel processes is the complexity of the process due to the many phases and chemical species involved. There are many different parameters in each stage that influence the final result. Furthermore the chemistry of sol-gel techniques is complex and not fully understood [38]. Many parameters are important in this system, such as the chemistry of the precursor solution(s)/sol/gel, the precursor used, the processing route and the possible addition of binders, fillers and other compounds [41].

Precursors for ceramic materials can be divided in three broad categories: metal salts, alkoxides and powders obtained from bulk material. Metal salts are usually quite soluble in the solvent and form colloids by hydrolysis and subsequent condensation of OH bridges, as described in [38]. Alkoxides on the other hand are metals bonded to the oxygen atom of a deprotonated alcohol and react rapidly with H_2O, combined with condensation, as is shown in reaction 2.4, taking an aluminium alkoxide as an example. Finally, powders obtained from bulk material only have to be properly dispersed to form a sol, assuming they are sufficiently small in size.

$$\mathbf{Al(OR)_3 + 2\ H_2O \rightarrow AlOOH + 3\ R\text{-}OH} \qquad \mathbf{(2.4)}$$

Chemical environment and concentrations of the species present have a significant influence on the hydrolysis and condensation reactions and therefore on the sol-gel process. This is mainly due to electrostatic interactions between the ionic and polar species present. Therefore, pH and polarity of the solvent are especially important for behavior and evolution of the system.

Another important parameter is the processing route, which is the way the system will evolve from the precursor solution(s) to the final product. Of critical importance here are the sol aging time and temperature, as these are critical to control gelation of the sol. This gelation is due to the aggregation of the colloidal particles. Due to brownian motion of very small particles, collisions are frequent and if attractive forces between the particles are larger than repulsive forces, they rapidly stick together and form a gel. Attractive forces between the particles are mainly Van-der-Waals forces [42], while repulsive forces that can prevent or delay this gelation are usually either electrostatic or steric [41].

2.2.2 Sol-gel coatings

Although sol-gel methods are very versatile, coating substrates using a sol-gel method usually requires the system to be a sol or at least not fully gelated, as is shown in Figure 2.12. And even though alumina is one of the most investigated materials produced by sol-gel, most of these are related to bulk alumina, especially for catalytic applications. However, coatings of alumina prepared by a sol-gel route have been investigated and used frequently for different applications [39] [43] [44].

Some processes use aluminium salts or sometimes combinations of salts and alkoxides [45] in an aqueous environment. Most of the investigations focus on the Yoldas method [46] though, which hydrolyzes an aluminium alkoxide in an aqueous environment to obtain alumina gels that can be used for coatings [44]. This route has been applied to many substrates with many different functions, of which the corrosion and scratch protection of stainless steel [41] and the coating of carbide cutting tools to protect against wear and high temperature oxidation [47].

It should be noted though that the stainless steel protective coating was not completely transformed to α-alumina and it therefore failed after a few or in some cases even one thermal cycle from room temperature to 900 °C and back to room temperature due to transformation stresses. This highlights the importance of proper heat treatment again and that sol-gel methods are sensitive to cracking from volume changes, which is also observed in many other investigations [41]. The coating of $MoSi_2$ with alumina by sol-gel has however not been investigated yet due to its excellent high-temperature oxidation resistance as a bulk material [29], except for the work of Carabat et al. [22].

An advantage of bulk materials is that application of the sol is relatively straightforward, as the component to be coated can simply be dipped in the aqueous sol and slowly pulled out, a process named dip coating [38]. Another possibility is the use of spin coating, which is also relatively straightforward. However, the proposed self-healing system requires that particles of 20-25 µm are coated. Therefore, these methods of sol application are not feasible and a different method has to be used.

Some investigations have been done on the coating of particles by sol-gel, for example on phosphors [48], magnetic particles [49] and silicon carbide particles [50] [51], in all cases with the goal to protect the particles from the environment. For the aforementioned articles, the Yoldas method with some modifications is used in all cases. The main difference is however that in all cases the particles are added before the alkoxide and water are mixed. Therefore the sol is formed while particles are already in suspension, aiding greatly in sol and gel formation on the particles instead of phase separation of a gel, which is also often observed [41]. These particles are however both smaller and with a lower density (except for the magnetic particles) than the $MoSi_2$ particles proposed in the self-healing system (0.5 µm instead of 20 µm) and therefore easier to disperse and to keep dispersed.

Although no work on $MoSi_2$ sol-gel coating with Al_2O_3 exists, the work done on SiC is very useful, due to the very similar surfaces, both consisting of a layer of native oxide SiO_2 [52]. When preparing a coating for particle shell molar ratios of 1:100 or 1:150 of aluminium alkoxide to water [50]. The effect of pH and temperature are also important and discussed in the next chapters.

2.2.3 Effect of pH

The effects of pH on the sol-gel coating process of SiC particles has been thoroughly investigated by Yang and Shih [51] and also by Yang and Troczynski [53]. They found that the effect of pH is twofold.

First, the acid changes the nature of the alumina species in the sol [54], which is shown in Figure 2.13. The exact species that can be present or are present in a given sol are disputed however [41]. Nevertheless, the species and therefore the pH have a signficant influence on both the crystallinity and the type of crystal of the resulting colloidal particles [51]. At high pH the sol forms bayerite ($AlOH_3$) with high crystallinity, while at lower pH a more amorphous structure of boehmite (AlOOH) is observed [41]. This is also reinforced by the observation that base-catalyzed sols in general allow for more growth of particles, resulting in larger and more crystalline colloids, while acid-catalyzed sols generally promote aggregation of small particles into a more homogeneous, but less crystalline gel network [38]. This results in a more homogeneous, dense and amorphous coating derived from acid-catalyzed gels and thought to be caused by partial dissolution of the constituents by the acid.

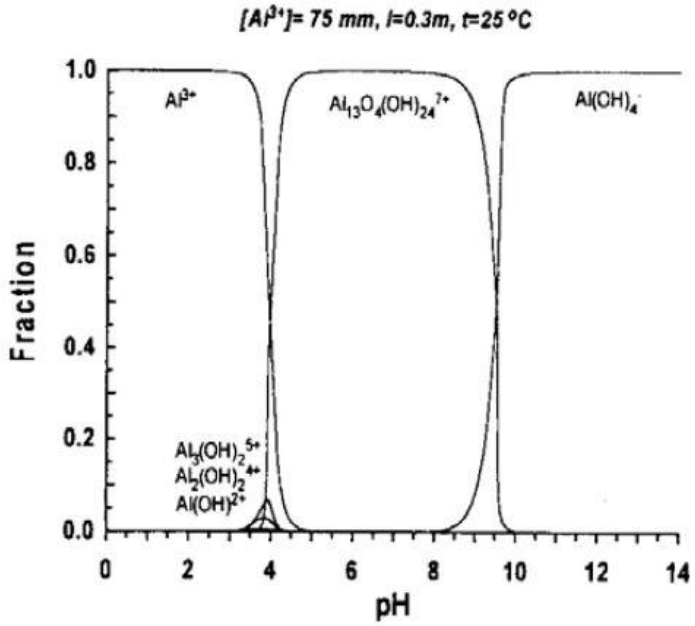

Figure 2.13: *The fraction of alumina species present in an aqueous solution as a function of pH at 25 °C [54].*

Yang and Shih also observed that bayerite is not able to coat SiC, even when additional acid is added. This can be explained by surface charges on the SiC particles. Ionic materials such as the SiO_2 on the surface of most silicides will absorb either protons (H^+) or hydroxyl ions (OH^-) in water depending on the pH, following the equilibrium described in equation 2.5. In this equation the reaction will move more towards the right with increasing pH. This results in the buildup of a charged double layer, measured by the so-called ζ-potential (zeta potential). Aqueous

$$\mathbf{M\text{-}OH_2^+ + H_2O \leftrightarrow H_3O^+ + M\text{-}OH + OH^- \leftrightarrow M\text{-}O^- + H_2O} \qquad \mathbf{(2.5)}$$

For every oxide, there is a so-called point of zero charge (PZC), at which the reactions balance each other out and the surface has no net electrical charge. For a pH>PZC, the surface will absorb more OH^- ions, which results in a negative electrical charge, while for pH<PZC, the surface will absorb more H^+ ions and the surface will be positively charged.

For SiO_2, this PZC is pH 2.5-3.0 [55], which means that in all experiments performed by Yang and Shih, the surface was negatively charged. As can be seen in Figure 2.13, bayerite also has a negative charge and the particles and sol will therefore repel each other. Boehmite on the other hand has a PZC

around 9 [55] and will therefore be positively charged for a pH below this. The significant attractive forces resulting from these opposite charges can be used easily to ensure complete and homogeneous coatings on particles. An example of this attraction and the subsequent increase in zeta potential as function of pH is shown in the research of Yang and Troczynski and shown in Figure 2.14.

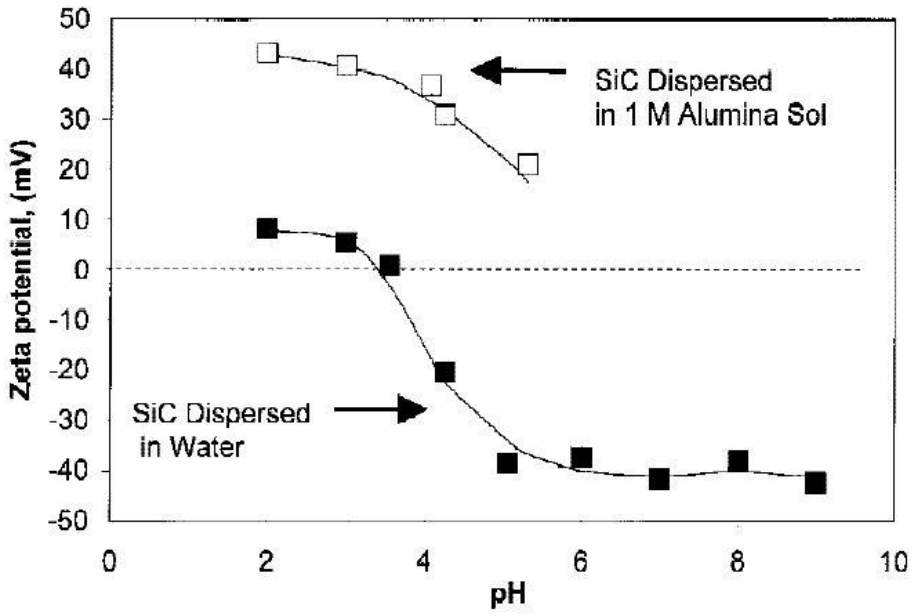

Figure 2.14: *Zeta potential for SiC in water and alumina sol as function of pH [53].*

2.2.4 Effect of temperature

Sol-gel is known as a low-temperature process, especially for ceramics, because it is a liquid phase process and therefore limited by the solvents freezing and boiling point. For water, this limitation is roughly between 0 and 100 °C, which is a narrow range for temperature effects. Nevertheless, the effect of temperature in alumina sols was investigated by Pierre and Uhlmann [56] and found a significant influence of temperature on sol and gel behaviour.

This research was based on acidic sols with varying ratios of nitric acid (HNO_3) to aluminium tri-sec-butoxide ($Al(OC_4H_9)$). They found that the density of the gel in a sol of 90 °C has a maximum at a ratio of HNO_3:Al of 0.07, while at room temperature, density decreased monotonously with increasing HNO_3 concentration. This indicates it is possible to control and maximize solid loading with pH at high temperature. Furthermore the structure was also found to be different, as crystallinity of the boehmite seemed to increase with higher temperature.

2.3 Atomic layer deposition (ALD)

The second method that was selected in appendix I is the Atomic Layer Deposition (ALD) method. This method, together with proper annealing techniques, should also be able to obtain the required microstructure and will be described here.

2.3.1 Atomic layer deposition chemistry

Atomic layer deposition is an elegant technique that is related to Chemical Vapour Deposition (CVD) and is an important technique for the deposition of thin films utilizing gas phase reactants. It is

characterized by the use of two self-limiting half-reactions with the surface to deposit conformal solid films on this surface. Because of these self-limiting reactions, the film thickness can often be controlled up to single atomic layers, hence the name atomic layer deposition [57].

One of the most common ALD deposition processes is that of alumina (Al_2O_3) from trimethylaluminium (TMA) and water (H_2O) [58]. This process is illustrated in Figure 2.15 and the two half-reactions and the final result of the two reactions are schematically shown in reaction 2.6, 2.7 and 2.8 respectively. Reaction 2.8 does never occur in pure ALD, as the precursors are never introduced in the reactor at the same time. It is the final result of the combinations of 2.6 and 2.7. In reactions with CVD, reaction 2.8 is likely to occur however.

It should be noted that reaction 2.6 also has another option in which one molecule of TMA reacts with two surface groups, leaving only one methyl group able to react with water. As can be seen in these reactions and the figure, TMA first reacts with hydroxyl groups present on the surface, followed by a purge step to remove excess reactant. Then water is added to the reactor to allow the oxidation of the other methyl groups present on TMA, forming new hydroxyl groups in the process. Finally the excess water is also purged and the process can be repeated to deposit another cycle [59].

$$\mathbf{M\text{-}OH + Al(CH_3)_{3\,(g)} \rightarrow M\text{-}O\text{-}Al(CH_3)_2 + CH_{4\,(g)}} \quad \textbf{(2.6)}$$

$$\mathbf{M\text{-}O\text{-}Al(CH_3)_2 + 2H_2O_{\,(g)} \rightarrow M\text{-}O\text{-}Al(OH)_2 + 2CH_{4\,(g)}} \quad \textbf{(2.7)}$$

$$\mathbf{2\,Al(CH_3)_{3\,(g)} + 3H_2O_{\,(g)} \rightarrow Al_2O_{3\,(s)} + 6CH_{4\,(g)}} \quad \textbf{(2.8)}$$

From this description, it is evident that any starting sample needs to have hydroxyl groups on the surface, which results in many materials being challenging or unsuitable for ALD. However, due to the thin native SiO_2 layer being present on the surface, $MoSi_2$ can easily be activated to form SiOH groups that would be able to react with TMA. This activation will be discussed later in this chapter.

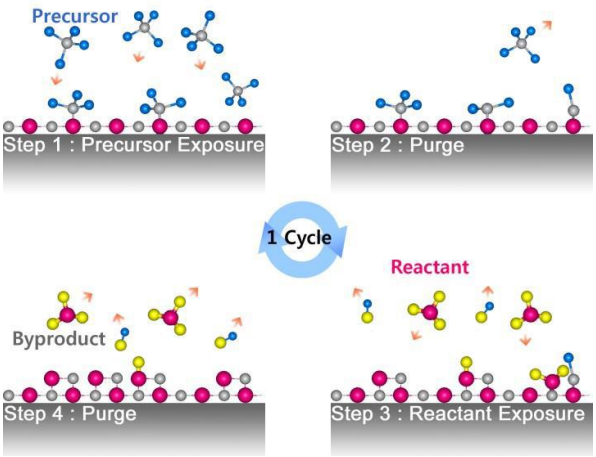

Figure 2.15: *A schematical overview of one cycle in the ALD process [60].*

2.3.2 ALD on particles

The current main application of ALD is for thin coating deposition on wafers and other relatively flat substrates. However, deposition on particles is possible although some additional challenges are present. The surface area to be coated is in general significantly larger than the same mass of wafers, which requires the supply of more reactant. Another problem is the slow mass transfer in a bed of

particles, even when porosity is relatively high. This would result in non-homogeneous coatings from retained TMA during the purge and lack of access of TMA to the least accessible surfaces or prohibitively long cycle times [61].

A solution to both of these problems is the use of a so-called fluidized bed to coat particles. In a fluidized bed, a gas is blown through a bed of particles with sufficient velocity to suspend the particles in this gas flow. This causes both the particles and gas to act as a fluid, increasing gas-solid contact and mixing enormously [62]. Furthermore, by using a carrier gas to fluidize the system and evaporation of the reactants, the amount of TMA that can be supplied to the reactor can be increased significantly. Although fluidization of particles smaller than roughly 20 µm can prove challenging [62], it is possible provided that some agglomeration is present [63]. These authors also found that ALD under atmospheric conditions (25 °C, 1 bar) is possible.

2.3.3 Atomic layer deposition with residual chemical vapour deposition (ALD/rCVD)

One of the remaining challenges for manufacturing high-temperature diffusion barriers with ALD however is the low thickness growth per cycle. This is advantageous for producing nanostructured materials, but for particles that require thicker coatings, this low growth again results in prohibitively long processing times. Although cycle times depend on the reactor used and especially the residence time of the gas in the reactor [63], a single cycle on lab scale usually requires between 10 and 30 minutes and as is evident from the TGO layer in the TBC system, alumina layers need to be at least several 100 nm in thickness. Utilizing pure ALD, which has a layer growth of 0.1-0.16 nm/cycle, this would take about 2000 cycles or 20000 minutes/14 days of continuous operation in the best case. In some cases the addition of catalysts that aid in decomposition of the precursor can be added to significantly increase growth per cycle, such as the well-known example of SiO_2 deposition being catalyzed by trimethylaluminium [64]. Unfortunately, no such catalyst is currently known for TMA itself.

However, another possibility has been found by Garcia-Trinanes and Valdesueiro [65] [63]. In this research, dosing a significant excess of both precursors compared to the amount of reactive groups present at the surface at ambient conditions resulted in higher growth per cycle rates. The explanation given in these articles is that operation of the ALD process below the boiling point results in condensation or physisorption of reactant molecules that can subsequently react with the other reactant during the next half-cycle, resulting in a CVD-like component of the ALD process.

The mechanism is not completely understood however. It has been shown that temperatures above the boiling point do indeed result in more ideal ALD with growth per cycle close to that of literature values [63]. For room temperature ALD, the effect of single precursors is not understood however and neither is the effect of purge time. One would expect that a shorter purge time would result in less re-evaporation of reactant and a resulting increase in growth per cycle, which corresponds with the findings of other authors that at low temperature partial CVD will occur when purge times become too short [66].

For the effect of single precursors, it is possible that both precursors condense, but also that only one of the precursors condenses in significant amounts, while the other precursor only reacts with the condensed precursor. Based on purge times required by Groner et al. [66] during low temperature ALD, H_2O takes significantly longer to remove from the reactor than TMA, hinting at water condensation being more important than TMA condensation.

Temperature also has an effect on the microstructure of the resulting coatings. According to Groner et al. [66] the density of alumina coatings deposited by ALD on PET substrates decreases significantly at lower temperatures, from 3.0 to 2.5 g/cm^3, as is shown in Figure 2.16. Both of these densities are however significantly lower than the bulk density of 3.99 g/cm^3 of α-alumina, or 3.5-3.7 g/cm^3 commonly reported for other amorphous alumina films [67]. This is partially explained by the ALD process depositing amorphous alumina instead of crystalline alumina [58], but another likely factor is the increased hydrogen and hydrocarbon content and microporosity resulting from the low temperature process [63].

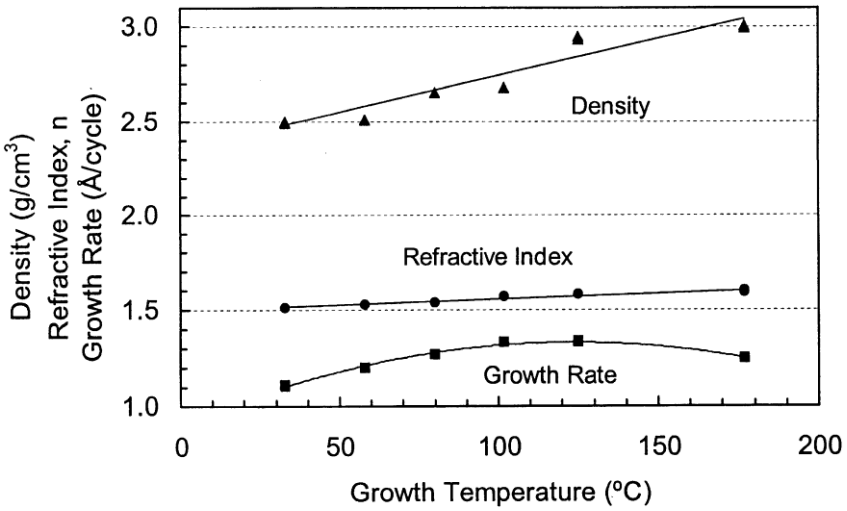

Figure 2.16: *Density, refractive index and growth rate of Al_2O_3 coatings on PET as function of temperature [66].*

2.3.4 Surface activation

Although it is already possible to use this process to coat SiC with only a native SiO_2 layer, improvements in growth per cycle can be achieved by activation of the surface with ozone [65]. A possible explanation could be that the reaction with ozone increases the number of reactive groups present on the surface, as is observed in Si wafer bonding [68] [69]. However, as the mechanism is expected to be based on condensation, a more likely explanation would be that this pre-treatment also has an effect on the condensation of reactants and possibly the deposited Al_2O_3 film, as the effect is also observed after many cycles with coatings several 100 nm thick. The nature of this effect is however unknown.

2.4 Heat treatment

Although closed and homogeneous films of Al containing material can be applied to $MoSi_2$ particles, these films are not yet in the stable α phase, as ALD films are generally amorphous, while the sol-gel films are usually boehmite (AlOOH) that is partially amorphous and partially in the γ phase [23]. Furthermore, the deposited alumina does not have the density required and some impurities left from the process are still present. To attain the desired dense α alumina films and remove combustible impurities and H_2O, heat treatment is required, which will be discussed here.

2.4.1 Transformation and kinetics sol-gel coatings

For sol-gel coatings consisting of AlOOH, transformation to the α phase requires following a transition sequence of multiple metastable aluminas. Before that however, removal of both water still contained in the gel and crystal water contained in AlOOH is necessary according to equation 2.9. The transformation of boehmite to γ-alumina usually takes place between 300 and 500 °C [23], which

is also the temperature range at which residual organic material can be burned away with sufficient access to oxygen.

$$2\ \gamma\text{-AlOOH}_{(s)} \rightarrow \gamma\text{-}Al_2O_{3\,(s)} + H_2O_{(g)} \qquad (2.9)$$

Further transformation from γ-alumina goes through δ-Al_2O_3 between approximately 700-800 °C, followed by θ-Al_2O_3 between 900-1000 °C and finally to the α-phase from 1000-1100 °C according to Levin et al. [23]. Because γ, δ and θ are metastable phases, it is possible for them to coexist in the sample depending on the annealing conditions, which makes distinguishing between them difficult.

Furthermore, all of these metastable phases have an oxygen anion packing in the FCC phase, while α-alumina has an HCP anion lattice. Due to this, the transformation from θ to α is the slowest step with the highest activation energy of 557 kJ/mol [70], which is also visible in the unusually high temperature required to obtain the thermodynamically stable α phase. This transformation is also thought to occur through a nucleation-growth based process, which makes the formation of grain boundaries unavoidable.

Another issue with the transformation of sol-gel coatings is the volume change, which causes stress buildup. This volume change results from the equilibrium densities of the transition aluminas being lower than that of α-alumina, with 3.6-3.7 g/cm^3 for most transition aluminas and 3.99 for the α phase [23]. Boehmite has a density of approximately 3.08 g/cm^3, with approximately 15% of this mass consisting of H_2O that will evaporate during the transformation. This significant difference in density results in high tensile stresses in the coating and can result in major cracking and spallation of alumina sol-gel coatings on bulk samples [41]. Heat treatment procedures should therefore aim to reduce these stresses with a proper temperature profile.

The evaporation of water, oxidation of hydrocarbons and decomposition of other contaminants such as nitrates also results in micropore formation during heat treatment [38]. These pores are the result of gaseous molecules escaping from inside the coating and should be closed during heat treatment by sintering to obtain a densified coating mostly free of porosity.

However, due to the formation of these pores, the substrate can be exposed to oxygen during thermal treatment, resulting in unwanted oxidation. Therefore, heat treatment should be performed in an inert atmosphere.

2.4.2 Transformation and kinetics ALD/rCVD coatings

The transformation sequence of coatings resulting from ALD/rCVD is unfortunately not as well understood and two possible sequences can be found in literature. Most coatings originating from CVD or CVD related processes deposit κ-alumina when performed at a temperature above 600 °C, which transforms directly to α-alumina around 1100 °C [23]. This is however very dependent on the substrate, as Andersson et al. could produce α-Al_2O_3 directly on a chromia substrate [71].

In low-temperature (150 °C) CVD experiments with reactive magnetron sputtering, the γ phase was produced directly however [72], which transformed directly to α-alumina as well. Other researchers have investigated alumina ALD coating crystallization, but did not report crystal structure [73], but based on temperature the α structure would be most likely. According to Levin et al. [23], most amorphous alumina films crystallize in the γ phase however and follow the same transition path as the sol-gel coatings. Based on this information, it is therefore more likely that γ-alumina is more likely

as a transition phase. However, all authors find that transforming ALD or CVD coatings to α-alumina requires very high temperatures in excess of 1100 °C and therefore a high activation energy, even in cases with a coating thickness in excess of 1 µm [72]. Because of this, grains that do form will likely remain smaller than those resulting from sol-gel when subjected to the same heat treatment.

ALD coatings suffer from some of the same problems as sol-gel coatings, in particular the volume change associated with the transformation of amorphous to crystalline coatings. However, although some impurities in the form of H_2O and hydrocarbons are present, their concentration is far lower than for sol-gel coatings, even for room temperature coatings. This prevents the formation of pores during heat treatment and reduces the need for further densification during heat treatment. The formation of porosity can however act as a stress relieving mechanism and ALD coatings could therefore have higher stresses present in the coating during heat treatment [38], making it more likely cracks will form.

2.5 Crack formation and healing in YSZ

Similar to most other ceramics, crack formation and failure in YSZ occurs in a brittle manner. In essence, brittle fracture occurs when the stress is sufficient to break the bonds between atoms in a solid material. However, without a stress concentration mechanism, this stress would be extremely high [74]. For ceramics, this stress concentration is usually at the tip of flaws present in the material. Due to a lack of stress relief mechanisms such as the formation of dislocations and other plastic deformation mechanisms, cracks can grow relatively rapidly and with little obstruction [75], which is why their behaviour is described as brittle. This is especially true for ceramics loaded in tension.

Due to the absence of significant plastic deformation, ceramics can usually be described by linear elastic fracture mechanics. Therefore, the system can be described with a stress intensity factor, which is defined in equation 2.10 in which K_I is the stress intensity factor, σ_y the far-field applied stress, a the crack length and f(φ) a dimensionless parameter correcting for crack and loading geometries and angle of loading. As is evident from this equation, fracture strength is not an intrinsic property of materials, but is dependent on the critical stress intensity factor or fracture toughness K_{IC} of the material and the flaw size and geometry of the system [75].

$$\boldsymbol{\sigma_y = \frac{K_I}{\sqrt{\pi * a}} * f(\phi)} \qquad \textbf{(2.10)}$$

Although this is a useful description for well-understood systems, TBCs are very complex and are loaded in multiple directions [9]. Furthermore, this description breaks down for flaw sizes that are too small, making it difficult to describe the onset of fracture well [74]. However, a study from Hille et al. [13] showed that cracking starts in the TGO as a result of thermal cycling and slow TGO growth due to further oxidation of the Al reservoir in the bond coat. Stresses and crack growth seem to increase in severity with a higher roughness of the interface between the TGO and the TBC. Upon growing sufficiently, they will grow into the TBC and follow the pattern described in chapter 2.1.1 of growth, coalescence, perpendicular growth and subsequent spallation. Arresting this crack growth by self-healing mainly aims to reduce the crack size to slow growth and fill the crack to remove it. As the $ZrSiO_4$ is tougher than the YSZ in the TBC, new cracks will have a tendency to grow around the healed area instead of through it.

Thermodynamics and Diffusion

This chapter will introduce the main thermodynamic and kinetic considerations of the self-healing TBC system. Because of the high temperatures involved in this system, transport of matter is relatively rapid and thermodynamic considerations become significantly more important than at lower temperatures. Therefore, as the original system is not the thermodynamically most stable system in an environment containing oxygen, the system will evolve towards a more stable system.

This chapter will therefore start with the kinetics of $MoSi_2$ oxidation, followed by a thermodynamic analysis of the interfaces between the different materials and the most likely evolution of the system. This will be followed by a description of diffusion at high temperatures through a coating and the construction of a diffusion model of the coated particle system. This model is then utilized to predict relevant time scales of particle stability.

3.1 Thermodynamics and kinetics of the self-healing TBC system

3.1.1 Oxygen and oxidation behaviour of $MoSi_2$

Owing to its use as heating elements in many high-temperature furnaces, among other high temperature applications, numerous studies on the high-temperature oxidation of $MoSi_2$ have been performed [76], [77], [21]. This oxidation behaviour is rather complex, mainly resulting from the two oxidizable components present in the system, molybdenum and silicon. Oxidation of $MoSi_2$ starts between 400 and 500 °C and follows reaction 3.1 at temperatures lower than 800 °C.

$$\mathbf{2\ MoSi_{2\,(s)} + 7\ O_{2\,(g)} \rightarrow 2\ MoO_{3\,(s)} + 4\ SiO_{2\,(s)} \quad (<800\ °C)} \qquad \mathbf{(3.1)}$$

However, thermodynamic calculations and experimental evidence by Zhu et al. [76] found that above approximately 800 °C (the melting point of MoO_3), the formation of Mo_5Si_3 and SiO_2 according to reaction 3.2 is thermodynamically more favourable than the formation of MoO_3. If sufficient additional oxygen is present, Mo_5Si_3 can oxidize further according to reaction 3.3. However, at this temperature, the vapour pressure of MoO_3 becomes significant, removing most MoO_3 that could still form. Therefore, 800 °C is also approximately the temperature at which a closed scale of SiO_2 starts to form, protecting the underlying $MoSi_2$ and Mo_5Si_3.

$$\mathbf{5\ MoSi_{2\,(s)} + 7\ O_{2\,(g)} \rightarrow\ Mo_5Si_{3\,(s)} + 7\ SiO_{2\,(s)} \quad (>800\ °C)} \qquad \mathbf{(3.2)}$$

$$\mathbf{Mo_5Si_{3\,(s)} + 10.5\ O_{2\,(g)} \rightarrow 5\ MoO_{3\,(g)} + 3\ SiO_{2\,(s)} \quad (>800\ °C)} \qquad \mathbf{(3.3)}$$

Below 800 °C, significant MoO_3 formation introduces porosity in the formed scale, a phenomenon often referred to as $MoSi_2$ pest oxidation, as this porosity prevents the formation of a protective coating. This allows the oxidation of $MoSi_2$ to continue at high rates if no initial protective coating is present and is a significant issue in bulk $MoSi_2$ applications. However, as mentioned before in the theory section, particles do need a protective coating in any case, due to the required thickness of the SiO_2 coatings being several µm. This would necessitate the consumption of a significant part of the healing particle to form this coating.

Due to its interesting high-temperature properties and intermetallic nature, attempts at alloying $MoSi_2$ have been performed as well [78]. Two of the more interesting elements are boron and aluminium. As mentioned before, Mao found that boron is able to stabilize the amorphous phase of SiO_2. However, boron is not very soluble in $MoSi_2$ and tends to form separate phases with

molybdenum, as is evident from the phase diagram presented in Figure 3.17. Boron does not seem to form any borides with silicon in the presence of molybdenum though [79]. This indicates that boron addition will most likely form a separate phase with molybdenum only and which one will depend mainly on the processing conditions of the $MoSi_2$ production. Because most molybdenum borides have a remarkably high hardness, boron is often added to $MoSi_2$ to increase hardness [80].

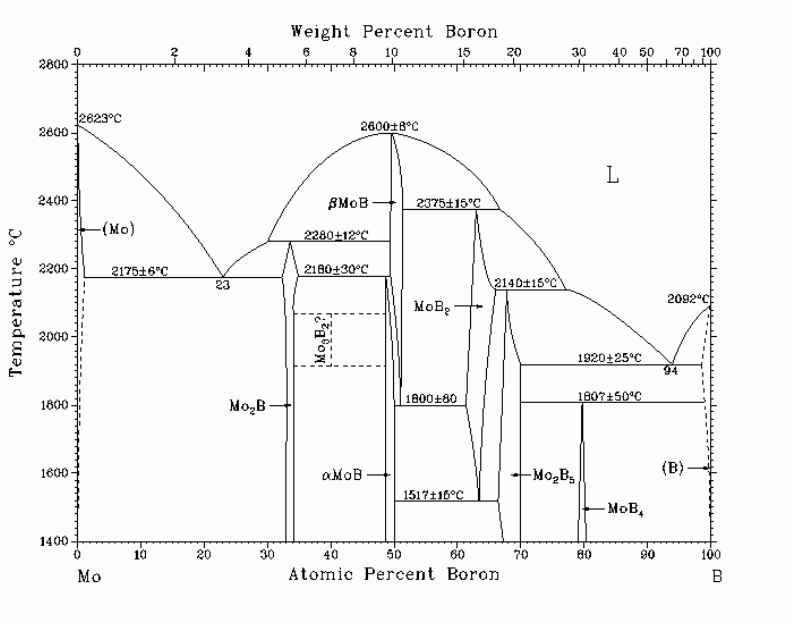

Figure 3.17: *The temperature dependent Mo-B phase diagram [81].*

Aluminium on the other hand can easily substitute for silicon in the $MoSi_2$ structure, although it is known to stabilize the usually metastable hexagonal phase of $MoSi_2$ [78]. This results in either a single phase of $MoSi_xAl_y$ or a two-phase system with both the hexagonal and tetragonal phase of $MoSi_xAl_y$ coexisting, depending on the molar ratios of the elements present. The main effect of the presence of aluminium is however its effect on oxidation behaviour. Because the ΔG of Al_2O_3 per mole of oxygen is significantly lower than that of either Mo or Si, aluminium is preferentially oxidized and is even able to reduce SiO_2 according to reaction 3.4 [82]. This limits pest oxidation and results in an Al_2O_3 scale instead of an SiO_2 scale, although some SiO_2 can still form, depending on the local Si, Al and O activities.

$$4\,Al_{(s)} + 3\,SiO_{2\,(s)} \rightarrow 2\,Al_2O_{3\,(s)} + 3\,Si_{(s)} \qquad (3.4)$$

The oxidation of components in $MoSi_2$ and subsequent reactions to form ternary oxides do result in significant changes in molar volume though. Although this is desired for the self-healing process, as it will aid in filling and closing cracks, premature oxidation will also result in accumulation of stress, as described in the theory section. This could result in coating fracture or damage and is therefore important to prevent. The presence of all these oxides also results in many possible interfaces, which will be discussed in the next parts.

3.1.2 Alumina/YSZ

The first interface and one of the more critical ones for particle opening is that of the alumina particle shell and the YSZ matrix. As the latter consists of both ZrO_2 and Y_2O_3, phase diagrams of Al_2O_3 with both oxides are presented in Figure 3.18 and Figure 3.19 respectively. As is clear from the first diagram, ZrO_2 and Al_2O_3 do not form any thermodynamically stable ternary compounds.

Furthermore, solubility between the oxides is limited, even being practically nonexistent for ZrO_2 in alumina.

For Al_2O_3 and Y_2O_3, solubility is very similar, also being practically non-existent for both compounds. However, alumina and yttria are able to form some ternary compounds at higher temperature. Of these, only $Y_3Al_5O_{12}$ and $YAlO_3$, the famous yttrium aluminium granate (YAG) and yttrium aluminium perovskite (YAP) are thermodynamically stable at lower temperatures, but other compounds can form at approximately 1100 °C, which is still close to TBC temperatures.

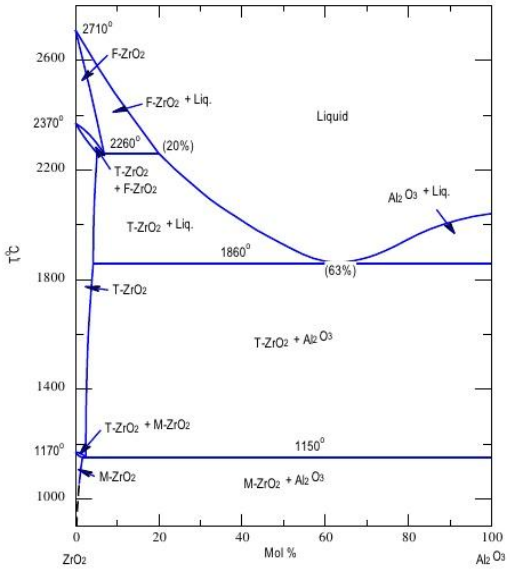

Figure 3.18: *The temperature dependent Al_2O_3-ZrO_2 phase diagram [83].*

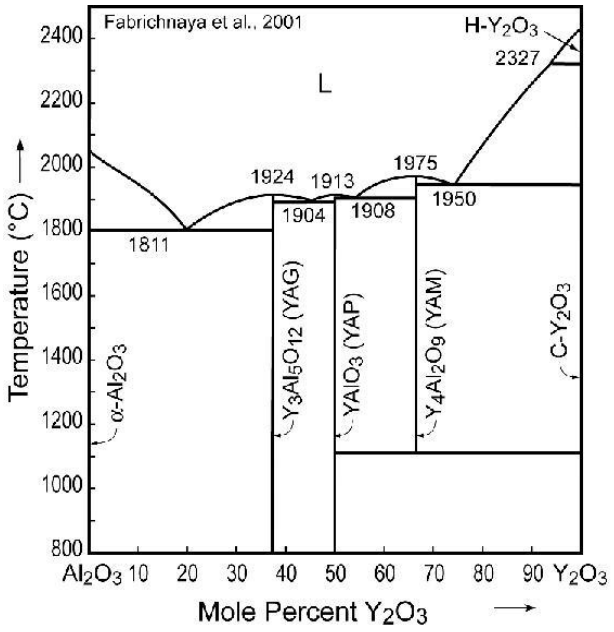

Figure 3.19: *The temperature dependent Al_2O_3-Y_2O_3 phase diagram [84].*

It should be noted though that yttria is present in YSZ in this case, not in its pure form. For YSZ and Al_2O_3 Lakiza et al. did show that ternary and quaternary compounds are indeed able to form and thermodynamically stable though [83]. This could be problematic for thin shells protecting the $MoSi_2$ particles.

However, studies on the YSZ-Al_2O_3 interface in TGO-TBC coatings by Suenaga et al. [85] found that this interface is easily detectable on a nanometer scale, with pure alumina and pure YSZ being separated by an interface of only 5-6 nm. This indicates that YSZ and alumina are relatively stable in contact with each other and even though it is thermodynamically possible to form ternary and quaternary compounds, kinetics for this seem to be relatively slow.

3.1.3 Alumina/$MoSi_2$

Another important interface is that between the shell and the healing agent. Tests with $MoSi_2$ including Al as an alloying element, mentioned in the oxidation section, indicate that although aluminium is soluble in the healing agent, its oxide is not soluble at all [78]. This is mainly evident by the segregation of Al2O3 in the bulk of their material, even in argon atmosphere.

Furthermore, no thermodynamically stable compounds of Al_2O_3 and either Si or Mo in reduced form are known. However, as already described in the theory section, $MoSi_2$ at its interface does not contain reduced Mo or Si, but most likely a thin native oxide layer of SiO_2. As will be described in the

next section, Al_2O_3 and SiO_2 do have a stable ternary compound and are able to form a strong interface. Therefore, it is likely that the interface between the shell and healing agent will consist mainly of this Al_2O_3-SiO_2 interface.

3.1.4 Alumina/Silica

The expected interface between the healing material and alumina is most likely based on SiO_2 and Al_2O_3. The phase diagram of these two oxides is shown in Figure 3.20 and shows one stable ternary compound, namely mullite ($Al_6Si_2O_{13}$), which is also thermodynamically stable at room temperature, even though not shown here. Mullite is an important engineering ceramic with many applications, an interesting one being in porcelain, as it is the compound that gives this material its strength.

Because of this, it is a well-studied ceramic and according to many studies, very likely to form at any interface between Al_2O_3 and SiO_2 at sufficient temperatures, usually around 1000 or 1100 °C in bulk materials [86]. This is also an explanation for the often strong interfaces found between alumina and silicon containing materials that have an SiO_2 native oxide layer. Many other aluminosilicates exist though and are likely to form, although these other aluminosilicates often require counterions to balance charges and the only known thermodynamically stable phase is mullite.

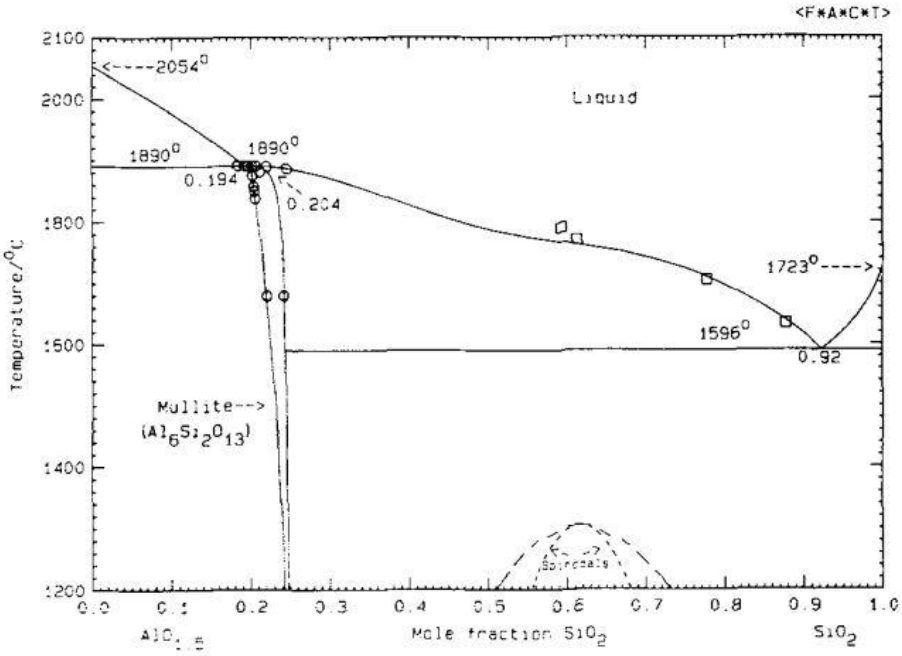

Figure 3.20: *The temperature dependent Al_2O_3-SiO_2 phase diagram [87].*

3.1.5 Silica/YSZ

The final interface that is of significant importance is that between SiO_2 and YSZ, as this is the interface that is most important for the healing behaviour. A ternary oxide phase diagram of SiO_2, ZrO_2 and Y_2O_3 is not available, but phase diagrams of SiO_2 with the individual oxides are known and shown in Figure 3.21 and Figure 3.22. the ZrO_2-SiO_2 phase diagram shows that there is only one ternary compound possible, which is zircon ($ZrSiO_4$). As described in the theory section, there is only one stable crystal structure for zircon as well. For yttria and silica, there are two different possible phases however, Y_2SiO_5 and $Y_2Si_2O_7$, with the latter having four different known polymorphs.

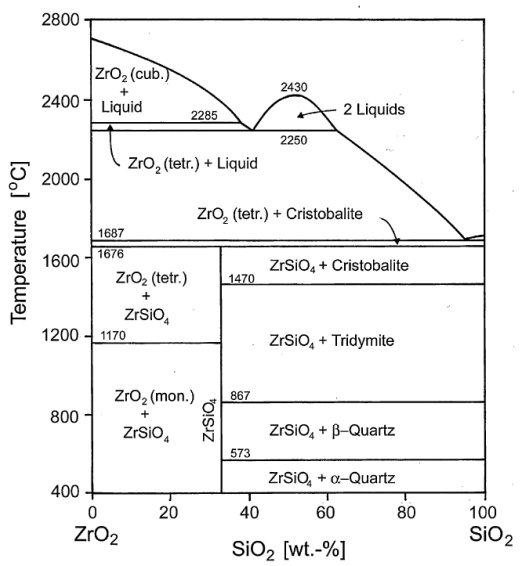

Figure 3.21: *The temperature dependent SiO_2-ZrO_2 phase diagram [88]*

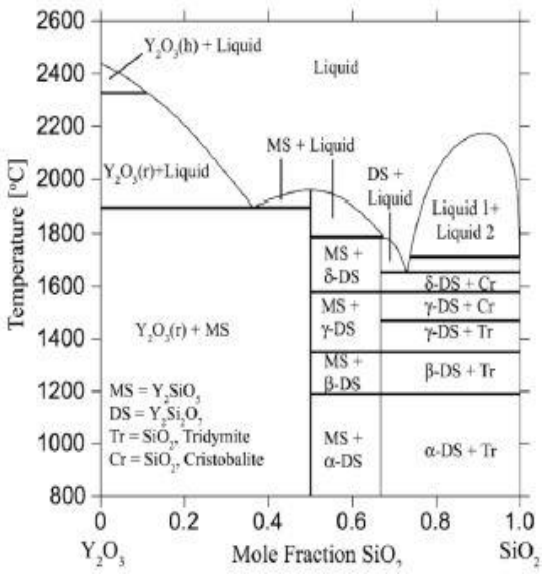

Figure 3.22 *The calculated temperature dependent Y_2O_3-SiO_2 phase diagram [89].*

Which of these phases forms preferentially is not known, but experiments on the healing mechanism by Mao [17] show that the formation of zircon is dominant in the SiO_2-YSZ system however. The presence of quaternary compounds was not discussed however and whether this system is able to form these is not known.

3.1.6 Coated particle system evolution

After discussion of the oxidation mechanism of $MoSi_2$ and the most likely possible interfaces, it is important to note that at temperatures present in the TBC system, which can reach to 1100 °C, the coated particle system will change over time. As is evident from the TGO, even an Al_2O_3 coating of several µm thick cannot prevent oxygen diffusion and oxidation of the substrate, only slow it down. Therefore it is important to understand how the system will most likely evolve over time, based on thermodynamics and diffusion. The idealized starting situation is therefore graphically depicted in Figure 3.23, while the Gibbs free energy of formation (ΔG_f) and equilibrium partial oxygen pressure calculated with eq 3.3 at 1000 °C of each compound present in the system is listed in Table 3.2. In this equation, $P_{O2,\,eq}$ is the equilibrium partial pressure of oxygen, or the P_{O2} at which the oxide and metal are in equilibrium, while K_p is the equilibrium constant for the oxidation reaction. ΔG_f is the Gibbs free energy of formation in J/mol O_2, R is the gas constant and T the temperature in K.

$$P_{O_2,eq} = \frac{1}{K_P} = exp(\frac{\Delta G_f}{R*T}) \quad \textbf{(3.5)}$$

Table 3.2: *Standard free energy of formation at 1000 °C for each oxide present in the system from its element, per mole of oxygen consumed, along with the equilibrium partial oxygen pressure.*

Compound	Standard free energy (ΔG_f, kJ/mol O_2)	Equilibrium P_{O2} (bar)
SiO_2	-677	1.68E-28
MoO_3 (g)	-189	1.74E-08
Al_2O_3	-845	2.13E-35
ZrO_2	-863	3.92E-36
$Y2O_3$	-1023	1.04E-42
B_2O_3	-641	5.08E-27

As can be seen from both the Gibbs free energy and the equilibrium P_{O2}, the most stable oxides are Y_2O_3 and ZrO_2, the latter closely followed by Al_2O_3. It is therefore clear that $MoSi_2$ both with and without boron is not able to reduce these oxides. This table also shows that of the compounds present in the $MoSi_2$, silicon will likely oxidize before molybdenum, which agrees with the discussion in the first part of this chapter. However, it will most likely also oxidize before boron, although the difference in free energy is significantly smaller. This does however depend on the energy of formation of $MoSi_2$ and the molybdenum-boron compound that is present in the $MoSi_2$, the latter of which is unfortunately not known.

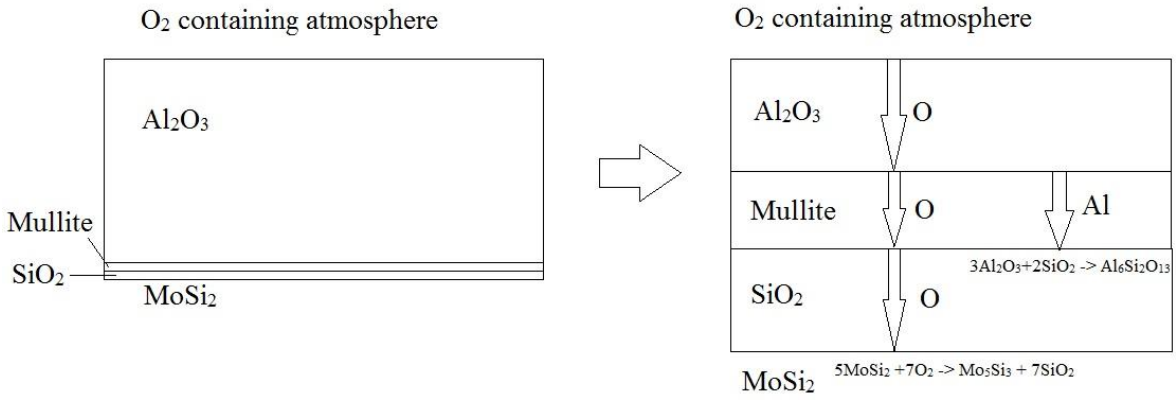

Figure 3.23: A schematic representation of the evolution of the coated $MoSi_2$ system at high temperatures in an oxygen-rich environment. In this system, it is assumed that yttria and zirconia are not able to diffuse through alumina and that molybdenum will not oxidize.

3.2 Diffusion of species in the coated healing particles

Diffusion in ceramics is an often complex process due to the complexity of diffusion in solids in general and the influence of atomic charges and charge separation. One of the main differences of diffusion in solids compared to liquids or gases is the presence of all kinds of defects that can act as a fast pathway for diffusion. Furthermore, another important aspect of diffusion of charged species is that charge neutrality should be maintained, which influences the speed of diffusion of all species involved. Therefore, this aspect of bulk diffusion will be described first, followed by defect diffusion. Afterwards, the diffusion model with its main assumptions will be introduced and the results from this model will be discussed.

3.2.1 Bulk diffusion

Bulk diffusion in ceramics in general is governed by movement of vacancies, electrons and/or holes. Sometimes, especially with diffusion of elements that are not part of the matrix and relatively small, these elements occupy interstitial positions and are able to move along these interstitial positions. Nevertheless, all these forms of diffusion proceed by the means of point defects, which are always present in ceramics, because it is thermodynamically favourable to form some defects such as Schottky, Frenkel and anti-Frenkel defects. As the transport of atoms is governed by both the concentration and mobility of these point defects and defect concentrations in oxides are also often dependent on the partial oxygen pressure of the gas in contact with the ceramic, it is important to understand the defect structure in the oxides present.

However, another important aspect is that this transport is driven by a difference in chemical potential, as the potential of the oxygen at the $MoSi_2$-SiO_2 interface is significantly more negative

than the chemical potential at the outer surface of the Al_2O_3 layer. These systems are different from systems with only self-diffusion being present in that the chemical potential gradient accelerates movement of ions in the direction in which the chemical potential is lower. In most systems this diffusion under the influence of a gradient is described by Fick's first law, but this law does not account for charged species.

To account for charged species, there are two important models to describe oxidation of metals with resulting film growth, the Cabrera-Mott model for very thin films and the Wagner model for thicker films. The former assumes that electrons can pass freely from the metal surface to the oxide-gas interface. This results in an uniform electrical field in the oxide, but restricts the applicability of this model to very thin films in which most of the film is charged and electrons can essentially tunnel from one side to the other. Although extensions have been developed for thicker films, this theory is usually only applied for films of at most several 10s of nanometers [90].

The Wagner model on the other hand assumes that oxidation is mainly governed by diffusion of charged particles in an oxide that is considered to be mostly neutral, which is usually the case for oxides thicker than the Debye length [90]. Therefore space charges are neglected in this model and any movement of ions must be balanced by either other ions or electrons and holes to retain charge neutrality. The main equation for the Wagner model is shown in equation 3.6.

$$J_i = -D_i \frac{\partial C}{\partial x} + \mu E C \tag{3.6}$$

In which J_i is the flux of species i in mol/(m^2*s), D_i the diffusion coefficient in the oxide in m^2/s, C the concentration of the respective defects in mol/m^3, x the distance in m, μ the mobility and E the electric field. As the Wagner model assumes charge neutrality and that the system is close to local equilibrium everywhere in the oxide layer to use equilibrium thermodynamics, equation 3.6 can be simplified to equation 3.8 with the aid of equation 3.7.

$$\frac{\partial C}{\partial x} = \frac{C_i}{RT} * \frac{\partial \mu_i}{\partial x} \tag{3.7}$$

$$J_i = -D_i * \frac{C_i}{RT} * \frac{\partial \mu_i}{\partial x} \tag{3.8}$$

In which D, J and x refer to the same property, while R is the gas constant in J/(K*mol), T the absolute temperature in K, C_i is in this case the concentration of the species in the bulk material in mol/m^3 and due to unhelpful use of μ for multiple different properties in literature, here μ refers to the chemical potential in J/mol. If most of oxide layer growth is dependent on the diffusion of only one element, equation 3.9 can then be used to calculate layer growth. By assuming chemical potential varies linearly over the oxide layer according to equation 3.10, equation 3.11 can be derived after integration of equation 3.9 for a single oxide layer.

$$\frac{\partial d_{ox}}{\partial t} = f_{i,MO_x} * \frac{M_{MO_x}}{\rho_{MO_x}} * J_i \tag{3.9}$$

$$\frac{\partial \mu_i}{\partial x} = \frac{\Delta \mu_i}{\Delta x} = \frac{{\mu_i}^{II} - {\mu_i}^{I}}{x^{II} - x^{I}} = \frac{\Delta \mu_i}{d_{ox}} \tag{3.10}$$

$${d_{ox}}^2 = f_{i,MO_x} * \frac{M_{MO_x}}{\rho_{MO_x}} * D_i * \frac{C_i}{RT} * \Delta \mu_i * t \tag{3.11}$$

With d_{ox} the oxide thickness in m, $f_{i, MOx}$ the amount of moles of the diffusing species needed to form one mole of the oxide MO_x, M_{MOx} the molar weight of the oxide in g/mol, ρ_{MOx} the density of the oxide in g/m^3 and t the time in s. Equation 3.11 is the famous parabolic growth rate law for an oxide scale on a substrate and describes the thickness of the oxide as a function of time. However, the behaviour of the three different oxides is slightly different and should be discussed individually, especially with regard to the diffusion coefficient and chemical potential.

Starting with alumina, which is one of the most studied materials regarding diffusion and therefore one of the most poorly understood materials. Or to quote the answer of A. Heuer on the question "Oxygen and aluminium diffusion in α-Al_2O_3: How much do we really understand?": "Not a great deal" [91]. The diffusion of most species in α-alumina is not very well understood, even to the extent that even the main defects responsible for this diffusion are still debated. It is however known that the self-diffusion coefficient $D_{ox} < D_{Al}$ under practically all conditions and at all temperatures in bulk diffusion [91]. This indicates that in defect-free materials, transport of Al is mainly responsible for oxidation at higher temperatures.

For mullite on the other hand, this is quite different, as was found by Fielitz et al. [92]. In their investigations on the formation of mullite from its constituent oxides Al_2O_3 and SiO_2, they found that aluminium and oxygen had very similar bulk diffusivities, while the Si diffusivity was several orders of magnitude lower. According to the authors, this can be attributed to the strong covalent bonds formed by SiO_4 tetrahedra, which limits movement of Si atoms.

This same effect is also observed in SiO_2 in which oxygen is again the faster-diffusing species [93], at least in amorphous silica, which is the most likely species to be present. The author explains this effect partially with strong covalent bonds between SiO_4 tetrahedra and the presence of many O atoms that are only bonded to a single Si atom (which is common in amorphous SiO_2). Another important effect however is the movement of gaseous/dissolved O_2 in the system that can move significantly faster than network oxygen.

3.2.2 Defect diffusion

As mentioned before, an important difference between diffusion in solids and fluids is the presence of defects in the former. These defects can exist in many forms and are usually described based on the amount of dimensions occupied by these defects. 0D or point defects have already been discussed in the previous part as they are the defects responsible for lattice diffusion.

1D or line defects can also accommodate diffusion along a line. The only example of this type of defect is a dislocation, which can accelerate diffusion along the dislocation. Although diffusion along dislocations can be relevant for metals with high dislocation densities, for brittle ceramics, dislocations are very complex and difficult to form. Therefore dislocation density is very low and the influence of diffusion along this type of defect can be neglected in this system.

2D or interface defects on the other hand are significantly more important and are one of two types. The first type of interface is a free surface, which is a gas-solid interface. This surface can either refer to an external surface or the surface of pores or cracks present in the material. It is often very rapid compared to bulk diffusion due to the significantly lower activation energy barrier, as no vacancies have to be formed in this type of diffusion.

Another important type of interface defect is the grain boundary, which is any interface between two crystallites with usually a different crystal orientation. For low angle grain boundaries (having a misorientation between crystallites < approximately 15°), this boundary consists of a row of regularly spaced dislocations, but for high angle grain boundaries, the boundary is both poorly defined and poorly understood. However, the atomic density is significantly lower in both grain boundaries, making the formation of defects and movement of atoms far easier [94]. Therefore, grain boundaries can and will often act as a fast pathway for diffusion, especially at intermediate temperatures.

Finally, the 3D defects, which are either be cracks, pores, any other type of gas-containing area in the ceramic or another phase included in the original phase. The first type of 3D defect, which is a gaseous inclusion in the solid material, can easily act as a fast pathway for O_2, as diffusion in gases is significantly faster than in either liquids or solids. Depending on the flaw size, this diffusion could be Knudsen diffusion in which the molecule mean free path is larger than the width of the flaw andgases interact significantly with the flaw walls. If the mean free path is small compared to the flaw size though, regular gaseous diffusion is the main mechanism. However, due to the high temperatures, the mean free path is generally in the same order of magnitude as the coating thickness (λ=350 nm at 1000 °C and 1 bar total pressure) and therefore, any diffusion of this type in the coated particle system is most likely Knudsen diffusion.

Diffusion in foreign phases is also possible if impurities are present. This type of diffusion will only act as a fast pathway if the diffusivity of the cation and oxygen are higher than in the matrix though. However, most impurities will have a higher diffusivity than Al_2O_3 though, as diffusion in alumina is relatively slow, as described in appendix I.

Calculation of diffusion in systems with fast diffusion pathways is often carried out with the use of an effective diffusion coefficient for the whole system, D_{eff}. These are generally sums of the diffusion coefficients in each of the defects with the volume fraction of that defect in the bulk material [90].

For the materials involved in the self-healing TBC system, Al_2O_3, SiO_2 and $Al_6Si_2O_{13}$ are the most important and will most likely be the most affected by any fast diffusion pathways. Therefore it is important to know how likely these fast pathways are to be present. As mentioned before, diffusion along dislocations can be neglected in ceramics. For SiO_2, grown from $MoSi_2$, 3D defects are not likely to be present as long as only SiO_2 is oxidizing, as thermally grown oxides generally have low porosity and crack formation as long as they remain sufficiently thin [25]. Furthermore, grain boundaries are obviously not present in an amorphous phase and other interfaces will most likely not form in the direction of diffusion.

For α-Al_2O_3 on the other hand, the formation of 3D defects is very dependent on the manufacturing method of the coating and subsequent processing. This also influences the presence of free surfaces significantly. However, the main defect that is almost unavoidable in alumina is the formation of grain boundaries that can act as a fast pathway in diffusion.

Although even less understood than bulk diffusion in alumina, many investigations on the grain boundary diffusion of especially oxygen are available, a good example of which is the work done by Smialek et al. [95, 96]. His work shows that grain boundary diffusion of both oxygen and aluminium is orders of magnitude faster than bulk diffusion and surprisingly, that oxygen grain boundary diffusion is actually significantly faster than aluminium grain boundary diffusion. Therefore, it is very important

to consider grain boundary diffusion for materials with small grains, which is likely to be the case in the coatings investigated here.

For mullite, grain boundary diffusion has not been investigated in great detail, but work performed by Fielitz et al. [92] found that grain boundary diffusion of Si is still significantly slower than Al and O grain boundary diffusion. All diffusivities were however found to be at most 4 orders of magnitude higher (depending mainly on temperature, but also other factors), which is a significantly lower increase than that of Al_2O_3 when comparing grain boundary and bulk diffusion. The presence of other defects is however not very likely, as formation of mullite is mainly due to Al and O diffusion and therefore the morphology is most likely more similar to that of the SiO_2 layer, lacking significant amounts of 3D effects. The only defect that would be likely to form is a crack, due to stress buildup from oxidation.

3.2.3 Diffusion model

Because of the complexity of diffusion in solid materials, some assumptions are necessary to create a diffusion model. In this model, the evolution of the system will be that described in section 3.1.6, with oxygen diffusing inwards through the Al_2O_3, mullite and SiO_2 layers and oxidizing $MoSi_2$ according to reaction 3.2. The formation of all of these layers is assumed to be completely diffusion limited with no external mass transfer or reaction limitations and the activity of Si at the $MoSi_2$-SiO_2 interface is assumed to remain sufficient to prevent any oxidation of molybdenum. Furthermore, as described in section 3.1.2, the interface between alumina and YSZ is very sharp, indicating very low diffusivity of Y and Zr in alumina. Due to this, it is assumed that diffusion of these into the alumina is negligible and can be ignored.

Due to the thick Al_2O_3 coating already present, it is likely that parabolic oxide growth rate law kinetics of $MoSi_2$ as described in the Wagner model will indeed be valid and that diffusion through the oxide layer is indeed the rate limiting step throughout the whole experiment. Furthermore, investigations of oxidation of $MoSi_2$ indicate that the diffusion of Si in $MoSi_2$ and Mo_5Si_3 is indeed significantly faster than the diffusion of oxygen through Al_2O_3, mullite or SiO_2 [97], supporting the validity of this assumption.

Furthermore, it is assumed that mullite is only formed by the inward diffusion of aluminium and oxygen through the mullite layer, as described in the work of Fielitz [92]. To model the diffusion, it is assumed that in this case the Wagner model with its assumptions of charge neutrality and local equilibrium can be used to describe the formation of all three layers. Although this is possible without question for the Al_2O_3 layer, the thickness of the mullite layer and SiO_2 layer might initially be too small to be described properly by the Wagner model. However, after a certain period of time, these layers will have grown sufficiently to ignore space charges and keep assumptions of the Wagner model valid and it would simplify the model significantly. Using equation 3.8 and the assumption of a linear chemical potential presented in equation 3.10, this would result in equation 3.12 for each chemical species in each layer.

$$J_i = -D_i * \frac{c_i}{R*T*d_{ox}(t)} * \Delta\mu_i \qquad \textbf{(3.12)}$$

It is assumed that only the oxide layer thickness will change with time and the other variables are only dependent on temperature or remain constant for a certain species and oxide layer. In this equation, the diffusion coefficient is an effective ambipolar diffusion coefficient taking into account

bulk and grain boundary diffusion. It is assumed the layer is perfect and no other defects are present that could act as a fast pathway for diffusion. To account for temperature, an Arrhenius dependence is used, which results in equation 3.13 for the effective diffusion coefficient. In this equation, f is the grain boundary volume fraction usually given by equation 3.14.

$$D_{i,eff} = (1-f) * D_{i,0,bulk} * e^{(-\frac{\Delta G_{act,i,bulk}}{R*T})} + f * D_{i,0,GB} * e^{(-\frac{\Delta G_{act,i,GB}}{R*T})} \quad \textbf{(3.13)}$$

$$f = \frac{2*\delta}{g} \quad \textbf{(3.14)}$$

In which D_0 is the pre-exponential factor in m^2/s and ΔG_{act} the activation energy in J/mol, δ the grain boundary width in m (usually taken as 1 nm for diffusion purposes [95]) and g the average grain size in m. As for most temperatures the grain boundary diffusion coefficient is at least 10^4 times higher than the bulk diffusion coefficient [95], [92], [91], equation 3.14 indicates that grains should be at least 20 μm to have equal contributions of bulk and grain boundary diffusion. Because of the coating thickness of less than 1 μm, it is likely that they are in general significantly smaller. It is therefore reasonable to assume bulk diffusion in alumina and mullite is negligible and that oxidation is governed solely by grain boundary diffusion of oxygen. As amorphous SiO_2 does not have any grain boundaries, the bulk diffusion should be used here.

For the change in chemical potential, equation 3.15 indicates how chemical potential changes with reactions and differences in partial oxygen pressure. In this equation, μ_O is the chemical potential of oxygen atoms in the system, while μ_{O2}^0 is the standard chemical potential of oxygen molecules, both in J/mol. R and T have their usual meaning and P_{O2} is the partial oxygen pressure at that location. For the formation of mullite, it is assumed that the $\Delta\mu_{Al}$ can be entirely attributed to the Gibbs free energy of reaction of the formation of mullite from the oxides, which would result in equation 3.16

$$\mu_O = \frac{1}{2}(\mu_{O_2}{}^0 + R * T * \ln(P_{O_2})) \rightarrow \Delta\mu_O = \frac{1}{2} * R * T * \ln(\frac{P_{O_2}{}^{II}}{P_{O_2}{}^{I}}) \quad \textbf{(3.15)}$$

$$\Delta\mu_{Al} = \frac{\Delta G_{form,mul}}{6} \quad \textbf{(3.16)}$$

As the system is diffusion limited, a quasi-steady state regime can be assumed in which the pressure at the gas-Al_2O_3 interface is the P_{O2} pressure of the bulk gas and the P_{O2} pressure at the SiO_2-$MoSi_2$ interface the equilibrium partial oxygen pressure of equation 3.2. Although not entirely correct, it is assumed that the chemical potential is linear over all three oxide layers without any discontinuities at the interfaces, because data of the latter is unfortunately not available. To simplify the model and to allow the evaluation of partial oxygen pressures at the interfaces, it is also assumed that diffusion of oxygen for mullite formation is independent from diffusion due to oxidation and that the charge balance of the latter is solely compensated for by electron and hole movement, which is reasonable for very thin layers. The pressures at the interfaces on both sides of the mullite layer can then be calculated using the equations 3.18 and 3.19, in which the k_i's are given by equation 3.17.

$$k_i = \frac{D_{O,i,eff} * C_{O,i}}{2 * d_{i,ox}(t)} \quad \textbf{(3.17)}$$

$$P_2 = \left(P_0^{\left(\frac{1}{\left(\frac{k_{Mul}}{k_{Al}}+1\right)}\right)} * P_3^{\frac{k_{Si}}{k_{Mul}}}\right)^{\left(\frac{1}{\left(\frac{k_{Si}}{k_{Mul}}+1-\frac{\frac{k_{Mul}}{k_{Al}}}{\left(\frac{k_{Mul}}{k_{Al}}+1\right)}\right)}\right)} \quad \textbf{(3.18)}$$

$$P_1 = \left(P_0 * P_2^{\frac{k_{Mul}}{k_{Al}}}\right)^{\left(\frac{1}{\left(\frac{k_{Mul}}{k_{Al}}+1\right)}\right)} \quad \textbf{(3.19)}$$

In which P_0 is the partial oxygen pressure at the gas-alumina interface, P_1 is the partial oxygen pressure at the Al_2O_3-mullite interface, P_2 the partial oxygen pressure at the mullite-SiO_2 interface and P_3 the equilibrium partial pressure of equation 3.2, all in bar. These equations are based on a mass balance of oxygen in which any oxygen that diffuses through alumina also has to diffuse through mullite and silica. Combining equation 3.9 and 3.12 and using equation 3.15 and 3.16 to calculate the chemical potential, this results in the following equations for the change of thickness in each layer as a function of time.

$$\frac{\partial d_{Al_2O_3}}{\partial t} = -f_{Al,\,Al_2O_3} * \frac{M_{Al_2O_3}}{\rho_{Al_2O_3}} * J_{Al,Mul} = \frac{M_{Al_2O_3}}{2*\rho_{Al_2O_3}} * \frac{D_{Al,Mul}*C_{Al,Mul}}{d_{Mul}(t)*R*T} * \frac{\Delta G_{form,mul}}{6} \quad \textbf{(3.19)}$$

$$\frac{\partial d_{Mul}}{\partial t} = f_{Al,\,Al_6Si_2O_{13}} * \frac{M_{Al_6Si_2O_{13}}}{\rho_{Al_6Si_2O_{13}}} * J_{Al,Mul} = -\frac{M_{Al_6Si_2O_{13}}}{6*\rho_{Al_6Si_2O_{13}}} * \frac{D_{Al,Mul}*C_{Al,Mul}}{d_{Mul}(t)*R*T} * \frac{\Delta G_{form,mul}}{6} \quad \textbf{(3.20)}$$

$$\frac{\partial d_{SiO_2}}{\partial t} = f_{Si,SiO_2} * \frac{M_{SiO_2}}{\rho_{SiO_2}} * J_{O,SiO_2} - f_{Si,Mul} * \frac{M_{SiO_2}}{\rho_{SiO_2}} * J_{Al,Mul} =$$
$$-\frac{M_{SiO_2}}{2*\rho_{SiO_2}} * \frac{D_{O,SiO_2}*C_{O,SiO_2}}{2*d_{SiO_2}(t)} * \ln\left(\frac{{P_{O_2}}^3}{{P_{O_2}}^2}\right) + \frac{2*M_{SiO_2}}{6*\rho_{SiO_2}} * \frac{D_{Al,Mul}*C_{Al,Mul}}{d_{Mul}(t)*R*T} * \frac{\Delta G_{form,mul}}{6} \quad \textbf{(3.21)}$$

In which the diffusion coefficients, the mullite Gibbs free energy of formation and the equilibrium partial pressure of oxygen are functions of temperature. The values used for all parameters in the evaluation of this model are presented in the matlab code The evaluation of this model was done numerically using the Matlab script presented in appendix III and the results are presented in the next part.

3.2.4 Results model

The main predictions of this model are shown in Figure 3.24, Figure 3.25, Figure 3.26 and Figure 3.27 and are somewhat surprising. From the first figure, it is clear that silica scale growth is very rapid and follows an approximately parabolic growth rate, but that mullite growth is significantly slower. The latter is expected though, as the diffusion of both oxygen and aluminium through mullite is generally considered to be very slow.

When investigating the effect of the main parameters temperature, partial oxygen pressure and grain size, it is clear that temperature has a significant influence. However, the actual influence of temperature seems smaller than would be expected, based on an Arrhenius relation. However, the formation of mullite is significantly increased at higher temperature due to accelerated aluminium diffusion, decreasing the total oxygen diffusion through the system significantly. This might be a very important prediction as particle lifetime could be significantly prolonged by promoting mullite formation during manufacture of the coating.

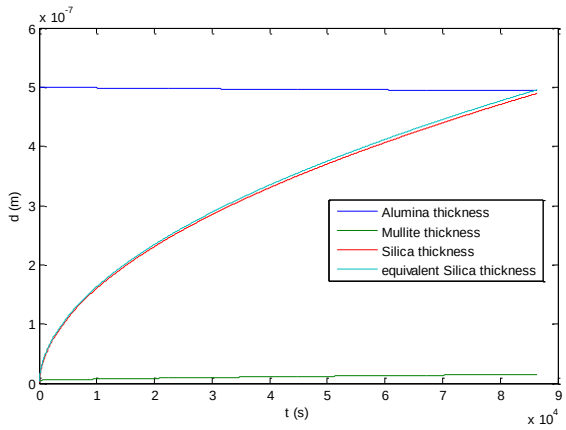

Figure 3.24: Example of the thickness of each layer after 24 hours at 1000 °C.

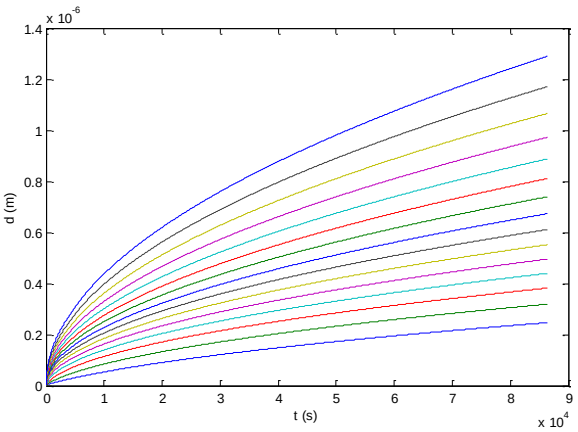

Figure 3.25: The influence of temperature on total oxidation (equivalent silica thickness) of the system after 24 hours for 900 °C to 1200 °C with 25 °C increments with the highest temperature having the highest oxidation rate.

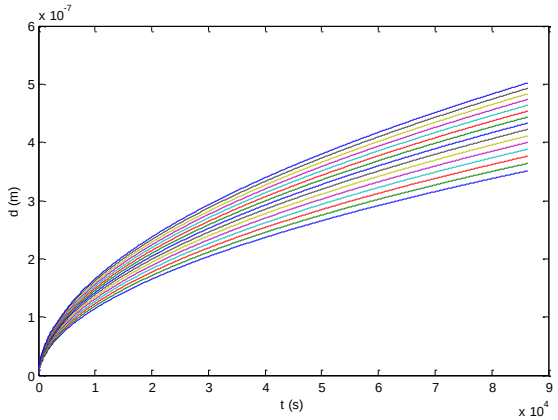

Figure 3.26: The effect of partial oxygen pressure on total oxidation after 24 hours at 1000 °C, with a partial pressure varied from 10^{-14} to 1 bar in power of 10 increments with the highest partial oxygen pressure having the highest oxidation rate.

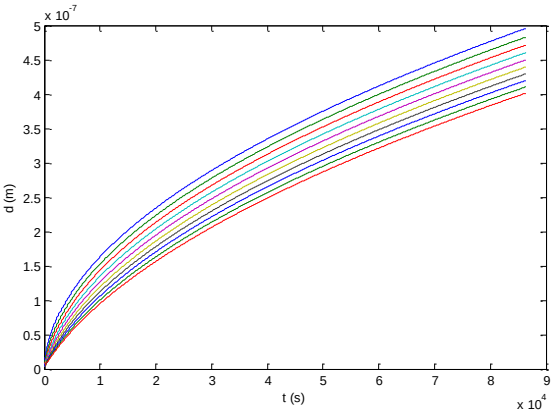

Figure 3.27: The influence of alumina and mullite grain size on total oxidation of the system after 24 hours at 1000 °C with grain size varied from 50 to 500 nm with 50 nm increments with the smallest grain size having the highest oxidation rate.

The effect of partial oxygen pressure on the other hand is extremely small, as the difference in final coating thickness between 10^{-14} and 1 bar of partial oxygen pressure is at most 150 nm, which is still less than 30% of the final coating thickness at 1 bar. At partial pressures that low, it is however very likely that external transport from the bulk to the surface might become rate limiting instead, lowering the final oxide layer thickness that would be found. Finally, grain size also has a minor influence on the oxidation kinetics, slightly lowering the total oxide thickness layer with larger grain size, as would be expected. However, the difference is relatively small compared to temperature.

To investigate the sensitivity of this model towards initial coating thickness, initial Al_2O_3, mullite and SiO_2 coating thickness were calculated, as shown in Figure 3.28, Figure 3.29 and Figure 3.30 respectively. This shows that both Al_2O_3 and SiO_2 initial coating thickness have a surprisingly minor influence on overall oxidation after 24 hours.

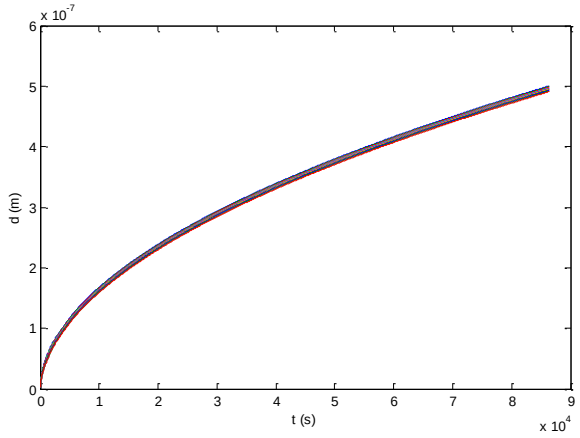

Figure 3.28: The influence of the initial alumina layer coating thickness, with coating thickness ranging from 10 to 1000 nanometers and the highest thickness having the lowest oxidation rate.

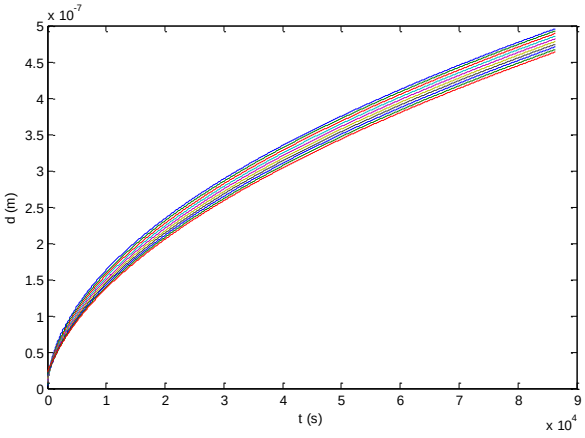

Figure 3.29: The influence of the initial mullite layer coating thickness, with coating thickness ranging from 5 to 50 nanometers and the highest initial thickness having the lowest oxidation rate.

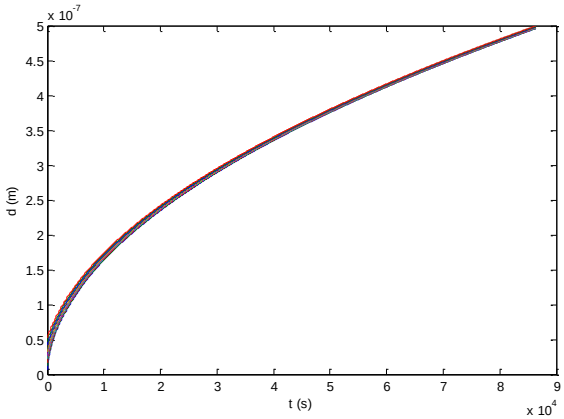

Figure 3.30: The influence of the initial SiO_2 layer coating thickness, with coating thickness ranging from 5 to 50 nanometers and the highest initial thickness having the lowest oxidation rate.

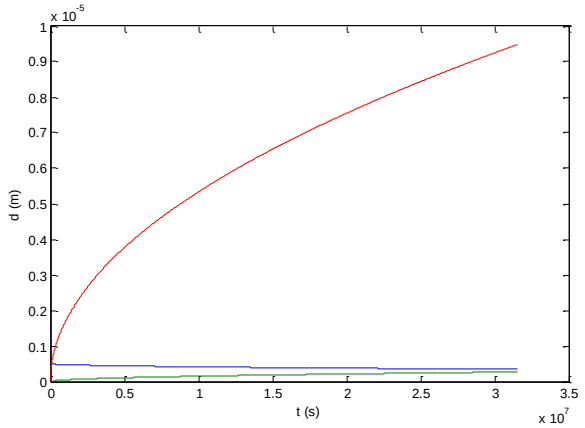

Figure 3.31: Example of the thickness of each layer after one year at 1000 °C.

A likely explanation for the somewhat surprising lack of influence of Al_2O_3 coating thickness might be the fast grain boundary diffusion in combination with small grains. Due to this, the effective oxygen diffusion coefficient is several orders of magnitude higher than the effective diffusion coefficient in either mullite or silica. This results in a significantly lower resistance to oxidation of the substrate and the influence of Al_2O_3 coating thickness being very small.

Initial mullite coating thickness on the other hand does influence the overall oxidation speed, which agrees with literature and other calculations showing the low diffusivity of oxygen in mullite. Because of this, it might be useful to promote the formation of mullite by either alloying $MoSi_2$ with additional Al or additional/longer heat treatment at higher temperatures with low oxygen partial pressures.

Finally, the effect of increasing time (assuming the oxidation layer does not fracture) is essentially the same as for most parabolic growth rate laws. At 1000 °C the total oxide thickness would grow close to 10 micron, indicating that most of the particle would be oxidized at this point.

Materials and Methods

In this section, a concise description of the methods used to synthesize, characterize and test coated molybdenum disilicide ($MoSi_2$) particles is presented. The chapter starts with a brief description of the wind sifting technique required to obtain the right size range of particles, followed by the various methods of coating synthesis, namely three different sol-gel procedures and (Atomic) Layer Deposition with residual Chemical Vapour Deposition (ALD/rCVD).

Subsequently, the methods of thermal treatment and determination of the optimal calcination and transformation are discussed. To obtain information about the material and coating properties of the particles, extensive characterization and performance testing was employed. The techniques used for the particle characterization are also presented.

4.1 Wind sifting

Wind sifting was performed prior to the coating process molybdenum disilicide powders to reduce polydispersity in the size distribution and decrease total surface area of the particles. This was necessary to remove particles that were considered too fine for incorporation in the final TBC and to ensure an acceptable volume ratio of coating material to healing material, which is discussed in more detail in appendix IV. Wind sifting was performed using an Alpine 100 MRZ laboratory zig-zag classifier, shown in Figure 4.32. In each experiment between 300 and 500 g of $MoSi_2$ powder (Chempur, D(V,0.5) = 18 µm) was loaded. Airflow was regulated at 15 m^3/h and the classifier rotational speed was kept at 5000 RPM. More information regarding the working principle of the wind sifting method is available in appendix V.

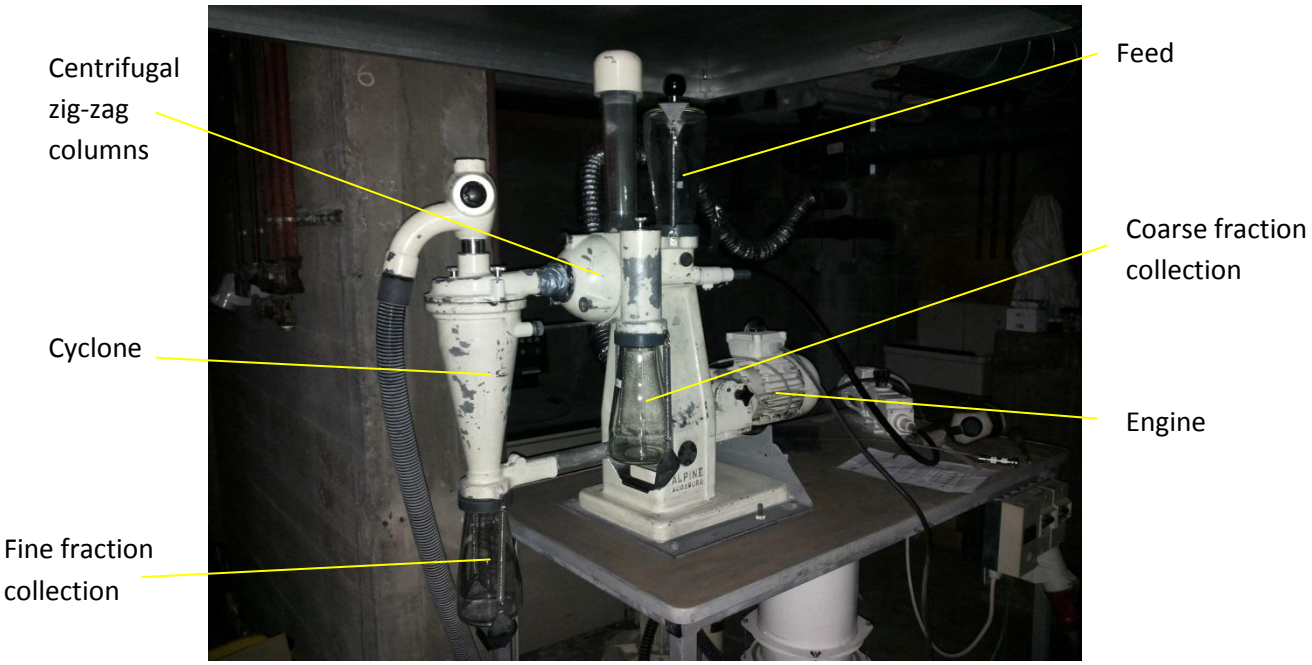

Figure 4.32: *The Alpine 100 MRZ laboratory zig-zag classifier used for wind sifting and its different parts.*

4.2 Sol-gel methods

Coating of particles using sol-gel methods was performed using a modified Yoldas procedure, a method based on alkoxides as precursor for boehmite sols, developed originally by Yoldas et al. [46]. The procedure was modified by Yang and Shih for silicon carbide particles [51], which was used as a

starting point for the sol-gel coating of $MoSi_2$ particles, due to the expected similar SiO_2 native oxide layer on the surface of both particles [52].

First, tests with aluminium oxalate ($Al_2(C_2O_4)_3$) were performed for obtaining critical information on the behaviour of $MoSi_2$ particles in sol-gel experiments, followed by experiments with aluminium isopropoxide ($Al(OCH(CH_3)_2)_3$) and aluminium tri-sec-butoxide ($Al(OCH(CH_3)C2H5)_3$), the structures of which are shown in Figure 4.33 a, b and c respectively. All sol-gel experiments were performed in the setup shown in Figure 4.34, which consisted of a glass beaker mounted on a heating and stirring plate with thermocouple to regulate temperature and stirring speed. If required, nitrogen gas was supplied to the reactor by a custom-made ring-shaped bubbler connected to a nitrogen supply, for a better dispersion of the substrate particles in the suspension.

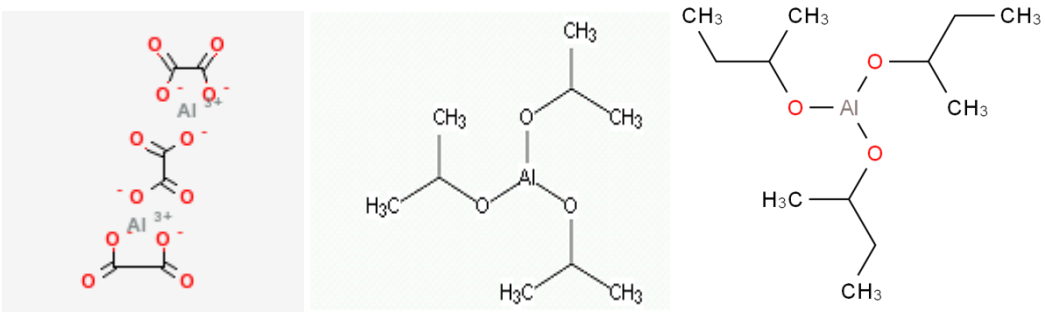

Figure 4.33: ***The molecular structures of (a) aluminium oxalate, (b) aluminium tri-isopropoxide and (c) aluminium tri-sec-butoxide, as provided by Sigma-Aldrich.***

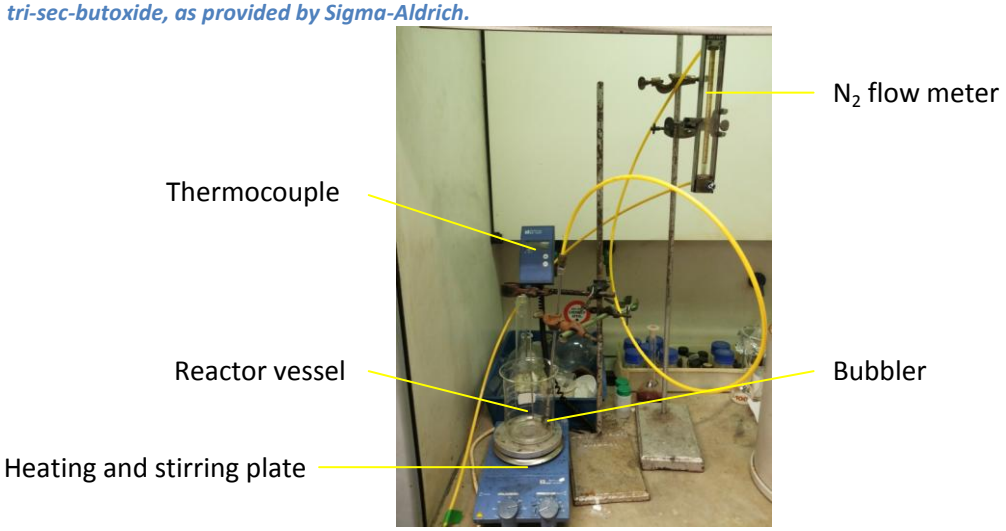

Figure 4.34: ***The setup used for sol-gel experiments with heating, stirring and nitrogen supply.***

4.2.1 Aluminium oxalate method

To obtain information regarding the behaviour of $MoSi_2$ particles and the interactions with the sol and gel during the coating process, aluminium oxalate was employed first, using the procedure mentioned above and adjusted based on the work of Wei et al. [98] and Saha et al. [99]. First, aluminium oxalate tetrahydrate was dissolved in a 1.0 M HNO_3 solution (prepared from 65 wt% HNO_3 solution, Sigma-Aldrich and distilled H_2O) and distilled water was added to obtain desired concentrations. Subsequently, the suspension was heated to 60 °C and stirred at 800 RPM for 30 minutes to dissolve the aluminium oxalate. Then the $MoSi_2$ particles were added and the temperature increased to 80 °C to initiate gelation of the aluminium oxalate and kept at this temperature for 90 minutes while continuing stirring.

Afterwards, solid particles and liquid were separated by vacuum filtration and the solid residue was washed with distilled water three times. Finally, the sample was dried overnight in an autoclave at 110 °C. The weight and volume of the added chemicals were varied significantly for each experiment and these values can be found in Table 4.3. Furthermore, pregelation of oxalate for 30 minutes at 80 °C and bubbling 200 mL/min of nitrogen through the suspension were both performed in separate experiments to increase dispersion of the $MoSi_2$ particles.

Table 4.3: ***Overview of conditions for each aluminium oxalate sample.***

Sample	*1.0 M HNO_3 solution added (mL)*	*distilled H_2O added (mL)*	*$Al_2(C_2O_4)_3$ added (g)*	*$MoSi_2$ powder added (g)*	*wind sifted $MoSi_2$ used*	*Pre-gela-tion*	*N_2 bubbling*
1	50	20	4.48	5	no	no	no
2	100	0	8.36	10	no	no	no
3	50	75	9.62	10	no	no	no
4	50	100	9.62	10	no	yes	no
5	50	250	9.62	10	yes	no	yes

4.2.2 Aluminium tri-isopropoxide method

For the sample based on aluminium tri-isopropoxide ($Al(OC_3H_7)_3$), 98%, Sigma-Aldrich), 8.467 g aluminium tri-isopropoxide was dissolved in 200 mL isopropanol (99.8%, Sigma-Aldrich) and 50 mL ethanol (99.8%, Sigma-Aldrich). 10 g of $MoSi_2$ powder was dispersed in 72 mL MilliQ and 72 mL of isopropanol by ultrasonication. Subsequently the dispersed powder was added to the dissolved $Al(OC_3H_7)_3$ solution, together with 3 mL of 1.0 M HNO_3 solution (prepared from 65 wt% HNO_3 solution, Sigma-Aldrich and distilled H_2O) and the system was heated to 90 °C to gelate for 35 minutes. The solution was cooled down afterwards, left overnight and filtered by vacuum filtration the next day. Finally, the powder was dried in an autoclave at 110 °C for 35 hours.

4.2.3 Aluminium tri-sec-butoxide method

The samples based on aluminium tri-sec-butoxide ($Al(OC_4H_9)_3$, 97 wt%, Sigma-Aldrich) were prepared by heating 300 or 600 mL of distilled H_2O, to obtain a molar ratio of 1:150 of $Al(OC_4H_9)_3$ to H_2O and 15 mL of a 1.0 M HNO_3 solution to 80 °C, adding 10 g of wind sifted $MoSi_2$ powder to this solution and then bubbling 200 mL N_2/min (99.999% nitrogen) through this suspension. When the temperature was stable at 80 °C again, either 5, 10 or 20 g of $Al(OC_4H_9)_3$ was added with approximately 25 mL of ethanol (96 wt%, Sigma-Aldrich) to aid in transfer of the viscous liquid. The ratio of aluminium tri-sec-butoxide to $MoSi_2$ powder was varied to study the influence of solid loading on thickness and resulting coating quality.

After addition of the precursor, the system was left to gelate for 60 minutes. Afterwards, the nitrogen flow and stirring were stopped and either left at 80 °C to evaporate all liquid or centrifuged, in both cases obtaining a paste. When centrifuged, the samples were also washed with distilled water three times. The resulting paste was then dried in an autoclave at 110 °C for 15 hours and ground in a mortar to obtain the coated powder.

4.3 Atomic Layer Deposition/residual Chemical Vapour Deposition

Atomic layer deposition with residual chemical vapour deposition (ALD/rCVD) on $MoSi_2$ particles was performed using a custom-built setup shown in Figure 4.35. This setup consists of a fluidized bed reactor in which the particles to be coated are fluidized, bubblers containing the precursors and gas

cleaning after the reactor to prevent unreacted precursor in the exhaust gases. More information on the setup and operation is presented in appendix VI.

Figure 4.35: ***The ALD setup used in this experiment, showing the whole setup including bubblers and gas cleaning (left) and the reactor with connections (right).***

In each experiment 11 g of wind sifted $MoSi_2$ powder was first dried for 14 hours at 110 °C to remove physisorbed water that could react with the aluminium precursor. Afterwards, the powder was activated in a plasma cleaner for 2 minutes and 20 seconds and loaded in the glass reactor column. To obtain gaseous precursors, a nitrogen gas flow (99.999% purity) of 0.6 L/min (yielding a superficial gas velocity of approximately 0.3 m/s) was passed through bubblers containing the liquid precursors trimethylaluminium (TMA, AKZO Nobel, semiconductor grade) and H_2O (MilliQ), to evaporate and transport the precursors to the reactor. To ensure proper fluidization, vibration at 50 Hz of the entire reactor was utilized. To prevent undesired reactions of TMA with water or oxygen, the whole reactor system was kept under pure nitrogen and at room temperature.

By variation of TMA and water dosage time, purge times and total surface area of the particles to be coated, the layer thickness increase (or layer growth) per cycle can be controlled, allowing for very precise control of final coating thickness. To find optimal conditions for rapid growth, independent variation of TMA dosage time, water dosage time, purge time and number of cycles was performed, summarized in Table 4.4.

Table 4.4: ***Overview of ALD sample conditions.***

Sample	*TMA dosage time (min)*	*H2O dosage time (min)*	*purge time (min)*	*number of cycles (-)*
1	2	5	10	9
2	4	5	10	9
3	6	5	10	9
4	8	5	10	9
5	4	0.5	10	9
6	4	5	5	9
7	6	5	5	10
8	4	5	5	25
9	4	5	5	40

4.4 Heat treatment procedures

To select the optimal heat treatment procedure, multiple tests were performed on coated samples. As mentioned in chapter 2.4 transformation of boehmite and amorphous alumina from sol-gel and ALD respectively to the stable α-alumina phase goes through a sequence of alumina phase transitions with associated volume changes [23]. Furthermore, carbon and water impurities are still present [63]. Therefore, after drying, a two-step calcination/annealing procedure was necessary.

For the first step, the sample was heated to 450 °C in air with a heating rate of 5 °C/minute and kept at this temperature for 30 minutes, followed by flushing with argon and continuing calcination at 450 °C overnight (12 hours). Subsequently the sample was cooled down to room temperature with a cooling rate of 5 °C/minute.

The second step consisted of heating to 900, 1000, 1100 or 1200 °C with a heating rate of 5 °C/minute, keeping the sample at that temperature for 1 hour and then cooling down to room temperature, again at a rate of 5 °C/minute.

4.5 Characterization and performance

In this part the characterization of the particles and composite will be discussed. Details on the working principles of the analysis techniques listed can be found in appendix V.

4.5.1 Characterization raw material

A variety of characterization techniques was performed on the prepared samples. The powders as delivered and the wind sifted samples were analysed using a JSM 6500F, JEOL Ltd. Scanning Electron Microscope (SEM) with an electron beam energy of 15 keV and a beam current of 600 pA to investigate morphology. Elemental analysis was performed with Energy-Dispersive X-ray Spectroscopy (EDS). Powder samples were deposited on carbon tape and if necessary, coated with a thin film of carbon to prevent charge buildup. Laser diffraction was performed to observe the particle size distribution with a Malvern Master Sizer X laser diffraction instrument (Malvern Instruments Ltd.). BET specific surface area was determined by N_2 physisorption, utilizing a TriStar II 3020, Micromeritics, in which approximately 9 g of powder was weighed, degassed at 300 °C overnight in an Autosorb Degasser from Quantachrome instruments and subsequently analysed.

4.5.2 Characterization coated particles

SEM and EDS were also used to characterize coated particles, again to see morphology of the samples and whether successful coating has been achieved and a homogeneous coating was obtained. The same parameters were used for SEM and EDS. X-ray photoelectron spectroscopy (XPS) was utilized to confirm successful coating application and to obtain information on the chemical nature of the surface. XPS was performed using a PHI 5400 ESCA from Physical Electronics Inc, equipped with a Mg/Al dual anode X-ray source and a hemispherical capacitor analyzer. The aperture of the input lens was a 3.5x1.0 mm aperture and emitted electrons were observed at a 45° angle with respect to the sample surface. In all cases, powders were pressed into a high purity indium foil for analysis and analyzed with with Mg Kα radiation (1.2538 keV). The x-ray source was operated with 13 kV acceleration voltage and 200 W power, while the vacuum of the analysis chamber was below $5 \cdot 10^{-9}$ mbar. Spectra were taken from 0 to 1100 eV with a step size of 0.5 eV and 100s acquisition time per step for a survey. For detailed peak analysis, step size was 0.2 eV with 200s acquisition time per step, while the range was varied depending on the element.

Furthermore, X-ray diffraction (XRD) was used to obtain information on crystalline phases present and to see whether obtained coatings are crystalline or X-ray amorphous. This was done with a Bruker D5005 diffractiometer from Bruker Corp. and equipped with a Huber incident-beam monochromator and a Braun position sensitive detector. Powders were dispersed in ethanol and deposited on a monocrystalline Si wafer. Cu Kα1 radiation (wavelength of 154 pm) was used to record diffractograms in a 2θ range of 15° to 90° with a step size of 0.039°.

To obtain information on the amount of alumina present and to obtain an estimate of coating thickness, Inductively Coupled Plasma-Optical Emission Spectroscopy (ICP-OES), X-ray Fluorescence (XRF) analyses and Electron Probe MicroAnalysis (EPMA) surface layer thickness determination [100] were performed.

For ICP-OES, approximately 40 mg of the sample was dissolved in a mixture of 6 mL 1.0M HCl solution with 2 mL 1.0 M HNO_3 and 2 mL 1.0 M HF solution with the aid of 30 min heating in the microwave at maximum power. After destruction, samples were diluted to 50 mL with milliQ and analyzed with a PerkinElmer Optima 4300 ICP-OES instrument at three different wavelengths per element. Concentrations of each element (Si, Mo and Al) were calculated with the aid of calibration solutions for each element, prepared on the same day.

XRF was performed utilizing an Axios Max WD-XRF spectrometer from Panalytical. To be able to measure the powder, 2.0 g of coated powder was weighed, mixed with a cellulose binder and pressed into a tablet. This tablet was then measured in the equipment in a vacuum.

To obtain thickness information based on EPMA analysis, the powder sample was deposited on carbon tape and coated with a thin layer of carbon to prevent charging. This sample was subsequently inserted in the SEM and K-ratios for four elements (Mo, Si, Al and O) were measured with the EDS detector by irradiation of two selected spots for two minutes in a central area on a surface perpendicular to the electron beam. For each sample this procedure was performed on ten different particles and afterwards coating thickness was calculated with the method of Goldstein et al. [100] using a numerical iteration program. Acceleration voltage was varied between 5 and 25 kV depending on the thickness of the coating to obtain approximately equal EDS count signals for Al and Si peaks. This was necessary to ensure high accuracy and the optimum acceleration voltage for each sample was determined by trial and error on a different particle before measurement started.

Cross-sections of the particles were also prepared to obtain better understanding of the interface and confirm coating thickness. Cross-sections were prepared by embedding the 10g and 20g aluminium tri-sec-butoxide coated particles and ALD 25 and 40 cycle samples in an epoxy resin (G2 epoxy resin, Gatan) between two Si wafers of approximately 5x5 mm. These wafers with the epoxy resin and particles were subsequently inserted in a cross-section ion polisher (SM-09010, JEOL Ltd.). Operating conditions were an acceleration voltage of 3.5 kV and an ion current of 18 µA, using Ar ions from 6N (99.9999%) Ar gas. Cross-sections were subsequently analyzed by SEM and EDS. Finally, to obtain information about required annealing conditions, Thermo-Gravimetric Analysis (TGA) was performed.

4.5.3 Characterization heat treated particles

Heat treated samples were characterized by SEM combined with EDS to obtain information on morphology and coating integrity upon annealing, especially to observe the appearance of cracks in the coating. Furthermore XRD was used to see whether coatings were crystalline and which phases were present. XRD was also used to estimate grain size of the α-alumina phase. For all methods mentioned here, equipment and analysis parameters were kept constant and the same as for characterization of the coated particles in chapter 4.5.2.

4.5.4 Performance testing final particles

To evaluate long-term shell integrity and stability of the particles, they were subjected to an oxidizing environment at high temperature using TGA. Weight change of approximately 25 mg of 10g and 20g aluminium tri-sec-butoxide and 25 and 40 cycle ALD samples that were heat treated at both 450 and 1200 °C, was monitored at isothermal hold for 100h at 1000 °C. Furthermore, wind sifted but uncoated $MoSi_2$ particles were also monitored to act as a blank. Finally an ALD 40 cycles sample that has only been heat treated at 450 °C was also monitored to investigate whether this would limit cracking observed in these samples and improve oxidation resistance due to the more amorphous structure at the start of the experiment. For investigation of the healing properties, the 20g sol-gel coating procedure and heat treatment at 450 °C and 1200 °C was repeated for wind sifted $MoSi_2$ particles that contained 2 wt% boron. Previous research by Mao [17] found that the addition of B to $MoSi_2$ improved oxidation and healing kinetics, allowing for healing at lower temperatures by inhibiting SiO_2 crystallization, which was the reason for the use of $MoSi_2$ with 2 wt% B.

Coated particles were mixed with yttria-stabilized zirconia powder (5.2 wt% Y_2O_3, basic grade, D(V,0.5) = 40 nm, Tosoh) by adding 5.58 g of coated particles to 22.0 g YSZ powder in a glass jar and mixing these powders on a roller mill. The mixed powder was subsequently divided in three equal portions, which were sintered with Spark Plasma Sintering (SPS). During SPS, the powder was first compressed with a force of 35 MPa, followed by heating to 1450 °C (heating rate 25 °C/min) and was kept at this temperature for 30 minutes to attain full densification. Sintering was monitored by piston movement and was assumed to be finished after the piston ceased to move (on average after 5 minutes pressing at maximum temperature). After isothermal holding at 1450 °C, pressure was released and heating stopped and the system was allowed to cool by subjecting it to a room temperature atmosphere. This resulted in three cylindrical tablets with a diameter of 20 mm and a thickness of 5 mm, containing 20 volume % of healing particles.

To investigate healing properties, damage was introduced in the samples by Vickers indentation with 10 kg force after polishing. Additional and more severe damage was also created in one of these tablets by using Vickers indentation with 20 kg force. The tablet that was only subjected to damage from 10 kg force was healed at 1200 °C for 30 minutes, introducing it directly in the furnace at 1200 °C without heating and cooling to prevent excessive oxidation. The tablet that was more severely damaged was healed at 1100 °C for 1h with heating and cooling rates of 5 °C/min to avoid thermal shock damage. The third tablet was kept at 1100 °C for 48h without polishing or damage to investigate thermal stability of the composite. Furthermore, several tablets containing only YSZ powder were also sintered, polished and indented with the same procedure to compare mechanical properties of composites and pure YSZ. Damage and healing were investigated with optical microscopy and SEM combined with EDS.

Results and Discussion

In this chapter, the results of the various methods of particle shell manufacture will be presented and discussed. The chapter will start with a discussion of the uncoated particles and the results of wind sifting. This is followed by the results of the two particle coating methods, starting with the sol-gel procedures and followed by the results of atomic layer deposition with residual chemical vapor deposition (ALD/rCVD). Afterwards, the heat treatment of coated particles resulting from both methods will be analyzed. The chapter will then continue with an analysis of the thermal stability of the particles and how this compares to the diffusion model and finish with the results of particles embedded in the self-healing composite.

The following abbreviations will be used in this chapter to address the main samples. Wind sifted molybdenum disilicide particles that have been coated with a sol/gel originating from 10 or 20 g aluminium tri-sec-butoxide per 10 g of particles will be referred to as SG-10g and SG-20g respectively. The wind sifted particles produced with the final ALD/rCVD method that underwent 25 and 40 cycles will be referred to as ALD-25C and ALD-40C respectively. Furthermore, $MoSi_2$ particles that contain 2 wt% alloyed boron will be referred to as $MoSi_2B$. This is however neither an accurate description of the boron content (which would be more closely resembled by Mo_3Si_6B), nor of the phase it is present in.

5.1 Characterization starting materials

5.1.1 Starting material

The $MoSi_2$ and $MoSi_2B$ powders from Chempur were first characterized as delivered. Particle size distribution (PSD) was studied by laser diffraction, shown in Figure 5.36. SEM analysis was also performed on $MoSi_2$ powder for investigating morphology, shown in Figure 5.37. Phase composition was studied by XRD, presented in Figure 5.38. BET specific surface was measured for the $MoSi_2$ powder with N_2 physisorption, the adsorption-desorption curve of which is shown in Figure 5.39, along with the measured BET specific surface area.

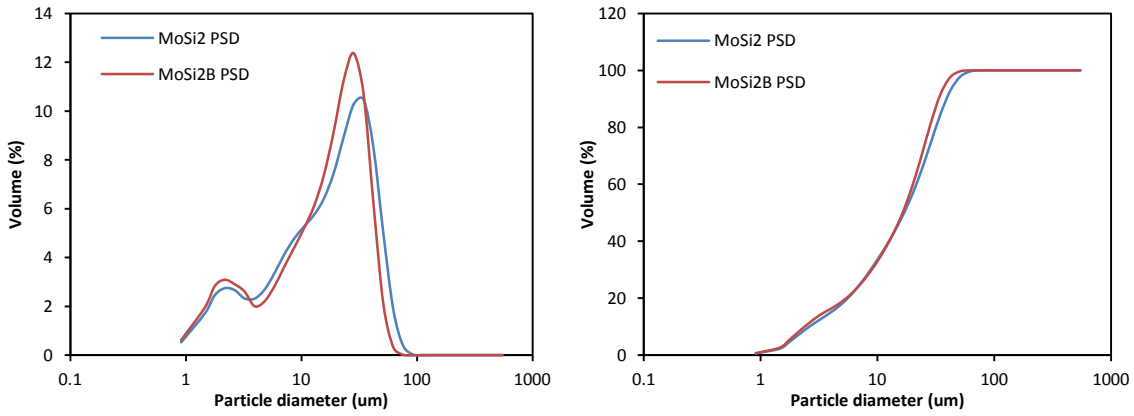

Figure 5.36: *Laser diffraction results for $MoSi_2$ and $MoSi_2B$ with the volume particle size distribution (left) and cumulative volume distribution (right).*

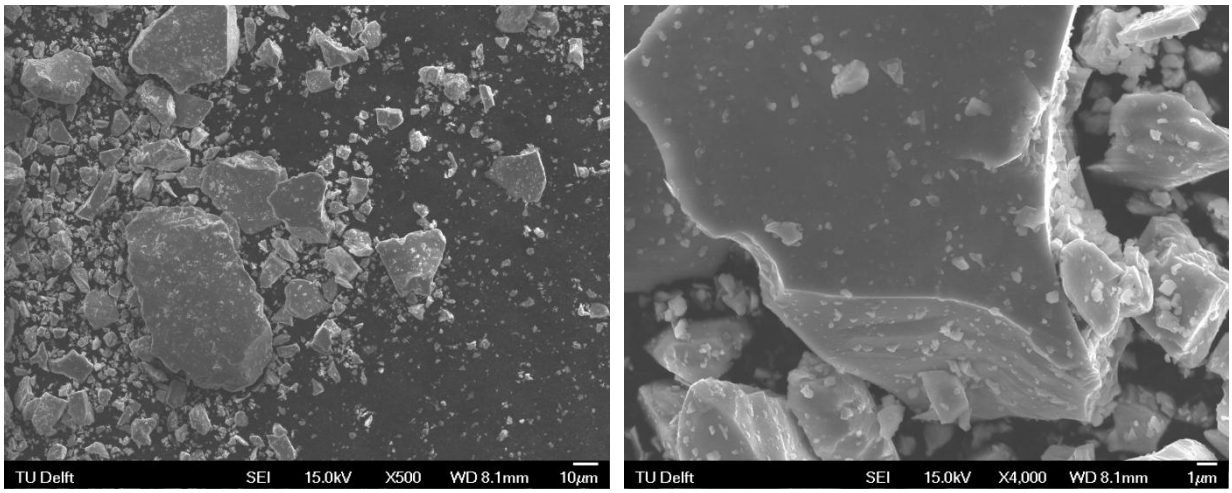

Figure 5.37: *Scanning Electron Microscope (SEM) images of untreated $MoSi_2$ powder at different magnifications.*

When investigating the obtained SEM and laser diffraction data, it is clear that the particle size distribution of both the $MoSi_2$ and the $MoSi_2B$ is very polydisperse and far from the 25 µm that would be the ideal particle size. This is also illustrated by a volume average diameter D(V,0.5) of 18.6 µm but a D(V,0.1) of only 2.9 µm. Due to the lens used during laser diffraction, particles smaller than 0.5 µm could not be measured during the $MoSi_2$ experiment, but SEM images indicate that such particles are very likely to be present as well. This would also explain the high BET surface area of almost 0.6 m^2/g found during N_2 physisorption, which is more than 10 times the surface area that would be expected for ideal spherical particles of 18 µm (0.053 m^2/g for $MoSi_2$The distributions for the raw materials are however very similar to each other, with the $MoSi_2B$ powder being only slightly finer than the $MoSi_2$ powder.

The SEM images also show that most particles are far from spherical. Many particles have sharp edges and characteristic cleavage steps and surfaces. These result from the manufacturing process of Chempur, which is crushing of sintered material, which could also explain the high polydispersity observed, as crushing is likely to yield a wider distribution than many other manufacturing methods.

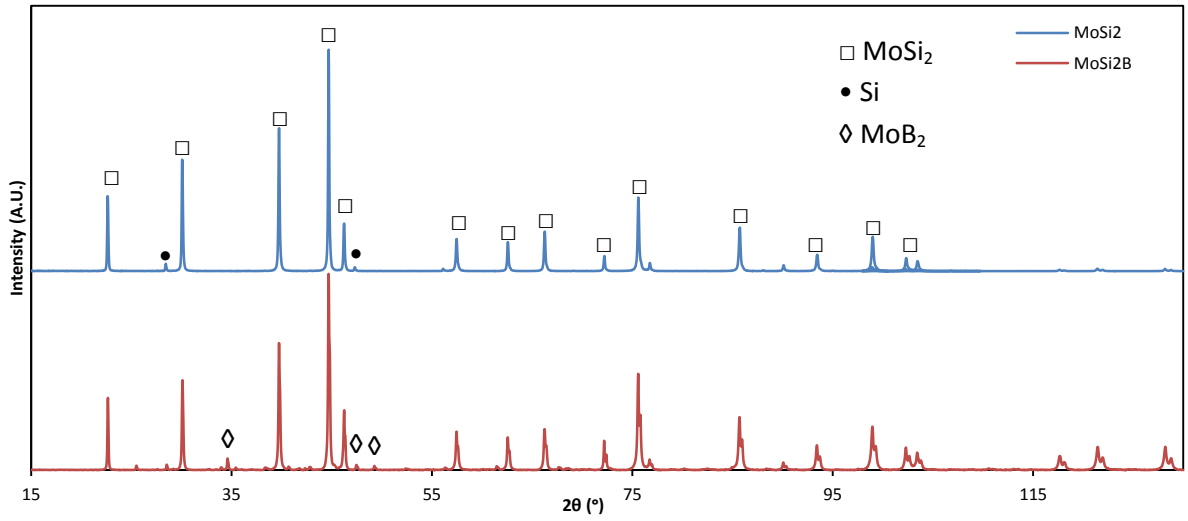

Figure 5.38: *X-ray diffractograms of $MoSi_2$ and $MoSi_2B$ with phases present.*

The X-ray diffractograms show that in both materials the main constituent is indeed $MoSi_2$ in its stable tetragonal form, as would be expected. It also shows the presence of some residual silicon, which is most likely due to the production process. As polycrystalline Si is significantly less expensive than Mo, a slight excess is often added to ensure complete reaction of molybdenum to $MoSi_2$ during sintering and prevent the formation of Mo_5Si_3 [101]. Both diffractograms do indeed not show any Mo_5Si_3 peaks.

Furthermore, the diffractogram of $MoSi_2B$ also has another phase, namely MoB_2. This indicates that boron segregates from the $MoSi_2$, instead of dissolving in the matrix. No peak shifts of $MoSi_2$ from lattice strain due to the presence of boron are observed either, which would be expected if boron would actually dissolve in significant amounts in the $MoSi_2$ matrix. Another observation supporting this is the presence of Si peaks of higher intensity compared to $MoSi_2$ peaks. As boron in MoB_2 replaces Si in certain phases, larger amounts of free Si should be present, which is exactly what is observed. The segregation of boron is important, as this could affect the healing capabilities of the capsules. As Mao discussed, the main effect of boron is the stabilization of the amorphous SiO_2 phase during oxidation. This does require the boron to be located close to Si though, which is why it is important for these segregated areas to not be too large. An attempt was made to obtain B distribution in the particles by EDS element mapping shown in appendix VII, but proved to be unsuccessful due to energy overlap with carbon (from carbon tape) and the low accuracy of the detector for low energy x-rays from B. The distribution nevertheless seemed relatively homogeneous over the $MoSi_2B$ particle, although another experiment is recommended.

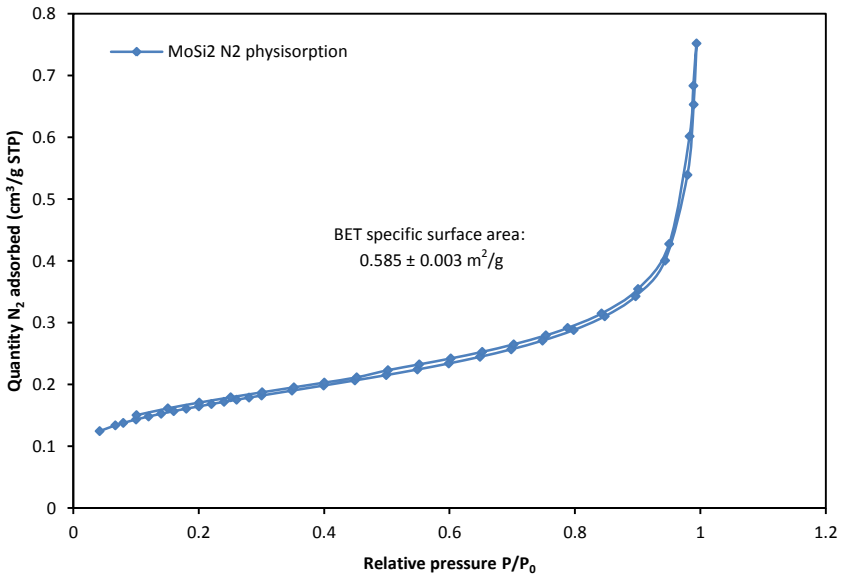

Figure 5.39: *N_2 physisorption adsorption/desorption curve of $MoSi_2$ base material, with reference pressure P_0 = 0.1 MPa.*

Finally, the N_2 physisorption isotherm allows both calculation of the surface area of the as received samples and the determination of porosity. The lack of a hysteresis between the adsorption and desorption curves indicates that no mesopores (2-100 nm in size) are present, while the low starting adsorption and lack of hysteresis at the start show the lack of micropores (<2 nm). The absence of larger pores is also clear, as these would be visible in the SEM images and no such pores have been observed. It is therefore concluded that the $MoSi_2$ particles are nonporous and sufficiently densified during manufacture.

As mentioned before, it is also possible to measure the surface area with N_2 physisorption using the Brunauer-Emmett-Teller (BET) physisorption model. For this $MoSi_2$ sample, the BET specific surface area was found to be 0.585 m^2/g, which is very high when a high thickness Al_2O_3 coating is necessary. Because of this and the presence of a significant amount of very small particles, wind sifting to separate fine and coarse particles was deemed necessary.

5.1.2 Wind sifting

Hence, the characterization of wind sifted particles is discussed here. PSD of both the coarse and fine fractions was again studied with laser diffraction, as shown in Figure 5.40 and Figure 5.41 and the PSD percentiles are shown in Table 5.5. N_2 physisorption isotherms of the two $MoSi_2$ batches are shown in Figure 5.42, along with the calculated BET surface areas in Table 5.6. SEM images of wind-sifted $MoSi_2$ and $MoSi_2B$ are shown in Figure 5.43. Finally, the possibility of contamination by the wind sifting equipment was investigated with XRF on $MoSi_2B$ before and after wind sifting, the results of which are shown in appendix VIII.

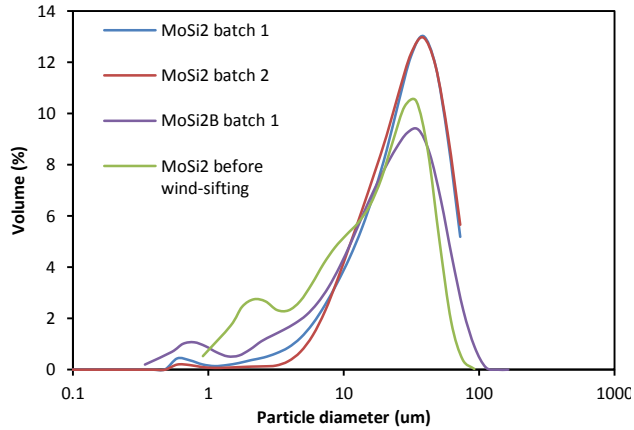

Figure 5.40: *Laser diffraction PSD results for the coarse fractions after wind sifting compared to the material before wind sifting.*

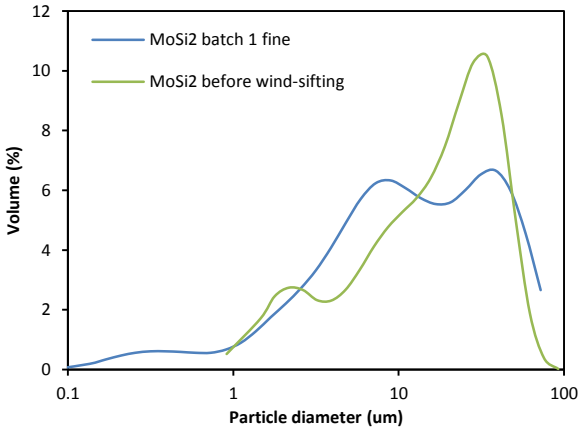

Figure 5.41: *Laser diffraction PSD results for the fine fraction of $MoSi_2$ batch 1 after wind sifting compared to the material before wind sifting.*

Figure Figure 5.40 and Figure 5.41 clearly show the classification abilities of the wind sifting machine. In both coarse fractions of $MoSi_2$ almost all particles below 7 µm in diameter have been removed from the as delivered powder, while retaining the larger particles. As is evident from the fine fraction analysis, this separation is not perfect though, as some of the larger particles are still present in the fine fraction. Their volume fraction has however been significantly decreased. The imperfect separation can be explained at least partially by the irregular shape of the particles. As the wind sifting separates based on density and hydrodynamic properties in an air flow, irregular shapes result in variation of the hydrodynamic properties with variation of orientation [102]. Therefore particles that are either too large or too small to be expected in the fine or coarse fraction respectively can still end up there. Another cause could be imperfect dispersion, causing several smaller particles to stick together or to a larger particle and end up in the coarse fraction.

The relative lack of the smallest particles of 1 µm or lower in the fine fraction can be explained by the imperfect cyclone that is supposed to separate all fine particles from the gas phase. This cyclone is not able to separate most of the very fine particles from the gas flow due to their low weight to surface area ratio. Due to this, the finest particles usually end up in the dust filter of the wind sifting machine.

As is clear from these figures however, good separation is possible and reproducible, as there is only a small difference between the two $MoSi_2$ batches. However, separation of fine particles has been less successful for the $MoSi_2B$ fraction even though a significant amount of fine material has been removed. This might be related to the material, as it was already observed in the XRD diffractogram that the $MoSi_2B$ material consists of multiple phases, the distribution of which is not completely known. If some particles contain a significantly higher percentage of MoB_2, their density is likely higher as well, which alters separation behavior in wind sifting.

Table 5.5: ***PSD percentiles and Sauter particle diameter for the measured samples calculated from laser diffraction data.***

Sample	*D (V,0.1)*	*D (V,0.5)*	*D (V,0.9)*	*Sauter diameter D (3,2)*
Specifications Chempur $MoSi_2$ (µm)	1.86	4.87	9.01	-
Actual measured $MoSi_2$ (µm)	2.88	18.63	42.89	8.16
$MoSi_2$ Wind sifted batch 1 coarse (µm)	8.315	28.79	57.42	13.78
$MoSi_2$ Wind sifted batch 2 coarse (µm)	10.24	29.16	58.23	17.65
$MoSi_2$ Wind sifted batch 1 fine (µm)	2.04	11.91	47.59	3.53

Table 5.5 reinforces this, showing a relatively large increase in the tenth percentile of the PSD, while showing a significantly smaller relative increase in the 90th percentile for both wind sifted batches compared to the starting material. The fine fraction shows a relatively small decrease of the tenth percentile however, strengthening the suspicion that most very fine particles are not collected in this fraction. This could also explain the observed loss of material, which was between 10 and 20 percent of the starting weight and the fact that the fine fraction weight usually consisted of less than 10 percent of the starting weight.

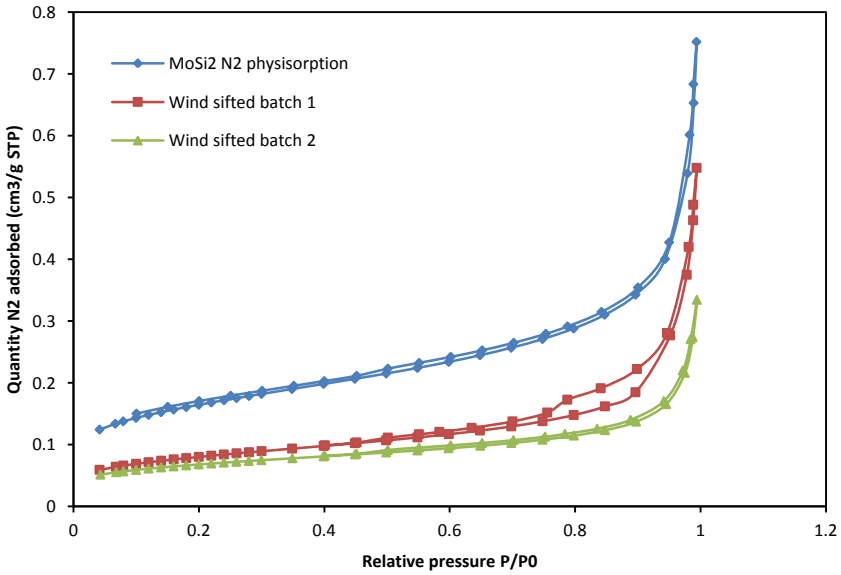

Figure 5.42: ***Nitrogen physisorption isotherms of the two wind sifted $MoSi_2$ coarse batches and the starting material.***

To confirm that a significant part of the fine material has been removed in the coarse samples and to measure the necessary decrease in specific surface area, N_2 physisorption was also performed. As is clear from Table 5.6 and Figure 5.42, there is indeed a significant decrease in surface area, as the total surface area is more than halved by wind sifting the material, which is also indicated by a lower total adsorption in both wind sifted batches. Surprisingly though, a small hysteresis can be observed

in the isotherm of batch 1. This would indicate that either wind sifting could introduce porosity in the particles, which is unlikely, or that some contamination by a porous material has occurred. A measurement error would also be possible, as these measurements are performed relatively close to the limit of the machine capabilities and it is not entirely sure that this hysteresis is significant.

Therefore, XRF was performed on the $MoSi_2B$ sample before and after wind sifting, the results of which are shown in appendix VIII. However, no significant changes in elements other than Mo and Si were found. This indicates that contamination is unlikely, as the higher Mo and lower Si concentrations can most likely be attributed to measurement errors. Another option might be that separate particles of pure Si are present, as the presence of Si in the base material was confirmed by XRD. The density of Si is also significantly lower than that of $MoSi_2$, which would result in significantly more and larger Si particles in the fine fraction. If contamination has occurred on the other hand, this would most likely result in an increase of Si instead, as the most likely contaminant would be fly ash, which consists mostly of silicates. An increase of concentrations of other elements would also be very likely upon contamination.

Table 5.6: ***The calculated BET specific surface areas based on isotherm data for each sample.***

Sample	*Sample mass measured (g)*	*BET surface area (m^2/g)*	*Error (m^2/g)*
$MoSi_2$ Starting material	9.2193	0.585	0.0026
$MoSi_2$ Wind sifted batch 1	10.6214	0.289	0.0007
$MoSi_2$ Wind sifted batch 2	7.4539	0.244	0.0009

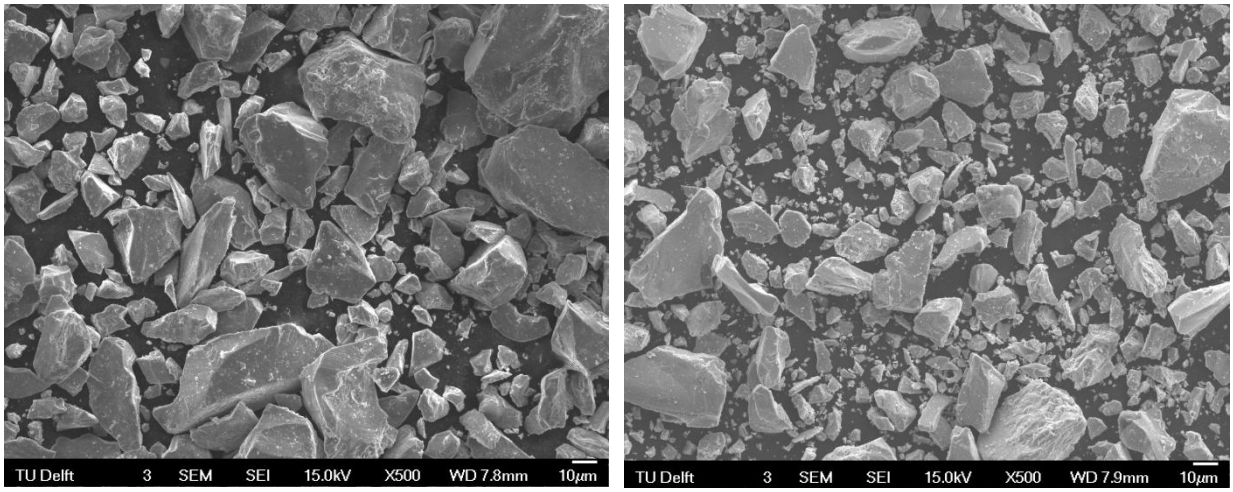

Figure 5.43: ***SEM images of $MoSi_2$ particles (left) and $MoSi_2B$ particles (right) after wind sifting.***

Finally, analysis of the SEM images in Figure 5.43 shows that the morphology of the particles remains unchanged, but the amount of fine particles has significantly decreased, confirming the results of the laser diffraction experiments. Some smaller particles, mainly stuck to the larger particles, are still observed however, indicating that dispersion is indeed not perfect. There is also an interesting difference between the $MoSi_2$ particles and $MoSi_2B$ particles, with the latter apparently containing more fine particles and having a smaller particle size in general. This does agree with wind sifting observations in which a larger fraction of fine material is found in the $MoSi_2B$ powder. It is also likely that this increase in the number of smaller particles also results in an increase in total surface area. This could have implications for resulting coating thickness and coverage.

5.2 Sol-gel coating

5.2.1 Oxalate method

Experiments with aluminium oxalate were performed to obtain critical information regarding the behavior of $MoSi_2$ particles in an acidic sol. Previous investigations by Carabat et al. [22] already found that dispersion of $MoSi_2$ particles in such a sol is difficult due to the high density of the particles. Furthermore, as mentioned in the theory part, complete coverage is very important. This coverage can be affected by dispersion, as settled particles will have less contact with the sol, often resulting in less material being deposited on these particles.

This was also observed in the aluminium oxalate experiments, as two separate morphologies could be distinguished for all experiments except experiment 2. An example of these two morphologies is shown in Figure 5.44, in which the more flaky phase consists mainly of aluminium and oxygen, as measured by EDS shown in Figure 5.44 and Table 5.7. The flaky phase was however mostly present on the surface of $MoSi_2$ particles and not separate as loose flakes. Two of the particles, namely at point four and five, on the other hand did not show any significant concentrations of aluminium and instead has molybdenum and silicon as its main constituents. Although, in the case of point four, the absence of molybdenum might indicate a problem with the EDS measurement for this point. Another option might be that this is a particle of pure silicon however, as XRD did show the presence of a separate Si phase.

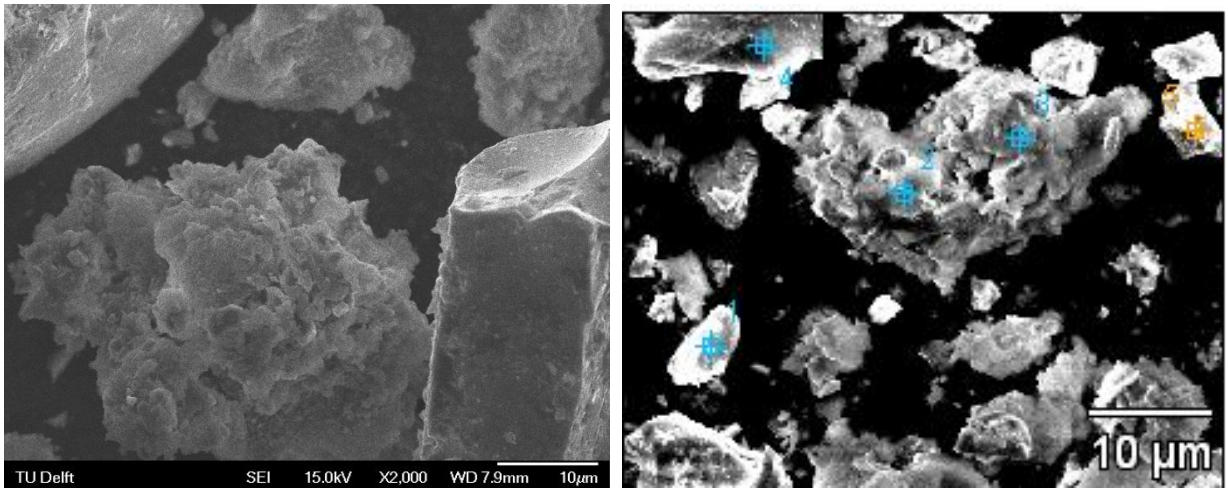

Figure 5.44: ***The two morphologies present for all aluminium oxalate sol-gel coatings except those resulting from experiment two, high-resolution (left) and low-resolution EDS image with measurement points indicated (right).***

However, in other cases, particles did show aluminium coverage as measured by EDS without a flaky morphology. An example of this can be seen for point 1, which does not contain significant traces of the flaky phase, but does seem to be covered with a significant amount of aluminium. Therefore it is likely that the flaky morphology is actually aluminium oxalate that did not dissolve completely, which is confirmed by the low solubility of aluminium oxalate [103], especially at a pH close to 7. Although aluminium oxalate solubility increases drastically in more acidic solutions, concentrations used in these experiments were sometimes higher than this solubility, as this aided in forming a sol and gel. Due to this, it is not possible to evaluate coating quality based on SEM observations alone. Therefore, to evaluate coverage, EDS was utilized as an additional observation.

Table 5.7: *EDS elemental concentration measurements in atom% of the points shown in Figure 5.44 b.*

	O content (atom %)	*Al content (atom %)*	*Si content (atom %)*	*Mo content (atom %)*
Point 1	45	4.6	35	16
Point 2	64	32.9	1.8	1.5
Point 3	54	25.7	14	6.4
Point 4	10	0.69	89	0.60
Point 5	-	1.2	65	34

In experiment 2, an attempt to increase dissolution by addition of more nitric acid was performed. As expected, this lowered the pH to roughly 2.5, measured with pH paper. An example of the resulting particles is shown in Figure 5.45. Although no flaky morphology was observed in this sample, another observation was the lack of coating on the particles in general with only small patches of the particle being coated. This is most likely due to electrostatic interactions between particles and sol, as discussed in chapter 2.2, resulting in both sol and substrate being positively charged and repelling each other. Another indication that this is the case is the observation that after filtration, the filtrate is light green, just like the precursor solution/sol before addition of the $MoSi_2$ particles. In all other aluminium oxalate experiments the filtrate was colorless.

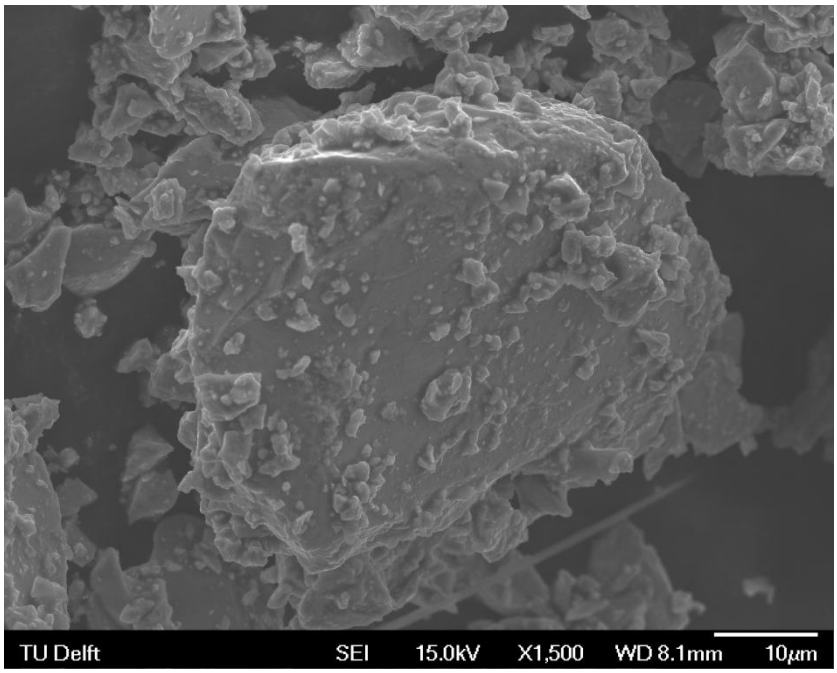

Figure 5.45: An *SEM image of particles resulting from experiment 2, only being coated by small patches of aluminium oxalate instead of almost complete coverage.*

An important conclusion from this would be that the surface is indeed behaving like a native SiO_2 layer with an isoelectric point near pH 3 and that electrostatic interactions between sol and substrate are very important in these systems. Therefore it is important to keep the pH of the sol around 4, as this allows for favorable electrostatic interactions between sol colloids and $MoSi_2$ surfaces and will improve coverage.

To further improve coverage of particles with the sol-gel method, three more experiments were performed, in which the effects of gelation before addition of the particles and nitrogen bubbling on the resulting coating were investigated. Both of these methods attempted to increase dispersion by a

higher viscosity and upward movement pulling the particles into suspension respectively. SEM images shown in Figure 5.46 show the resulting morphologies for the three different experiments. The experiment with pregelation also formed a significant agglomeration at the bottom, that was separately investigated and shown in Figure 5.46 d.

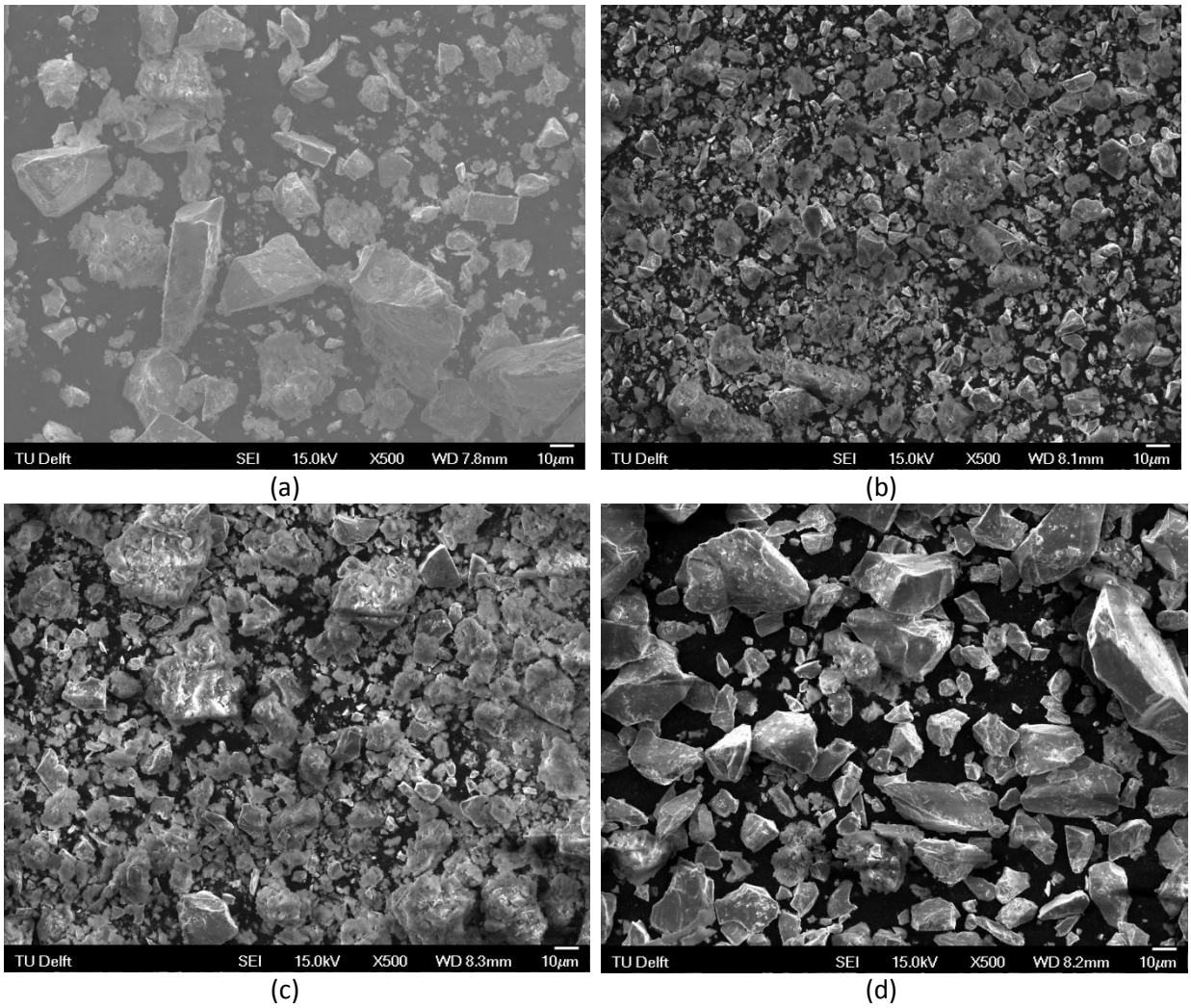

Figure 5.46: ***SEM images of the three final sol-gel experiments, with neither pregelation nor nitrogen bubbling (a), dispersed phase after pregelation (b), with nitrogen bubbling (c) and the agglomerated part at the bottom after pregelation (d).***

The figure shows significant difference in resulting morphology, especially related to the presence of the flaky phase on the particles. In the case of nitrogen bubbling (Figure 5.46 c), the amount of this phase seems to have increased significantly compared to the sample in which neither of the methods was used. Although some increase in this phase on the particles seems to be present when comparing the pregelated phase that remained in suspension with the original sample, the sediment of that sample does not show any of this phase. Another observation from these images is the significantly larger particles being present in the latter phase, indicating that sedimentation of larger particles in particular is indeed a problem in this method.

However, as was observed before, coating is difficult to observe solely based on morphology, which is why the samples were also compared with EDS measurements. The individual measurements can be found in appendix IX, while these results are summarized in Table 5.8. For each sample a certain amount of points were measured with EDS and were compared based on the amount of points that

did not show a significant amount of Al, as defined by the EDS software. This significance is a peak in the EDS spectrum that is at least three times the value of the background noise with an acceleration voltage of 15 kV. Another comparison was made that lists the amount of points that did have a significant aluminium detection, but less than 0.90 atom percent. In these cases, the accuracy of the EDS detector is still uncertain and such a low Al percentage would result in very thin coatings in any case and is therefore used as another comparison value.

Table 5.8: ***Combined EDS measurements for each sample and the number of measurements with significant Al detected.***

Sample	Total EDS measurements	No significant Al detected by EDS	Significant Al detected, but <0.90 atom%	Percentage of total (%)
No pregelation, no bubbling	15	2	2	27
Pregelation, dispersed	16	0	6	38
Pregelation, agglomerated	13	0	5	39
Bubbling	53	3	10	25

This table confirms the findings based on SEM images that both pregelation and nitrogen bubbling result in an increase in coverage of particles when comparing whether the Al signal was significant according to the detector software. When investigating whether more than 0.9 atom % of Al was present, the difference is however less pronounced, with the pregelation method actually performing significantly worse and bubbling only performing slightly better. However, due to the limited number of points measured for the first sample, this difference is probably not significant and more measurements should be performed if definite conclusions are to be drawn based solely on EDS.

The higher number of particles with low amount of coating could be accounted for by the higher amount of solvent required to retain a bubbling regime, with 300 mL being necessary as opposed to 125 mL for the original sample. With the same amount of precursor, this most likely results in less gelation due to lower overall concentration.

Another interesting observation is that there is also no significant difference between the agglomerated and dispersed powders in the pregelation experiment. This indicates that coating also deposits on the particles present in the sediment. The amount of coating detected by EDS is somewhat less though, which agrees with SEM observations showing almost complete absence of the flaky phase.

Based on these measurements, the main conclusion is that coating is possible using aluminium oxalate sols. The resulting coating morphology consists of both a flaky phase that is most likely non-dissolved aluminium oxalate and a thin adherent layer on top of particles that is difficult to distinguish without EDS. Furthermore, nitrogen bubbling is beneficial to contact between sol and particles and could aid in coverage improvements, while the effect of pregelation is most likely detrimental to coverage, as was expected according to previous findings described in section 2.3. Finally, electrostatic interactions are very important in the alumina-$MoSi_2$ particle system and can be regulated by pH, which should be carefully regulated around 4 to have attractive interactions between Al sol and the $MoSi_2$ particles.

5.2.2 Aluminium tri-isopropoxide method

Another precursor investigated was aluminium tri-isopropoxide, an alkoxide that forms a boehmite (AlOOH) sol and gel upon reacting with water. Due to this reaction, dissolution of the precursor in anhydrous alcohols was necessary and particles and water were added at the same time. The resulting coated particles were investigated by SEM, the results of which can be found in Figure 5.47.

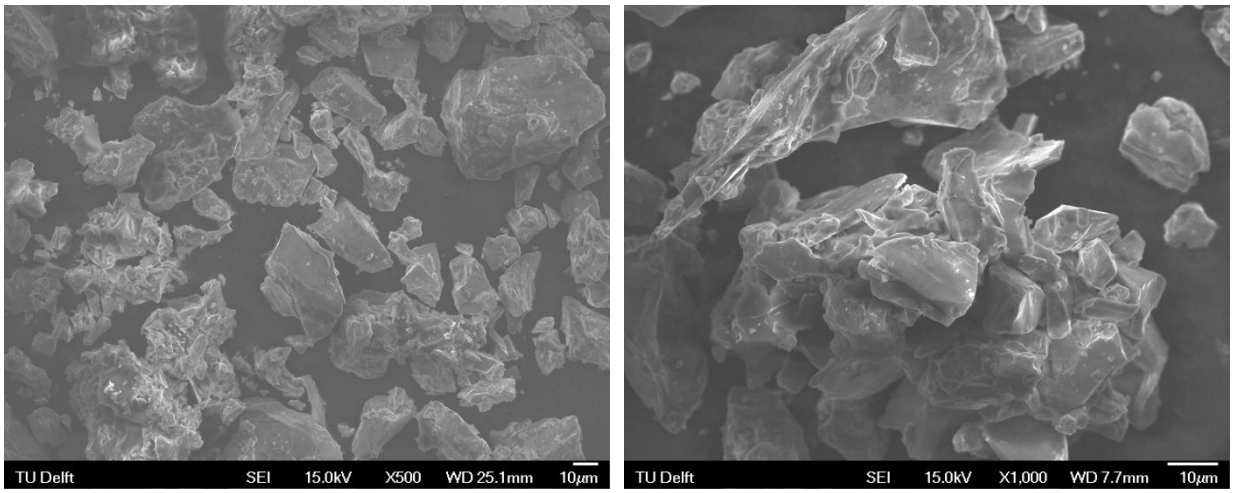

Figure 5.47: ***Particles coated with aluminium tri-isopropoxide precursor based gel at different magnifications.***

As with the aluminium oxalate based samples, two different morphologies can be observed again. One that is very similar to the uncoated particles and another that consists of somewhat sharp crystals with a morphology somewhat different from the base material. However, when performing EDS analysis, both morphologies contain aluminium in significant amounts, although for the latter morphology significantly higher concentrations are detected. When performing the same analysis of the EDS measurements as for the oxalate samples in chapter 5.2.1, only 2 out of 12 points or 17% contain less than 0.9 atom % aluminium. Individual EDS measurements are tabulated in appendix IX.

These results indicate that the formation of boehmite from aluminium tri-isopropoxide results in a sol that has a more advantageous interaction with the $MoSi_2$ substrate than sols derived from aluminium oxalate, as the coating has an improved coverage and is more homogeneous, as is evident from the SEM images and EDS data. An explanation for this observation could be the formation of boehmite by a chemical reaction, which forms a sol with significantly different morphology than one formed from metal salt solutions, as explained in chapter 2.2.1. However, a significant disadvantage of aluminium tri-isopropoxide is its low solubility in most solvents, even its own parent alcohol, isopropoxide. It is also very difficult to dissolve, making this route very complex and limiting the amount of alumina that can be deposited on the particles by this method.

5.2.3 Aluminium tri-sec-butoxide

To circumvent the problem of low solubility that aluminium tri-isopropoxide faces, another very similar alkoxide, aluminium tri-sec-butoxide was also utilized as a precursor. This alkoxide is liquid at room temperature and miscible with H_2O, although it reacts rapidly. Due to these properties, dissolution of the precursor in advance was not necessary, resulting in a significantly simpler process.

Different ratios of precursor to $MoSi_2$ particles were used with 5g, 10g or 20g of precursor per 10g $MoSi_2$ to yield particles with an approximate thickness of 100, 200 or 400 nm Al_2O_3 after heat treatment respectively if all formed boehmite deposited on the particles. Due to the formed gel

blocking the filter pores, separation of particles and liquid could not be performed by filtration. Therefore liquid evaporation and centrifugation were used as alternative separation methods. These samples were again characterized with SEM, the results of which can be found in Figure *5.48* for all 10 and 20 g samples. EDS analysis of coating thickness and presence is summarized in Table 5.9, with the individual measurements available in appendix IX.

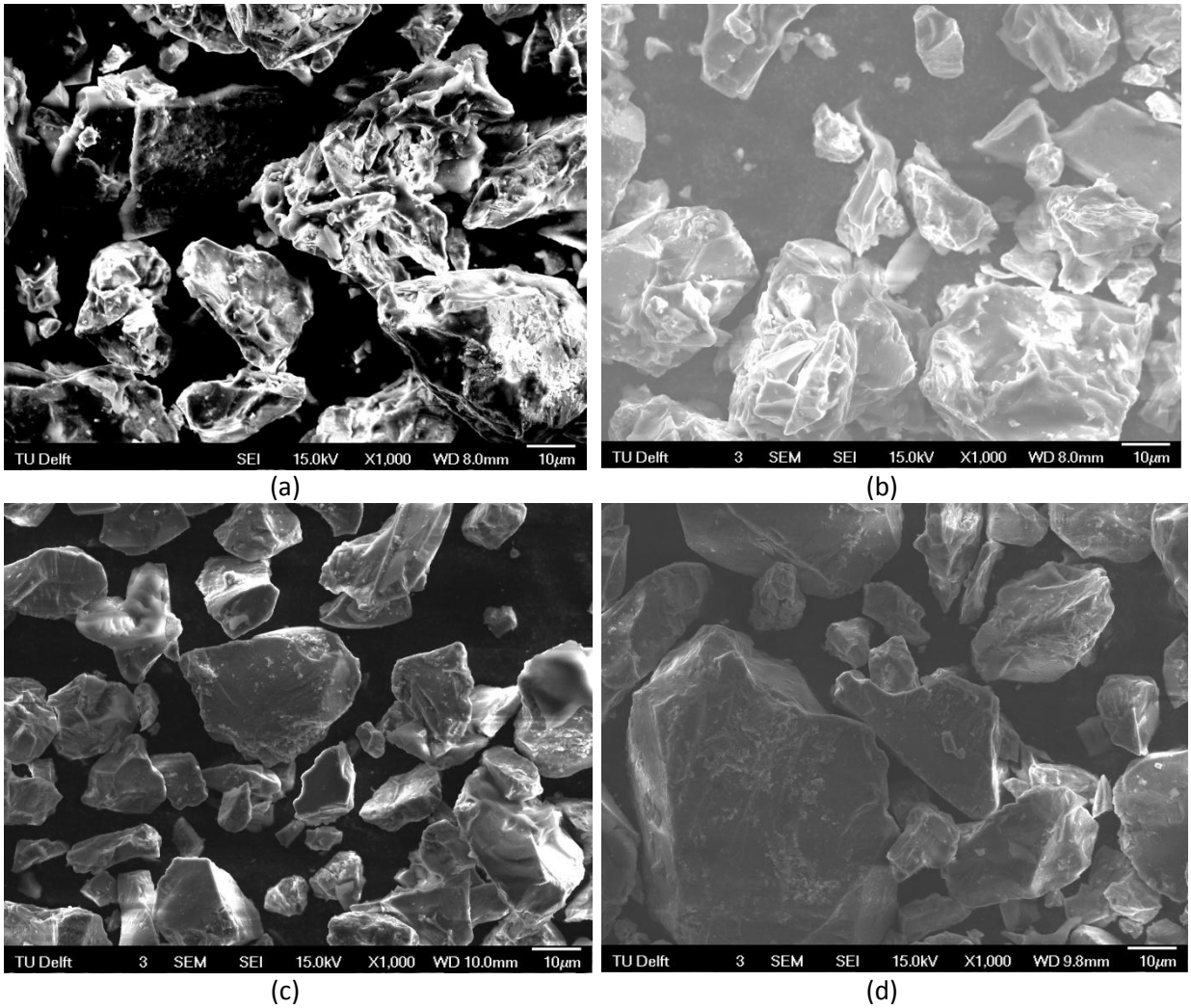

Figure 5.48: ***SEM images of four of the aluminium tri-sec-butoxide experiments, with 10g (a) and 20g (b)*** *$Al(OC_4H_9)_3$ separated by evaporation and 10g (c) and 20g (d) $Al(OC_4H_9)_3$* ***separated by centrifugation.***

These SEM images show that both the evaporated SG-10g and SG-20g have a very similar morphology as the aluminium tri-isopropoxide sample, containing a significant amount of coating material. The 5g sample is not shown here, but did show a very similar morphology. However, for the centrifuged samples it is very different, bearing more similarities with the uncoated material.

EDS investigations in Table 5.9 confirm this, showing a significantly lower average amount of coating material and more points with less than 0.9 atom% Al. None of the evaporation samples showed any points with less than 0.9 atom%, indicating that coverage of these samples was complete. XPS data shown in appendix XI agrees, showing very minor peaks of Si and Mo for the sol-gel samples, while aluminium, oxygen and carbon are the main constituents detected for the samples that have not been heat treated yet. EDS also shows an increased average loading on the particles with increasing ratio of precursor to particle mass, as would be expected. This trend is visible for both evaporated

and centrifuged samples, although the significance of the centrifuged samples is uncertain due to the low number of total measurements.

Table 5.9: ***Combined EDS results for the aluminium tri-sec-butoxide samples with average atom% Al detected and the amount of measurements that found less than 0.9 atom% Al.***

Sample	Total measurements (-)	Measurements with <0.90 atom% Al detected (-)	Average atom% Al detected by EDS with 15kV beam (atom %)
5g evaporation	8	0	8.8
10g evaporation	24	0	14.8
20g evaporation	26	0	23.5
10g centrifugation	2	1	1.0*
20g centrifugation	8	1	4.3

**Average of only two measurement points, one of which did not detect any Al and therefore not significant.*

Based on these results, it can be concluded that the centrifuged samples have a significantly thinner coating than the liquid evaporation samples. A possible explanation for this observation is that bonding of the gel coating is relatively weak and the forces required to separate liquid and solid particles could also be strong enough to remove gel from the particles as well. This agrees well with other authors that found that boehmite gel derived from alkoxides is generally weakly bonded [38, 41].

Furthermore, this could explain the findings of Dey et al. [50] in which a boehmite coating on SiC significantly thinner than expected was found, which was nevertheless strongly bound. As they used centrifugation too, it is very likely that in their case the weakly bonded material was removed by centrifugation as well, leaving only a thin layer of strongly bound material. This strongly bound material is most likely material that is bound to the particle by electrostatic forces between the support and the colloidal boehmite particles. As the only heat treatment performed was drying at 110 °C, the formation of an interfacial phase between the boehmite and the SiO_2 native oxide layer is not likely, because this usually requires significantly higher temperatures.

Therefore it is likely that the coated particles prepared by evaporation of solvent consist of both a thin, strongly adherent layer of boehmite and a boehmite gel on top of those particles that is more weakly bound by Van der Waals forces originating from boehmite condensation reactions as explained in chapter 2.2.1. After centrifugation, the latter layer would be removed, but the former would still be present, which agrees with EDS data still detecting a measurable amount of Al for most measurement points, but detecting significantly less overall Al compared to the evaporated sample that is expected to still contain this layer.

When comparing SG-10g with the N_2 bubbling aluminium oxalate sample and the aluminium isopropoxide sample, which all have an approximately similar amount of aluminium, coverage seems to have increased significantly, especially compared to the oxalate sample. Furthermore, the loading of aluminium on the particles has significantly increased. In the case of aluminium isopropoxide, the lack of nitrogen bubbling could explain a part of this difference, but better dispersion and mixing of the precursor is most likely also a factor.

To evaluate coverage and investigate sample behavior during heat treatment, thermogravimetric analysis (TGA) in synthetic air (80 vol% N_2, 20 vol% O_2) was performed for the 10g aluminium tri-sec-butoxide sample, the aluminium isopropoxide sample, the aluminium oxalate sample with neither pregelation nor nitrogen bubbling and wind sifted $MoSi_2$ as a blank. The results of these TGA measurements are shown in Figure 5.49.

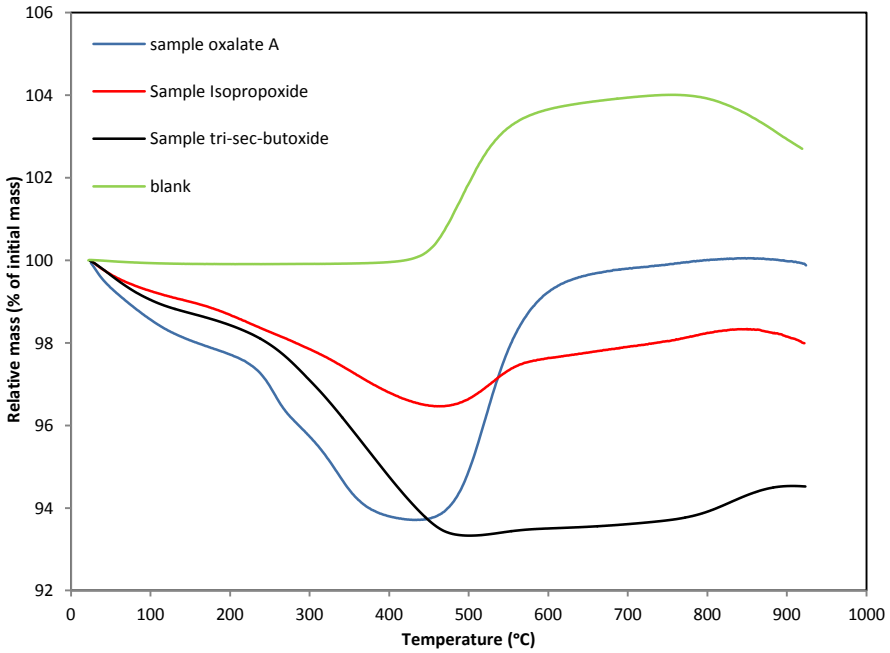

Figure 5.49: *TGA results for an appropriate sample of each type of precursor compared to uncoated $MoSi_2$ as a blank.*

This figure shows that the uncoated and wind sifted $MoSi_2$ mostly follows the expected behavior as described in chapter 3.2. No change in mass is visible before approximately 450 °C and after that temperature, mass starts to increase due to oxidation. Around 550 °C, mass gain slows down though, most likely due to the formation of a protective oxide, as sublimation of MoO_3 usually starts to become noticeable only above 800 °C. This temperature is also the temperature at which a decrease in mass can be observed, indicating that MoO_3 is indeed evaporating at this point.

However, even at the final temperature reached in this TGA, only a small part of the total mass has oxidized. This is because the highest possible relative mass would be 174% of the total initial mass upon complete oxidation without any MoO_3 evaporation. Upon complete evaporation of MoO_3 however, the final mass of the remaining SiO_2 would be 79% of the initial mass. Although some oxidation is observed, the weight of this sample does not rise above 104%, indicating that oxidation in this experiment is not limited by the amount of sample present.

For all sol-gel samples, an initial drop can be observed, which is mainly caused by two different processes: the evaporation of water present on the particles and in the gel and the decomposition of the precursors boehmite and oxalate to aluminium oxide. The former process occurs at lower temperatures, usually below 200 °C and the latter usually at temperatures between 250 and 450 °C [38].

For oxalate, a distinct two-step decomposition can be observed in the mass change graph shown in appendix X, which according to literature corresponds to the loss of crystal water in oxalate and the decomposition of the oxalate itself [104]. Upon oxidation, a large mass gain is observed in the same

temperature range as the bare substrate. What is surprising however, is that this mass gain is actually larger than the blank. An explanation is that this sample was not prepared with wind sifted material, resulting in a larger surface area and associated higher oxidation. The aluminium oxalate did not seem to influence this oxidation in any way significant way though.

Both of the alkoxide precursors have a similar profile, but contrary to the oxalate sample, do have a significant influence on the mass gain around 550 °C. Especially in the case of aluminium tri-sec-butoxide, the mass gain upon oxidation is very small and also seems to be delayed to a higher temperature around 800 °C. For aluminium tri-isopropoxide, the mass gain is still visible around 550 °C, but is significantly smaller than the mass gain of the blank.

These results indicate that the coating is actually present and can already act as a barrier towards oxidation, even before annealing. It also agrees with SEM and EDS observations in which aluminium oxalate does not yield a very good coverage, while aluminium isopropoxide and aluminium tri-sec-butoxide do have better coverage. The latter was also found to have the best coverage and thickest coatings, which would correspond to the best oxidation protection. This can also be observed in the TGA.

Investigating total mass loss in the first part of the TGA also confirms the SEM observations that aluminium tri-sec-butoxide contains more aluminium. As all samples have been dried before TGA, most water that was introduced during the sol-gel procedure should have evaporated and most of the mass loss is due to decomposition of the precursors. The total mass loss of the tri-sec-butoxide is significantly larger than the mass loss of the isopropoxide sample and slightly larger than the oxalate sample. As both alkoxides result in boehmite formation on the particles and aluminium oxalate decomposition results in significantly higher mass loss per mole of alumina, this indicates that significantly more precursor was present in the tri-sec-butoxide sample.

Although this mass loss can be used to estimate coating thickness, accuracy is limited due to evaporation of crystal water that might be present or combustion of residual organic material that is always present. For example estimating the average thickness of SG-10g by this method would yield an approximate average thickness of 0.4 µm, while the highest possible average thickness would be 0.2 µm.

Therefore, Inductively Coupled Plasma Optical Emission Spectroscopy (ICP-OES), the EPMA method mentioned previously in chapter 4.5 and the preparation of cross-sections were utilized as methods to estimate thickness. Due to interference between the elements molybdenum and aluminium, ICP-OES gave inconclusive results for coating thickness. The EPMA thickness estimate method could not converge and yield results for a significant part of the measurement points due to the large variation in thickness and associated difficulty to tune the acceleration voltage.

Therefore thickness of SG-10g and SG-20g was only measured based on cross-sections. One of the SEM backscatter electron image (BSE) images for each sample is shown in Figure 5.50, while the thickness distributions measured for all particles imaged by cross-section combined are shown in Figure 5.51 and Figure 5.52. Thickness was measured in ImageJ with the measurement function. The cross-section images used were backscatter electron images for better contrast. Measurements were performed completely around each particle with a regular distance between each measurement. Images used can be found in appendix XII.

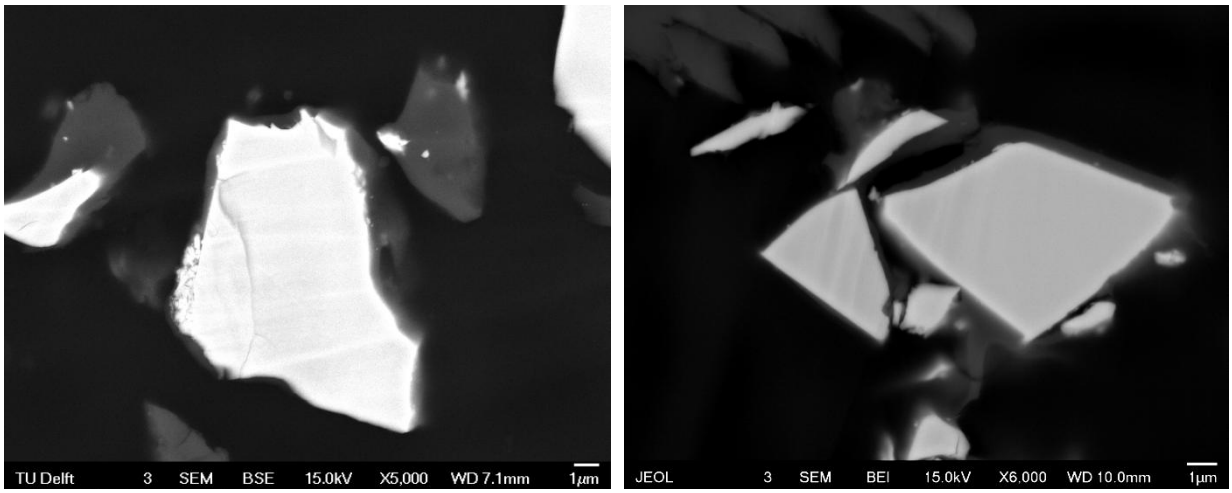

Figure 5.50: *Cross-section SEM-BSE images of coated particles for the SG-10g sample (left) and the SG-20g sample (right).*

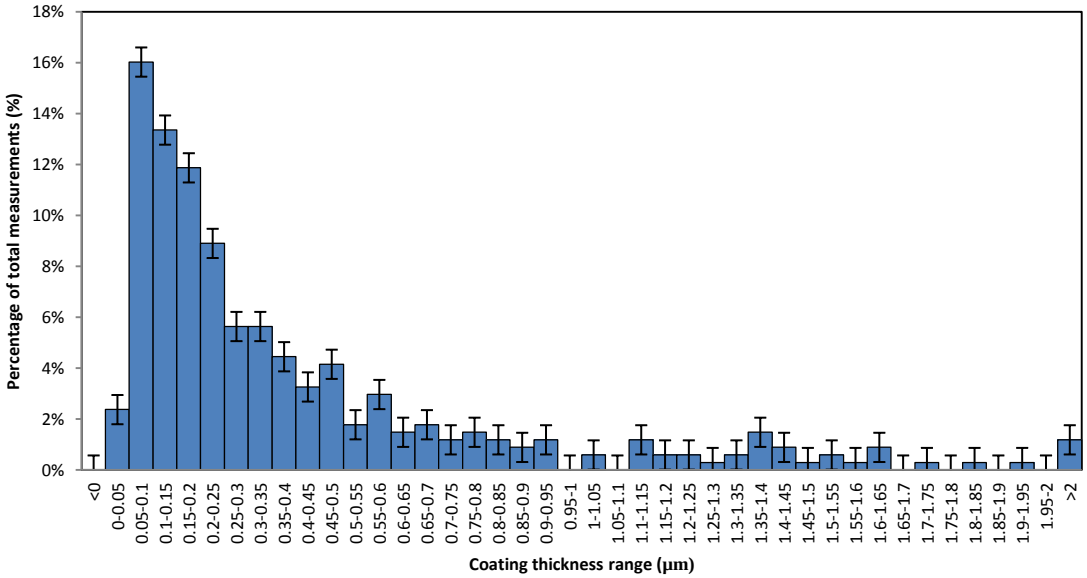

Figure 5.51: *Coating thickness distribution for the SG-10g sample from cross-section analysis.*

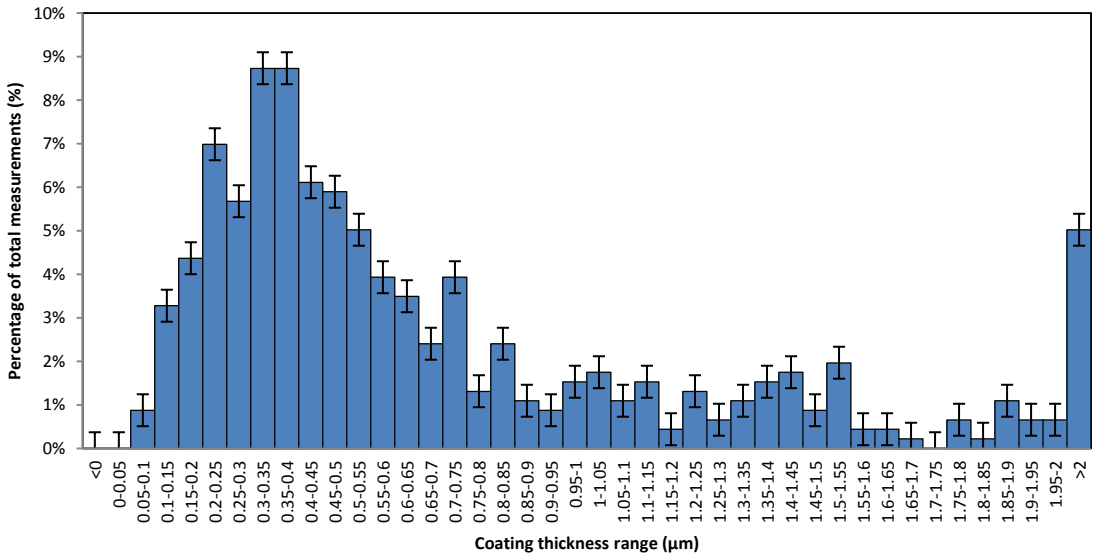

Figure 5.52: *Coating thickness distribution for the SG-20g sample from cross-section analysis.*

In Figure 5.50, the white areas on the BSE images are the $MoSi_2$ particles, while the light gray areas represent aluminium containing coatings. The black area surrounding both is the resin used to embed the particles. This agrees with Mo and to a lesser extend Si being significantly heavier elements than Al or O, which in turn are heavier than C, which makes up most of the resin. Compositions have been confirmed with an EDS line scan shown in chapter 5.3.2.

These cross-sections also clearly show that every particle has indeed been coated for both the SG-10g and SG-20g sample. Another observation is that coating thickness varies significantly within the same sample and even on individual particles. This was already expected, as sol-gel coatings on particles in general are not uniform in thickness and due to the difficulty of thickness measurements by the EPMA method. Although in some places on the particle the presence of coating might be disputed, upon further magnification, a visible thin coating was observed. However, as is clear, this thinner coating is present on part of a significant number of particles, especially for the SG-10g sample, possibly compromising the oxidation resistance of these particles, as the thinnest part is likely to experience rapid local oxidation.

Coating thickness could also be difficult to measure due to the maximum depth from which backscatter electrons originate, if the particle surface below the cutting plane for the cross-section is not perpendicular to this cross-section plane. That would result in small density differences that can be detected by the BSE detector and result in hazy edges on some sides of the particles, even though the whole particle is in focus. This effect introduces an additional error in thickness measurements and could obstruct the observation thin coatings to a certain extend.

When comparing the SG-10g and SG-20g samples however, it is clear that there is a difference in coating thickness, with the SG-20g sample having significantly thicker coatings. This is even more evident in the distributions shown in Figure 5.51 and Figure 5.52, in which the SG-20g sample shows a significantly higher average thickness, with a maximum around 0.4 μm, while for the SG-10g sample this maximum is closer to 0.1 μm.

It is also interesting to note that the thickness of the dried boehmite gel for the SG-20g sample is actually close to, but somewhat higher than the calculated average of 0.4 μm for the fully densified Al_2O_3, indicating that most of the precursor did indeed deposit on the particles instead of segregating. This is of course assuming that the density of the gel is close to its expected maximum density of 3.0# g/cm^3, which is not always the case [50]. For the SG-10g sample, the coating thickness is surprisingly lower than expected though.

Nevertheless these results show that $MoSi_2$ particles can indeed be coated successfully with boehmite, using aluminium tri-sec-butoxide as a precursor. The amount of precursor is also directly related to the thickness of the coating, as would be expected. These sol-gel coatings were also found to have significant variations in thickness and most likely consist of two layers, one of which is thin, strongly bound and close to the particle, while the outer layer is thicker, but relatively easily removed. Furthermore, both proper dispersion of particles and gel and electrostatic interactions originating from pH were found to be important parameters in successful coating. TGA heating tests show that the coatings from aluminium alkoxides already have a protective effect compared to the bare particles.

5.3 Atomic Layer Deposition/Residual Chemical Vapor Deposition

5.3.1 Mechanism

To elucidate the mechanism of Atomic Layer Deposition with Residual Chemical vapor deposition (ALD/rCVD), several ALD experiments have been performed in which precursor dosage time and purge time between precursor dosage were varied independently. Calculations of precursor addition based on precursor vapor pressure under atmospheric conditions (25 °C, 1 bar pressure) were performed to ensure reactant addition was not limiting to coating thickness.

To investigate the resulting microstructure after coating, SEM and EDS was performed, the results of which are shown in Figure 5.53 and Table 5.10. The resulting morphology for all thin ALD coatings (<100 nm) was very similar for different samples and was not significantly different from the morphology of the raw material. EDS results did show however that all particles were coated with a thin layer of alumina. XPS analysis of the thicker samples shown in appendix XI confirms the coating of the entire particle, with no Mo being detected and very little Si on the coated particles, which means coating has been successful and coating might even be more complete than in the case of sol-gel. This indicates that a very conformal coating was deposited on all particles. It is also an indication for the thickness being substantially higher than pure ALD samples, as the latter would result in coatings of approximately 1 nm thick, which would be very difficult to detect with an acceleration voltage of 15 kV and the EDS detector utilized in this research.

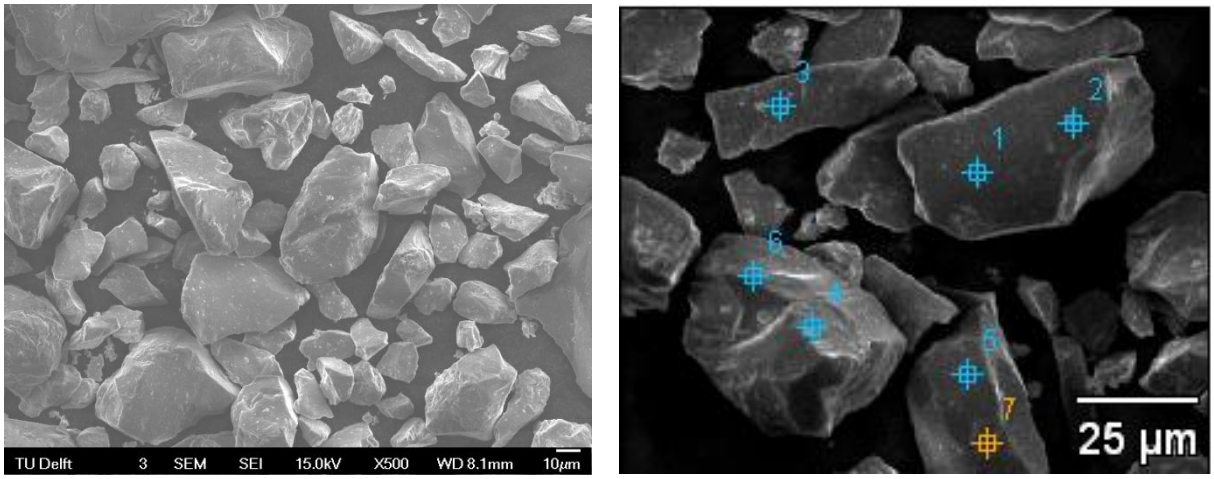

Figure 5.53: ***SEM image of particles coated by ALD with morphology characteristic for all ALD experiments with a resulting thin (<100 nm) coating (left) and an image with EDS measurement points indicated (right).***

Another observation visible in Figure 5.53 is that compared to the wind sifted material, the amount of small particles present is significantly lower. Although laser diffraction after ALD/rCVD was not possible due to the lack of sufficient material, SEM images for all ALD/rCVD samples show this decrease in small particles. A possible explanation is that during fluidization these particles do not remain in the fluidized bed and instead remain suspended in the gas flow and end up in the cyclone. This often happens in fluidized beds, as a gas flow sufficient to fluidize larger particles is often able to retain smaller particles in polydisperse powders [105]. It also agrees with the observation during the experiment that a small fraction of the powder sticks to the distributor plate on top of the glass reactor, approximately 0.5 m above the top of the bed. However, most of the material fluidized properly.

Table 5.10: *EDS elemental concentration measurements in atom% of the points shown in Figure 5.53 b.*

	O content (atom %)	*Al content (atom %)*	*Si content (atom %)*	*Mo content (atom %)*
Point 1	65	5.8	20	10
Point 2	43	4.8	35	17
Point 3	41	1.9	38	19
Point 4	62	3.4	24	11
Point 5	42	1.7	38	18
Point 6	58	2.7	27	13
Point 7	43	1.8	37	18

Although the EDS results in Table 5.10 show that Al is indeed present on all particles measured, which was also observed for other samples, there is some variation in Al content. Most of this variation could be explained by the fact that EDS actually measures X-rays originating from a region at and below the surface, as explained in appendix V combined with the observation that the particles are not flat, but irregularly shaped. Nevertheless, the amount of Al present has significantly less variation than the sol-gel samples, indicating that coating thickness might be more homogeneous. The EDS results also show a surprisingly high concentration of oxygen, the origins of which are not clear. A possible explanation might be the presence of water, as these particles have not been dried after the ALD/rCVD process, which always ends with the addition of H_2O precursor and subsequent purging for safety reasons. Furthermore, the plasma activation process might have induced some additional oxidation of $MoSi_2$.

Coverage and behavior of an ALD/rCVD sample, namely the sample with 4 minutes TMA and 5 minutes purge, was also investigated by TGA, the results of which are shown in Figure 5.54. This figure clearly shows the protective function of particles coated by this method. Weight gain at higher temperatures is significantly lower than the uncoated material and significantly delayed as well. When comparing this sample to the sol-gel samples, the weight changes at high temperature are slightly lower than those of the SG-10g sample, even though this coating is thinner, as is shown in the next section. Furthermore, there is almost no weight loss at lower temperatures, indicating that no or very limited decomposition is necessary and that the coating does not contain a very significant amount of water.

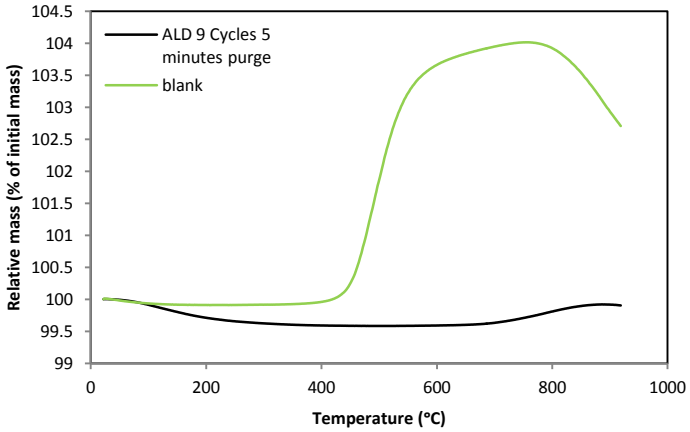

Figure 5.54: *TGA results for the 4 minute TMA, 5 minute purge ALD/rCVD sample compared to uncoated material.*

To obtain more information regarding the mechanism, thickness was measured using multiple different methods. These methods were ICP-OES and XRF, both combined with surface area measurements by N_2 physisorption to calculate coating thickness with equation 5.1 and as a third method the EPMA method. All of these methods use the density found by [66] for ALD at 25 °C to calculate coating thickness, which was 2500 kg/m^3. In this equation, a homogeneous coating thickness is assumed. The parameters are as follows: x is the weight fraction Al measured by ICP, M is the molar weight of the corresponding compound in g/mol, ρ the density in g/m^3, S the specific surface area of the compound as measured by N_2 physisorption in m^2/g and δ the thickness in m.

$$\delta = \frac{(x_{Al,meas} - x_{Al,blank}) * M_{Al2O3}}{2 * M_{Al} * \rho_{Al2O3}} * \frac{1}{\left(1 - \frac{(x_{Al,meas} - x_{Al,blank}) * M_{Al2O3}}{2 * M_{Al}}\right) * S_{MoSi2}} \quad \textbf{(5.1)}$$

When analyzing the results of these methods, XRF was found to give an overestimation of the Al content due to an inhomogeneous distribution of elements in the sample. ICP-OES results, shown in appendix XIII on the other hand yield a significant underestimation, most likely due to difficulties with dissolving the most likely formed aluminosilicates. The EPMA surface layer measurement method was able to measure thickness, the results of which are shown in Figure 5.55 and Figure 5.56. Its accuracy was verified by cross-section analysis of a thicker coating, as shown in chapter 5.3.2. The cross-section and EPMA method agreed well in thickness estimate, indicating that this might be the most accurate method.

For the EPMA method, measurements shown in the figures below show some interesting details regarding the mechanism. As can be observed in the graphs, the error based on the discrepancy in resulting thickness for the various points is large. However, the origin of these errors is not only in the measurement error, but also in the small variation in coating thickness that is often observed in ALD with rCVD and sometimes in pure ALD as well. This variation was also observed in the cross-section. As only 20 points were measured, a distribution could not be made. Due to this, the actual measurement error is most likely smaller than presented here and these points can be seen as an average coating thicknesses for each sample.

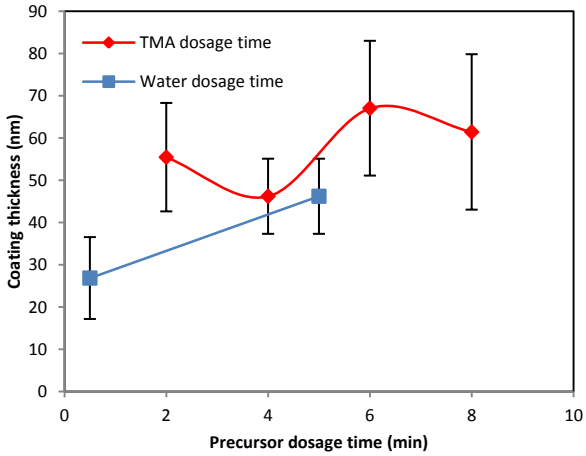

Figure 5.55: *The effect of TMA and water dosage time on resulting average coating thickness as obtained by the EPMA method.*

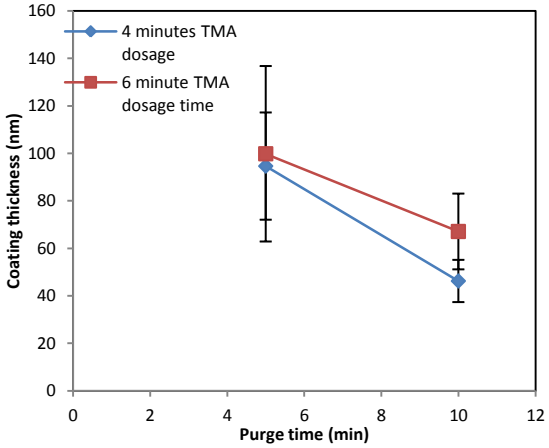

Figure 5.56: *The effect of purge time on resulting average coating thickness for two different TMA dosage times as obtained by the EPMA method.*

Figure 5.55 shows the effect of precursors and as is clear, a large variation in thickness for the different experiments is observed. For variation of TMA precursor, no clear trend can be observed. The experiment with 9 cycles of 4 minutes TMA dose was the first experiment performed, which could explain the relatively low coating thickness found in this experiment compared to the other experiments. As ALD experiments are relatively complex, some problems might have occurred during this first experiment that resulted in a lower coating thickness.

If this would indeed be the case, the other samples indicate that the effect of a higher TMA loading does not increase coating thickness significantly. This is reinforced by the two separate samples at lower purge times in Figure 5.56, in which hardly any difference in coating thickness could be detected. Therefore TMA condensation is not likely to be an important factor in residual CVD, which agrees with findings of other authors [66].

The increase of water dosage on the other hand seems to have a more significant effect, especially if the coating thickness of sample with five minutes H_2O and four minutes TMA dosage time would be lower than expected due to the aforementioned challenges with the first ALD experiment. However, due to this observation being based on only two samples, the preparation of more samples is necessary to ensure that water condensation is indeed an important factor. Based on previous research discussed in the literature section, this is likely though.

The most significant effect in increasing coating thickness is however in purge time reduction, as shown in Figure 5.56. For two different TMA dosage times, a decrease of purge time from ten to five minutes resulted in a significant increase in coating thickness. Based on these experiments combined with previous work that found that higher temperatures could eliminate rCVD [63], condensation of reactants, in particular H_2O, is indeed the most likely mechanism for the rCVD part of ALD/rCVD. Therefore, if high coating thickness is desired, the rCVD component should be maximized by short purges and low temperatures to limit re-evaporation of precursor and precursor amounts sufficient to allow for maximum condensation and reaction on particle surfaces. The amount of precursor added should also be significantly more than necessary for complete surface coverage with a single monolayer, which would correspond to pure ALD.

5.3.2 Increased number of cycles

These recommendations of short purge times, low temperatures and sufficient addition of water and TMA were therefore followed along with an increased number of cycles to obtain coatings of sufficient thickness for high temperature protection. The microstructure and morphology of these particles was again investigated with SEM and EDS, the results of which are shown in Figure 5.57. Whether an increase in coating thickness was indeed achieved was investigated with the EPMA method, the results of which are shown in Figure 5.58. To investigate the accuracy of this method, cross-sections were made for the ALD-25C and ALD-40C samples, an example SEM-BSE image of which is shown in Figure 5.59 and the coating thickness distributions, shown in Figure 5.60 and Figure 5.61 were compared to the results of the EPMA method.

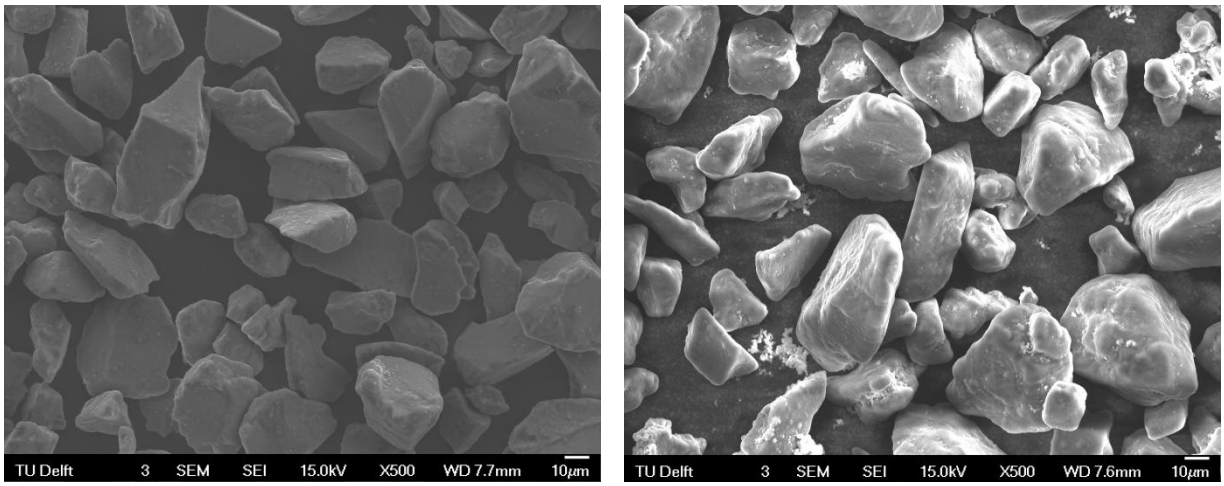

Figure 5.57: ***SEM images of the two samples with thicker coatings, namely ALD-25C (left) and ALD-40C (right).***

The SEM images show that the final result of the ALD/rCVD samples with an increased number of cycles is similar to the other ALD/rCVD samples. Again, most smaller particles have been removed from the powder. However, the morphology is slightly different, having a distinctly smoother surface with edges that are less sharp, indicating that a coating is present. This is confirmed by EDS, which detects significant quantities of Al on each particle.

The ALD-40C image also shows some small brighter particles that have a different, more flaky morphology. Images with a higher magnification and EDS measurements show that these particles are pure alumina particles. These particles most likely formed on the distributor plate and contaminated the sample during unloading of the powder. However, they are inert and can be distinguished easily during analysis and do therefore not interfere significantly with other measurements.

Analysis of the thickness measurements by both the EPMA method and the average of all cross-section measurements in Figure 5.58 confirms that there is indeed a significant amount of alumina present in these samples. Coatings were found to be significantly thicker than expected based on extrapolation of the growth per cycle for the samples with lower cycles, with the 25 cycle sample having an average thickness of approximately 0.65 µm and the 40 cycle sample having a thickness of 1.9 µm, according to the cross-section data. This does mean that growth in this experiment is distinctly nonlinear though. The most likely explanation is the continuous removal of smaller particles during the experiment, especially at the moments the distributor plates have to be changed due to clogging, significantly lowering the total surface area to be coated.

Unfortunately, calculation of the ALD-40C sample coating thickness was not possible due to numerical instability of the code at these conditions. Therefore, only the cross-section analysis is available for that sample and no comparison between the EPMA method and the cross-section can be made for this sample. However, for the ALD-25C sample, both the cross-section and the EPMA analysis was successful. As is clear from Figure 5.58, these average measurements correspond very well with each other, the average result of the EPMA method being 665 nm coating thickness and the average of the cross-section measurements being 650 nm. This difference is well within the margin of error and therefore it can be concluded that the EPMA based method is a suitable and accurate method to estimate coating thickness in these samples.

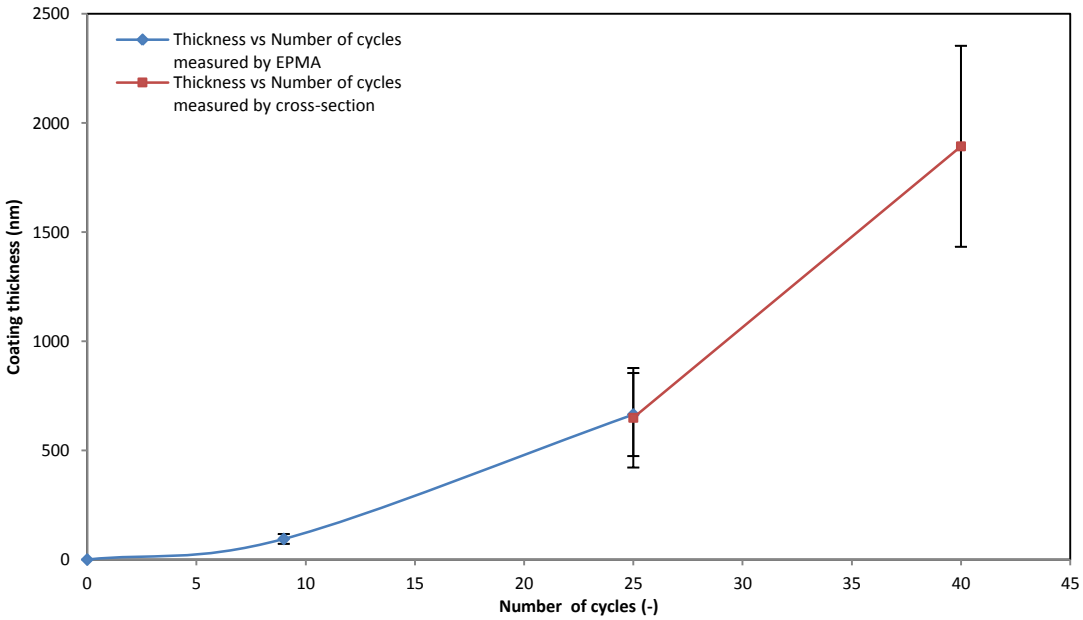

Figure 5.58: ***Measured thickness for ALD/rCVD samples with different number of cycles, all with 4 minutes of TMA dosage, 5 minutes water dosage and 5 minutes purge per cycle.***

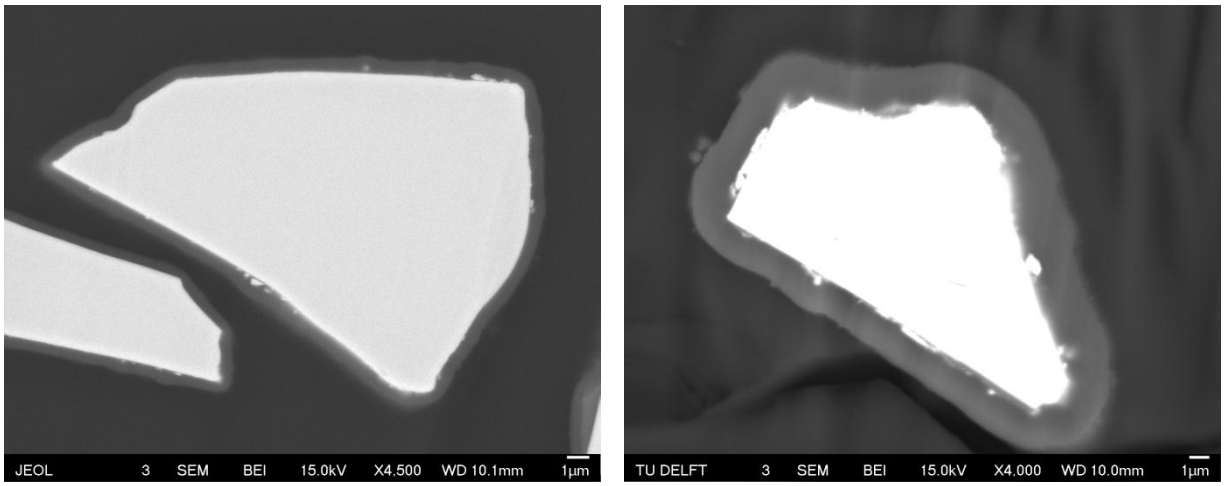

Figure 5.59: ***Cross-section SEM-BSE images of coated particles for the ALD-25C sample (left) and the ALD-40C sample (right).***

As is clear from Figure 5.59, Figure 5.60 and Figure 5.61, there is indeed clearly a coating present, which is quite homogeneous in thickness, especially when compared to the sol-gel coatings. Especially noteworthy is the complete absence of very thin coating layers, smaller than 0.35 µm for the ALD-25C sample and smaller than 1.2 µm for the ALD-40C sample. This would limit local oxidation at high temperature significantly. The distribution also shows that coating thickness is significantly more homogeneous than the sol-gel coatings. There is still a distribution, as the deposition from the rCVD component can vary like regular CVD. Furthermore, there is a human measurement error associated with measurements from images and another error from the SEM-BSE images, as described in the sol-gel chapter, which could introduce some additional distribution.

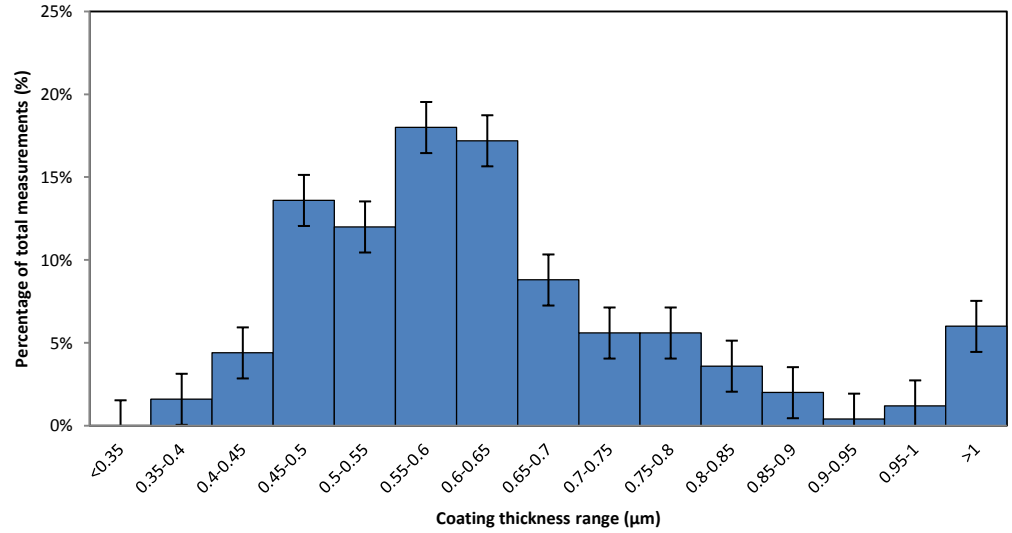

Figure 5.60: *Coating thickness distribution for the ALD-25C sample from cross-section analysis.*

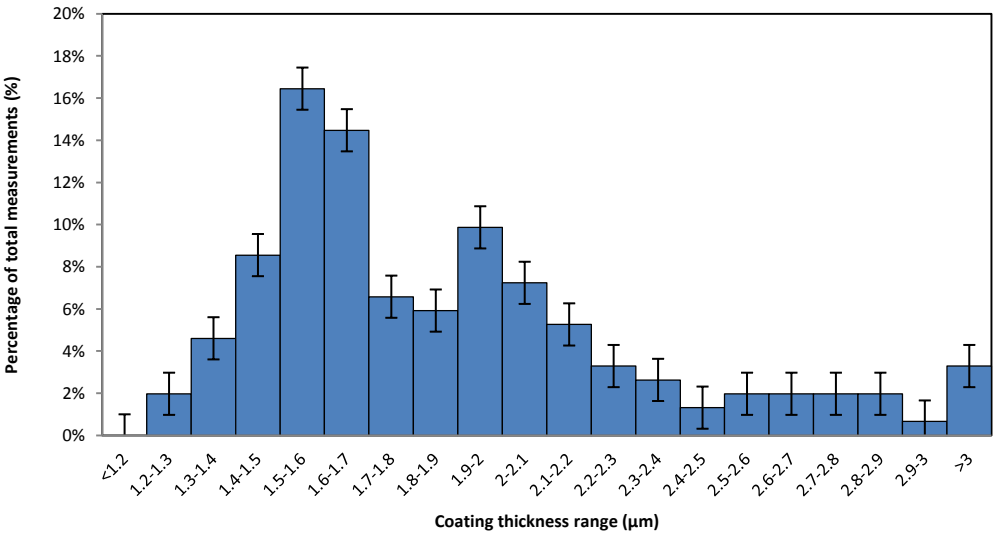

Figure 5.61: *Coating thickness distribution for the ALD-40C sample from cross-section analysis.*

Finally, to ensure that the light gray coatings were indeed Al containing coatings, an EDS linescan was performed. This linescan is shown in Figure 5.62 and shows clearly that alumina is only present close to the middle of the scan, which is also the location of the light gray coating surrounding all particles. Oxygen is also at a maximum in this region, as the expected compound would be Al_2O_3. The ratios are not perfect though, as the polymer also contains significant amounts of oxygen and as explained in appendix V, the EDS detection is actually in a relatively wide area below the surface. This also explains the presence of Mo and Si in the part of the coating close to the particle.

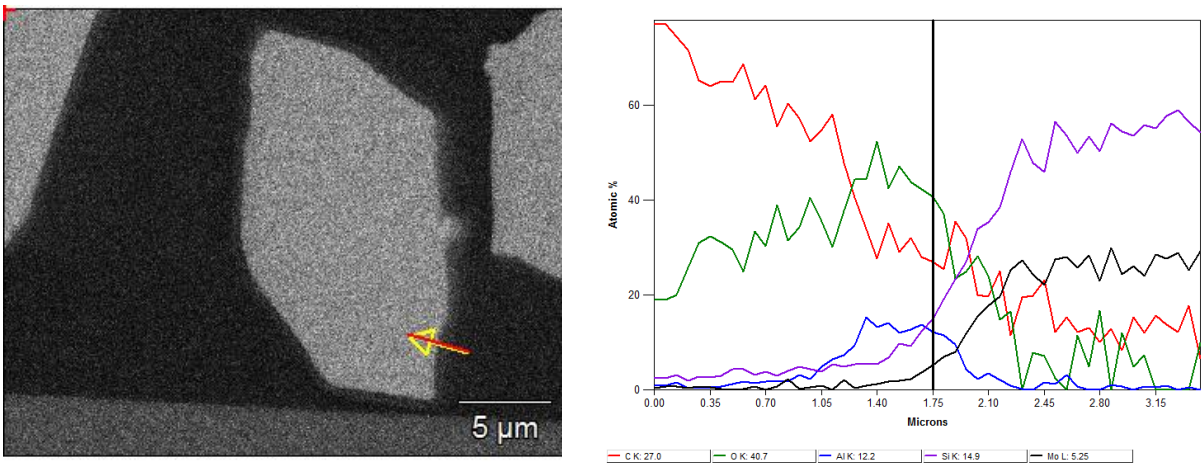

Figure 5.62: *A linescan of the coating of the ALD-25C sample with the scanned region (left) and the atomic percentages detected for each element as a function of distance (right).*

5.4 Heat treatment

The main goal of heat treatment of particles is to obtain a completely densified coating of α-Al_2O_3 without damaging the particles or the coating. This chapter will however show that this is not very straightforward and will show the required precautions necessary to prevent damage. First, the coatings resulting from selecting an oxygen containing annealing atmosphere will be shown, followed by heat treatment of sol-gel coatings under an atmosphere of pure argon. Afterwards, the heat treatment of ALD/rCVD coated particles will be discussed.

5.4.1 Effect of atmosphere

The main effect of atmosphere is related to the presence of oxygen or oxygen providing molecules such as H_2O and CO_2. Before annealing, coatings are not yet fully densified and might be sensitive to any oxygen providing molecules. To test this, a small part of the SG-10g sample has been subjected to heat treatment in air instead of argon. Both precalcination at 450 °C only and high temperature annealing at 900 °C were tested, the results of which are shown in Figure 5.63.

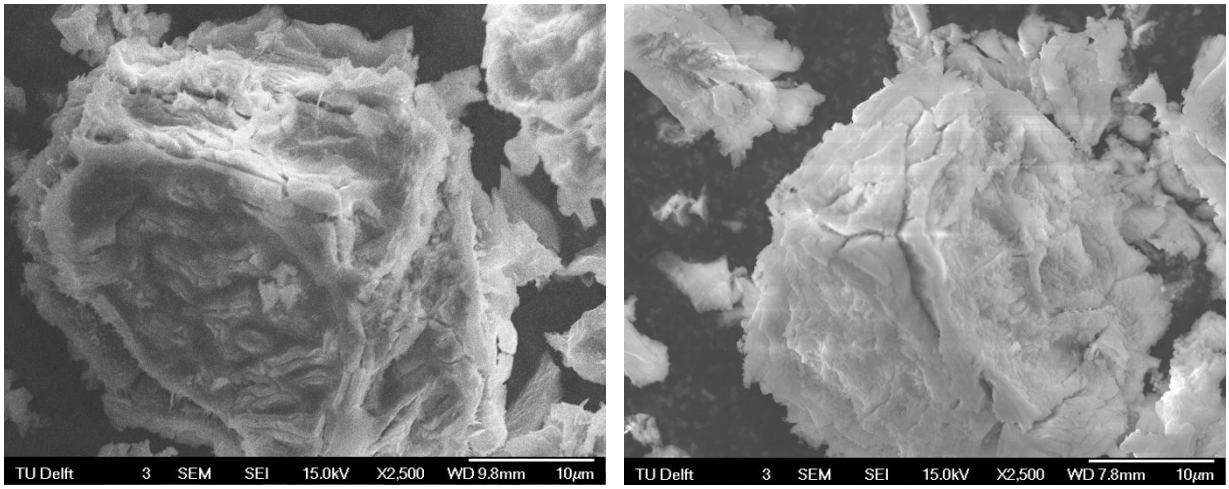

Figure 5.63: *SEM images of precalcined SG-10g sample (left) and high temperature annealed sample (right).*

These two images clearly show the problem of annealing in air, which leads to significant cracking, most likely due to oxidation of the $MoSi_2$ and resulting stress buildup beneath the coating. This effect is already observed during the precalcination that is only performed at 450 °C, which is apparently still too high to prevent significant oxidation of the substrate. This agrees with the known oxidation

behavior of $MoSi_2$, which usually becomes significant around 400 °C [17] and with the observations during TGA in which the blank started to oxidize around 450 °C. Based on these observations, it was decided to perform the entire procedure in argon, except for the first 30 minutes of precalcination to allow oxygen to burn away residual carbon.

5.4.2 Heat treatment of sol-gel coatings

As the main goal of heat treatment was to obtain an intact and completely densified α-Al_2O_3 coating, both morphology and crystal structure were investigated by SEM and XRD respectively. Interestingly, morphology was found to be very similar for all heat treated sol-gel coatings. An example of these morphologies is shown in Figure 5.64. Furthermore, XRD diffractograms for the SG-10g and SG-20g samples annealed at different temperatures are shown in Figure 5.65 and Figure 5.66 respectively.

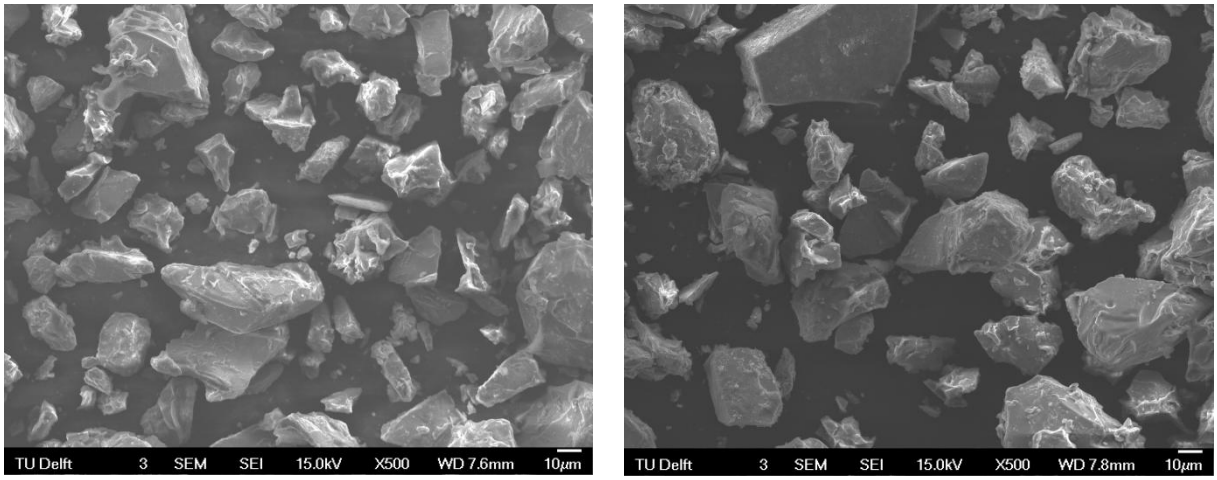

Figure 5.64: ***Morphology of sol-gel samples after heat treatment with the precalcined (450 °C, 14h) only SG-20g sample (left) and the SG-20g sample subsequently annealed at 1200 °C (right).***

These images show that the sol-gel coatings are still intact after heat treatment, which according to literature is quite surprising. Sol-gel coatings often have a tendency to crack on many substrates, due to tensile stresses resulting from densification to the equilibrium density as described in chapter 2.4.1. Although some very small cracks were observed in some of the samples, most of the particles did not show any cracks large enough to be visible on the SEM.

The most likely explanation for this is the precalcination in combination with annealing in pure argon. Previous investigations found that cracking was more likely when the precalcination step was not performed, due to the significantly faster densification. The stresses caused by this densification result in fracture of the coating, as there is no time for any stress relaxation with temperatures of 900 °C. However, chapter 5.4.1 clearly shows the necessity of pure argon or another inert gas that does not contain any oxygen. Therefore it is concluded that both precalcination and argon are necessary for prevention of crack formation.

The x-ray diffractograms in Figure 5.65 and Figure 5.66 show some interesting results. First of all, $MoSi_2$ is still the main phase, as would be expected. Furthermore, all diffractograms except for the sol-gel samples that were annealed at 1200 °C show the presence of a small amount of Si, which indicates that oxidation was mostly prevented during annealing. The most striking observation however is the almost complete absence of the α phase for all samples except for the 1200 °C samples and the SG-20g 1100 °C sample. This is however in agreement with most literature, as the $\theta \rightarrow \alpha$ transition often occurs at temperatures above 1100 °C [23].

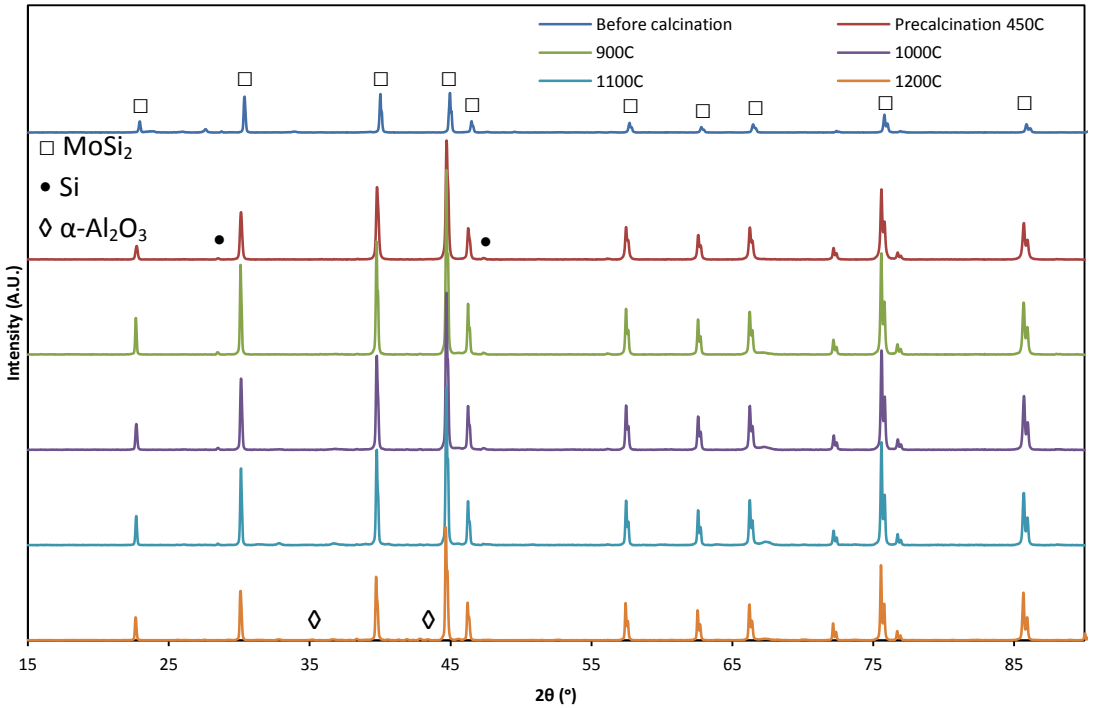

Figure 5.65: *XRD diffractograms of the SG-10g sample annealed at different final temperatures and including the sample before any heat treatment and after precalcination.*

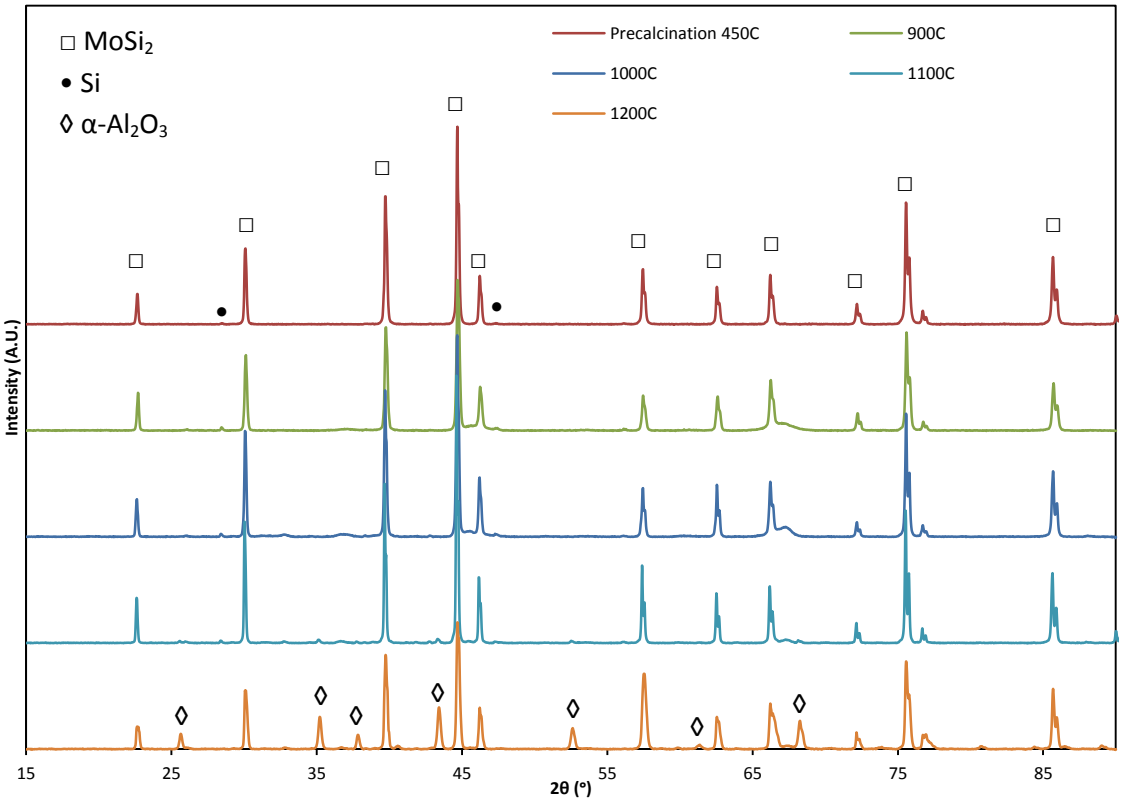

Figure 5.66: *XRD diffractograms of the SG-20g sample annealed at different final temperatures and including the sample after precalcination.*

Furthermore, the diffractograms show that transformation kinetics are very dependent on coating thickness, as the SG-20g sample shows the presence of significantly more α-alumina than the SG-10g

sample. Furthermore, even though transition alumina's are likely to form, the peaks associated with them are relatively small. They are present however, although the lattice constants of the various transition phases are very similar, making it difficult to distinguish these phases. A good example for this behavior would be the small peak next to the $MoSi_2$ peak at a 2θ of 66°, where most of the transition aluminas give a signal. This peak increases in intensity with increasing temperature, but intensity decreases again at 1100 °C and 1200 °C, which is a good indication that the transition alumina sequence is indeed a likely transformation path for these coatings. Based on these XRD diffractograms, it is however not possible to determine the precise transition aluminas formed during heat treatment.

A possible explanation for the relative lack of transition phase peaks could be the small grain size, which would cause significant peak broadening in XRD analysis. As these aluminas form from an amorphous gel, grains are often small and do not grow significantly until the sample reaches higher temperatures. At these temperatures however, the transformation to other aluminas and the final α phase is also more likely, reducing the amount of transition alumina phase that could be detected. This would also explain why the α-Al_2O_3 peaks are relatively broad as well.

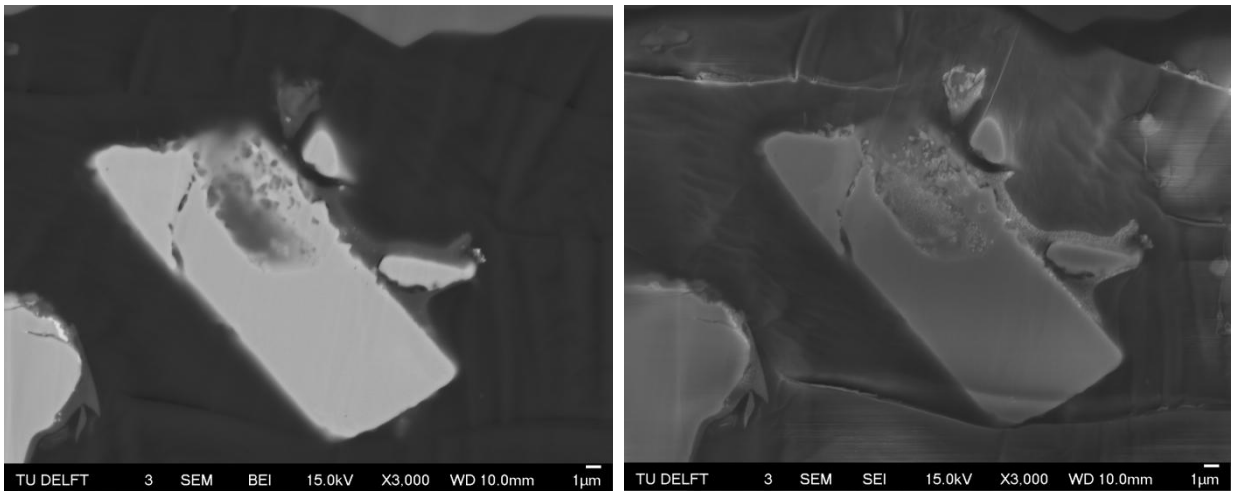

Figure 5.67: ***Cross-section SEM images of a heat treated particle, namely SG-20g at 1200 °C (with precalcination), showing a BSE image (left) and a SEM image (right).***

To investigate other changes in morphology and changes in thickness during calcination, a cross-section of the SG-20g sample calcined at 1200 °C was also prepared. SEM images of this cross-section are shown in Figure 5.67 and the coating thickness distribution is shown in Figure 5.68. Comparing the SEM-BSE images, no significant differences can be observed. When comparing the SEM-SEI images however, the coating seems to contain significant amounts of white spots that were not present in the coatings that were not heat treated. These small white spots are most likely α-alumina grains and their size corresponds surprisingly well with the calculations from the XRD analysis, measuring approximately 50 nm on the SEM-SEI images.

Analysis of the coating thickness distribution reveals that there is surprisingly little difference between annealed and fresh coating thickness. Some difference is visible in the range of coating thickness of more than 1 µm, but for coatings with a thickness lower than 1 µm, there is no statistically significant difference. This might indicate that the coating has not completely densified and transformed during heat treatment, especially in the regions of thinner coatings. This is in agreement with the SEM-SEI observations in which the white spots were mainly found in the thicker

parts of the coating. If this is indeed the case, heat treatment at higher temperatures and for longer periods of time might be necessary to transform the coating completely to α-alumina.

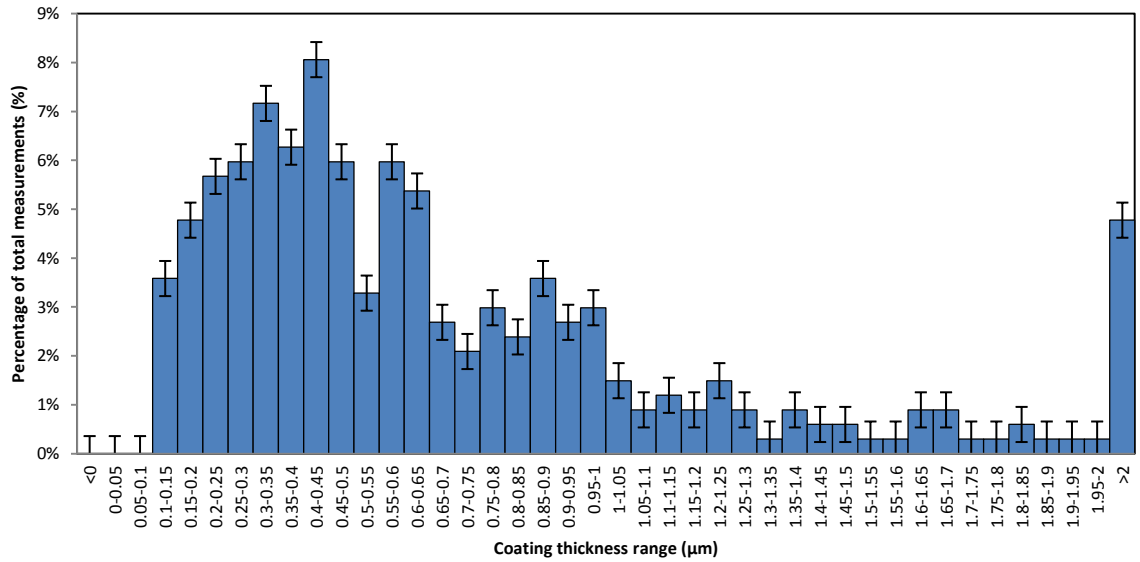

Figure 5.68: *Coating thickness distribution for the SG-20g sample heat treated at 1200 °C.*

5.4.3 Heat treatment of ALD/rCVD coatings

The goal for heat treatment of ALD/rCVD coatings was the densification of the coating combined with the transformation from an amorphous layer to α-alumina, while retaining shell integrity. SEM image of ALD-25C and ALD-40C are shown in Figure 5.69 and were used to investigate integrity, while XRD spectra of the samples annealed at different temperatures are shown in Figure 5.70 and Figure 5.71 to observe transformations.

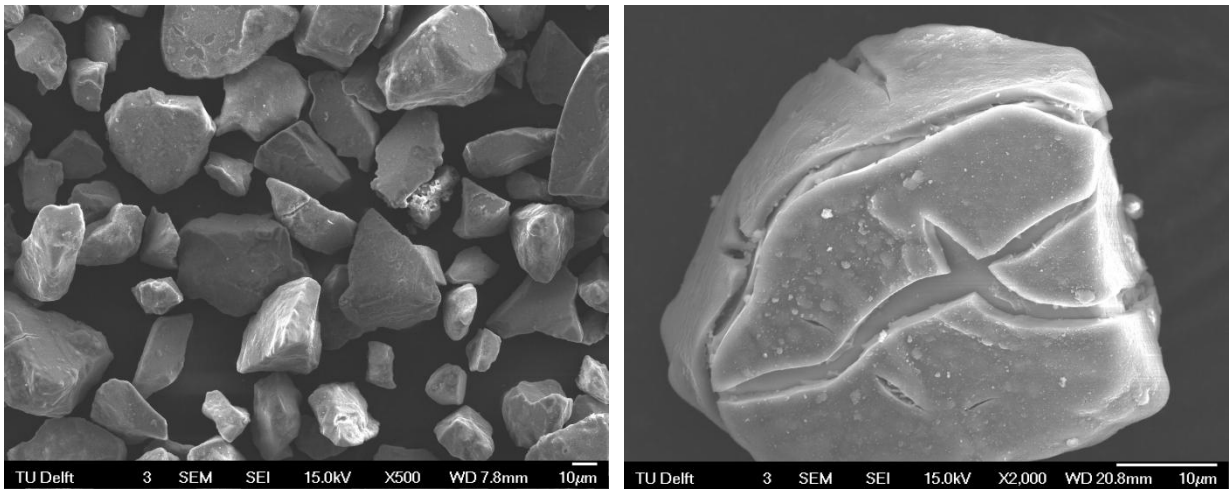

Figure 5.69: *Morphology of ALD samples after heat treatment with the 25 cycle sample (left) and the 40 cycle sample (right), both annealed at 1200 °C.*

The most striking observation is the appearance of significant cracks in the coating, especially in the ALD-40C sample. For the ALD-40C sample, most particles had a very similar morphology to the particle shown in Figure 5.69. An EDS map of the particle shown in this figure was also prepared to ensure these were indeed cracks and that they reached through the entire coating. These elemental maps are available in appendix XIV and do indeed show the presence of only Al and O outside the cracks, but significant amounts of Mo and Si and hardly any Al inside the cracks.

The ALD-25C sample on the other hand did show a few particles with cracks, but most particles did not contain any. This indicates that thickness is indeed a significant factor, as described in chapter 2.5. Opposed to sol-gel coatings, ALD/rCVD particles do not have any mechanisms to relieve stress from densification and transformation, such as pore formation or evaporation of water, resulting in more fracture. However, as is clearly shown by the ALD-25C sample, manufacturing coatings with appropriate thickness can circumvent this problem almost entirely, as would also be expected.

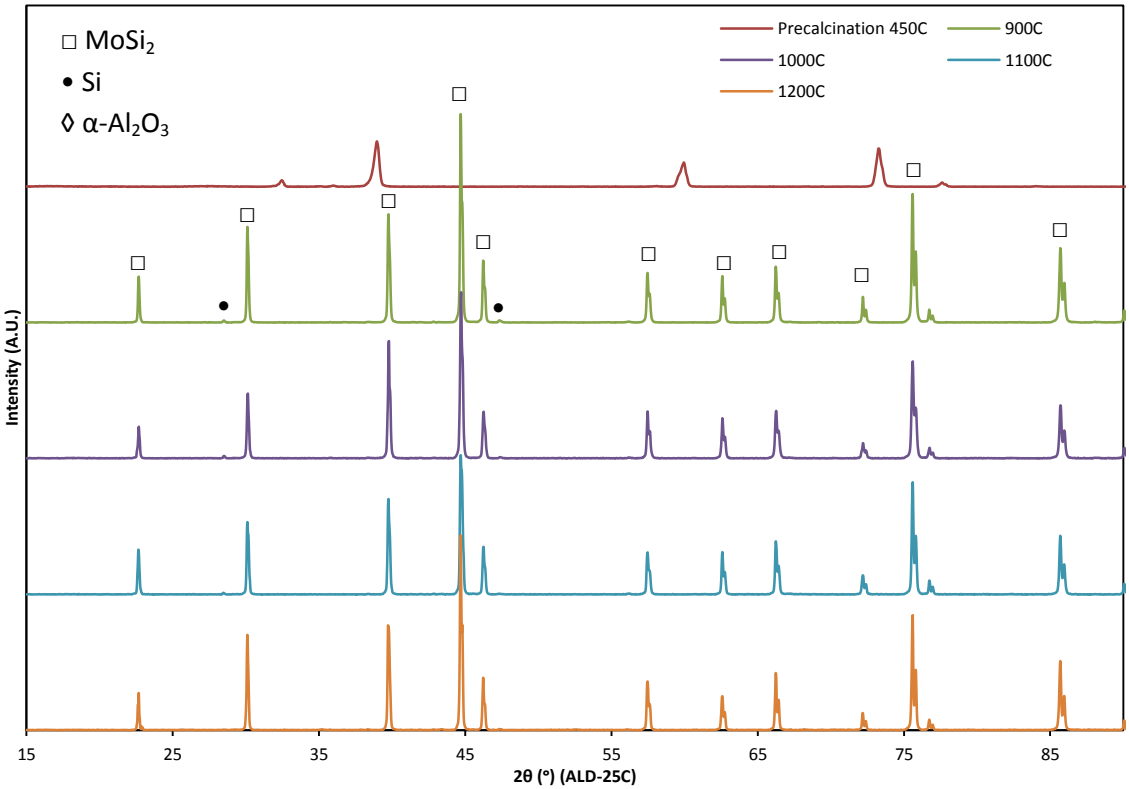

Figure 5.70: ***XRD diffractograms of the ALD-25C sample annealed at different final temperatures and including the sample after precalcination.***

Analysis of the XRD results reveals some additional interesting observations. Similar to the sol-gel coatings, $MoSi_2$ is the main component and some small Si peaks are present. Again, annealing at 1200 °C results in the disappearance of the Si peak, most likely due to some minor oxidation. However, no alumina can be detected in any sample other than the ALD-25C sample that was annealed at 1200 °C and the ALD-40C samples that were annealed at 1100 and 1200 °C. And even in those cases, the α-Al_2O_3 peaks that are detected, are very small, especially compared to the sol-gel derived coatings.

Based on this, it can be concluded that the transformation of ALD/rCVD based coatings to the stable α-alumina coatings is significantly more difficult than the transformation of the sol-gel based coatings and most likely means that this transformation has a significantly higher activation energy. This agrees with observations in literature, in which this transformation was indeed found to be difficult, as described in the theory section regarding heat treatment.

Another observation is the complete absence in any sample of peaks of any of the sol-gel transition aluminas. This might be caused by the transition sequence following the amorphous → κ → α transition, as some hints of κ-alumina were detected. Furthermore, both κ and α alumina have an

HCP anion packing, making differentiation between these phases on XRD more difficult. However, this might also be caused by the relatively small amount of crystallized alumina detected in general, combined with the small grain size of the α-alumina. More experiments with higher amounts of crystallized Al_2O_3 would be necessary to draw definite conclusions, but the κ → α transformation seems the most likely explanation based on these XRD analyses.

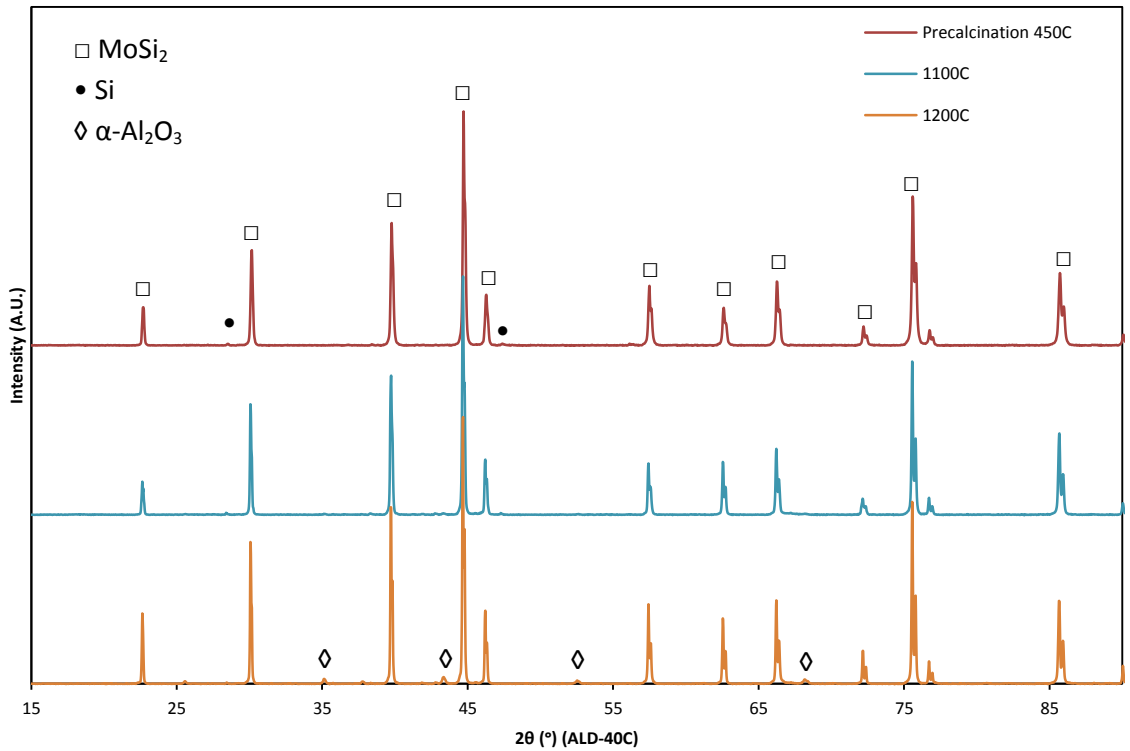

Figure 5.71: ***XRD diffractograms of the ALD-40C sample annealed at different final temperatures and including the sample after precalcination.***

It can definitely be concluded however that not all alumina has transformed to the stable α-Al_2O_3 phase. The cracks present in the ALD-40C sample do however show that the alumina has densified significantly, although not completely due to the limited amount of α alumina detected, which is the densest form of alumina. Therefore, ALD/rCVD coatings would need higher annealing temperatures and probably longer annealing times to obtain a coating containing mostly the stable α phase.

5.5 Performance

5.5.1 Thermogravimetric stability

To test whether coated particles would be able to resist oxidation for the time required, a small amount of 30 mg was supposed to be loaded in a TGA and kept at 1000 °C for 100 h. Unfortunately, due to time limitations and equipment failure, only a $MoSi_2$ and $MoSi_2B$ blank were tested, along with a sample of $MoSi_2B$ alloyed with additional 6 wt% of Al and with the sol-gel method, using 20 g of aluminium tri-sec-butoxide. The results of these tests are shown in Figure 5.72. Although the $MoSi_2$ sample has a slow mass increase at 1000 °C as would be expected due to the formation of a slow-growing SiO_2 layer, there is surprisingly little weight loss at the start of the experiment, in which significant MoO_3 would be expected to evaporate.

For $MoSi_2B$ on the other hand, the weight gain is significantly more than expected at the start, followed by a surprisingly fast weight loss. This trend is however not as sharp as the graph shows, but is rather continuous during the first hour. It is uncertain whether this is due to machine errors or due to rapid initial oxidation in which the boron present could limit the formation of a closed scale, as in the regular $MoSi_2$.

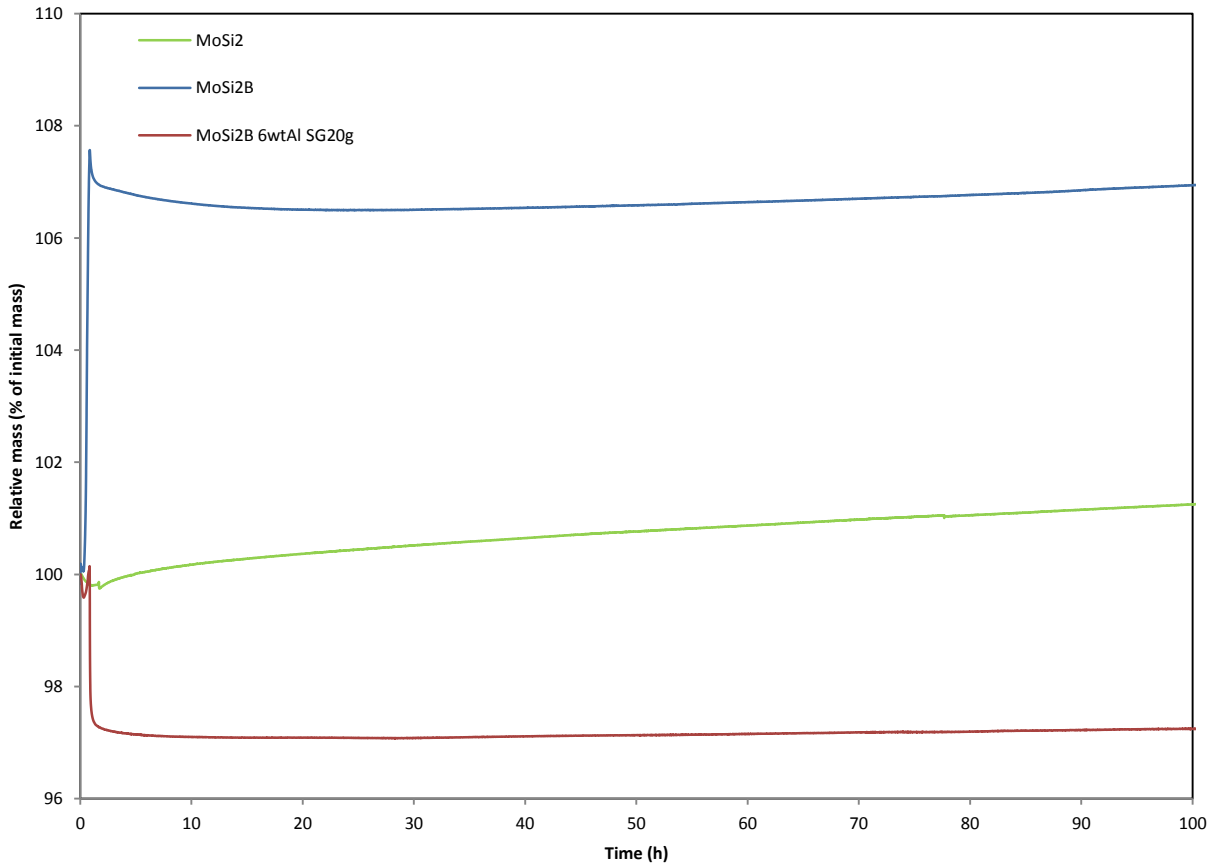

Figure 5.72: Relative weight change as a function of time for two blanks and the $MoSi_2B$ 6wt% Al SG20g coated sample during a TGA test at 1000 °C in synthetic air for 100h.

Finally, the coated sample seems to have no weight change at all any more after a rapid initial weight loss. This weight loss might be caused again by a problem with the machine or mass loss from evaporation of water or carbon species that were not removed during annealing and could rapidly oxidize due to contact with oxygen at a high temperature. Nevertheless, after this initial weight loss the coating seems to protect the sample well, even compared to the blanks. This might however also be partially due to the formation of mullite instead of SiO_2 due to $MoSi_2$ alloying with Al, which would limit oxidation significantly, as was shown in chapter 3. An attempt to test the model and this possibility with coated Si wafers was unfortunately not possible due to time limitations.

5.5.2 Embedded particle stability and healing

An important aspect of testing coated particles is investigating their performance in an actual thermal barrier coating (TBC). To this end, the SG-20g sol-gel procedure was repeated with wind sifted $MoSi_2B$ particles, which were subsequently mixed with yttria-stabilized zirconia (YSZ) to obtain a composite consisting of 80 V% YSZ and 20 V% healing particles. The results of the repeated coating procedure are shown in Figure 5.73 (SEM) and Figure 5.74 (XRD). EDS results presented in appendix

XV show that also in this case complete coverage with Al_2O_3 was most likely achieved, as all measurement points do again show the presence of significant amounts of Al.

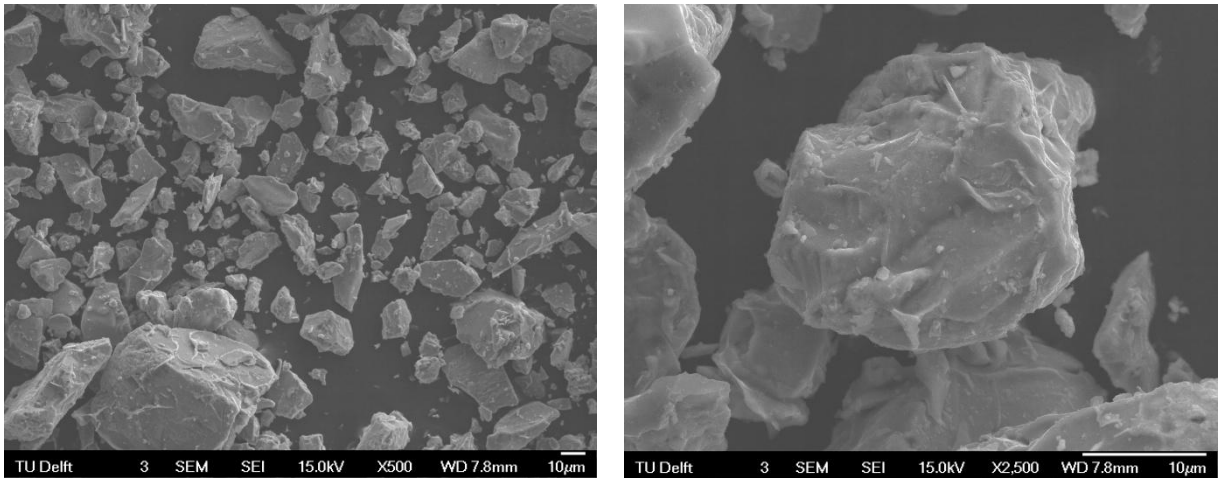

Figure 5.73: ***SEM images at different magnifications of $MoSi_2B$ coated with Al_2O_3 according to the SG-20g sol-gel procedure and heat treated at 450 °C and 1200 °C in argon.***

Both the SEM images and the XRD diffractograms are very similar to the SG-20g sample, indicating that both morphology and behavior during heat treatment and under high temperature conditions are similar. The main difference in the $MoSi_2B$ sample is the presence of MoB_2 in the samples before heat treatment. Surprisingly, this MoB_2 seems to disappear during heat treatment, and minor amounts of Mo seem to appear.

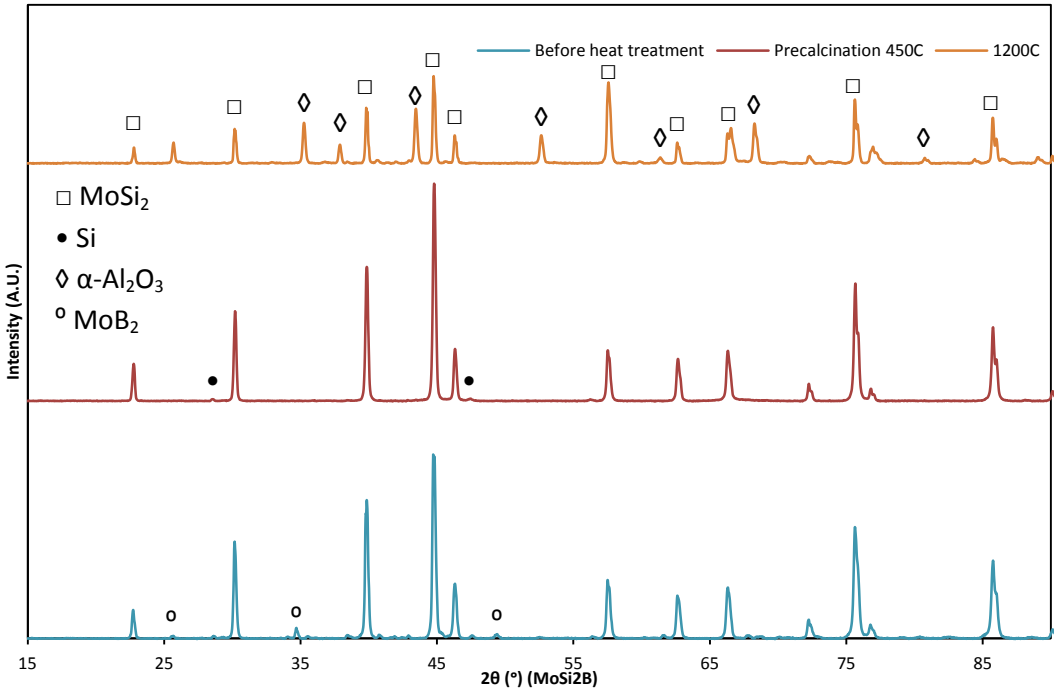

Figure 5.74: XRD diffractograms of the coated $MoSi_2B$ particles before and after heat treatment.

An explanation for this behavior could be limited oxidation of the sample during heat treatment, as boron oxidizes before silicon or molybdenum and in this sample the residual Si peak is still detected. It is also very difficult to completely prevent the presence of oxygen in a furnace without utilizing a

reducing atmosphere. However, this oxidation is not necessarily problematic as long as the coating does not crack or gets damaged and sufficient boron is still present in the particles. It could even be beneficial as it could also remove some organic impurities that might still be present. Furthermore, the main peaks of MoB_2 overlap with some of the main peaks of corundum, making detection of MoB_2 more difficult once α-Al_2O_3 forms. Therefore it is likely that there is still some MoB_2 present, but that it is not detectable anymore because of the presence of corundum.

In any case the main conclusion from this data is that the sol-gel procedure is reproducible and able to coat $MoSi_2$ particles with and without boron with a closed layer of α-Al_2O_3 after appropriate heat treatment.

For embedding particles in YSZ, several samples without $MoSi_2B$ powder were first prepared to investigate spark plasma sintering (SPS) of YSZ. The XRD diffractograms of these pure YSZ samples and the powder from which they were prepared are shown in Appendix XVI and show the presence of major carbon and minor ZrC and ZrB_2 impurities originating from reactions with graphite mould and boron nitride lubricant necessary during the SPS process. Furthermore, stress development and sintering is studied by investigating peak broadening at the peak with the highest intensity, which is the tetragonal ZrO_2 peak at a 2θ of 30°. These overlapping peaks are also presented in Appendix XVI and show significant differences in peak broadening compared to the powder. These two observations indicate that some heat treatment might be necessary to relieve stresses and remove impurities after SPS.

Damage for self-healing was introduced by indentation and also tested on the blank samples. By using equation 5.2 [106], fracture toughness of the composite can be calculated and compared to the regular YSZ samples. In this formula, K_{IC} is the fracture toughness in MPa√m, E is the Young modulus in GPa, H is the measured hardness in GPa, P is the maximum force achieved during indentation in N, C_0 is the total crack length as measured from the center of the indent in m and § is a correction factor for the equipment and conversion of Pa to MPa combined, with a value of $1.6*10^{-8}$ [106]. The results of these calculations are shown in Table 5.11. The Young modulus of 200 GPa for YSZ was based on the work of Christel et al. [107].

$$K_{IC} = \S * \left(\frac{E}{H}\right)^{\frac{1}{2}} * \frac{P}{C_0^{\frac{3}{2}}} \qquad \textbf{(5.2)}$$

Table 5.11: Measured hardness and crack length from Vickers HV10 indentation and resulting fracture toughness for an SPS sample of YSZ and the YSZ-$MoSi_2B$ composite.

Sample	K_{IC} ($MPa*m^{0.5}$)		Youngs Modulus E (Gpa)	Hardness measured (GPa)		Force used (N)	crack length micrometer	
YSZ	11.7	±0.45	200	1.32	±0.014	98.1	140	±3.3
$MoSi_2B$	9.3	±0.78	200	1.24	±0.060	98.1	167	±9.7

When comparing YSZ toughness measured here with the data of Christel et al. [107] and other authors, a fracture toughness of 11.7 MPa√m is significantly higher than most values for partially yttria stabilized zirconia, which are usually between 9 and 10 MPa√m. A possible explanation for this might be contamination with carbon and boron during SPS, which might be able to produce carbides and borides of zirconia that could increase toughness. This contamination is observed in XRD diffractograms of the SPS samples.

Another possibility might be that cracks formed by indentation with HV10 are slightly too short for accurate measurements. This would result in an overestimation of fracture toughness, as crack length is measured from the center of the indent. The second explanation seems more likely, as the toughness of both ZrC [108] and ZrB_2 [109] are significantly lower than the toughness of YSZ.

When comparing the composite with the YSZ sample, a clear difference in fracture toughness is observed, with the composite containing 20 V% $MoSi_2B$ having a significantly lower fracture toughness. As sintering parameters were the same, it is likely that this difference is caused by the particles. Although the manufacture of composites often results in a higher fracture toughness, in this case a lower toughness could be expected, as $MoSi_2B$ has a significantly lower K_{IC} than YSZ [110]. Therefore, addition of 20 V% particles of this more brittle material could easily decrease the overall fracture toughness of the composite. Furthermore, as explained in chapter 3 it is likely that the interface between the Al_2O_3 coating and YSZ is relatively weak, providing another crack path with lower resistance.

Investigation of SEM images of the composite samples themselves, presented in Figure 5.75, also shows some interesting results. The first and main result is that particles are indeed properly dispersed in the YSZ powder and that they are still intact after SPS. EDS maps shown in appendix XVII also indicate that the particle shell was able to protect the $MoSi_2B$ particles against reactions with YSZ, as no O or Zr was detected in the particles, while Mo and Si were the only elements detected there in significant amounts. Attempts to manufacture a double layer system of uncoated $MoSi_2$ and YSZ did show reactions between the two powders under SPS conditions, indicating that the coating is indeed able to protect particles to a certain extend.

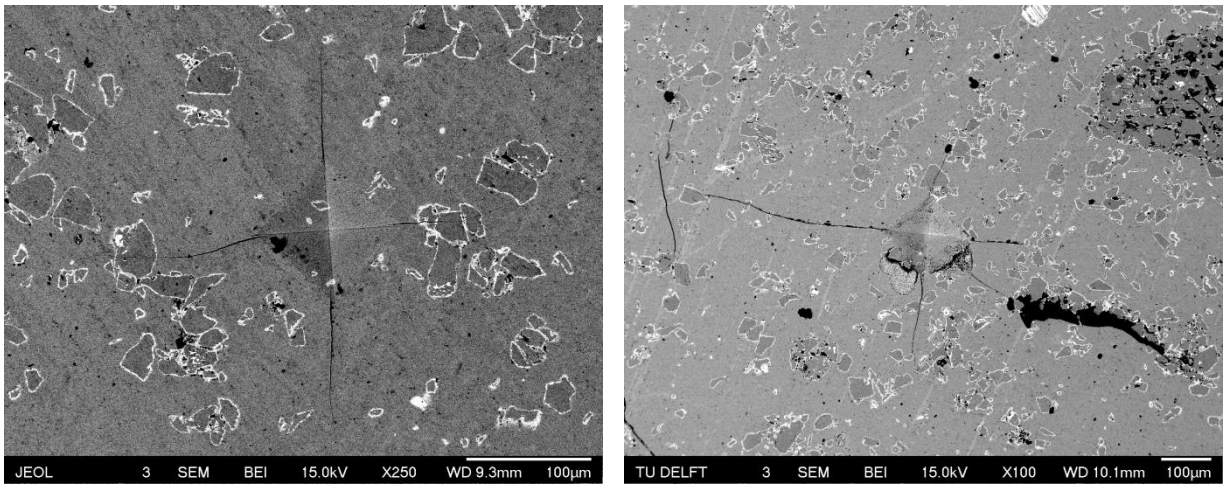

Figure 5.75: ***SEM-BSE images of two different indents at different magnifications with HV10 (left) and 200N force (right).***

SEM images also indicate that indentation is a suitable method to introduce damage. Cracks are sometimes relatively short compared to the indent itself though, making calculation of fracture toughness less accurate. Another observation is that cracks in general grow through the healing particles instead of deflecting. This was not exactly as expected, as computer models predicted that cracks would often grow around particles, but proves that crack growth through the shell is possible.

It has to be noted though that indentation in this project was performed at room temperature, while damage usually occurs during engine cooling and therefore at higher temperatures. $MoSi_2$ is significantly less brittle at temperatures above 1000 °C, which might change crack growth behavior. It

is therefore recommended to attempt damage introduction at higher temperatures as well to observe crack growth behavior under operating conditions.

Healing behavior was also investigated by annealing the sample in air at 1100 or 1200 °C. SEM images of one of the indents before and after healing is shown in Figure 5.76. One of the clear main problems is the clearly visible extensive fracture after heat treatment in air. This fracture is visible everywhere on the composite and not just close to the indents. The suspected cause is premature oxidation and associated volume expansion of particles without any crack nearby. This is supported by formation of cracks and oxidation products in the sample that was subjected to 48h of air at 1100 °C without damage introduction. Furthermore, significant swelling was observed after heat treatment of the composites, but only on the side that was in contact with the gas phase.

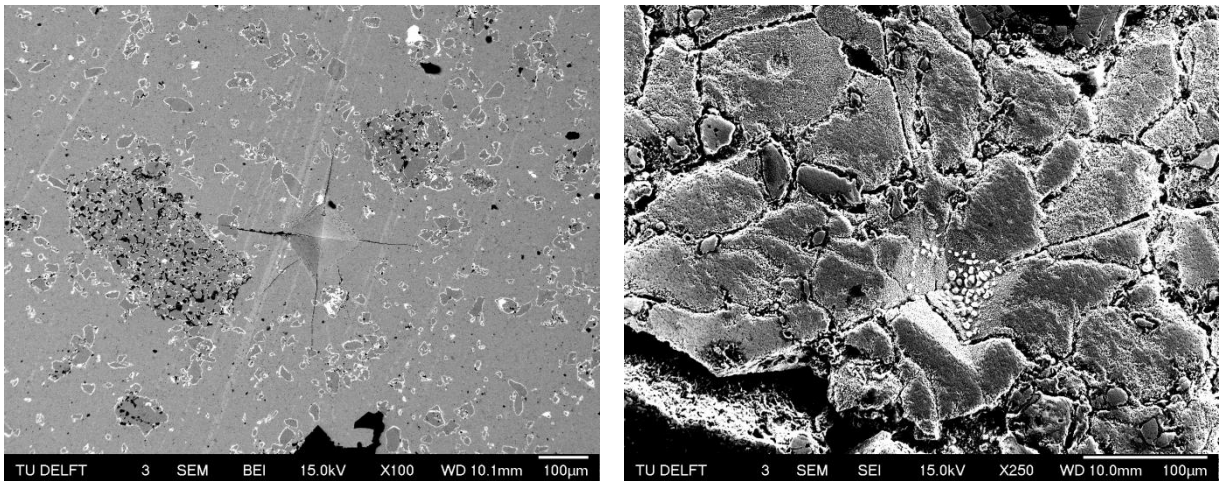

Figure 5.76: ***SEM images of an indent before (left) and after (right) heat treatment in air at 1100 °C for 1 hour (heating and cooling rate 5 °C/min).***

However, as shown in Figure 5.77, both smaller cracks and larger cracks that were already present at the start, do actually fill with material. Based on the BSE image, this material also contains low amounts of heavier elements, indicating that this is indeed Si filling and possibly healing the cracks.

Based on these observations, better self-healing might be obtained by adjustment of the healing parameters, such as creating indents with smaller loads, which would result in smaller cracks to heal and less significant residual stresses. These smaller cracks could then in turn be healed at lower temperatures or shorter times. Thicker coatings to limit oxidation of non-damaged particles might also help, although modelling does not seem to agree with this and a more detailed TGA investigation is recommended. Furthermore, the addition of a small amount of Al to the $MoSi_2B$ could aid in limiting premature oxidation by acting as a sacrificial element that would protect the $MoSi_2B$ from further oxidation. Lowering the content of healing material could also decrease swelling and still allow for sufficient healing material to repair any damage. This would also decrease toughness reduction of the composite, at the cost of having less healing material available.

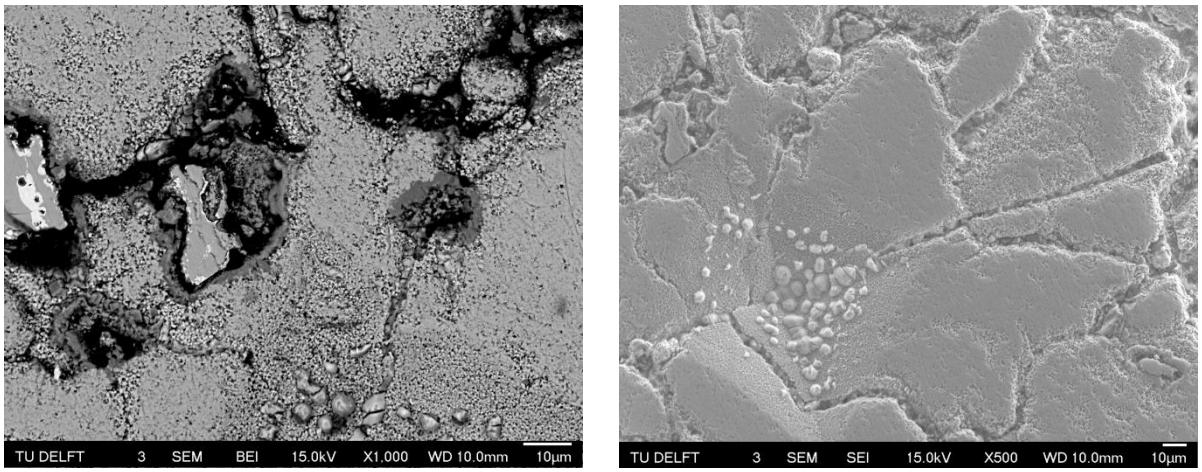

Figure 5.77: ***SEM images of cracks close to an indent with a BSE image (left) and a SEI image (right), showing the presence of crack filling.***

Conclusions and Recommendations

6.1 Conclusions

The goal of this thesis was to find an optimal route to produce Al_2O_3 coated $MoSi_2$ particles and show the validity of the self-healing Thermal Barrier Coating (TBC) concept. To this end, two chemical methods were optimized for coating $MoSi_2$ particles, namely Atomic Layer Deposition and a sol-gel method.

Initial calculations and oxidation modeling did however show the necessity to reduce surface area to limit the volume fraction of inert coating material in the healing particles. This reduction in total surface area, along with an increase of average particle size and a removal of most small particles was successfully accomplished using wind sifting.

For the sol-gel method, the main challenge was found to be proper coverage of the particles with coating material. This was successfully solved by ensuring prolonged contact between the alumina gel and the particles with nitrogen bubbling in a slurry bubble column reactor setup, selecting a suitable precursor and controlling pH to ensure favorable electrostatic interactions between particle surfaces and the gel. It was found that liquid aluminium tri-sec-butoxide was the most suitable precursor due to its miscibility with water and its reactivity, resulting in rapid gel formation.

For ALD the main challenge was reaching reasonable thickness in a feasible number of cycles. It was found that by utilizing residual chemical vapor deposition (rCVD), growth per cycle could be increased dramatically, resulting in coatings of several 100s of nanometers up to 1.8 μm in only 25-40 cycles. The rCVD component is thought to be governed mainly by H_2O condensation and the subsequent reaction of trimethylaluminium with this condensed water.

To obtain stable α-alumina coatings, heat treatment was also necessary. It was found that heat treatment in argon was necessary to prevent premature oxidation. This two-step heat treatment resulted in the formation of detectable α-alumina in the coatings of both the final sol-gel and ALD/rCVD samples, according to the XRD results. This formation of alpha alumina was without significant crack formation in all samples except for the thickest ALD coating. Therefore it can be concluded that both methods are suitable to produce $MoSi_2$ coated with α-Al_2O_3 as long as coating thickness is properly controlled.

Comparison of the two different methods shows a difference in both microstructure and coating morphology. Although comparable average coating thickness can be obtained and was approximately obtained between the SG20g and ALD25C samples, the thickness distribution was found to be significantly wider for the sol-gel method. Furthermore, behavior during heat treatment was very different, with transformation to the stable α phase being significantly easier in coatings produced with the sol-gel method, compared to the transformation of the coatings produced by ALD. The most likely explanation for this lower activation energy of the transformation sequence in sol-gel coatings would be a different transformation pathway, with the γ→δ→θ→α being the most likely path for sol-gel, while the amorphous→κ→α being the most probable transformation pathway for the ALD samples. XRD data is however inconclusive on this and further research is recommended. Due to these differences in transformation kinetics, it is likely that sol-gel coatings will have a larger alumina grain size.

Resistance of the produced Al_2O_3 coatings to oxidation was modeled using a Wagner model approach and found by varying the most important parameters that surprisingly Al_2O_3 initial coating thickness was not an important parameter, while alumina grain size, temperature and mullite layer thicknes were found to be very influential parameters in the prevention of oxidation. Unfortunately, experimental validation of these predictions was not possible due to time constraints. Nevertheless, this does indicate that it is important to promote the formation of larger α-Al_2O_3 grains and mullite formation by higher annealing temperatures and/or aluminium alloying in the $MoSi_2$.

Based on TGA stability tests, the model does however overestimate the oxidation speed, even of the bare sample, although the order of magnitude seems to be correct. The coating does however aid in protection for the $MoSi_2B$ 6wt% Al sample coated with the sol-gel method, when comparing this sample with the $MoSi_2$ and $MoSi_2B$ blanks, although no $MoSi_2B$ 6wt% Al blank was available. Due to the presence of Al in the base material, mullite formation during oxidation might be the main reason for this though. Furthermore, there is some uncertainty regarding the validity and accuracy of the TGA results.

Finally, it was found that embedding coated particles in a matrix of yttria-stabilized zirconia (YSZ) is possible by SPS and that the alumina coating is able to prevent oxidation during the manufacturing process. However, oxidation and volume expansion of particles during operation was found to be a problem which resulted in swelling and damage to the composite, indicating that care must be taken with designing healing composites. However, evidence of crack filling, SiO_2 transport along cracks and zircon formation has also been found with SEM and EDS, showing the feasibility of this self-healing concept.

6.2 Recommendations

For the continuation of this research, the composite results indicate that the stability of the particles might be a major challenge. It is therefore recommended to experimentally validate the oxidation model and its main conclusion that mullite formation is important in preventing further oxidation of particles.

Furthermore, it is important to perform TGA analyses on the coated and heat treated powders to investigate whether they are stable under operation conditions and whether there is a significant difference between the two methods of coating manufacture.

If the thickness of the alumina is indeed found to be less important, it is recommended to continue coating particles with the sol-gel method, as it is a less sensitive, less dangerous and more straightforward method. If there is a significant difference between the methods though, a careful analysis between the advantages and disadvantages of each method is recommended.

Regarding the production methods, it is recommended to try annealing at higher temperatures to transform more alumina to the stable alpha phase, especially for the ALD samples. Addition of α-alumina nanoparticles might also be an option to increase the transformation kinetics of the stable phase. Furthermore, annealing at higher temperatures might promote formation of additional mullite, protecting the particles even more.

However, due to the high grain boundary diffusivity found in alumina, it might be even more interesting to retain as much of the amorphous phase as possible, as this phase does not have any

grain boundaries that could act as a fast pathway for diffusion. For sol-gel samples this is very difficult, but for ALD/rCVD samples, this might be feasible if the pathway is indeed through κ alumina. As shown in the results, the formation of alpha alumina is challenging even at 1200 °C, indicating that the amorphous phase might be stable sufficiently long at regular TBC operating temperatures. If this pathway is preferred, it is also recommended that the transformation kinetics of the ALD/rCVD samples are investigated more thoroughly by XRD.

If the ALD/rCVD coating path turns out to be the more suitable coating production method, it might be necessary to perform more experiments to determine the exact mechanism of the rCVD component and whether the growth mechanism is indeed nonlinear or whether this is only due to a reduction in total surface area. More experiments will also help in establishing a number of cycles-thickness relation that will be necessary if the coating thickness is to be controlled.

Finally, for optimization of the self-healing system, the first recommendation is to investigate the influence of alloying Al in the $MoSi_2B$ particles, especially to find out whether the added Al can decrease swelling by reducing oxidation of particles free of damage and nearby cracks. Varying the volume percentage of healing particles added might also influence the swelling and damage creation observed and is therefore also recommended. Furthermore, careful consideration of the testing procedure for damage healing might change the performance during healing, as it is suspected that indentation with large loading might damage the composite more than expected. Decreasing the indentation load or using a different method for healing tests might give more accurate results.

Acknowledgements

This project would not have been finished without the contributions of several important people and I would like to thank you all for your help and advice. First of all, I would like to express my sincere gratitude to my daily supervisors Alexandra-Lucia Carabat and Wim Sloof for their support and guidance during this project and for their valuable advice both regarding the project and many other topics. I would also like to thank Ruud van Ommen and Erik Kelder for supervising me during this project and for the great and helpful discussions. Furthermore, thanks to professor Sybrand van der Zwaag for being part of the thesis committee and undoubtedly asking those surprising questions that nobody else could think of.

I would also like to express my thanks to the people of the groups I had the pleasure to work in, namely the Virtual Materials and Mechanics group of Materials Science and the battery group and Product and Process Engineering group of Chemical Engineering. In particular I would like to thank Mojgan Talebi, Wim van Oordt, Henk Nugteren and David Valdesueiro for their help with atomic layer deposition and wind sifting, both of which I was not familiar with at all at the start of this project. I would also like to thank Aris Goulas and Filipe Lopez for not bringing a velociraptor suit to my defence.

From the Virtual Materials and Mechanics group I would like to thank Hans Brouwer, Kees Kwakernaak and Ruud Hendrikx in particular for their help with all the beautiful (and expensive) "toys" present in the materials science department. Without their help, it would have been impossible to do all those characterization experiments required for this work.

Finally I would like to thank everyone that I did not mention for helping me out when I was stuck, giving me such a great time during my master thesis and for creating such an enjoyable atmosphere in all of the groups I worked in. It was a pleasure to work with you all and I hope to see you again in the future!

Bibliography

1. Meadows, D.H., et al., *The limits to growth.* New York, 1972. **102**.
2. Kitching, C., *The true cost of transatlantic travel: Infographic reveals how passengers pay £152 in tax on a London to New York flight (that's a QUARTER of your ticket price)*, in *The Daily Mail*. 2015: London.
3. Tipler, P.A. and G. Mosca, *Physics for scientists and engineers*. 2007: Macmillan.
4. Duhl, M.G., DN, and A. Giamei, *The development of single crystal superalloy turbine blades.* Superalloys 1980, 1980.
5. Clarke, D.R., M. Oechsner, and N.P. Padture, *Thermal-barrier coatings for more efficient gas-turbine engines.* MRS Bull, 2012. **37**(10): p. 891-898.
6. Sloof, W.G., *Self healing in coatings at high temperatures*, in *Self Healing Materials*. 2007, Springer. p. 309-321.
7. Carabat, A.L., S. Zwaag, and W.G. Sloof, *Creating a Protective Shell for Reactive MoSi2 Particles in High-Temperature Ceramics.* Journal of the American Ceramic Society, 2015.
8. Langston, L.S., *efficiency by the numbers*, in *From the editors Desk; The official blog of ASME's Mechanical Engineering magazine*, J. Falcioni, Editor. 2012, Mechanical Engineering Magazine.
9. Padture, N.P., M. Gell, and E.H. Jordan, *Thermal barrier coatings for gas-turbine engine applications.* Science, 2002. **296**(5566): p. 280-284.
10. Clarke, D.R. and S.R. Phillpot, *Thermal barrier coating materials.* Materials Today, 2005. **8**(6): p. 22-29.
11. Iacovides, H. and M. Raisee, *Recent progress in the computation of flow and heat transfer in internal cooling passages of turbine blades.* International Journal of Heat and Fluid Flow, 1999. **20**(3): p. 320-328.
12. Vaßen, R., et al., *Overview on advanced thermal barrier coatings.* Surface and Coatings Technology, 2010. **205**(4): p. 938-942.
13. Hille, T.S., et al., *Damage growth triggered by interface irregularities in thermal barrier coatings.* Acta Materialia, 2009. **57**(9): p. 2624-2630.
14. Turteltaub, S., *Powerpoint presentation: Self-healing Thermal barrier coatings based on MoSi2*. 2013.
15. Guimard, N.K., et al., *Current Trends in the Field of Self-Healing Materials.* Macromolecular Chemistry and Physics, 2012. **213**(2): p. 131-143.
16. Van der Zwaag, S., et al., *Self-healing behaviour in man-made engineering materials: bioinspired but taking into account their intrinsic character.* Philosophical Transactions of the Royal Society of London A: Mathematical, Physical and Engineering Sciences, 2009. **367**(1894): p. 1689-1704.
17. Mao, W., *Kinetics of self-healing reaction in TBC with MoSi2 based sacrificial particles*. 2013, TU Delft, Delft University of Technology.
18. Sloof, A.L.C.W.G., *Powerpoint presentation: Encapsulation of MoSi2 self-healing particles for high temperature applications*. 2014.
19. Eaton, H.E., et al. *EBC Protection of SiC/SiC Composites in the Gas Turbine Combustion Environment: Continuing Evaluation and Refurbishment Considerations*. in *ASME Turbo Expo 2001: Power for Land, Sea, and Air*. 2001. American Society of Mechanical Engineers.
20. Singhal, S., *Advances in solid oxide fuel cell technology.* Solid state ionics, 2000. **135**(1): p. 305-313.
21. Knittel, S., S. Mathieu, and M. Vilasi, *The oxidation behaviour of uniaxial hot pressed MoSi 2 in air from 400 to 1400 C.* Intermetallics, 2011. **19**(8): p. 1207-1215.
22. Carabat, A., S. Van der Zwaag, and W. Sloof. *Encapsulation of sacrificial silicon containing particles for SH oxide ceramics via a boehmite precursor route*. in *ICSHM 2013: Proceedings of the 4th International Conference on Self-Healing Materials, Ghent, Belgium, June 16-20, 2013*. 2013. Ghent University; Delft University of Technology.

23. Levin, I. and D. Brandon, *Metastable alumina polymorphs: crystal structures and transition sequences.* J. Am. Ceram. Soc., 1998. **81**(8): p. 1995-2012.
24. Patnaik, P., *Handbook of inorganic chemicals*. Vol. 28. 2003: McGraw-Hill New York.
25. Strafford, K., *'Protective oxide scales and their breakdown'.* Materials Science and Technology, 1998. **14**(11): p. 1200.
26. Moulijn, J.A., M. Makkee, and A.E. Van Diepen, *Chemical process technology*. 2013: John Wiley & Sons.
27. Askeland, D.R. and P.P. Phulé, *The science and engineering of materials.* 2003.
28. Chiang, Y.-M., W.D. Kingery, and D.P. Birnie, *Physical ceramics: principles for ceramic science and engineering*. 1997: J. Wiley.
29. Thomas, O., et al., *Molybdenum disilicide: crystal growth, thermal expansion and resistivity.* Solid state communications, 1985. **55**(7): p. 629-632.
30. d'Heurle, F., C. Petersson, and M. Tsai, *Observations on the hexagonal form of MoSi2 and WSi2 films produced by ion implantation and on related snowplow effects.* Journal of Applied Physics, 1980. **51**(11): p. 5976-5980.
31. Fujiwara, H. and Y. Ueda, *Thermodynamic properties of molybdenum silicides by molten electrolyte EMF measurements.* Journal of alloys and compounds, 2007. **441**(1): p. 168-173.
32. Subbarao, E. and K. Gokhale, *Thermal expansion of zircon.* Japanese Journal of Applied Physics, 1968. **7**: p. 1126.
33. Singhal, S.C. and K. Kendall, *High-temperature solid oxide fuel cells: fundamentals, design and applications: fundamentals, design and applications*. 2003: Elsevier.
34. Lide, D.R., *CRC handbook of chemistry and physics*. 2004: CRC press.
35. Koike, C., et al., *Infrared Spectra of Silica Polymorphs and the Conditions of Their Formation.* The Astrophysical Journal, 2013. **778**(1): p. 60.
36. Lager, G.A., J. Jorgensen, and F. Rotella, *Crystal structure and thermal expansion of α-quartz SiO2 at low temperatures.* Journal of Applied Physics, 1982. **53**(10): p. 6751-6756.
37. Heaney, P.J., *Structure and chemistry of the low-pressure silica polymorphs.* Reviews in Mineralogy and Geochemistry, 1994. **29**(1): p. 1-40.
38. Pierre, A.C., *Introduction to sol-gel processing*. Vol. 1. 2013: Springer Science & Business Media.
39. Brinker, C.J. and G.W. Scherer, *Sol-gel science: the physics and chemistry of sol-gel processing*. 2013: Academic press.
40. Atkins, P. and J. De Paula, *Elements of physical chemistry*. 2013: Oxford University Press.
41. Dressler, M., *Sol-gel preparation and characterization of corundum based ceramic oxidation protection coatings.* 2006.
42. Shi, J., *Steric stabilization.* Croup Inorganic Materials Science–Literature review, The Ohio State University. Columbus, USA, 2002.
43. Attia, Y., *Sol-gel processing and applications*. 2012: Springer Science & Business Media.
44. Kobayashi, Y., T. Ishizaka, and Y. Kurokawa, *Preparation of alumina films by the sol-gel method.* Journal of materials science, 2005. **40**(2): p. 263-283.
45. Wang, D. and G.P. Bierwagen, *Sol–gel coatings on metals for corrosion protection.* Progress in Organic Coatings, 2009. **64**(4): p. 327-338.
46. Yoldas, B.E., *Alumina gels that form porous transparent Al2O3.* Journal of Materials Science, 1975. **10**(11): p. 1856-1860.
47. Chen, Y.-C., et al., *Ceramic-coated carbide tools by sol-gel process.* Journal of materials science letters, 2000. **19**(16): p. 1469-1472.
48. Avci, N., et al., *Stability improvement of moisture sensitive CaS:Eu2+ micro-particles by coating with sol–gel alumina.* Optical Materials, 2011. **33**(7): p. 1032-1035.
49. Li, Y., et al., *Fe 3 O 4@ Al 2 O 3 magnetic core–shell microspheres for rapid and highly specific capture of phosphopeptides with mass spectrometry analysis.* Journal of Chromatography A, 2007. **1172**(1): p. 57-71.

50. Dey, A., et al., *Investigation of thermal oxidation of Al 2 O 3-coated SiC powder.* Thermochimica Acta, 2014. **583**: p. 25-31.
51. Yang, C.Y. and W.H. Shih, *Effect of acid on the coating of boehmite onto silicon carbide particles in aqueous suspensions.* Journal of the American Ceramic Society, 1999. **82**(2): p. 436-440.
52. Beyers, R., *Thermodynamic considerations in refractory metal-silicon-oxygen systems.* Journal of applied physics, 1984. **56**(1): p. 147-152.
53. Yang, Q. and T. Troczynski, *Dispersion of alumina and silicon carbide powders in alumina sol.* Journal of the American Ceramic Society, 1999. **82**(7): p. 1928-1930.
54. Wang, M. and M. Muhammed, *Novel synthesis of Al 13-cluster based alumina materials.* Nanostructured materials, 1999. **11**(8): p. 1219-1229.
55. Dumont, F., D. Van Tan, and A. Watillon, *Study of ferric oxide hydrosols from electrophoresis, coagulation, and peptization measurements.* Journal of colloid and interface science, 1976. **55**(3): p. 678-687.
56. Pierre, A.C. and D.R. Uhlmann, *Gelation of aluminum hydroxide sols.* Journal of the American Ceramic Society, 1987. **70**(1): p. 28-32.
57. George, S.M., *Atomic layer deposition: an overview.* Chemical reviews, 2009. **110**(1): p. 111-131.
58. Puurunen, R.L., *Surface chemistry of atomic layer deposition: A case study for the trimethylaluminum/water process.* Journal of applied physics, 2005. **97**(12): p. 121301.
59. Leskelä, M. and M. Ritala, *Atomic layer deposition chemistry: recent developments and future challenges.* Angewandte Chemie International Edition, 2003. **42**(45): p. 5548-5554.
60. Kim, H., *ALD Nanodeposition*.
61. Van Ommen, J. and A. Goulas, *ENCAPSULATING PARTICLES WITH NANOSCALE PRE-CISION USING ATOMIC LAYER DEPOSITION.* 2015.
62. Valverde Millán, J., *Introduction. The Classical Geldart's Diagram and the New Type of Gas-Fluidization Behavior*, in *Fluidization of Fine Powders*. 2013, Springer Netherlands. p. 1-6.
63. Valdesueiro, D., et al., *Gas-Phase Deposition of Ultrathin Aluminium Oxide Films on Nanoparticles at Ambient Conditions.* Materials, 2015. **8**(3): p. 1249-1263.
64. Hausmann, D., et al., *Rapid vapor deposition of highly conformal silica nanolaminates.* Science, 2002. **298**(5592): p. 402-406.
65. Garcia-Trinanes, P., et al., *Enhancing the activation of silicon carbide particles with gas-phase coating of aluminum oxide.*
66. Groner, M., et al., *Low-temperature Al2O3 atomic layer deposition.* Chemistry of Materials, 2004. **16**(4): p. 639-645.
67. Weast, R.C., *Handbook of chemistry and physics.* The American Journal of the Medical Sciences, 1969. **257**(6): p. 423.
68. Farrens, S.N., et al., *Chemical free room temperature wafer to wafer direct bonding.* Journal of the Electrochemical Society, 1995. **142**(11): p. 3949-3955.
69. Amirfeiz, P., et al., *Formation of silicon structures by plasma-activated wafer bonding.* Journal of the Electrochemical Society, 2000. **147**(7): p. 2693-2698.
70. Yoldas, B.E., Ceramic bulletin, 1975(54): p. 286.
71. Andersson, J.M., et al., *Microstructure of α-alumina thin films deposited at low temperatures on chromia template layers.* Journal of Vacuum Science & Technology A, 2004. **22**(1): p. 117-121.
72. Musil, J., et al., *Thermal stability of alumina thin films containing γ-Al2O3 phase prepared by reactive magnetron sputtering.* Applied Surface Science, 2010. **257**(3): p. 1058-1062.
73. Zhang, L., et al., *Annealing of Al 2 O 3 thin films prepared by atomic layer deposition.* Journal of Physics D: Applied Physics, 2007. **40**(12): p. 3707.
74. Freiman, S.W. and S. Ward, *Fracture mechanics applied to brittle materials*. Vol. 678. 1979: ASTM International.

75. Ghosh, S.K., *Self-healing materials: fundamentals, design strategies, and applications*. 2009: John Wiley & Sons.
76. Zhu, Y.T., et al., *Thermal Oxidation Kinetics of MoSi2-Based Powders.* Journal of the American Ceramic Society, 1999. **82**(10): p. 2785-2790.
77. Liu, Y., G. Shao, and P. Tsakiropoulos, *On the oxidation behaviour of MoSi 2.* Intermetallics, 2001. **9**(2): p. 125-136.
78. Shan, A., et al., *Microstructure and Mechanical Properties of MoSi2-X (X= Al, B, Nb) Alloys Fabricated by MA-PDS Process.* Materials Transactions, 2002. **43**(1): p. 5-10.
79. Kuznetsov, S.A., et al., *Synthesis of molybdenum borides and molybdenum silicides in molten salts and their oxidation behavior in an air–water mixture.* Surface and Coatings Technology, 2005. **195**(2–3): p. 182-188.
80. e Silva, A.C. and M. Kaufman, *Synthesis of MoSi 2-boride composites through in situ displacement reactions.* Intermetallics, 1997. **5**(1): p. 1-15.
81. Liao, K.E.S.P.K., *The B-Mo phase diagram*.
82. e Silva, A.C. and M. Kaufman, *Applications of in situ reactions to MoSi 2-based materials.* Materials Science and Engineering: A, 1995. **195**: p. 75-88.
83. Lakiza, S.M. and L.M. Lopato, *Stable and metastable phase relations in the system alumina–zirconia–yttria.* Journal of the American Ceramic Society, 1997. **80**(4): p. 893-902.
84. Fabrichnaya, O., et al., *The assessment of thermodynamic parameters in the Al2O3-Y2O3 system and phase relations in the Y-Al-O system.* Scandinavian journal of metallurgy, 2001. **30**(3): p. 175-183.
85. Suenaga, K., et al., *Investigations of alumina/spinel and alumina/ zirconia interfaces by spatially resolved electron energy loss spectroscopy.* Journal of the European Ceramic Society, 1998. **18**(10): p. 1453-1459.
86. Schneider, H., J. Schreuer, and B. Hildmann, *Structure and properties of mullite—a review.* Journal of the European Ceramic Society, 2008. **28**(2): p. 329-344.
87. Degterov, S. and A. Pelton, *Critical evaluation and optimization of the thermodynamic properties and phase diagrams of the CrO-Cr2O3-SiO2 and CrO-Cr2O3-SiO2-Al2O3 systems.* Journal of phase equilibria, 1996. **17**(6): p. 488-494.
88. Butterman, W.F., W. , *Zircon stability and the ZrO2-SiO2 phase diagram.* Am. Mineral., 1967: p. 880-885.
89. RouNSow, K., G. Grsns, and P. eNn, *The structure of zircon: a comparison with garnet.* Am. Mineral., 1971. **56**: p. 782-790.
90. Springer, T. and R. Lechner, *Diffusion in Condensed Matter.* Vieweg, Wiesbaden, 1998: p. 59.
91. Heuer, A., *Oxygen and aluminum diffusion in α-Al 2 O 3: How much do we really understand?* Journal of the European Ceramic Society, 2008. **28**(7): p. 1495-1507.
92. Fielitz, P., et al., *A diffusion-controlled mullite formation reaction model based on tracer diffusivity data for aluminium, silicon and oxygen.* Philosophical Magazine, 2007. **87**(1): p. 111-127.
93. Lamkin, M., F. Riley, and R. Fordham, *Oxygen mobility in silicon dioxide and silicate glasses: a review.* Journal of the European Ceramic Society, 1992. **10**(5): p. 347-367.
94. Lejcek, P., *Grain boundary segregation in metals*. Vol. 136. 2010: Springer Science & Business Media.
95. Smialek, J.L., et al., *Oxygen Permeability and Grain-Boundary Diffusion Applied to Alumina Scales*. 2013, NASA/TM—2013-217855, 1–14.
96. Smialek, J.L., *Diffusivity in Alumina Scales Grown on Al-MAX Phases*. 2014.
97. Yoon, J.-K., et al., *Microstructure and growth kinetics of the Mo 5 Si 3 and Mo 3 Si layers in MoSi 2/Mo diffusion couple.* Intermetallics, 2003. **11**(7): p. 687-696.
98. Wei, X. and D. Chen, *Synthesis and characterization of nanosized zinc aluminate spinel by sol–gel technique.* Materials Letters, 2006. **60**(6): p. 823-827.
99. Saha, S.K. and P. Pramanik, *Aqueous sol-gel synthesis of mullite powder by using aluminium oxalate and tetraethoxysilane.* Journal of materials science, 1994. **29**(13): p. 3425-3429.

100. Goldstein, J.I., et al., *The influence of oxide surface layers on bulk electron probe microanalysis of oxygen—application to Ti-Si-O compounds.* Scanning, 1993. **15**(3): p. 165-170.
101. Yao, Z., J. Stiglich, and T. Sudarshan, *Molybdenum silicide based materials and their properties.* Journal of Materials Engineering and Performance, 1999. **8**(3): p. 291-304.
102. Rosenbrand, G.G., *The separation performance and capacity of zigzag air classifiers at high particle feed rates*. 1986, Dissertation TU Eindhoven.
103. Lumsdon, D.G. and V.C. Farmer, *Solubility of a proto-imogolite sol in oxalate solutions.* European Journal of Soil Science, 1997. **48**(1): p. 115-120.
104. Dollimore, D. and D. Griffiths, *Differential thermal analysis study of various oxalates in oxygen and nitrogen.* Journal of Thermal Analysis and Calorimetry, 1970. **2**(3): p. 229-250.
105. Rhodes, M.J., *Introduction to particle technology*. 2008: John Wiley & Sons.
106. Anstis, G., et al., *A Critical Evaluation of Indentation Techniques for Measuring Fracture Toughness. I.--Direct Crack Measurements.* Journal of the American Ceramic Society, 1981. **64**(9): p. 533-538.
107. Christel, P., et al., *Mechanical properties and short-term in vivo evaluation of yttrium-oxide-partially-stabilized zirconia.* Journal of biomedical materials research, 1989. **23**(1): p. 45-61.
108. Sciti, D., S. Guicciardi, and M. Nygren, *Spark plasma sintering and mechanical behaviour of ZrC-based composites.* Scripta Materialia, 2008. **59**(6): p. 638-641.
109. Chamberlain, A.L., et al., *High-Strength Zirconium Diboride-Based Ceramics.* Journal of the American Ceramic Society, 2004. **87**(6): p. 1170-1172.
110. Morris, D.G., M. Leboeuf, and M. Morris, *Hardness and toughness of MoSi 2 and MoSi 2–SiC composite prepared by reactive sintering of powders.* Materials Science and Engineering: A, 1998. **251**(1): p. 262-268.

Table of contents Appendices

Appendix I: Protective coatings for $MoSi_2$ for self-healing Thermal Barrier Coatings

1. Introduction

One of the major challenges these days is the increasing scarcity of energy. The realization of fossil fuels being a finite resource is dawning and emissions of carbon dioxide become increasingly problematic for earth's climate. Many solutions are being investigated that focus on using different sources of energy or increasing the efficient use of energy. However, for many applications, especially gas turbines, increasing efficiency requires increasing the operating temperature. High temperatures combined with stresses acting on the components, is an extremely demanding environment and requires very specialized materials.

Even with specially developed materials such as nickel superalloys, there is a limit to the operating temperature because of creep damage. To protect the structural components of gas turbines, they are cooled on the inside and insulated by thermal barrier coatings on the outside. One of the challenges of this protection is that the thermal barrier coating is almost always a refractory ceramic, yttria-stabilized zirconia being the most prevalent in modern gas turbines and engines. Because of the significant mismatch in thermal expansion coefficient of these ceramics and the metallic base material, stresses arise during heating and cooling, resulting in significant spallation damage and the necessity to replace the coating often.

A solution to this problem, which has been developed at Delft, University of Technology, is to use a coating that is able to autonomously repair the damage by including a so-called healing agent. If a crack is present, the material is able to oxidize and fill the crack, thereby healing it. The problem with this system is however that due to the thermal barrier coating being transparent to oxygen, the healing agent oxidizes even when no crack is present. To prevent this, the particle has to be coated with a material that is impermeable to oxygen, but allows the crack to grow through the coating.

The goal of this study is therefore to find suitable materials to protect the healing agents, compare them and select the most suitable materials for further investigation. Another important aspect of this is the method of application of this coating, which is not trivial. Therefore the second goal is to find suitable routes to obtain the protective barrier and select the most promising combinations of protective material and application route.

To achieve this, first the system of the thermal barrier coating and important requirements for the coating of the self-healing agents are described in chapter 2, followed by a thorough analysis of the possible materials to coat the agent in chapter 3. As the main function of the coating is to prevent oxygen from reaching the inner part of the oxide, a small analysis on the oxygen diffusion is performed in chapter 4, along with diffusion calculations and required coating thickness to prevent oxidation. Using calculated thickness, suitable methods of producing this coating are presented in chapter 5. Finally, in chapter 6 a selection of the most promising material and application method combinations is performed.

2. The Thermal Barrier Coating system

In this chapter, the system of the thermal barrier coatings (TBCs) is discussed to better understand the challenges present and extract from this information the main requirements for the protective coating for the healing agent.

The full system is shown in figure 1 (courtesy of W. Sloof) and shows first the location of the coating in a jet engine. TBCs are present in the hot zone of the engine, mainly on top of turbine blades made from nickel superalloys. A bond coating is used for growing a protective layer of Al_2O_3 on top for protection against corrosion. Although compositions for both alloy and bond coating can vary significantly, some typical compositions are shown in table 1. On top of that oxide layer, a layer of ZrO_2 with approximately 6-8 wt% of Y_2O_3 is deposited by plasma spraying as thermal barrier coating.

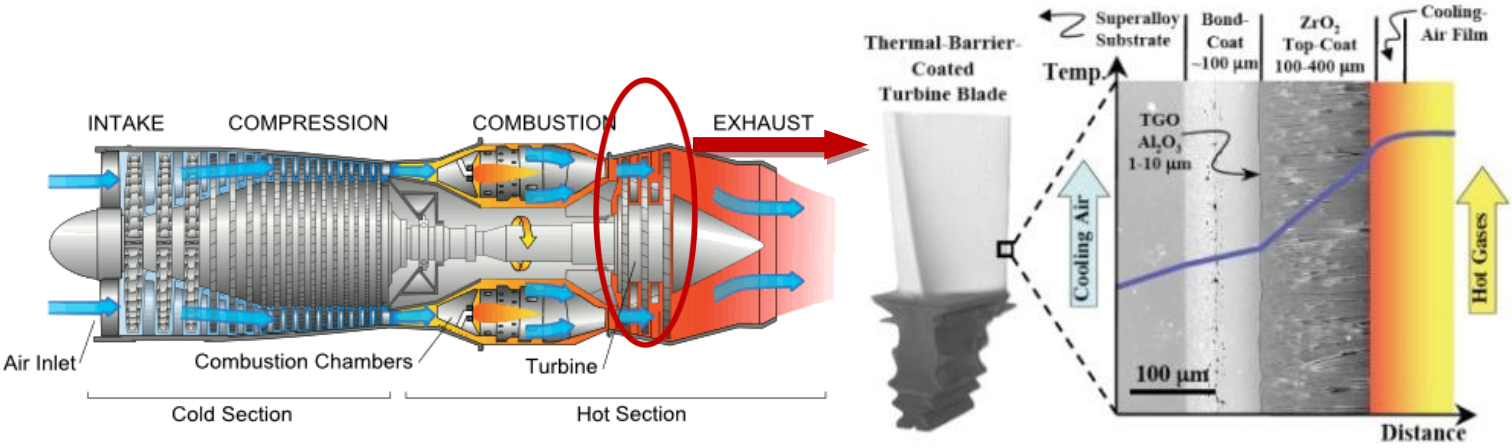

Figure 1: Jet engine layout (a) and interface between turbine blade and hot gas (b). (Source: Introduction presentation W. Sloof and A. Carabat)

Table 1: Elemental composition of some single crystal nickel superalloys and a typical bond coating (weight %). (Source: Lecture W. Sloof on high temperature material applications)

Alloy	Cr	Co	Mo	Re	W	Al	Ti	Ta	Nb	Hf	Y	Ni
CMSX-2 (first generation)	8	4.6	0.6	-	8	5.6	1	6	-	-	-	66.2
CMSX-6 (first generation)	9.8	5	3	-	-	4.8	5.7	2	-	0.1	-	69.6
Rene N4 (first generation)	9	8	2	-	6	3.7	4.2	4	0.5		-	62.6
CMSX-4 (second generation)	6.5	9	0.6	3	6	5.6	1	6.5	-	0.1		61.7
Rene N5 (second generation)	7	8	2	3	5	6.2	-	7	-	0.2		61.6
CMSX-10 (third generation)	2	3	0.4	6	5	5.7	0.2	8	0.1	0.03		69.57
Bond coating	19	18	-	-	-	21	-	-	-	-	0.2	41.8

As mentioned in the introduction, the TBC is subject to high stresses upon heating and cooling from the thermal expansion mismatch between the coating and the substrate. This is partially compensated by structuring the thermal barrier coating with long and thin grains, allowing some of the stresses to be accommodated. Nevertheless, cracks will still grow, first perpendicular to the surface of the TBC, but when the crack gets close to the interface with the protective Al_2O_3 scale, it can be deflected and start to grow horizontally. When too many cracks have grown in the horizontal direction, this will result in debonding of the TBC and part of it will break off.

To prevent this, a self-healing concept based on $MoSi_2$ particles has been proposed, which is shown in figure 2. If these particles are added to the TBC close to the alumina interface and a crack grows through them, they will oxidize according to:

$$2\ MoSi_2\ (s) + 7\ O_2\ (g) \rightarrow 2\ MoO_3\ (g) + 4\ SiO_2\ (s)$$

In which the volatile MoO_3 escapes and the SiO_2 fills the crack due to the volume expansion compared to the original $MoSi_2$. Furthermore, SiO_2 can react with ZrO_2 to form $ZrSiO_4$ for good adhesion. Small cracks have even been shown to be completely filled with $ZrSiO_4$, according to previous research.

However, Yttria stabilized zirconia is very transparent to oxygen, especially at temperatures used for these coatings. Therefore $MoSi_2$ will even oxidize without a crack being present, creating additional stresses close to the TBC-Al_2O_3 interface due to volume expansion. Therefore, a protective coating for this healing agent is required.

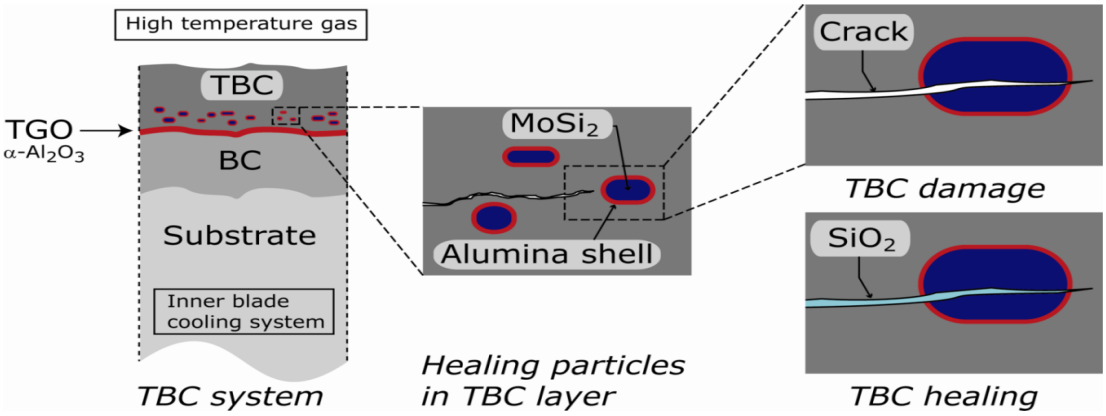

Figure 2:Proposed self-healing mechanism based on coated $MoSi_2$ particles. (Source: Introduction presentation W. Sloof and A. Carabat)

The two main functions of this coating would be to protect the $MoSi_2$ against oxidation when closed and to open when a crack is growing close to the particle, preferably even attracting the crack to grow into the particle. For the first function, it is very important that the coating material forms a closed shell that remains closed at operating temperatures and has a low oxygen diffusivity at these temperatures. For the second function, numerical modeling has shown that interface strength is a critical parameter. A relatively weak interface between $MoSi_2$ and the coating and a stronger interface between the coating and the yttria stabilized zirconia would yield the best results for attracting growing cracks.

Therefore the main requirements for the first function is that the shell is mechanically, thermally and chemically stable in an oxygen-containing environment (P_{O2} between 10 Pa and 10000 Pa). Furthermore, it should have a very low oxygen diffusivity and be thick enough to efficiently block transport of oxygen and other charged species. For a reasonable adhesion on the particle, it is also important that thermal expansion coefficients match and that the crystal structure and lattice parameter of the coating is coherent enough with that of $MoSi_2$.

As can be seen, many properties are influenced by the interfaces of the coating. Therefore it is critical to consider these in more detail. However, these interfaces can be influenced by many factors and require a more detailed investigation. It is therefore proposed to include the interface chemistry and behavior as an important part of the thesis work.

3. Materials

In this chapter, various suitable materials are discussed. For a suitable coating, the first requirement would be that it is stable in the range of room temperature up to 1473K and in the presence of oxygen with a partial pressure somewhere between 10 and 10000 Pa. Although many materials exist that would be able to sustain such a temperature, oxidation is a significant problem. Therefore, common carbides and nitrides (such as SiC, Si_3N_4, TiN etc.) were found to be unsatisfactory for oxidation protection. This also holds for metals, as most metals that are still solid at 1473K have a tendency to oxidize, resulting in most cases in a significant volume expansion. Due to this, only oxides have been considered for further investigation. An overview of the oxides considered, along with some important properties, can be found in table 2, along with yttria stabilized zirconia and $MoSi_2$ data for comparison.

These oxides were selected because they were either common in corrosion protection applications (such as SiO_2, Al_2O_3, Cr_2O_3, TiO_2 and ZnO), were used in other applications as high temperature barriers (Ta_2O_5, HfO_2,MgO) or were considered because they were both stable at high temperature and had a high energy of vacancy formation, indicating a low cation and anion vacancy concentration, indicating slow diffusion of species. The first important properties are of course related to stability of the material, as it needs to be both solid and stable. Therefore melting temperature was presented, along with the Gibbs free energy of formation of the oxide from its parent metal(s) and oxygen gas at 1473K. This free energy is taken from Ellingham diagrams provided by an online tool of the University of Cambridge.

Table 2: An overview of various oxides used at high temperature, along with important properties.

Material	Melting temperature (K)	Gibbs free energy at 1473K (kJ/mol O2)	thermal conductivity (W/m/K)	crystal structure	coefficient of thermal expansion (10^-5 K-1)
Al_2O_3	2345	-801.71	39	corundum	0.8
SiO_2	1873-1998	-617.89	1.4	quartz	0.059
ZnO	2248*	-354.6	21	Wurtzite	0.4
Ta_2O_5	2145	-569.11	Not measured	disputed	0.45
HfO_2	3031	-806.25	1.1	fluorite	0.94
ZrO_2	2988	-821.375	2	fluorite (monoclinic)	1.03
$ZrSiO_4$	2820	-729.3	3.5	silicate (tetragonal)	0.5
Mullite ($Al_6O_9Si_2O_4$)	1923	-585.5	6	silicate (orthorhombic)	0.54
MgO	3125	-893.47	37	rocksalt	1.35
CaO	2886	-968.87	0.3	rocksalt	1.48
Cr_2O_3	2708	-491.69	10.0-33	corundum	0.54-0.75
TiO_2	2116	-679.375	11.7	rutile	0.85
$MgAl_2O_4$	2403	-857.96	15	spinel	0.745

Ta (metal)	3290	-48.7	54	bcc	0.65
ZrO_2 (Yttria stabilized)	2988	-806.25	2	fluorite (cubic)	1.03
$MoSi_2$	2303	-130	70	tetragonal	0.7-0.8

**decomposes at mentioned temperature*

Unfortunately, not all of these oxides were found to be suitable. Cr_2O_3 and ZnO were found to be not stable under these conditions for prolonged time due to slow sublimation of ZnO (becoming noticeable around 1400K and atmospheric oxygen partial pressures) and oxidation of Cr_2O_3 to the gaseous species CrO_3. Furthermore, CaO is quite reactive and can easily dissolve in the zirconia matrix (as it is also used to stabilize zirconia), making it not very suitable as a coating material.

Although unstabilized (and therefore undoped) zirconia is in itself a reasonable oxygen barrier, phase transformations with large volume changes make this material unsuitable to form a protective coating. TiO_2 is very stable, but has a tendency to be reduced at higher temperatures in the presence of a reductant ($MoSi_2$ not being extremely noble could be able to do this), which is not desirable. SiO_2 will also react with the zirconia, as the self-healing mechanism is partially based on this reaction and is therefore also not suitable as coating.

The zirconia lattice of the surrounding material can also accommodate significant amounts of MgO, HfO_2 and Al_2O_3 and these are also sometimes used to stabilize zirconia instead of yttria, but the rate at which these materials are able to diffuse in ZrO_2 is not known and important for further investigation if these materials are to be used. However, MgO has a significantly higher thermal expansion coefficient, indicating that using this material as coating could lead to severe stresses at the $MoSi_2$-MgO interface. Ta metal was considered because of the formation of its protective oxide, but might be problematic due to the significant volume expansion upon oxidation. Its oxide is also interesting, because the crystal structure is not very well defined and consists of two crystalline phases and an amorphous region. In the range between 1250K and 1600K there is a very slow phase transformation to the phase stable at higher temperature, but without a significant volume change.

4. Diffusion and Coating thickness

Another major and important property of the coating is to prevent oxidation. Calculating diffusion in oxidic ceramics is not the easiest task however and due to time limitations, a simpler model based on Ficks diffusion law, coupled with diffusion coefficients found in literature and summarized in table 3, has been used for the ceramics that have not been rejected yet in the previous chapter.

Table 3: Diffusion coefficients at 1473K for the dominant species responsible for oxidation.

Oxide	**D (m^2/s)**
Al_2O_3	5.75E-18
Ta_2O_5	5.21E-18
HfO_2	1.30E-13
$ZrSiO_4$	1.94E-20
Mullite ($Al_6O_9Si_2O_4$)	1.101E-20
$MgAl_2O_4$	1.30E-12

Then using ($\varphi_m{}^{"}$ being flux, D the diffusion coefficient, c the concentration and x distance):

$$\varphi_m{}^{"} = D * \frac{dc}{dx}$$

And assuming the particle to be a perfect sphere with a radius of 10 µm and the problem to be a steady state problem (as the goal is negligible oxidation), this results in the well-known diffusion equation for a sphere in steady state:

$$\Delta c = \frac{\varphi_m}{4 * \pi * D} * (\frac{1}{R_1} - \frac{1}{R_2})$$

Here, Δc is the concentration gradient of oxygen over the coating. It is assumed the concentration of oxygen is exactly 0, as inside, its concentration is so low, it can be neglected. Outside, assuming a partial pressure of roughly 10 kPa, the concentration at the oxide is roughly 0.81 mol/m^3. D is taken from the table above and R_1 is 10 micrometer or 10^{-5} m. To determine ϕ_m, or the maximum allowable mass transport, it is assumed that all other parameters will remain constant and no more than 0.1 wt% of the $MoSi_2$ particle will oxidize over the period of 1 year at 1473K. For a particle of 10 micron, this means over the lifetime, a total of approximately $1.21*10^{-12}$ mole of O atoms should pass through the coating and react. This results in a maximum allowable flux of $3.83*10^{-20}$ mol O/s. Then using the equation for a perfect sphere:

$$R_2 = \frac{1}{\left(\frac{1}{R_1}\right) + \frac{\Delta c * 4 * \pi * D}{\varphi_{m,max}}}$$

Then, calculating the coating thickness: $d_c = R_2 - R_1$. This results in the coating thicknesses presented in table 4. As can be seen, some error is made in the case of mullite and zircon. Due to their low diffusion coefficient, a coating thickness of only 0.5 nm should be enough according to the calculations. This is obviously impossible. However, for the other coatings, an interesting estimate is presented. It is clear that both hafnia and spinel are not very good high temperature oxygen barriers, as the coating has to be very thick at these temperatures (the criterion cannot be attained with these diffusion coefficients, hence the negative value).

Table 4: Calculated required coating thicknesses for the selected oxides.

Oxide	Thickness (nm)
Al2O3	156.7
Ta2O5	141.6
HfO2	-1.003E04
ZrSiO4	0.521
Mullite (Al6O9Si2O4)	0.295
MgAl2O4	-1.0003E04

5. Application methods

Another important aspect of the coating is the method of application. Here, the most interesting application methods will be listed with the main advantages and disadvantages.

Precipitation

The creation of a separate solid phase by exceeding the solubility limit of the solid or liquid it is in. In the case of deposition, this is often bringing two solutions with soluble salts together and in a chemical reaction, an insoluble salt is formed, that then deposits on the desired substrate. Often a subsequent calcination step required. This is a relatively easy method with good mixing and an homogeneous distribution of reactants. However, control over coating thickness and morphology is difficult.

Selective oxidation

Alloying the desired material with the metal precursor to the oxide and selectively oxidize that metal on top of the substrate. Results in a very good control of coating thickness and reasonable control over morphology, but requires alloying of the component and obtaining required thickness might be difficult for protective oxides, as growth speed will decrease significantly with coating thickness (therefore high temperature required). Inhomogeneous coating thickness over the particle might be obtained too, as well as limited surface chemistry control.

Sol-gel

Conversion of dissolved monomeric metal alkoxides or hydroxides into a stable colloid solution, followed by evaporation of solvent and polymerization to form a gel on a substrate. Subsequent firing results in the oxide material that is desired. Advantages are the relatively simple and low temperature processing and good control over structure, morphology and interface chemistry. It also generates a very homogeneous coating and gives slightly more control over coating thickness than precipitation, but it is still limited. Deposition of the gel onto small particles is also something that might prove slightly more difficult.

Chemical Vapor Deposition

The deposition of a thin solid film by well-controlled chemical reactions on the substrate surface by volatile precursors. In the case of particles best performed in a fluidized bed reactor. Main advantages include a good coating with easily controllable thickness and good homogeneity. Many thicknesses can be attained. However, also here a high temperature is required and quite volatile and toxic chemicals are required. Furthermore, some issues with sticking of particles have been mentioned, which is not desired. Control of interface chemistry limited and quite a complex growth process.

Atomic Layer Deposition

The growth of a layer by depositing alternating monolayers of precursor on the substrate and subsequent firing. Again for particles best performed in a fluidized bed. The main advantage is that this method gives a very high quality film with very good control over thickness, composition, structure and morphology. Its main limitation however is the limited coating thickness, as each cycle only adds one monolayer of material. Even though cycles can be performed very rapidly (a few seconds per pulse), a thickness of more than 100-200 nm is probably not very feasible using this method. Interface chemistry is also limited in control.

Thermal Spraying

Spraying liquid material on the particles, either metal or oxide. Main advantage is that it is relatively simple and yields good closed coatings. Main disadvantage is that to spray oxides, extremely high temperatures are needed, often higher than the melting point of the $MoSi_2$ and when spraying precursor metals, selective oxidation is still needed. Poor control of interface chemistry, but reasonable control of thickness and a quite homogeneous coating.

Dry powder coating techniques

Usually involves the use of temperature and pressure in the form of milling balls to mill smaller particles of the oxide on a larger substrate particle. This is a relatively simple method, but gives poor control over homogeneity, interface chemistry, thickness, structure and morphology. Furthermore, the application method damages the material and the coating and introduces stresses and it is difficult to obtain a closed shell.

Electroless deposition combined with selective oxidation

The use of a metallic precursor and an organic reductant (for example formaldehyde) to precipitate a metallic layer on top of the particle and subsequently selectively oxidizing that metal to form an oxide coating with a small metallic layer beneath. Main advantages are again a relatively simple process, easy control of thickness, closed shell formation and some control over interface chemistry, composition and morphology. Another benefit might be an additional interface if some metal is left. This can both act as a barrier to oxygen diffusion and a reserve of oxide forming material if the metal is not very noble (which gives some additional oxide growth without oxidation of the $MoSi_2$). Disadvantages are the same as for selective oxidation and that additional oxidation during lifetime might increase local volume, introducing stresses. Furthermore, the metal should be solid at 1473K.

6. Selection

Previous information shows that only some oxides are suitable for use as a high temperature barrier coating. Of these, Al_2O_3, Ta_2O_5, zircon and mullite seem to be the most interesting due to their stability and difficult diffusion at elevated temperatures. For suggested routes, precipitation of alumina and mullite has already been investigated to a certain extend and is therefore not included. Dry powder coating and thermal spraying do not seem to be very appropriate methods for this application due to often poor protective coating properties and difficulty of handling liquid oxides respectively. CVD was also advised against due to some sticking problems and general complexity.

For zircon and mullite, electroless deposition is probably a process too complex, as these are formed by two different metallic precursors and therefore both deposition and oxidation will become very difficult to achieve stoichiometrically. Therefore for these materials, selective oxidation is also advised against. A sol-gel method would probably work very well for these oxides, as good stoichiometry and crystal structure could be easily achieved with the right precursors. If a better diffusion calculation finds that layer thickness can remain very thin, ALD might work in the case of these combined oxides too.

For Al_2O_3 formation, selective oxidation, ALD (combined with some CVD-like characteristics) and sol-gel are quite interesting methods. Electroless deposition might be possible, but care must be taken to oxidize all Al during the subsequent oxidation step, as it becomes liquid around 900K, which is way below operating temperatures. Therefore selective oxidation with alloying seems to be better. ALD might be interesting, but the required thickness of alumina seems to be very high, making ALD quite difficult.

For Ta_2O_5, electroless deposition will work, but care must be taken that the volume expansion of oxidized tantalum during operation of the full thermal barrier coating is not too significant. Ta_2O_5 can also be prepared by sol-gel methods and deposited by ALD, although again in the latter case, thickness might be an issue again. Selective oxidation might be possible, but is difficult, as the cation has relatively low mobility.

As these options are still many, a discussion on the best way to proceed is important. In my opinion it is worthwhile to look into zircon and mullite further, as literature suggests they seem to be very suitable corrosion protection oxides at high temperature. Alumina is also a very interesting oxide, as it is one of the most important oxides for many applications, including high temperature corrosion protection. Utilizing selective oxidation, ALD (if feasible) and sol-gel can lead to interesting insights regarding different morphology and interface chemistry of the different coating techniques. Furthermore, the coefficient of thermal expansion matches very well with the substrate and it is a relatively cheap material.

For tantalum oxide: according to literature, the difference in protective properties between Ta_2O_5 and Al_2O_3 are not very significant and together with the phase transformation in the operating temperature and being significantly more scarce and expensive, it is recommended to not include this oxide in further research.

It is also still very important to do some more extensive diffusion calculations and research and understand the interfaces present in the overall system and how they influence both transport and fracture behavior.

Appendix II: Proposal MSc thesis Mark Meijerink

Title: Synthesis of high-temperature oxidation-resistant coatings on $MoSi_2$ healing particles for use in self-healing thermal barrier coatings.

Introduction

With rising energy prices and increasing scarcity of inexpensive energy, the demand for increasingly efficient gas turbines and other high-temperature turbines is increasing. The best option to increase efficiency is to increase operating temperature (1). However, current turbines are already operating far above the limit of the used nickel superalloys. To prevent breakdown of the structural parts, (~0.5 mm) thermal barrier coatings (TBC) in combination with internal gas cooling are applied to prevent overheating and allow the turbine blades to endure these extreme environments (2).

However, due to thermal expansion coefficient mismatch between the TBC, usually made of yttria-stabilized zirconia (7 wt% Y_2O_3–ZrO_2, YSZ) and the nickel superalloys, application of these coatings is difficult and significant mismatch stresses arise during heating and cooling of the engine. Even though a (~250 µm) bond coat (BC) with a (0.6-3.0 µm) thermally grown oxide (TGO) for oxidation protection is applied, this mismatch results in unavoidable crack growth and spallation damage in the TBC and frequent replacement of the coating is therefore required (2). However, the work of Zwaag et al. (3) used a different approach to repair damage autonomously, based on the inclusion of sacrifical $MoSi_2$ healing particles that oxidize, expand and fill the crack when it is close to the particle. However, as YSZ is very transparent to oxygen at operating temperatures (1250-1500K depending on engine and location in the TBC (2)), significant premature oxidation of $MoSi_2$ is present and a coating that protects against oxidation is required. The proposed system including coated healing particles is shown in figure 1.

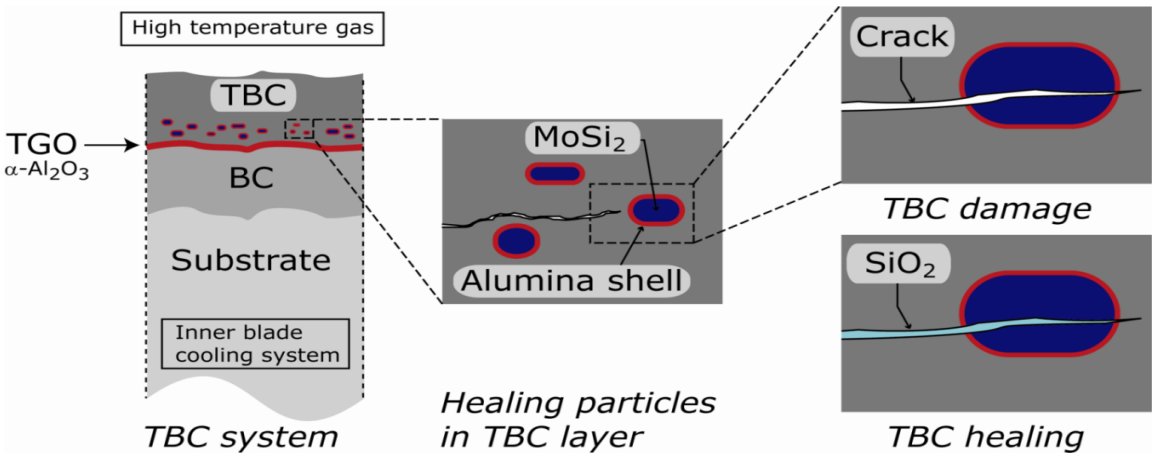

Although many different protective materials exist, α-alumina (α-Al_2O_3), zircon ($ZrSiO_4$) and mullite ($Al_6Si_2O_{13}$) were found to be exceptionally suitable for this application (4). However, application of coatings on $MoSi_2$ has rarely been investigated, mainly due to the excellent oxidation resistance of the bulk material at high temperature, resulting from the formation of a thick homogeneous SiO_2 layer. Some research has for example been performed on mullite coatings produced by alloying the $MoSi_2$ with some aluminium and subsequent selective oxidation (5), but as most $MoSi_2$ applications

are bulk material applications, coating of molybdenum disilicide particles has not been investigated yet, except for work performed by A. Carabat et al. on sol-gel coating with $AlCl_3$ (not published yet) (6).

In the case of particles with a size in the range of 5-20 µm, formation of a coating by oxidation of the $MoSi_2$ would not be feasible, as a significant portion of the material will then be oxidized even before incorporation in the TBC system. Therefore, a protective coating has to be applied beforehand, preferably by methods that also add the metallic components during the procedure (or methods that utilize specially alloyed particles with metallic incorporations that already account for controlled oxidation to form a coating). Methods that were found to be most promising during a study of the available literature were using a sol-gel application procedure and atomic layer deposition (ALD).

Therefore, the focus of this project is on the synthesis and characterization of a protective Al_2O_3 coating on $MoSi_2$ particles by sol-gel methods and atomic layer deposition. As the main aim of these coatings is prevention of oxidation of the substrate, special attention will be given to the influence of coating thickness and coating microstructure (especially defects present) on oxidation behaviour. Furthermore, as crack growth through the healing particle is vital for the self-healing mechanism, the influence of thickness, microstructure and interface properties on crack growth in the TBC system will also be investigated. Finally, if time allows, the use zircon as coating material will also be investigated, because diffusion in zircon is reported to be significantly slower than in alumina (7), allowing for thinner coatings. Also, literature suggests that amorphous zircon is stable at the desired operating temperature (8), resulting in far fewer defects that can act as a fast pathway for diffusion.

Research question

During this thesis project, the aim is to answer the following research question:

How can an $Al_2O_3/ZrSiO_4$ coating be created around $MoSi_2$ healing particles for use in self-healing thermal barrier coatings that prevents premature high temperature oxidation and attracts nearby cracks?

To help answer this question, the following sub-questions are to be answered:
-What thickness should such a protective coating have to limit diffusion to acceptable levels?
-How do microstructure and defects influence diffusion behaviour in the coating?
-How do microstructure, defects and thickness affect crack attraction and crack growth into the particle?
-How can ALD and sol-gel methods influence microstructure, amount and type of defects and thickness and what are the differences between these methods?
-How does thermal treatment affect microstructure, amount and type of defects and thickness?

Approach

To answer these questions, an approach based on literature study, experimental work and limited diffusion modelling is required. It is important to develop a model for diffusion in these coatings to be able to quantify diffusion through the coatings by different pathways and to obtain information on required thickness. As mentioned before, experimental work will first focus on coating particles with alumina and an investigation of coating properties.

As mentioned before, no reports in literature exist for coating of $MoSi_2$ particles, but alumina has been used as a coating for a variety of other substrates (9). Examples include stainless steel (10), magnetic particles (11) and SiC particles (12) (13) (14). For this method, it is paramount to first succeed in coating particles. The work of Kim et al. (14) on coating with dispersed boehmite gels or that of Yang and Shih (13) using aluminium sec-butoxide produced boehmite coatings on SiC particles that after annealing transformed into α-Al_2O_3 coatings. Due to very similar surfaces (both SiC and $MoSi_2$ have a thin SiO_2 layer at their surface) and particle sizes not too dissimilar from the $MoSi_2$ particles to be coated, these methods are expected to yield similar coatings on the healing particles and will therefore be the start of the sol-gel investigation.

As many parameters play an important role in sol-gel procedures, not all can be investigated and therefore it is proposed to optimize coating synthesis procedures by:

- Precursor concentration/solid loading
- Time of reaction
- Thermal treatment procedures (drying time and temperature, annealing time and temperature and the influence of an intermediate chemical water drying step)
- Particle surface charge in combination with precursor charge

In the case of ALD, alumina is one of the most common materials for coating particles (15) and the most frequently used precursor is trimethylaluminium ($Al(CH_3)_3$ or TMA) (15). Different oxygen containing precursors exist, but the most common one is H_2O. Many other oxygen precursors exist, but water is by far the most used (15). The main challenge for ALD however is producing the required thickness of the coating, as using the TMA/H_2O system usually yields between 1 and 1.5 Å al Al_2O_3 per cycle (16)and due to long residence times in the required fluidized bed reactor and large surface areas to coat, such a cycle often takes more than 10 minutes to finish.

A way around this problem is the approach used by García-Triñanes et al. (17) to use an ALD/CVD system to increase growth per cycle, while still working in a linear regime for optimal coating thickness control. However, this approach was tailored to produce porous coatings, which is undesired in the case of protective coatings. Another option might be to combine this approach with using the TMA/Aluminium isopropoxide ($Al(O\text{-}CH_2\text{-}(CH_3)_2)_3$) used by Ritala et al. (18) to deposit more alumina per cycle depending on the reaction rate of TMA with the alkoxide compared to water. In normal ALD growth per cycle of this mechanism is however in the same range as the TMA/H_2O system.

Characterization of the particles is a very important part of the research and to understand the various properties of the material, analysis could be done with the following techniques:

- Scanning Electron Microscopy (SEM) for morphology and thickness of the coating.
- X-ray diffraction (XRD) for analysis of the various crystalline phases present.
- N_2 physisorption (or another suitable physisorption technique) for particle surface area and porosity.
- X-ray photoelectron spectroscopy (XPS) for coating composition and chemical bonding.
- Thermogravimetric analysis (TGA) for high temperature stability investigation and for investigation of suitable annealing profiles (possibly augmented by differential scanning calorimetry (DSC)).

- Fracture tests on particles incorporated in YSZ by spark plasma sintering (SPS) to obtain information about crack growth behaviour.

Other analysis techniques such as ICP-OES to obtain more information on the overall composition and the Si/Al ratio (how much healing potential is present for a certain mass), nano-indentation, transmission electron microscopy (TEM) for interface layers and other techniques might also be considered.

Planning (starting date: 4 august 2014)

Month	**Activities**
August	-Initial literature survey -Writing thesis proposal
September	-Literature study + report writing -Diffusion model development -Start with sol-gel trial experiments alumina -Alumina sol-gel coating experiments and characterization (includes fracture tests)
October	-Literature study + report writing -Safety training for working with TMA (start of the month) -First alumina ALD experiments and characterization -Have a working sol-gel procedure for alumina (end of the month)
November	-Literature study + report writing -Synthesis of different thickness coatings of alumina by sol-gel -Synthesis of high thickness and low porosity ALD alumina coatings -Characterization of coatings -Progress report and discussion
December	-Literature study -Alumina ALD and sol-gel coating synthesis and characterization
January	-Literature study -Alumina ALD and sol-gel coating synthesis and characterization -Annealing and drying of samples with different procedures and characterization -Midterm presentation
February	-Literature study -Continue on sol-gel and ALD parameter optimization -Trial experiments with zircon coating synthesis and characterization
March	-Literature study -Continue on sol-gel and ALD parameter optimization -Continue on zircon and have working procedures at the end of the month
April	-Literature study -Continue on sol-gel and ALD parameter optimization -Continue on zircon with amorphous/crystalline and thermal treatment
May	-Literature study -Continue on sol-gel and ALD parameter optimization -Continue on zircon
June	-Literature study -Finalize experiments -Full-time report writing
July	-Finalize reports -Final presentation(s)

Bibliography

1. *Overview on advanced thermal barrier coatings.* **Robert Vaßen, Maria Ophelia Jarligo, Tanja Steinke, Daniel Emil Mack, Detlev Stöver.** 2010, Surface & Coatings Technology, pp. 938-942.
2. *Development of coatings for protection in specific high temperature environments.* **M. Schütze, M. Malessa, V. Rohr, T. Weber.** 2006, Surface & Coatings Technology, pp. 3872–3879.
3. *Self-healing behaviour in man-made engineering materials: bioinspired but taking into account their intrinsic character.* **S van der Zwaag, N.H van Dijk, H.M Jonkers, S.D Mookhoek, W.G Sloof.** 2009, Philosophical transactions of the Royal Society, pp. 1689-1704.
4. **Meijerink, M.J.** Protective coatings for MoSi2 for self-healing Thermal Barrier Coatings: Materials and application routes. June 2014.
5. *The mullite coatings on heaters made of molybdenum disilicide.* **P.S. Kisly, V.Y. Kodash.** 1989, Ceramics International, pp. 189-191.
6. **W.G. Sloof, A.L. Carabat.** Encapsulation of MoSi2 self-healing particles for high temperature applications. Delft : s.n., 2014.
7. *Oxygen diffusion in zircon.* **E.B. Watson, D.J. Cherniak.** 1997, Earth and Planetary Science L.etters, pp. 527-544.
8. *Effect of matrices on the phase transformation of ZrOz in the ZrO2-MOx (MOx = SiOa, AIzO3) system.* **Y. Kanno, T. Suzuki.** 1989, JOURNAL OF MATERIALS SCIENCE LETTERS, pp. 41-43.
9. *Preparation of alumina films by the sol-gel method.* **Y. Kobayashi, T. Ishizaka, Y. Kurokawa.** 2005, Journal of Materials Science, pp. 263-283.
10. *Alumina coating of austenitic stainless steel by sol-gel process.* **K. Miyazawa, T. Sakuma.** 1991, Engineering Fracture Mechanics, pp. 967-973.
11. *Fe3O4@Al2O3 magnetic core–shell microspheres for rapid and highly specific capture of phosphopeptides with mass spectrometry analysis.* **Li, Y.** 2007, Journal of chromatography, pp. 57-71.
12. *Investigation of thermal oxidation of Al2O3-coated SiC powder.* **A. Dey, N. Kayal, A.R. Molla, O. Chakrabarti.** 2014, Thermochimica Acta, pp. 25-31.
13. *Effect of acid on the coating of boehmite onto silicon carbide particles in aqueous suspensions.* **C. Yang, W. Shih.** 1999, Journal of the American Ceramic Society, pp. 436-440.
14. *Sol-gel alumina environmental barrier coatings for SiC grit.* **H. Kim, M. Chen, Q. Yang, T. Troczynski.** 2006, Materials Science and Engineering, pp. 150-154.
15. *Crystallinity of inorganic films grown by atomic layer deposition: Overview and general trends.* **V. Miikkulainen, M. Leskelä, M. Ritala, R. L. Puurunen.** 2013, Journal of Applied Physics.
16. *Atomic Layer Deposition: An Overview.* **George, S.M.** 2010, Chem. Rev., pp. 111-131.
17. **García-Triñanes, P.** Enhancing the activation of silicon carbide particles with gas-phase coating of aluminium oxide. 2014.
18. *Atomic Layer Deposition of Oxide Thin Films with Metal Alkoxides as oxygen sources.* **M. Ritala, K. Kukli,A.i Rahtu,P.i I. Raisanen, M. Leskela,T. Sajavaara, J. Keinonen.** 2000, Science.

Appendix III: Matlab code used for the diffusion model

```
function y = Scaledeveloptest(x);
%Parameters to be adjusted
T=1273;                          %Temperature of the system in Kelvin
P0=0.2;                         %Partial pressure of oxygen in the gas phase
                                    in bar
t=24*3600;          %Time in seconds the simulation should cover (3600s=1h,
                              86400s=1 day 31536000s=1 year)
deltt=t;            %number of steps to solve for
d_Al_ini=500;       %Thickness of the initial alumina layer in nanometer
d_Mul_ini=5;        %Thickness of the initial mullite layer in nanometer
d_Si_ini=1;         %Thickness of the initial silica layer in nanometer
G_Al=50;            %Grain size in alumina in nm (for GB diffusion)

%Defined parameters (for diffusion coefficients: first letter(s) is species
%diffusing, second is phase diffusion is happening in.
R=8.3145;           %Gas constant in J/K*mol
M_Al=101.96;        %Molecular weight Al2O3 in g/mol
Rho_Al=3.98*10^6;   %Density Al2O3 in g/m3
M_Mul=426.06;       %Molecular weight mullite in g/mol
Rho_Mul=3.22*10^6;  %Density mullite in g/m3
M_Si=60.08;         %Molecular weight amorphous SiO2 in g/mol
Rho_Si=2.196*10^6;  %Density amorphous SiO2 in g/m3

D_O_Al=(2/(G_Al*10^-9))*1.8*10^-10*exp(-375000/(R*T));
%Total oxygen diffusion coefficient in alumina (including GB diffusion)
C0_O_Al=3*Rho_Al/M_Al;                                              %Bulk
concentration O in Al2O3 based on theoretical density and molecular weight
Al2O3 (mol/m3)
D_O_Mul=(2*1*10^-9/(G_Al*10^-9))*1.32*10^-(6-4)*exp(-397000/(R*T));
%Total oxygen diffusion coefficient in mullite (including GB diffusion)
C0_O_Mul=13*Rho_Mul/M_Mul;                                          %Bulk
concentration O in mullite based on theoretical density and molecular
weight Al6Si2O13 (mol/m3)
D_Al_Mul=(2*1*10^-9/(G_Al*10^-9))*9.2*10^-(3-4)*exp(-517000/(R*T));
%Total aluminium diffusion coefficient in mullite (including GB diffusion)
C0_Al_Mul=6*Rho_Mul/M_Mul;                                          %Bulk
concentration Al in mullite based on theoretical density and molecular
weight Al6Si2O13 (mol/m3)
D_O_Si=4.4*10^-15*exp(-121000/(R*T));
%Total oxygen diffusion coefficient in amorphous silicon
C0_O_Si=2*Rho_Si/M_Si;                                              %Bulk
concentration O in SiO2 based on density and molecular weight amorphous
SiO2 (mol/m3)

Delt_Mu_Mulform=((-6888.12+0.26597*T)-3*(-1675.7+0.0592*T)-2*(-
910.7+0.04146*T))/(6*R*T); %Chemical potential per atom Al over mullite
barrier corrected for RT
P3=exp(1000*(-910.7+0.18*T)/(R*T));
%Equilibrium partial pressure of oxygen at Si-SiO2 interface in bar d(:,3)+

k_Al=D_O_Al*C0_O_Al/(2*d_Al_ini*10^-9);
k_Mul=D_O_Mul*C0_O_Mul/(2*d_Mul_ini*10^-9);
k_Si=D_O_Si*C0_O_Si/(2*d_Si_ini*10^-9);

tspan=linspace(0,t,deltt).';
d_ini1=d_Al_ini*10^-9;
d_ini2=d_Mul_ini*10^-9;
d_ini3=d_Si_ini*10^-9;
```

```
d0=[d_ini1, d_ini2, d_ini3];
Vdata=[D_O_Al, C0_O_Al, M_Al, Rho_Al, D_O_Mul, C0_O_Mul, M_Mul, Rho_Mul,
D_Al_Mul, C0_Al_Mul, D_O_Si, C0_O_Si, M_Si, Rho_Si, P0, P3,
Delt_Mu_Mulform];
ode = @(t,d) Scalediftest(t,d,Vdata);
[t,d] = ode45(ode, tspan, d0);

deq=d(:,3)+d(:,2)*Rho_Mul/M_Mul*2*M_Si/Rho_Si;
end

function dddt=Scalediftest(t,d,Vdata);
D_O_Al=Vdata(1);
C0_O_Al=Vdata(2);
M_Al=Vdata(3);
Rho_Al=Vdata(4);

D_O_Mul=Vdata(5);
C0_O_Mul=Vdata(6);
M_Mul=Vdata(7);
Rho_Mul=Vdata(8);
D_Al_Mul=Vdata(9);
C0_Al_Mul=Vdata(10);

D_O_Si=Vdata(11);
C0_O_Si=Vdata(12);
M_Si=Vdata(13);
Rho_Si=Vdata(14);

P0=Vdata(15);
P3=Vdata(16);
Delt_Mu_Mulform=Vdata(17);

k_Al=D_O_Al*C0_O_Al/(2*d(1));                          %kinetic factor for
Al combining all relevant parameters, for abbreviation purposes
k_Mul=D_O_Mul*C0_O_Mul/(2*d(2));                       %kinetic factor for
Mul combining all relevant parameters, for abbreviation purposes
k_Si=D_O_Si*C0_O_Si/(2*d(3));                          %kinetic factor for
Si combining all relevant parameters, for abbreviation purposes

P2=(P0^((1/(k_Mul/k_Al+1))/((k_Si/k_Mul)+1-
((k_Mul/k_Al)/((k_Mul/k_Al)+1))))*P3^((k_Si/k_Mul)/((k_Si/k_Mul)+1-
((k_Mul/k_Al)/((k_Mul/k_Al)+1)))));    %Calculation O2 partial pressure at
mullite-SiO2 interface with linear profile
P1=(P0*P2^(k_Mul/k_Al))^(1/(k_Mul/k_Al+1));
%Calculation O2 partial pressure at Al2O3-mullite interface with linear
profile
J_O_Al=-k_Al*log(P1/P0);
%Calculation O flux in Al layer
J_Al_Mul=-(D_Al_Mul*C0_Al_Mul/(d(2)))*Delt_Mu_Mulform*1000;
%Calculation Al flux through mullite layer
J_O_Si=-k_Si*log(P3/P2);
%Calculation O flux through Si layer

if ((3/2)*J_O_Al)>=J_Al_Mul;                                                %To
ensure that SiO2 layer does not obtain a negative thickness if aluminium
diffusion through mullite becomes too large.
    dddt_1=-J_Al_Mul*M_Al/(2*Rho_Al);
    dddt_2=J_Al_Mul*M_Mul/(6*Rho_Mul);
    dddt_3=J_O_Si*M_Si/(2*Rho_Si)-J_Al_Mul*M_Si/(3*Rho_Si);
else
```

```
    dddt_1=-J_O_Al*3*M_Al/(2*Rho_Al);
    dddt_2=J_O_Al*M_Mul/(4*Rho_Mul);
    dddt_3=0;
end
dddt=[dddt_1; dddt_2; dddt_3];
end
```

Appendix IV: Required coating thickness and amount of coating

One of the more important aspects of coated healing particles is the volume of these particles that can be utilized for healing. The thinner the coating and the smaller the surface area that has to be covered, the smaller the volume fraction of coating. This results in a larger volume fraction being healing material that can be used to restore the material.

Therefore, to minimize the presence of inert coating material, total surface area and coating thickness should be reduced as much as possible. As coating thickness is determined by lifetime requirements and material, both of which are fixed, it is important to reduce the particle surface area as much as possible. This importance is shown in the two figures below, one of which calculates the volume fraction of alumina present in the system as function of the total surface area to be covered as if the surface is a completely flat surface for different relevant coating thicknesses. This results in the first equation to calculate total alumina volume fraction. The second figure calculates the alumina volume fraction by assuming perfectly spherical particles of uniform size, resulting in the second equation. Also indicated in both graphs are the theoretical minimum surface area of particles with a volume average diameter of 18 µm (the starting material) and the surface area as measured by N_2 physisorption.

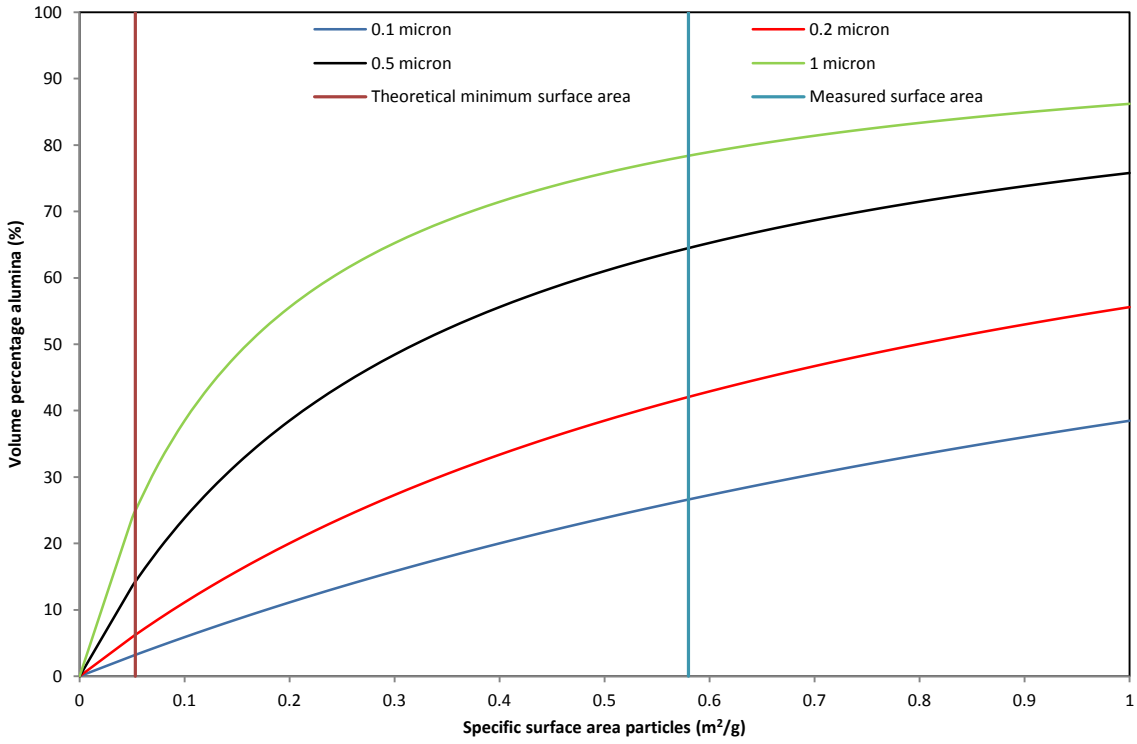

$$V_{Al} = \frac{S_{MoSi2} * \delta_{Al}}{S_{MoSi2} * \delta_{Al} + (\frac{1}{\rho_{MoSi2}})} * 100\%$$

In which V_{Al} is the volume percentage of alumina present in the system in %, S_{MoSi2} the specific surface area of the $MoSi_2$ particles in m^2/g $MoSi_2$, δ_{Al} the coating thickness of the alumina in m and ρ_{MoSi2} the density of $MoSi_2$ in g/m^3.

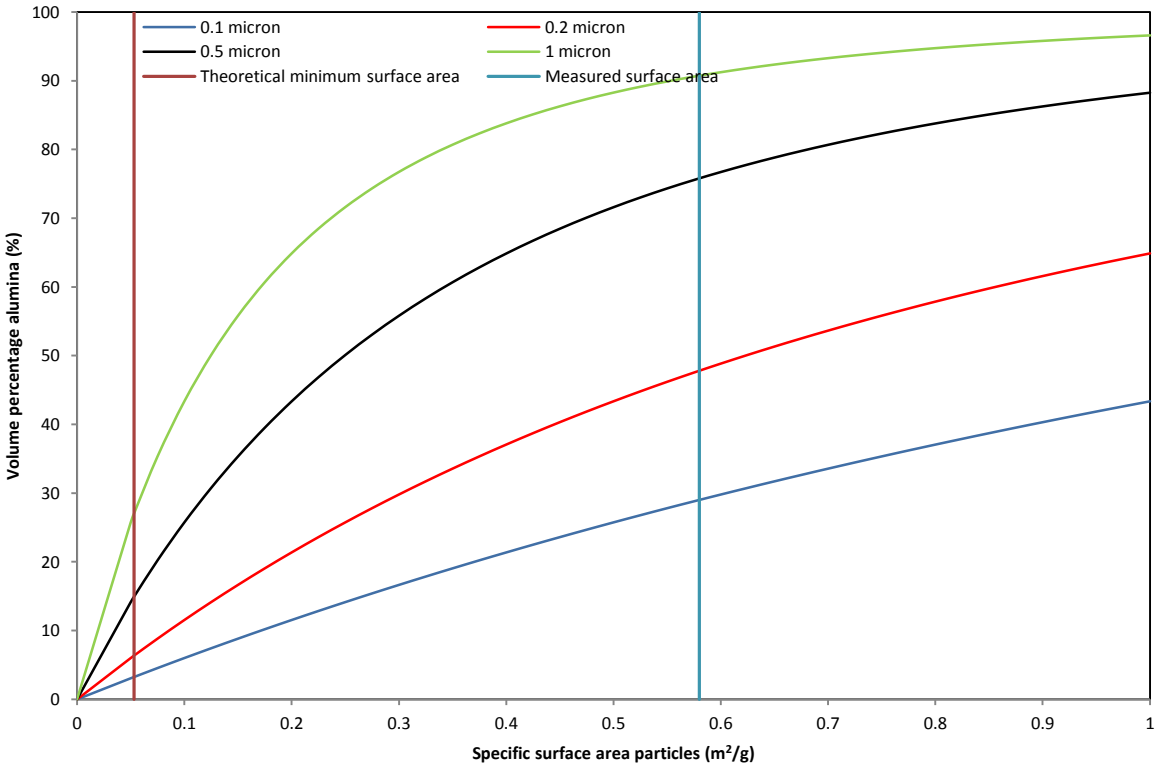

$$V_{Al} = (1 - \frac{(\frac{6}{S_{MoSi2} * \rho_{MoSi2}})^3}{(\frac{6}{S_{MoSi2} * \rho_{MoSi2}} + \delta_{Al})^3}) * 100\%$$

In which V_{Al} is the volume percentage of alumina present in the system in %, S_{MoSi2} the specific surface area of the $MoSi_2$ particles in m^2/g $MoSi_2$, δ_{Al} the coating thickness of the alumina in m and ρ_{MoSi2} the density of $MoSi_2$ in g/m^3.

Both of these calculations clearly show the need for appropriate control of total surface area, as even a coating of 0.1 micron would result in a volume fraction close to 25 volume % alumina with both calculations, even though the particles have an average size of 18 micron. For thicker coatings, the volume percentage increases rapidly, which in turn means that the amount of healing particles needs to be increased significantly to obtain the same healing potential.

It is also shown that these particles have a significantly higher specific surface area than would be expected based on the average particle size. This indicates either a large polydispersity, particles that are largely nonspherical or a combination of both. If a high size polydispersity is present, surface area might be significantly decreased by removal of smaller particles, which contribute most to the total surface area. As the most ideal particle size for healing purposes was determined to be somewhere between 25 and 30 micron, this removal of small particles would not be a problem for the self-healing system.

Appendix V: Principles characterization methods used

This appendix will introduce the characterization methods used in this thesis and the main principles involved.

Wind sifting

Wind sifting, also often called zig-zag air classification, is a process in which particles are separated based on their falling behavior in an upwards air flow. This process is schematically shown in the figure below (Rosenbrand 1986). The classifier works by introducing powder in the middle of a zig-zag channel (hence the name zig-zag classification) and introducing a gas flow at the bottom. As the powder falls from one part of the channel into the other, it is mixed with the turbulent stream of gas and aerodynamically light particles disperse in the gas flow and mostly end up in the light fraction at the top of the classifier. The heavier particles continue falling to the bottom and end up in the heavy fraction. This essentially results in a countercurrent flow of gas with lighter particles and heavy particles, with mixing at each change of direction.

Due to the many channels present, particles are separated very accurately depending on their hydrodynamic diameter, which is mainly dependent on the surface area and weight of the particle. Therefore the density, porosity and shape of the particle are very important in determining which particles end up in the light or heavy fraction. In the system used at TU delft, the setup has been modified slightly, with the channels mounted on a rotating shaft and the centrifugal force replacing gravity for the heavier particles. This possibly significantly higher force allows significantly smaller particles to be separated, with a lower limit of approximately 1-2 µm depending on the material and other powder properties. By regulating centrifugal force (by changing the rotation speed) and the gas velocity, particles can be separated in a very narrow size range.

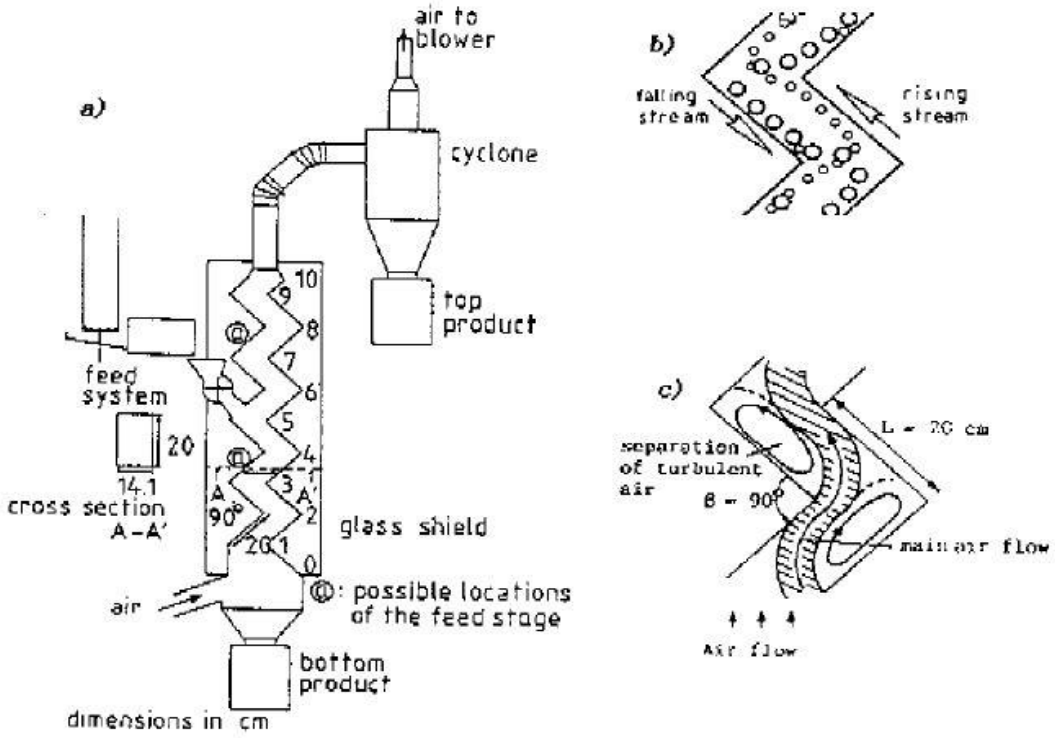

Scanning Electron Microscopy (SEM) and Energy Dispersive x-ray Spectroscopy (EDS)

A scanning electron microscope (SEM) produces images of a sample by scanning the surface with high energy electrons. These electrons interact with the material and produce many different signals, as illustrated in the image below (centre). The main signals are backscattered electrons (BES), Secondary Electrons (SEI) and characteristic X-rays.

Backscatter electrons are electrons that are reflected which can subsequently be detected by an appropriate detector. As scattering is more likely when sample electron density is higher, solids with heavier elements (higher electron density) generally scatter more electrons. Therefore these materials often appear brighter on a BES image, due to the higher intensity of electrons detected from that area. If elements and phases present in the sample are known, this allows for easy distinction between different phases in a SEM.

Secondary electrons on the other hand are electrons expelled from the sample by the primary electrons. These electrons have low energy and are therefore have a short mean free path in a solid material (with a maximum of approximately 10 nm for most materials). Due to this short mean free path, constructing an image with SEI allows for high spatial resolution of the surface of a sample.

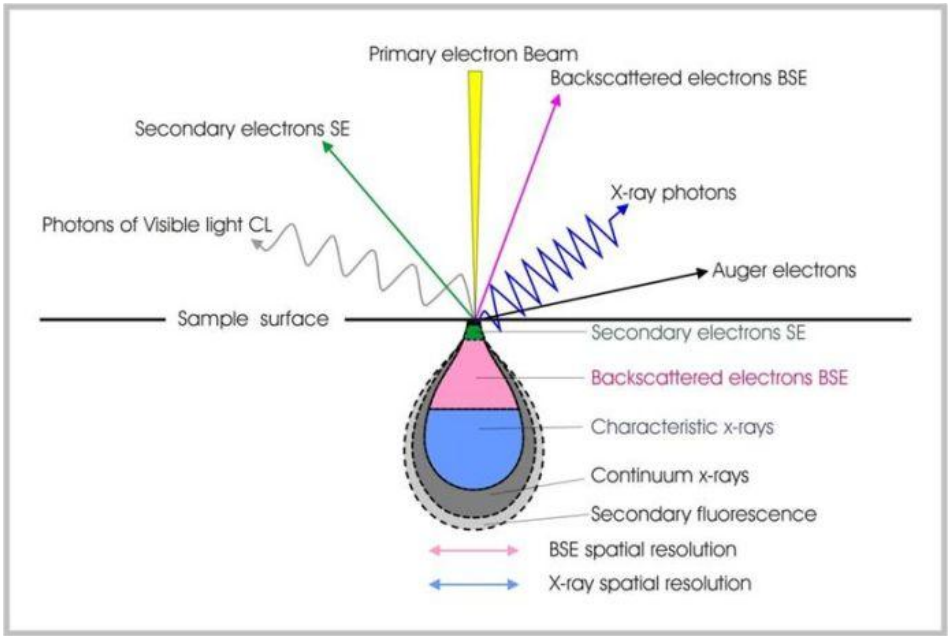

The third important signal, the characteristic x-rays, originate from primary electrons removing another electron from some of the inner orbitals. One of the electrons from a shell above that will subsequently fall back into this orbital of lower energy, releasing the excess energy as a characteristic x-ray. As these x-rays are element specific, these can be used to locally identify elements present in each phase.

As these characteristic x-rays can be formed at any depth in the sample at which the primary beam still has sufficient energy to remove an electron from the respective core shell and this penetration depth is known for most acceleration voltages, this effect can be utilized to calculate coating thickness. Assuming that the material densities and compositions are known, appropriate iterative procedures can be used to calculate layer thickness, which is described in the article of Goldstein et al (Goldstein, Choi et al. 1993).

X-ray Diffraction (XRD)

X-ray diffraction is capable of measuring the electron densities of a material and thereby determining the crystal structure(s) present in the sample under investigation. XRD is the scattering of monochromatic X-rays by interactions with electrons. As electron density in a crystalline solid is repetitive in certain directions due to the repetition of the atoms and wavelengths of X-rays are in the same order of magnitude as the atomic distances in a crystalline lattice, interference between the photons and the solid occurs and regular scattering can take place.

When these scattered waves are not in phase, there is destructive interference, which means the photons extinguish each other when they are not in phase and no X-rays can be detected at that angle. However, when they are in phase, there is constructive interference and the X-rays can be detected. This can be described with Braggs law:

$$n*\lambda = 2*d*\sin\theta$$

In which n is an integer, λ is the wavelength of the incident X-rays, d is the distance between the atoms in the lattice and θ is the angle of incidence and diffraction. A schematic overview can be seen in the figure below (Moulijn, van Leeuwen et al. 1993).

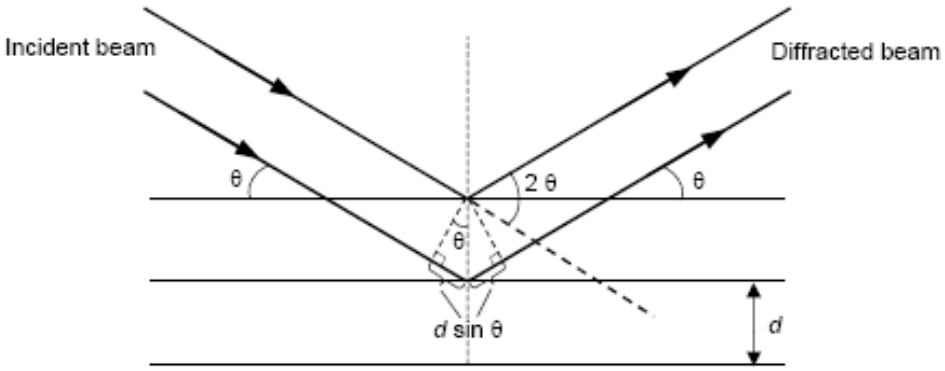

For small particles, the crystal structure is only regular for relatively short distances, resulting in peak broadening due to uncertainty. Due to this effect, particle or grain size can be estimated using the Scherrer equation:

$$D = \frac{K * \lambda}{b * \cos\theta}$$

In which D is the average crystal diameter in nanometers, K is a constant depending on the crystalline shape, λ is the wavelength of the radiation used in nm, b is the diffraction broadening, measured as the full width of the peak at half the maximum height and θ is again the diffraction angle of the peak under consideration. However, significant stresses in the material on a small scale can also cause atomic distances to change slightly, also resulting in peak broadening. Therefore, the presence of microstresses should be verified and taken into account.

Due to macroscopic stresses in a certain direction, atomic distances can also change, but in a regular way, resulting in a peak shift. This peak shift is dependent on the magnitude of the stress and can therefore be used to calculate the macroscopic stresses being present.

N_2 physisorption

N_2 Physisorption is a method to study some of the physical properties of the sample. This characterization technique uses nitrogen as an adsorbate and is carried out at exactly the boiling point of liquid nitrogen, which is 77.3 K. After weighing and degassing the sample, it is brought into a high vacuum and cooled to the required temperature. Then small and known volumes of gas are introduced, while simultaneously measuring the pressure. After each addition of gas, part of the adsorbate will be adsorbed on the sample. When equilibrium is reached in between the additions, indicated by an absence of change in N_2 pressure with time, the total amount of nitrogen adsorbed on the sample can be calculated from the pressure change. This yields the adsorption isotherm.

After the final pressure has been reached, the pressure is slowly reduced by taking away small volumes of gas, which is the desorption part. Depending on the material, the adsorption and desorption curve can be the same or very different. The difference in these curves is mostly caused by mesoporosity, originating from capillary condensation effects inside these pores.

The physical interpretation of the isotherm is that as the nitrogen pressure increases, a layer of nitrogen molecules gets deposited on the surface, due to weak, physical attractive interactions between the N_2 and the surface of the material. If more nitrogen becomes available, subsequent layers start to form. Because the attractive forces are stronger in the pores as more surface is available and also closer, multilayers start to form earlier inside the smallest pores. Therefore, the micropores will be completely filled with nitrogen first and at higher pressures, also the meso- and macropores will be filled. Due to this effect, that is called pore condensation, the specific surface area of the total sample, the pore size and pore size distribution can be calculated from the isotherm.

For calculating the specific surface area of a sample, the BET method is used. This is a modification of the Langmuir theory developed by Brunauer, Emmett and Teller that takes the simultaneous formation of monolayers and multilayers into account. For the pore size and volume distribution, the t-method can be used.

X-ray Photoelectron Spectroscopy (XPS)

In X-ray Photoelectron spectroscopy (XPS), a sample surface is irradiated with X-rays, which by the photoelectric effect subsequently emits electrons. The different binding energies for each element causes these photoelectrons to have different energies depending on the x-ray source used, the element from which the electrons originate and the binding state of the element.

Therefore this technique can be used to analyze the top 10 nm of a surface for elemental composition and with a detector with appropriate accuracy, also the chemical and electronic environment of each element, yielding valuable information regarding the surface of the material under investigation.

Laser diffraction

Laser diffraction is a technique that uses the scattering of a laser by solid particles to determine the geometric dimensions of these particles. The Fraunhofer diffraction theory states that the angle of long-range diffraction of light is inversely proportional to the size of the particle diffracting it. Therefore, particle size can be estimated by measuring the diffraction angle of a laser passing through a suspension containing these particles.

If particles of multiple sizes are present, the light intensity of each angle is an indication for the amount of particles in that size range being present. This allows for easy measurement of a particle size distribution of a powder.

ThermoGravimetric Analysis (TGA)

Thermogravimetric analysis (TGA) is a thermal analysis method in which weight changes are measured in time at high temperatures. Often either temperature is kept constant for a certain period of time or the temperature is increased/decreased with a constant rate, in both cases measuring weight change of the sample over this period of time.

This analysis technique provides valuable information regarding thermal stability of a sample and phenomena that cause the sample to either gain or lose weight. Common processes for weight change are oxidation or other solid-gas reactions, chemisorption/physisorption, decomposition or evaporation. If the sample composition and environment are carefully controlled, important data on the rate at which these processes occur at certain temperatures can be gathered and the extend of these processes can be measured.

X-Ray Fluorescence (XRF)

X-ray fluorescence (XRF) is a technique that also uses X-rays to excite electrons, like XPS. However, the main difference is that in XRF, characteristic X-rays originating from the falling back of outer electrons to a vacant orbital in the core shells are measured instead of photoelectrons. These characteristic X-rays are also element specific, allowing for qualitative analysis. By measuring the intensities of each wavelength and proper calibration and correction, quantitative analysis is also possible. As X-rays do not interact in the same way as electrons with solids, energy loss by scattering is not possible and therefore the penetration depth is usually sufficient for bulk elemental analysis.

Inductively Coupled Plasma Optical Emission Spectroscopy (ICP-OES)

The ICP-OES technique works by introducing the completely dissolved sample into an argon plasma, in which the sample is subsequently ionized. Due to the constant ionization and recombination of the atoms present in the plasma, radiation with characteristic wavelengths of the elements present is constantly emitted. This radiation is then detected and the intensity of each wavelength is a good indication of the quantity of that element present.

centre, U. o. G. I. s. a. a. Scanning Electron Microscopy.
Goldstein, J. I., S. Choi, F. Van Loo, H. Heijligers, G. Bastin and W. Sloof (1993). "The influence of oxide surface layers on bulk electron probe microanalysis of oxygen—application to Ti-Si-O compounds." Scanning **15**(3): 165-170.
Moulijn, J. A., P. W. van Leeuwen and R. A. van Santen (1993). Catalysis: an integrated approach to homogeneous, heterogeneous and industrial catalysis, Elsevier.
Rosenbrand, G. G. (1986). The separation performance and capacity of zigzag air classifiers at high particle feed rates, Dissertation TU Eindhoven.

Appendix VI: The ALD setup

This appendix shows a flowchart of the ALD setup that was used in this research project.

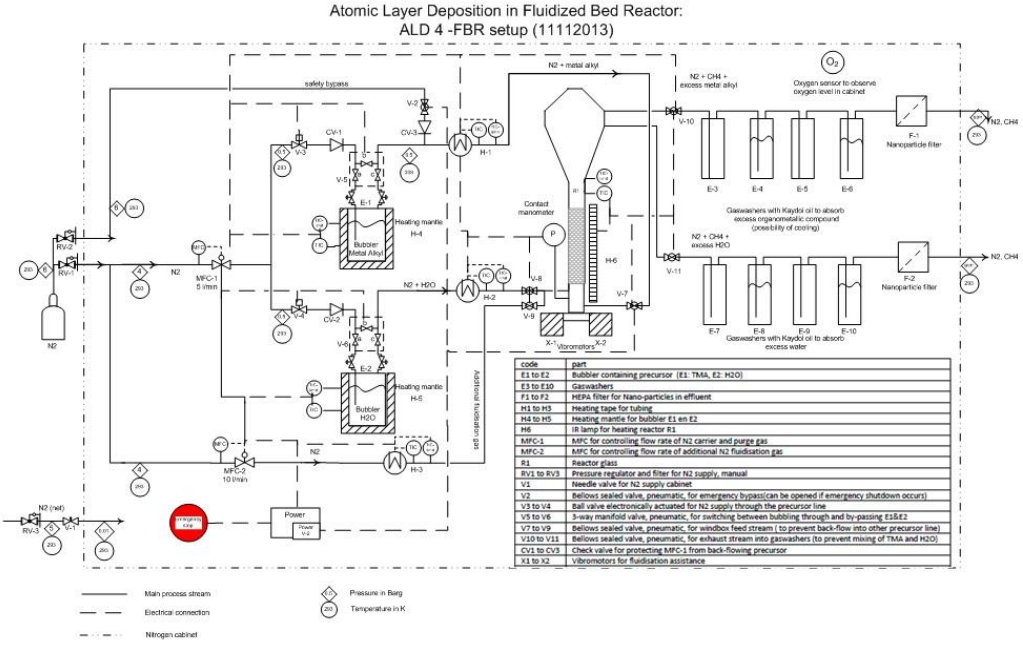

code	part
E1 to E2	Bubbler containing precursor (E1: TMA, E2: H2O)
E3 to E10	Gaswashers
F1 to F2	HEPA filter for Nano-particles in effluent
H1 to H3	Heating tape for tubing
H4 to H5	Heating mantle for bubbler E1 en E2
H6	IR lamp for heating reactor R1
MFC-1	MFC for controlling flow rate of N2 carrier and purge gas
MFC-2	MFC for controlling flow rate of additional N2 fluidisation gas
R1	Reactor glass
RV1 to RV3	Pressure regulator and filter for N2 supply, manual
V1	Needle valve for N2 supply cabinet
V2	Bellows sealed valve, pneumatic, for emergency bypass(can be opened if emergency shutdown occurs)
V3 to V4	Ball valve electronically actuated for N2 supply through the precursor line
V5 to V6	3-way manifold valve, pneumatic, for switching between bubbling through and by-passing E1&E2
V7 to V9	Bellows sealed valve, pneumatic, for windbox feed stream (to prevent back-flow into other precursor line)
V10 to V11	Bellows sealed valve, pneumatic, for exhaust stream into gaswashers (to prevent mixing of TMA and H2O)
CV1 to CV3	Check valve for protecting MFC-1 from back-flowing precursor
X1 to X2	Vibromotors for fluidisation assistance

Appendix VII: EDS maps of wind sifted $MoSi_2B$ particles

This appendix shows the elemental maps of wind sifted $MoSi_2B$ particles, as measured by EDS (acceleration voltage: 15 kV). In these images, the upper left figure shows the SEM-SEI image of the mapped area and the other figures are intensity maps of the indicated elements.

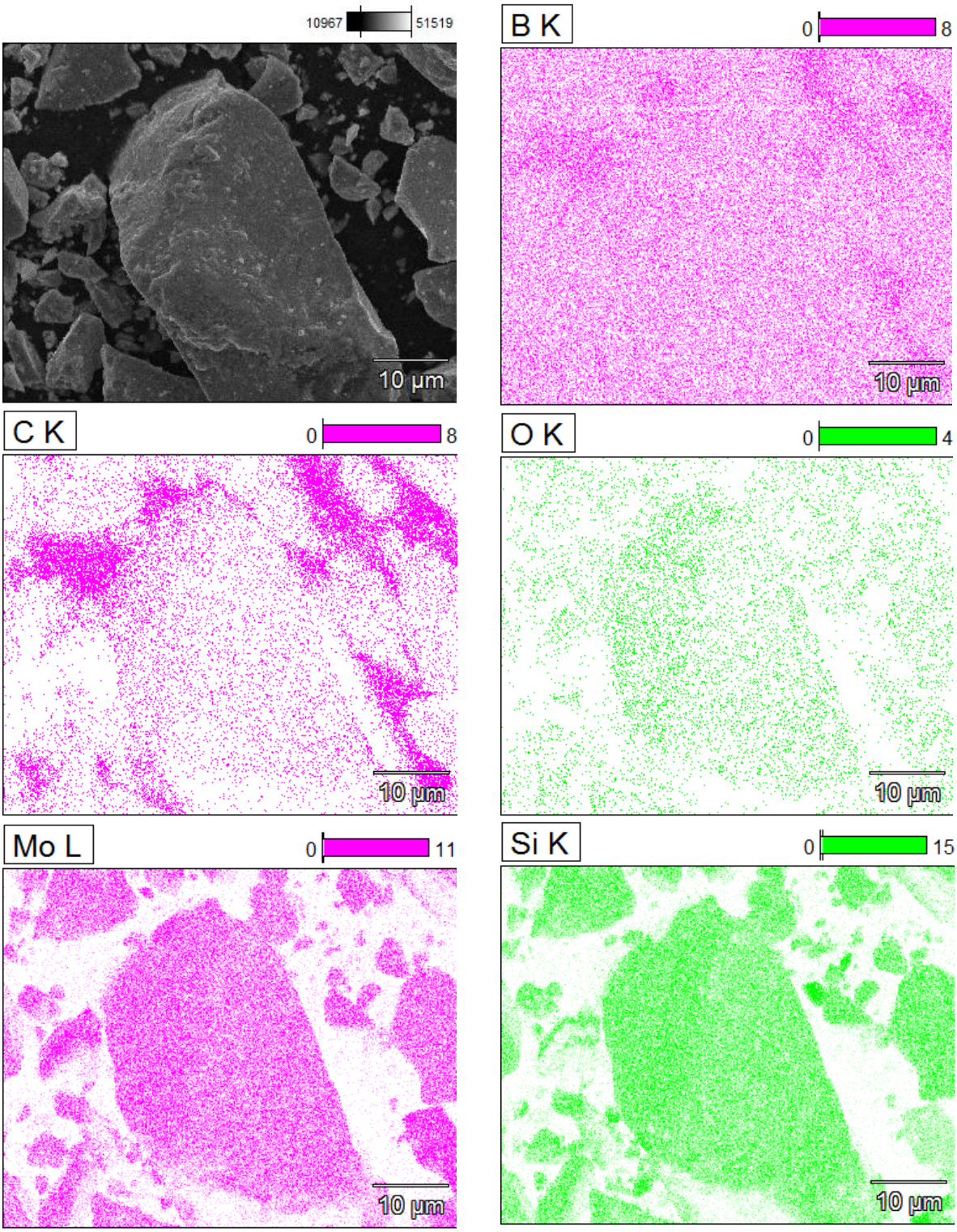

Appendix VIII: XRF results of $MoSi_2B$ particles

Presented in the table below are the elemental concentrations of the $MoSi_2B$ before and after wind sifting, as measured by X-Ray Fluorescence (XRF).

MoSi2B as received			MoSi2B wind sifted		
Element	Concentration (wt%)	absolute error (wt %)	Element	Concentration (wt%)	absolute error (wt%)
Mo	58.8	0.1	Mo	68.9	0.2
Si	40.5	0.1	Si	30.5	0.1
Fe	0.23	0.01	Fe	0.193	0.01
Zr	0.071	0.008	Mg	0.117	0.01
Mg	0.063	0.008	Al	0.049	0.007
W	0.061	0.007	Zr	0.047	0.007
Al	0.057	0.007	W	0.042	0.006
Cr	0.039	0.006	Cr	0.042	0.006
Bi	0.035	0.006	Ti	0.033	0.005
Ti	0.027	0.005	Ni	0.023	0.005
Ca	0.024	0.005	Cu	0.014	0.003
Cu	0.023	0.005			
Ni	0.021	0.004			

Appendix IX: EDS individual data points aluminium alkoxide coatings

This appendix shows the individual EDS measurements for the samples coated with an alkoxide as precursor.

Alumium isopropoxide sample		**Aluminium tri-sec-butoxide 20g evaporated**		**Aluminium tri-sec-butoxide 10g evaporated**	
Concentration Al detected (atom %)	error (atom %)	Concentration Al detected (atom %)	error (atom %)	Concentration Al detected (atom %)	error (atom %)
3.18	+/- 0.40	28.58	+/-0.20	18.51	+/-0.45
1.27	+/- 0.16	29.17	+/-0.20	11.48	+/-0.43
1.5	+/- 0.20	31.77	+/-0.24	17.25	+/-0.76
0.43	+/- 0.17	21.27	+/-0.21	21.98	+/-1.06
2.85	+/- 0.39	22.23	+/-0.18	7.16	+/-0.42
0.29	+/- 0.18	24.18	+/-0.16	2.83	+/-0.43
18.77	+/- 0.30	7.19	+/-0.19	17.19	+/-0.51
3.12	+/- 0.37	3.7	+/-0.22	6.77	+/-0.63
25.63	+/- 0.35	28.97	+/-0.20	16.56	+/-0.41
46.29	+/- 0.64	26.04	+/-0.17	11.35	+/-1.98
32.79	+/- 0.63	30.38	+/-0.21	11.23	+/-0.45
26.42	+/- 0.34	7	+/-0.25	12.53	+/-0.39
		18.3	+/-0.72	11.07	+/-0.40
Aluminium tri-sec-butoxide 5g evaporated		2.4	+/-0.11	8.03	+/-1.19
Concentration Al detected (atom %)	error (atom %)	27.25	+/-0.18	19.11	+/-0.68
12.91	+/-0.92	21.5	+/-0.15	9.01	+/-0.60
11.16	+/-1.27	21.87	+/-0.15	12.29	+/-0.48
7.42	+/-0.27	24.73	+/-0.16	26	+/-0.40
6.4	+/-0.45	31.82	+/-0.24	46.93	+/-1.13
13.06	+/-1.53	36.77	+/-0.35	15.68	+/-0.64
1.63	+/-0.23	31.94	+/-0.32	15.32	+/-0.47
8.27	+/-0.35	30.08	+/-0.21	12.29	+/-0.43
9.56	+/-0.43	34.03	+/-0.29	21.81	+/-0.57
		33.6	+/-0.29	2.46	+/-0.45
		25.66	+/-0.17		
		11.07	+/-0.34		

Aluminium tri-sec-butoxide 10g centrifuged	
Concentration Al detected (atom %)	error (atom %)
2.04	+/-0.23
0	?

Aluminium tri-sec-butoxide 20g centrifuged	
Concentration Al detected (atom %)	error (atom %)
1.65	+/-0.23
1.54	+/-0.27
1.7	+/-0.22
10.61	+/-0.72
2.47	+/-0.18
0.49	+/-0.08
14.11	+/-0.82
2.09	+/-0.14

Appendix X: TGA mass change graphs

This appendix shows the mass change graphs of the sol-gel samples that were tested with ThermoGravimetric Analysis (TGA) after coating to obtain important information regarding annealing behaviour. In this graph, the starting point at 25 °C is a mass change of exactly 0 mg/min.

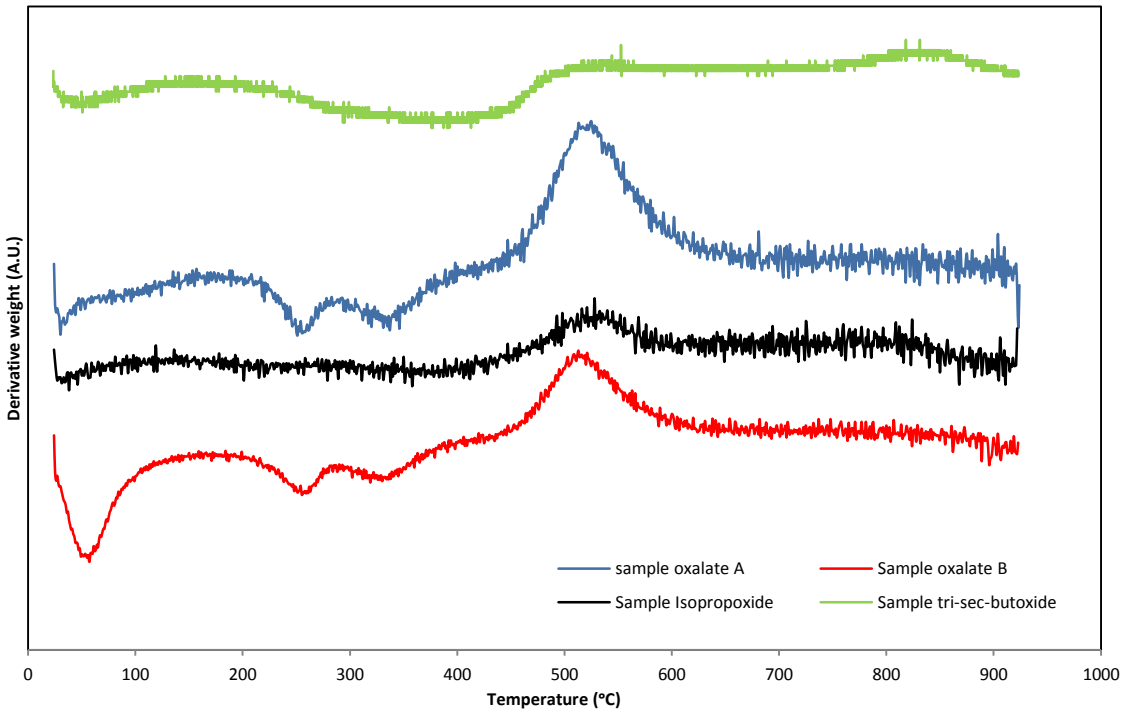

Appendix XI: XPS results main samples

This appendix presents the results of the XPS analyses performed on the sol-gel samples prepared with 10 and 20 g of aluminium tri-sec-butoxide (SG10g and SG20g respectively) and the ALD/rCVD samples that underwent 25 and 40 cycles (ALD25C and ALD40C respectively). The first figure shows the entire spectrum recorded with peaks indicated. The two figures below that show the results for the O 1s and the Al 2p peaks in more detail.

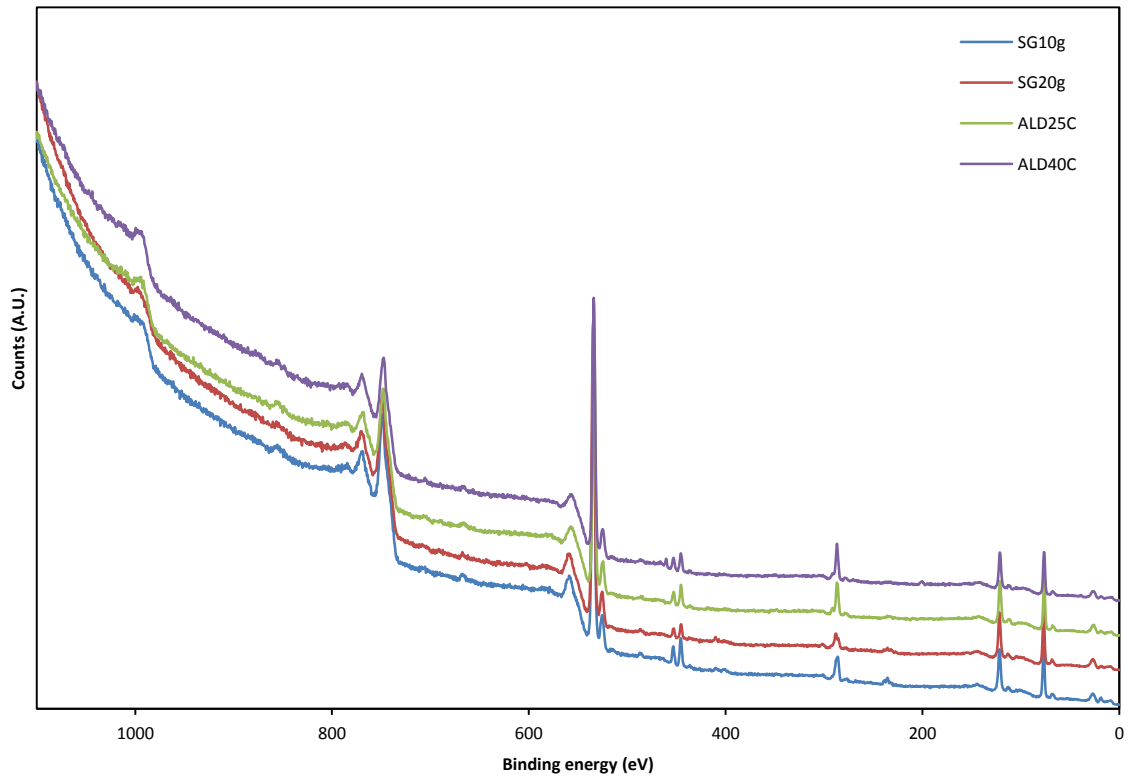

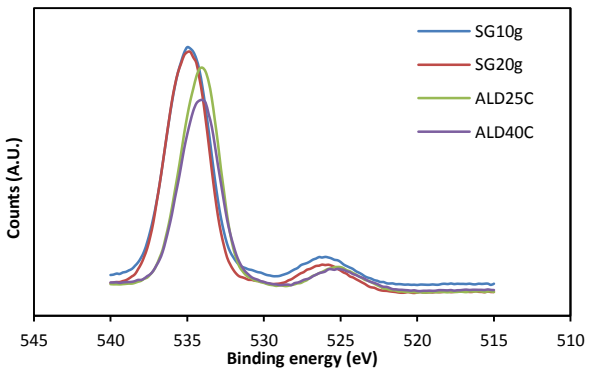

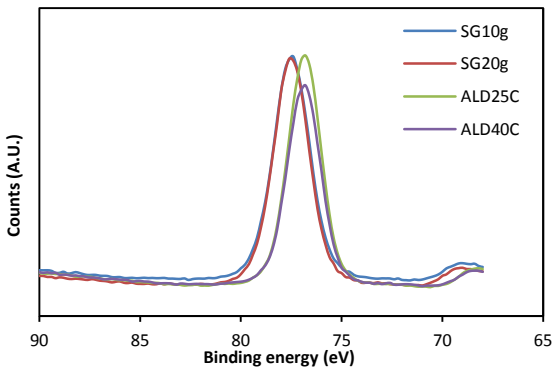

These results clearly show that the main constituent elements are as expected Al and O on the surface. The indium was detected because of the indium plates used as support in this analysis. When investigating the O 1s and Al 2p peaks, an interesting difference is visible between the sol-gel and ALD samples, but not between the two ALD samples or sol-gel samples themselves. This indicates a clear difference in chemical environment at the surface of the coatings produced with sol-

gel compared to ALD. This would be expected as the sol-gel samples should be consisting of boehmite (AlOOH) while the ALD samples should most likely consist of pure Al_2O_3 with some hydroxyl groups on the surface.

For both the O and Al binding energies, the shift is 1 eV between sol-gel and ALD (535.0 eV vs 534.0 eV for the O 1s and 77.8 vs 76.8 for the Al 2p energy), with the sol-gel being slightly more #weakly or strongly?# bound. Deconvolution and attribution of the various peaks is however difficult, as the literature peak values are slightly lower (between 530 and 532 eV for the O 1s and around 75 eV for the Al 2p) than measured here. It is however clear that there is a difference in chemical environment between the two production methods.

Furthermore, hydroxyl groups seem to have a tendency to shift the binding energy to slightly higher values, which would indicate that the sol-gel samples are likely to contain more hydroxyl groups than the ALD samples. This would be as expected, due to the expected lower hydroxyl content from the production process of ALD samples. If this is indeed the case, this is another argument in favor of the proposed mechanism of water condensation, as TMA condensation would likely result in a significantly higher content of hydroxyl groups in the bulk of the material due to the excess of water present during the water addition step.

Finally, XPS also gives an indication of coverage. If the intensity of elements present in the support is limited, this indicates that coating was successful. The first figure already shows a very low intensity for Mo and Si in the sol-gel samples and no peaks for the ALD samples. To ensure that this is indeed the case, a more detailed analysis of the Mo 3d5 peaks was made, which confirms the absence of Mo at the surface of the ALD particles and the very limited presence of Mo in the sol-gel samples, indicating that coating was successful with both methods.

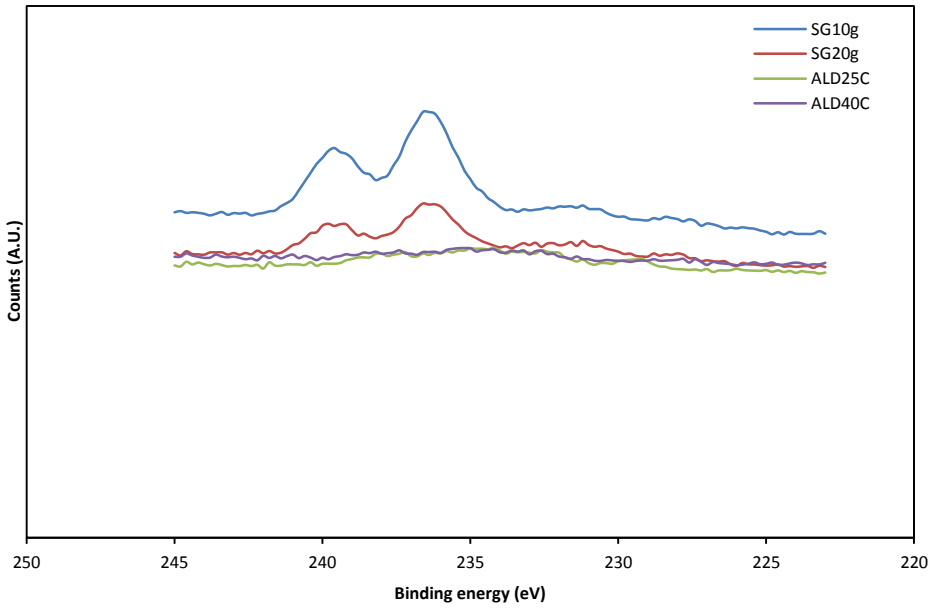

Appendix XII: Cross-section thickness measurement images

This appendix shows the Scanning Electron Microscopy Backscatter Electron Spectrum (SEM-BES) images used to construct the coating thickness distributions shown in the results chapter.

Sol-gel 10g images

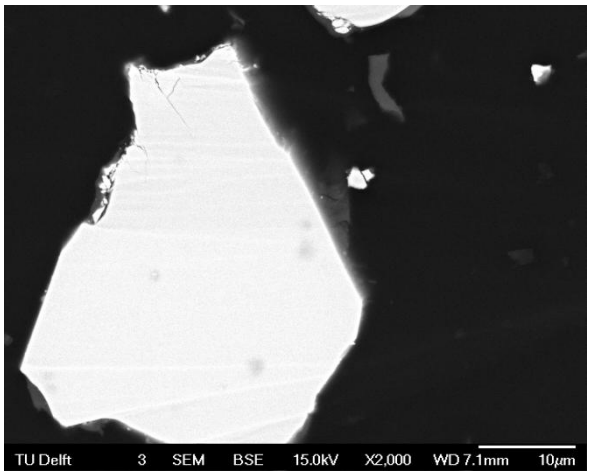

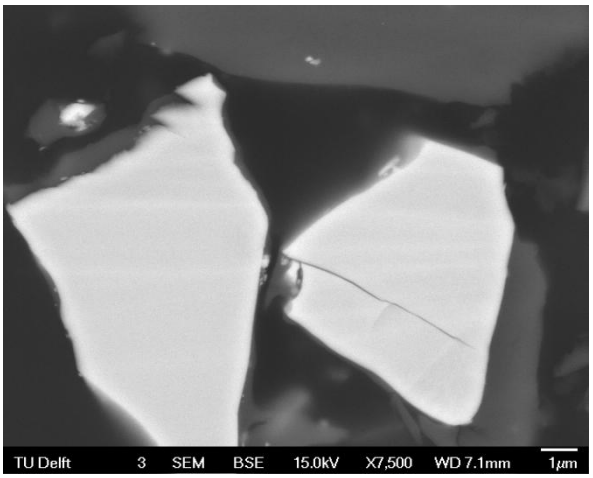

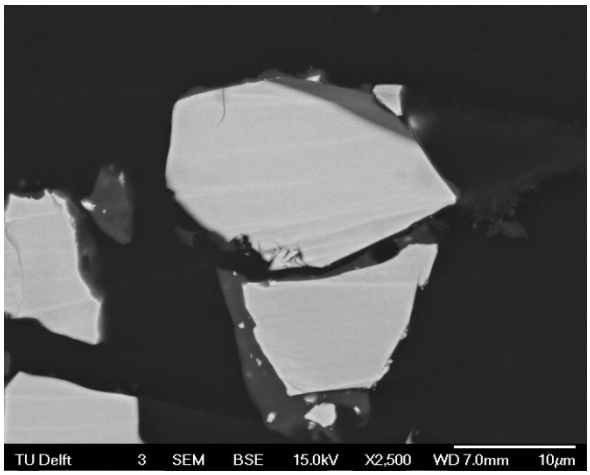

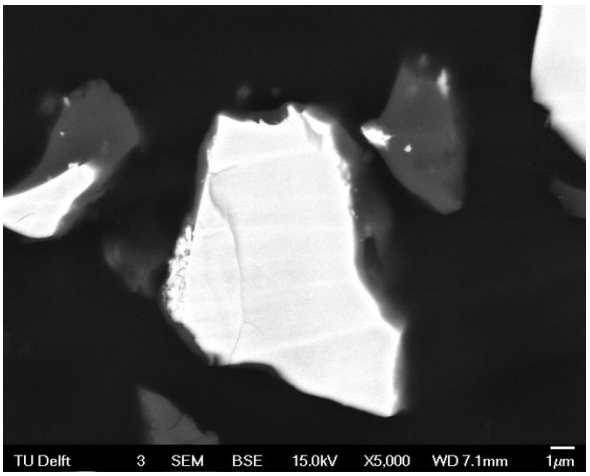

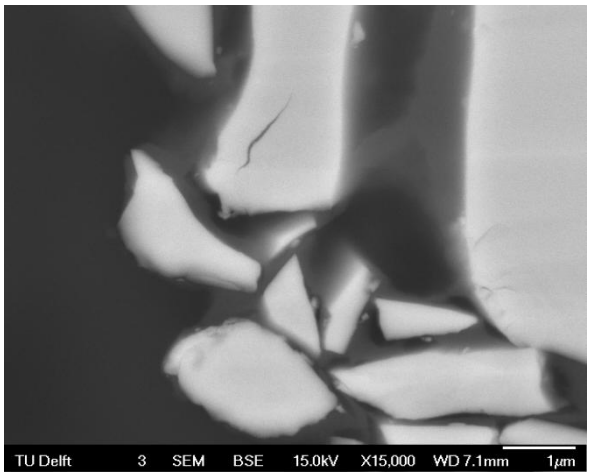

Sol-gel 20g

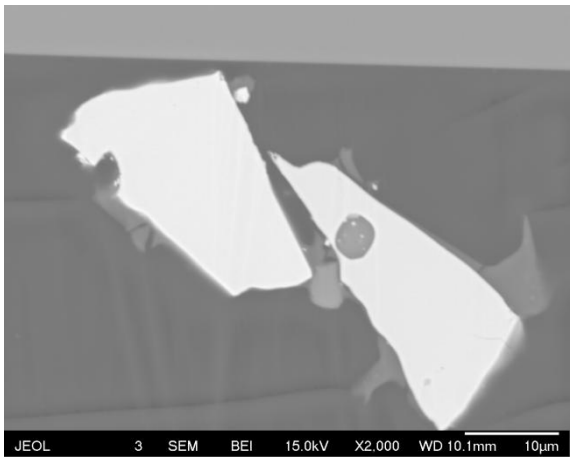
JEOL 3 SEM BEI 15.0kV X2,000 WD 10.1mm 10µm

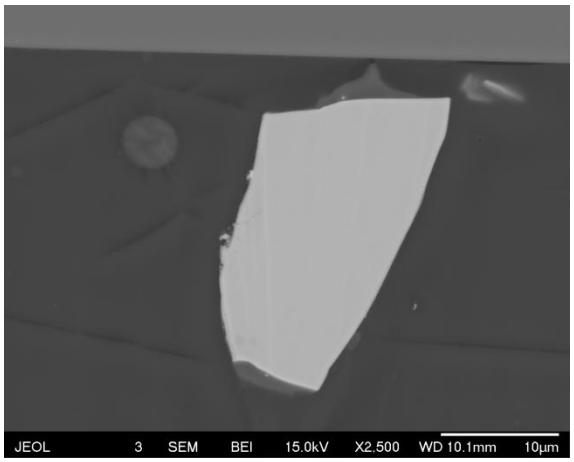
JEOL 3 SEM BEI 15.0kV X2,500 WD 10.1mm 10µm

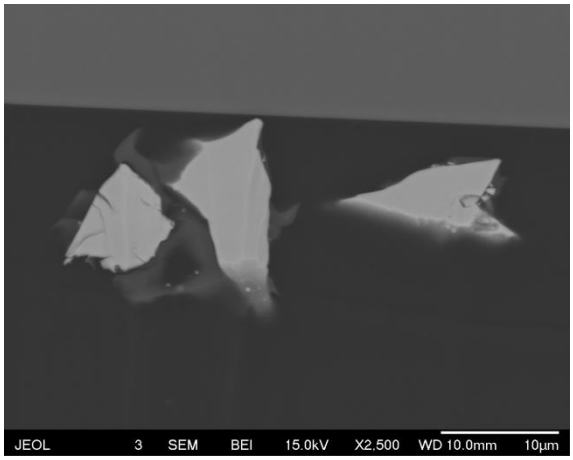
JEOL 3 SEM BEI 15.0kV X2,500 WD 10.0mm 10µm

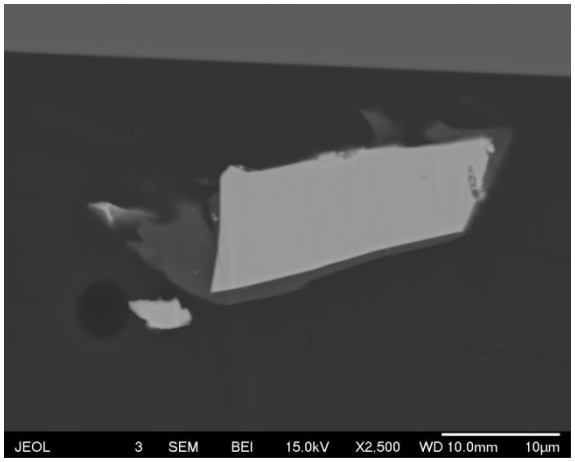
JEOL 3 SEM BEI 15.0kV X2,500 WD 10.0mm 10µm

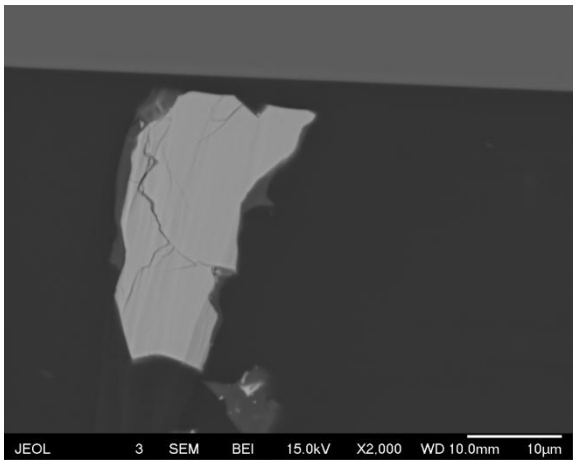
JEOL 3 SEM BEI 15.0kV X2,000 WD 10.0mm 10µm

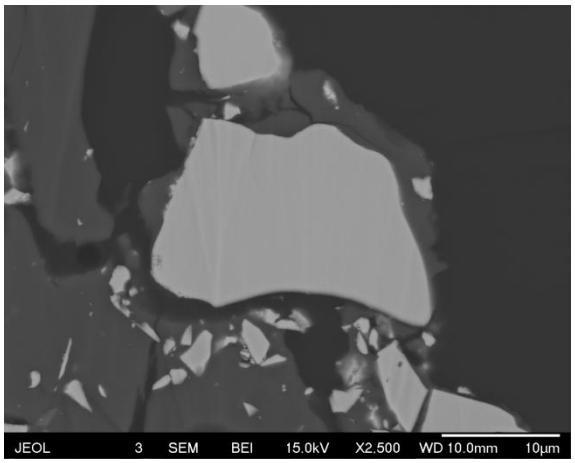
JEOL 3 SEM BEI 15.0kV X2,500 WD 10.0mm 10µm

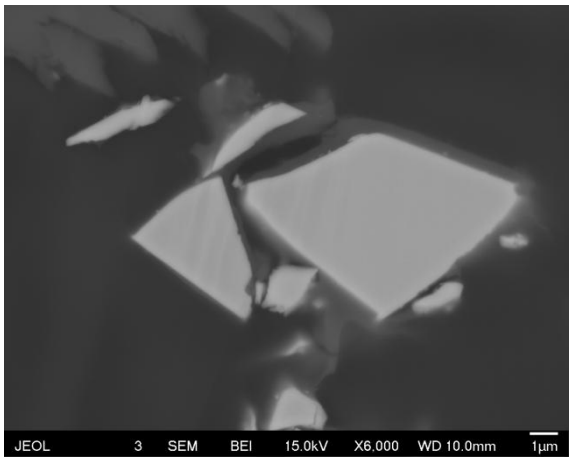

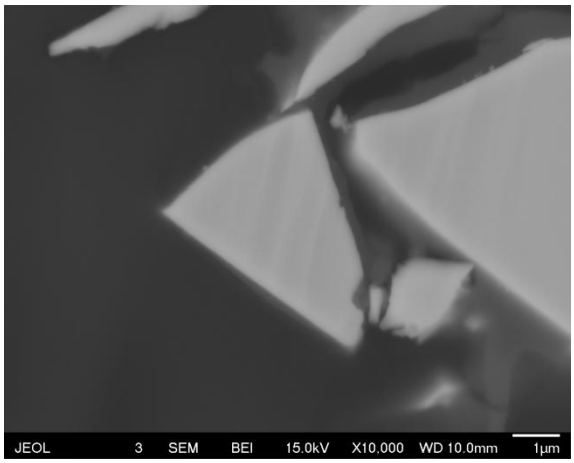

Sol-gel 20g after heat treatment at 1200 °C

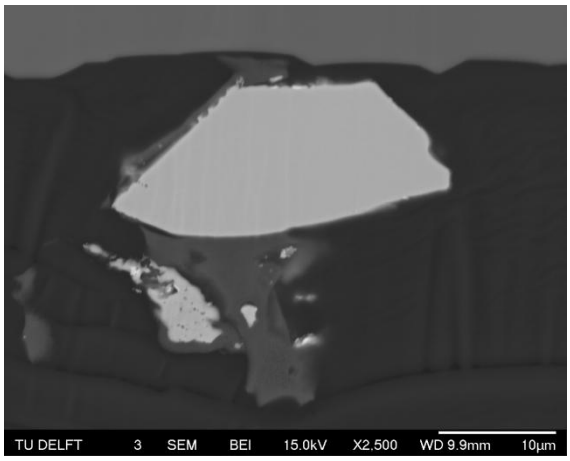

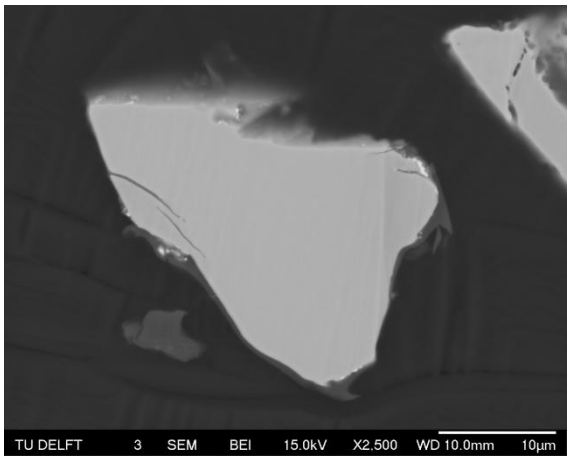

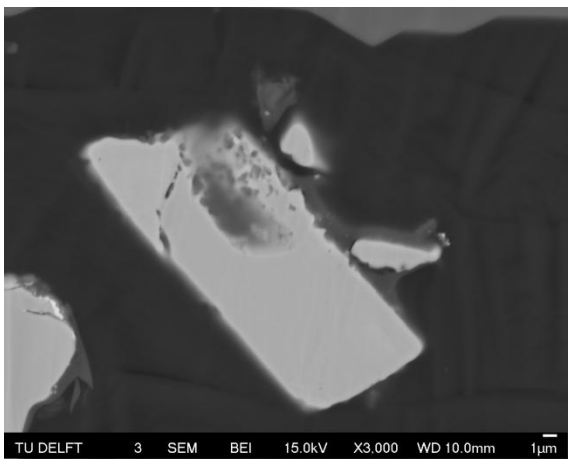

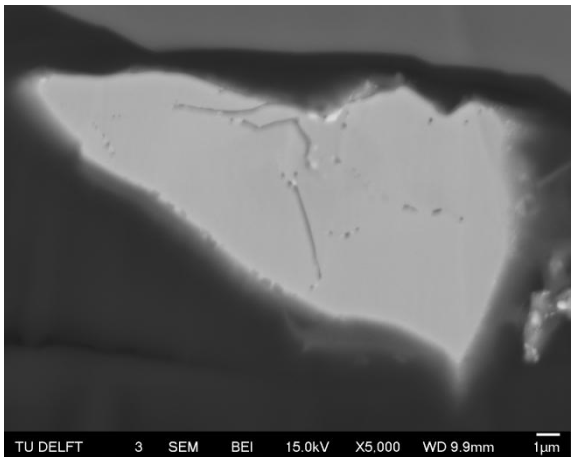

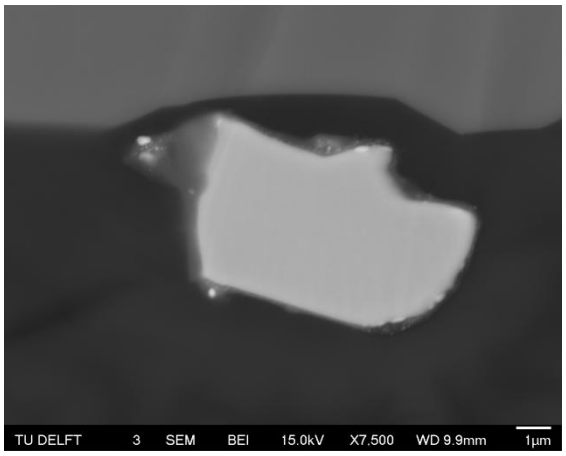

ALD 25 cycles

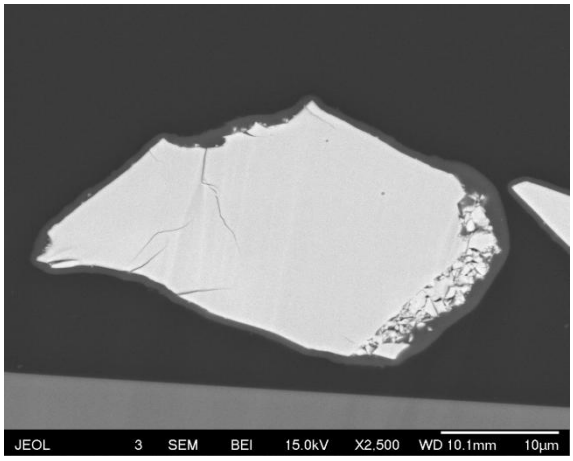

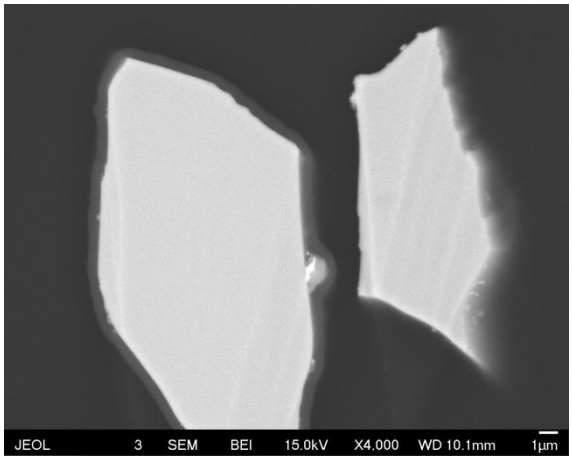

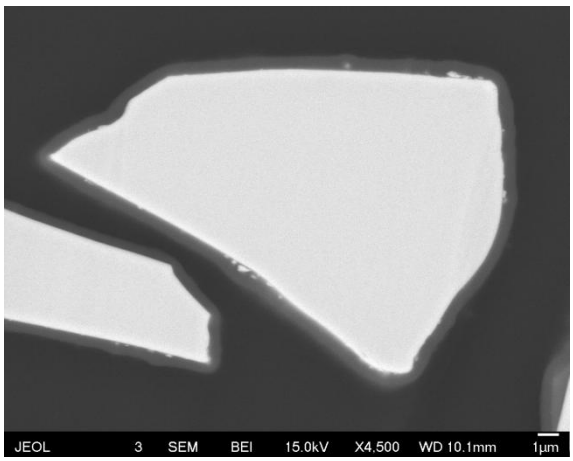

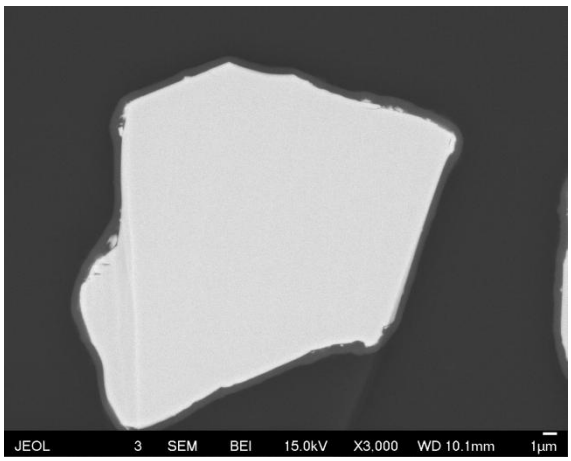

ALD 40 cycles

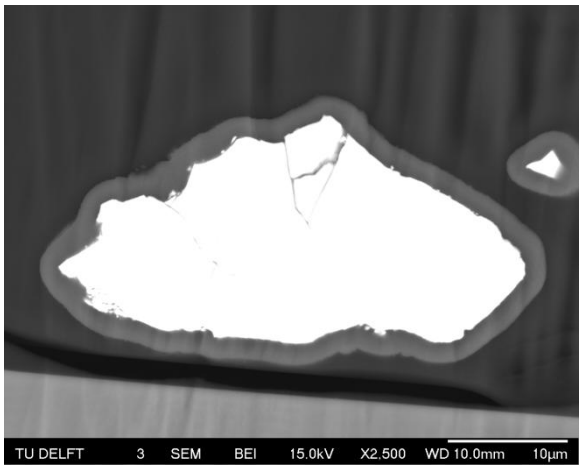

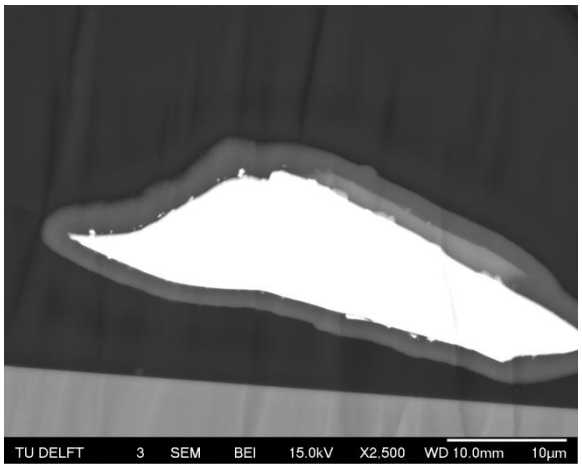

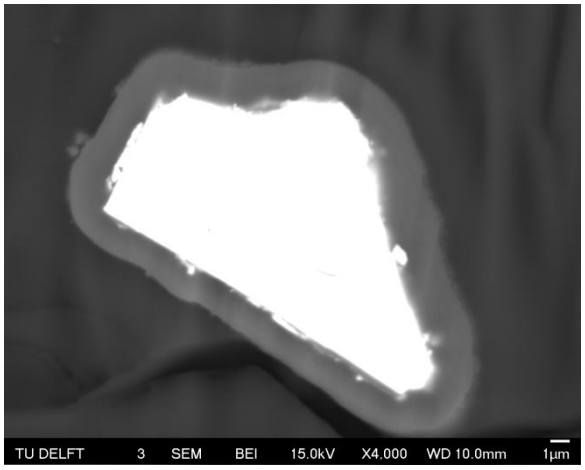

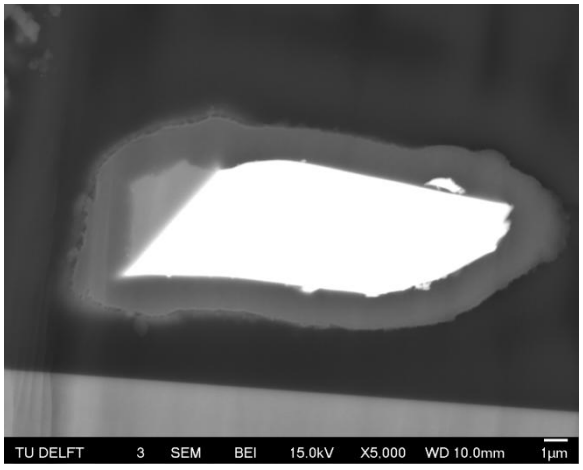

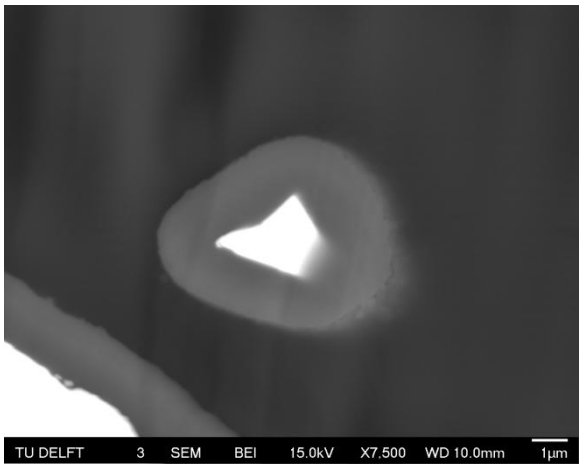

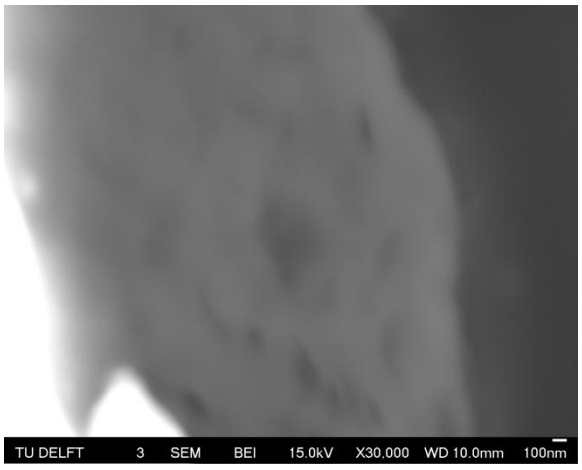

Appendix XIII: ICP-OES results for ALD samples

ICP-OES results for some of the samples are shown in the table below and did give results significantly lower than those of the EPMA method for those samples. This discrepancy most likely stems from the difficulty of dissolving aluminosilicates that most likely formed at the interface. However, due to Al and Mo interference, precision and accuracy were also limited, adding another factor that could explain this observation. This is evident from the blank, which contained less than 0.01 wt% Al, already containing 0.70 wt% Al according to ICP-OES. This is a significant amount compared to the 0.8-1.0 wt% detected in the other samples that were coated by alumina. #Should ICP results be reported? Not sure whether results relevant enough#

Table 5.1: ***ICP-OES results and calculated thickness of the alumina layer.***

Sample	Measured Al weight percentage (wt%)	calculated thickness alumina layer (nm)
Blank	0.7	-
4 min TMA	0.99	8.7
8 min TMA	0.99	8.9
0.5 min H2O	0.83	3.8

Appendix XIV: ALD 40 cycle particle EDS map

This appendix shows the elemental maps of a particle coated by ALD with 40 cycles, after heat treatment at 1200 °C, as measured by EDS (acceleration voltage: 15 kV). In these images, the upper left figure shows the SEM-SEI image of the mapped area and the other figures are intensity maps of the indicated elements.

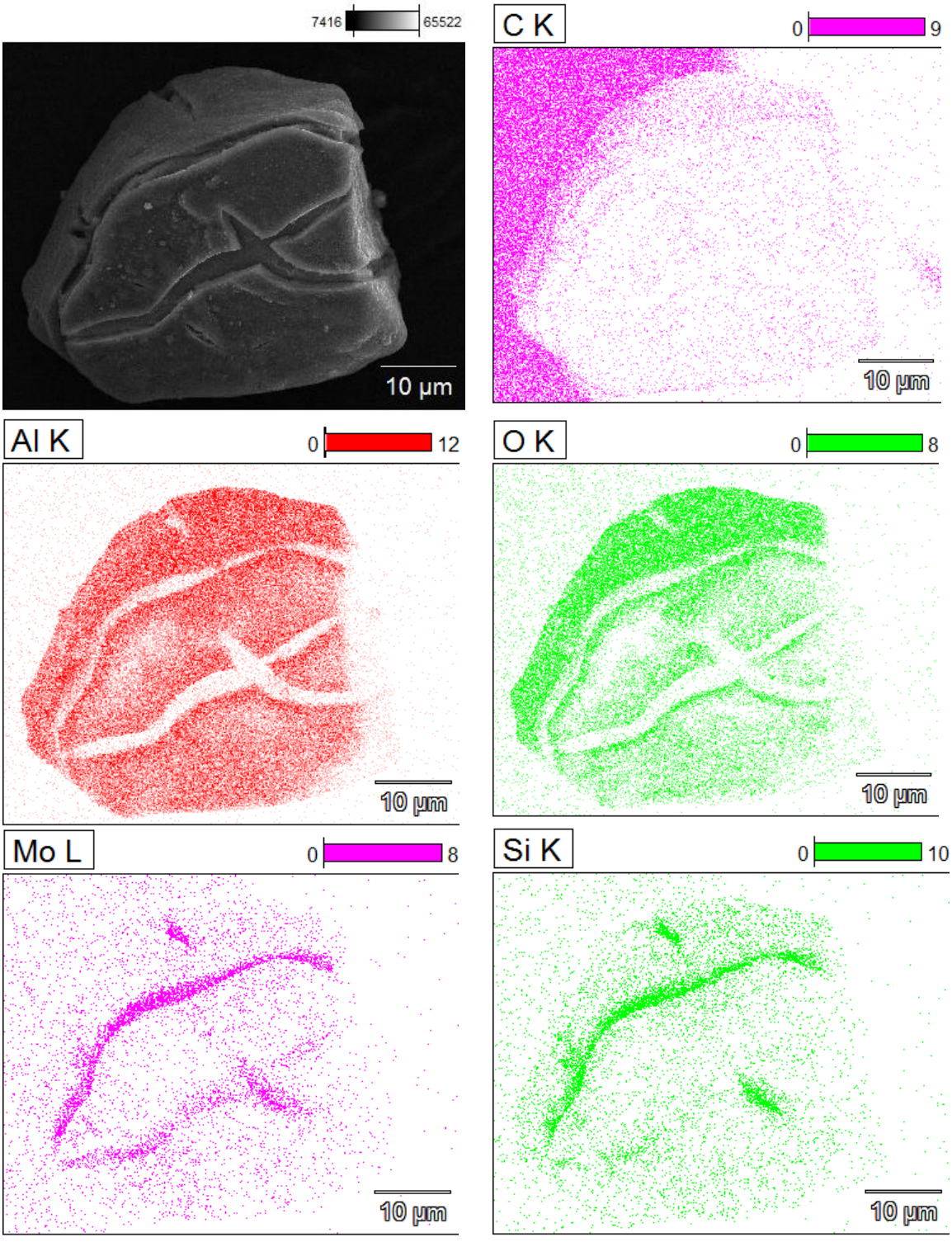

Appendix XV: EDS data of coated $MoSi_2B$ particles

This appendix shows the EDS data of $MoSi_2B$ particles coated with the sol-gel procedure mentioned in chapter 4 and annealed at 1200 °C. The SEM image indicates the locations of the points, while the detected atom % concentrations of each element can be found in the table below.

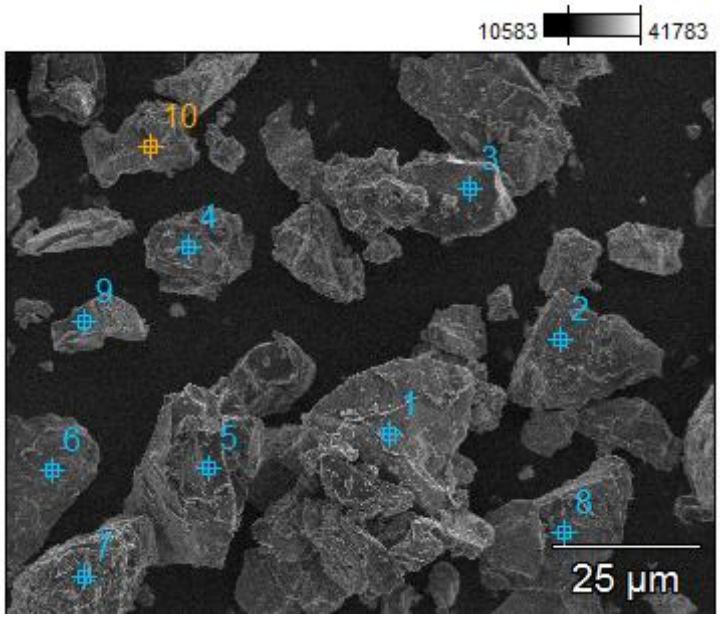

Table with atom % of each element detected.

	C-K	*O-K*	*Al-K*	*Si-K*	*Mo-L*
Point 1	20.72	17.37	4.9	38.38	18.63
Point 2	13.25	32.99	6.5	32.75	14.51
Point 3	9.25	39.52	13.29	26.4	11.53
Point 4	12.76	30.82	4.09	36.51	15.81
Point 5	12.16	51.7	31.58	3.72	0.84
Point 6	17.38	11.62	2.66	44.23	24.1
Point 7	2.96	48.34	37.86	9.01	1.84
Point 8	17.08	9.37	2.06	46.09	25.39
Point 9	9.77	55	25.36	6.52	3.36
Point 10	12.02	16.56	6.69	43.39	21.34

Appendix XVI: XRD diffractograms of YSZ powder and SPS samples

This appendix shows the XRD results of the investigation on the YSZ powder from Tosoh and three of the dummy SPS samples manufactured under different conditions. The powder did not receive any heat treatment after manufacture, while SPS-253 was processed in the SPS with a maximum temperature of 1350 °C for 10 minutes and both SPS 266 and 267 were processed at 1450 °C for 5 minutes. Pressure exerted by the machine was 35 MPa in all cases, but sample SPS 266 received an additional heat treatment in air for 1 hour at 1000 °C (heating and cooling rate 5 °C/min). XRD results are shown in the two figures below, with the first figure showing the entire diffractogram and the second figure magnifying the area around the largest tetragonal ZrO_2 peak around a 2θ of 30°.

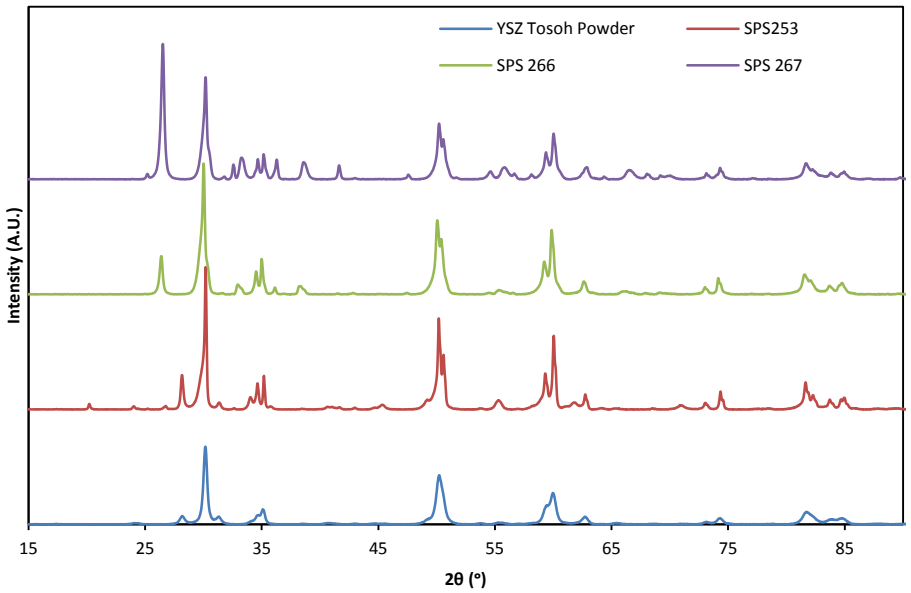

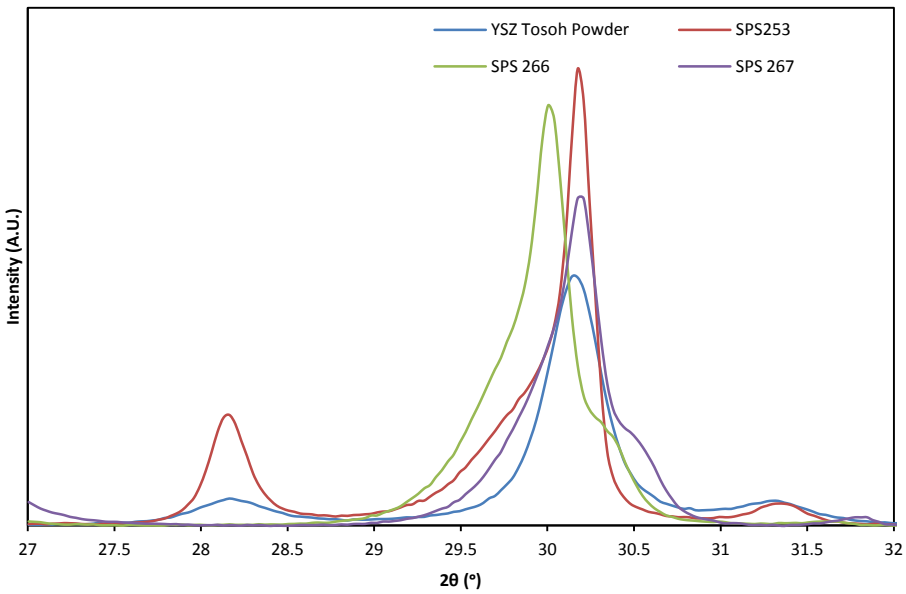

Appendix XVII: EDS maps of the YSZ/$MoSi_2B$ composite

This appendix shows the elemental maps of two areas of the YSZ/coated $MoSi_2B$ composite before and after heat treatment at 1200 °C for 1h, as measured by EDS (acceleration voltage: 15 kV). In these images, the upper left figure shows the SEM-SEI image of the mapped area and the other figures are intensity maps of the indicated elements, starting with the before images.

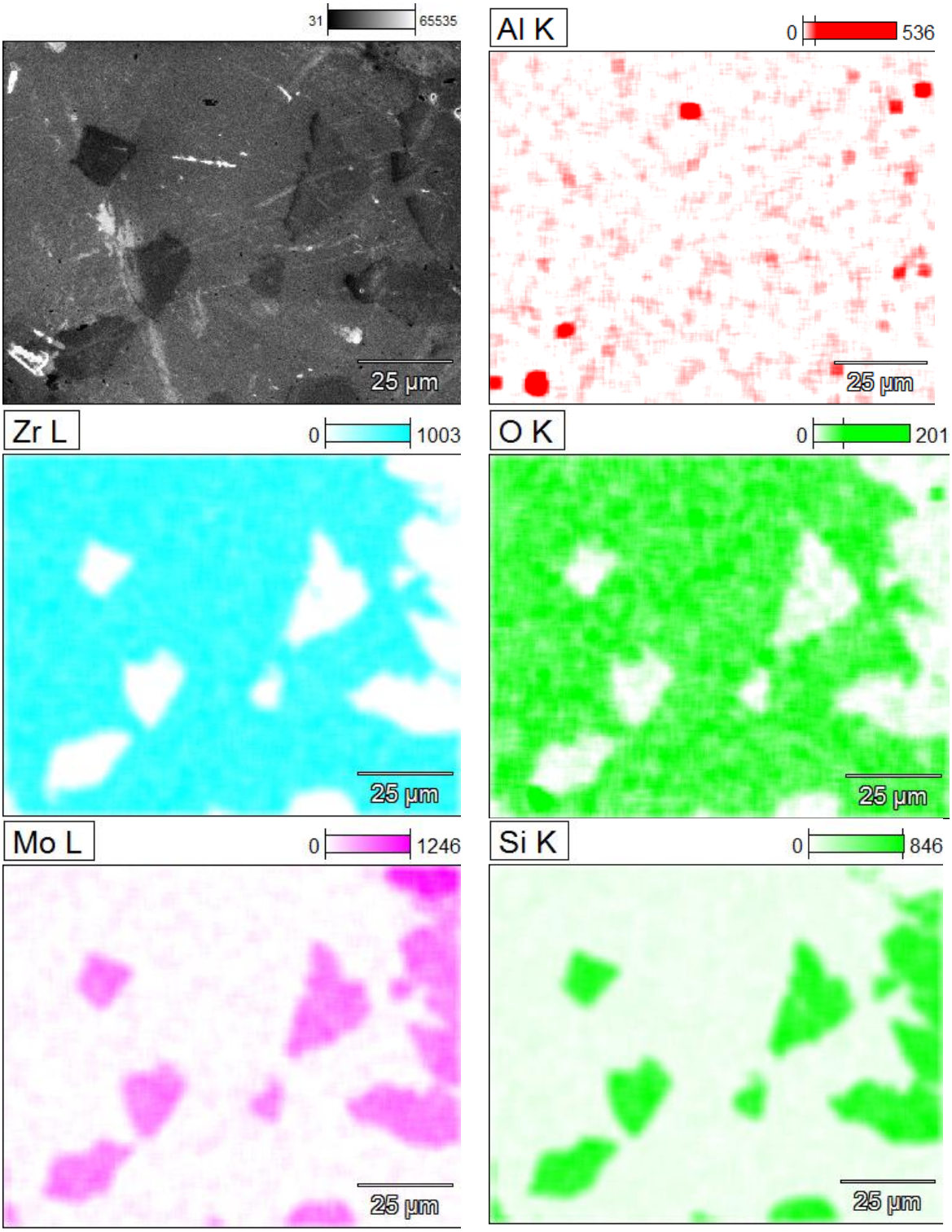

After healing for 1h at 1200 °C (different area).